Surface Chemistry of Halloysite Nanotubes

As Investigated by Adsorption Reactions and Imaging Analysis

Volume 1 of 1

Nia Bethan Gray-Wannell

Submitted to Swansea University in fulfilment of the requirements for the Degree of Doctor of Engineering

Swansea University

2020

Summary

Interest in halloysite clay minerals has increased steadily over the last 20+ years, in part, due to their nanotubular shape and size, high aspect ratio and potential technological applications (Churchman *et al*., 2016). Throughout this thesis the surface chemistry of halloysite nanotubes is investigated by employing several analytical and advanced microscopy techniques to obtain a greater understanding of their internal and external surface features and surface adsorption reactions. This multifaceted analysis approach investigates a range of tubular halloysites of two morphologies, cylindrical and polygonal prismatic, where comparison of the two forms a framework for the presentation and discussion of the results.

The results presented in Chapter 3 demonstrate the phosphate adsorption capacity of halloysite nanotubes is influenced by pH and maximum adsorptions of 1.3 mg/g and 0.5 mg/g were obtained for the cylindrical and polygonal prismatic morphologies respectively. Use of advanced microscopy techniques in Chapter 4 showed the external surface of the polygonal prismatic nanotubes have multiple steps and edges, which may act as additional adsorption sites, as has been shown for other clay minerals (Siretanu *et al*., 2016). In addition, use of cross-section transmission electron microscopy provided evidence of the link between the two morphologies, where the cylindrical nanotubes appear to be the template from which the larger polygonal prismatic nanotubes grow, as previously postulated by Hillier *et al*. (2016). In further novel work (Chapter 5), gold nanotags have been functionalised with a variety of anionic and neutral terminated linkers and used as nanoscale probes to study adsorption to the surface of halloysite nanotubes Here, transmission electron microscopy proved that the adsorption occurred primarily on the nanotube inner lumen and edges. The final technical chapter, Chapter 6, focuses on the structure and dynamics of interlayer water in halloysite through the use of neutron scattering techniques, where the initial results demonstrated that the interlayer water appears to move via both rotations and translations within the interlayer.

The research presented ascertains that the surfaces of the halloysite nanotubes are more complex than often depicted for technological applications and that the specific tubular morphology is important in the functionality and behaviour of the nanotubes. This fundamental work contributes towards optimisation of halloysite nanotubes for technological applications.

REFERENCES

Churchman, G.J., Pasbakhsh, P. & Hillier, S. (2016) The rise and rise of halloysite. *Clay Minerals*, **51**, 303-308.

Hillier, S., Brydson, R., Delbos, E., Fraser, T., Gray, N., Pendlowski, H., Phillips, I., Robertson, J. & Wilson, I. (2016) Correlations among the mineralogical and physical properties of halloysite nanotubes (HNTs). *Clay Minerals*, **51**, 325-350.

Siretanu, I., van den Ende, D. & Mugele, F. (2016) Atomic structure and surface defects at mineral-water interfaces probed by *in situ* atomic force microscopy. *Nanoscale*, **8**, 8220-8227.

Declarations and Statements

This work has previously not been accepted in substance for any degree and is not being concurrently submitted in candidature for any degree.

Nia Gray-Wannell

24/07/2020

This thesis is the result of my own investigations, except where otherwise stated and other sources as acknowledged by explicit references and a bibliography is appended.

Nia Gray-Wannell

24/07/2020

I hereby give consent for my thesis, if accepted, to be available for photocopying and for inter-library loan, and, for the title and summary to be made available to outside organisations.

Nia Gray-Wannell

24/07/2020

Contents Page

Acknowledgements

There are so many people to thank and acknowledge that it is hard to know where to begin. I should start by thanking Steve, first for giving me a job and then for (several years later) allowing me to take a career break to undertake this PhD. I would also like to thank Steve, Peter, and Chris for all of their guidance, advice and thought-provoking questions throughout the PhD and write up. A special thanks goes to my PhD funders, the Macaulay Development Trust, for enabling me to undertake this PhD.

From the Hutton Institute a big thanks to Ian, Helen, Evelyne, Laura-Jane, Carol, Fiona, Susan, Renate, Reza, Angie and Jean for all of their analytical expertise and allowing instrument/lab access when required. A special thanks to Tony for imparting some of his vast FTIR wisdom towards understanding and interpreting the spectra.

I really appreciate all the work that Peter and Chris put into ensuring that my time spent at Swansea Bay Campus was productive and I learnt a lot from Chris' synthetic chemistry knowledge and practical skills. In all, thanks to him and Eurig for their assistance when I was visiting and for being so welcoming. Also, to James for the excellent XPS analysis and Lee for the STA analysis.

Thanks to Pablo at Durham for his expertise, knowledge and patience for the AFM analysis and my tiny samples! Thanks also to Chris for facilitating these visits.

Many thanks to Zabeada and Rik at Leeds for all their TEM knowledge and skill and to the Royce Institute for funding the instrument time. In addition, Martin who prepared the thin sections for TEM analysis.

Many thanks to Neal, Aasim, Andrew, Sanghamitra and Tom for sharing on their neutron scattering knowledge and for their patient assistance and teamwork during the experiments. I learnt a lot and really enjoyed my time spent at ISIS for the neutron work.

My husband Neal deserves a special acknowledgement for his unwavering support which included early morning drop offs and late night pick-ups for the long lab days, constant encouragement and faith in me as well as his (over)enthusiasm to go through any maths problems that arose from first principles. Finally, a special thanks to baby GW whose imminent arrival ensured I handed in on time and who, with every kick and wriggle, provided a reminder to stay calm and relaxed whilst writing up this thesis.

List of Tables

List of Figures

Definitions and Abbreviations

AFM: Atomic force microscopy

BET SSA: Brunauer-Emmett-Teller specific surface area

DMF: Dimethylformamide

DTG: Derivative thermogravimetric curves

EDS: Energy dispersive analysis

FTIR: Fourier transform infrared

HNTs: Halloysite nanotubes.

ICP-MS: Inductively coupled plasma - mass spectrometry

ICP-OES: Inductively coupled plasma- optical emission spectroscopy

PVP: Polyvinylpyrrolidone

QENS: Quasi-elastic neutron scattering

SAEDP: Selected area electron diffraction patterns

SEM: Scanning electron microscopy

STA: Scanning thermal analysis

TBAB: Tert-butylamine-borane

TEM: Transmission electron microscopy

TGA: Themogravimetric analysis

XRPD: X-ray powder diffraction

Chapter 1

Introduction

Area of Study

This thesis will focus on the study of halloysite clay minerals, with emphasis on their surface chemistry and surface features. Throughout this thesis the effect of the tubular morphology, either cylindrical and polygonal prismatic, will be investigated and their respective surface features and adsorption behaviours compared. The work presented in Chapter 3 of this thesis aims to investigate the effect of the different morphologies on the anion adsorption capacities of halloysite nanotubes with use of the phosphate anion, as well as investigating the effect of the hydration state of the halloysite on phosphate adsorption. In addition, in Chapter 4, in-depth surface feature analysis of halloysites has been conducted using a variety of microscopy methods to gain a greater understanding of the external surface features of the nanotubes. This is especially relevant since they are often depicted as simplistic models when used in technological applications. Furthermore, the relationship between the two aforementioned tubular morphologies of halloysite is one that is currently not very well understood. This is likely an artifact of their nanoparticle size (generally <500 nm long) and their high aspect ratios, which result in much smaller tubular cross-sections, making imaging the particles themselves challenging. To date, this has meant that much of the reported morphological data has focussed mainly on coarse external features such as shape. To address this, cross-section image analysis has been conducted using transmission electron microscopy (TEM), which, in conjunction with atomic force microscopy (AFM) imaging of the external surface features aims to contribute to this hypothesis by providing some evidence of the link between the two morphologies. This work is presented in Chapter 4.

Chapter 5 of this thesis links up the two preceding chapters by employing synthesis and use of metal nanotags with specific anionic linkers designed to adsorb to the surface of the halloysite nanotubes, with the overall aim of then using electron microscopy methods to observe this adsorption on the halloysite surfaces through visualisation of the nanotags.

A further key question in halloysite nanotube research is the function of the naturally occurring interlayer water, and its effect on the nanotube formation and subsequent adsorption reactions. In Chapter 6 of this thesis initial neutron scattering experiments and results are presented to begin to understand more about this unique, but difficult to study, feature of halloysite nanotubes.

To put the thesis studies into context, this introductory chapter includes a detailed literature review which provides a complete overview of the background and relevance of the scientific challenges and aims outlined for this thesis.

Literature Review

1.1 HALLOYSITES AND CLAY MINERALS, AN INTRODUCTION

1.1.1 General background

Clay minerals are typically classified by geologists as hydrous layered aluminosilicates with a particle size of <2 μm (Huggett, 2005) and are present in most of the Earth's surface environments, where the surface environments can be further defined as soil systems, sea-beds and rock formations, for example.

Clay minerals can be classed in several ways, typically mineralogists refer to clay minerals as either 2:1 or 1:1 clay minerals, where the ratios refer to the different stacking of octahedral sheets which are composed of 6-fold coordinated aluminium sandwiched between two planes of oxygens/hydroxyls ($Al_2(OH)_6$) and tetrahedral sheets which consist of corner sharing silicon tetrahedra (SiO_4^{4-}). For a 1:1 clay mineral, the two types of sheets are stacked in a 1:1 ratio. In a 2:1 clay mineral, the layer stacking occurs with an octahedral sheet sandwiched between two tetrahedral sheets (Figure 1.1). Bates *et al*. (1950) calculated that the *b* dimension, usually defined in halloysites as the elongated tube around which the halloysite rolls, of the kaolin tetrahedral sheet is 8.93 Å, whilst the *b* dimension of the octahedral sheet is 8.62 Å, resulting in a mismatch between the two layers. The consequences of this size mismatch in halloysite will be discussed later in this chapter (Section 1.2.2).

Further classifications of clay minerals can be made by considering the occupancy of the octahedral sheet where a dioctahedral clay mineral has 2 out of 3 octahedral

positions occupied, leaving one octahedral site vacant whilst a trioctahedral clay has all 3 octahedral positions occupied, creating an electrostatically neutral sheet.

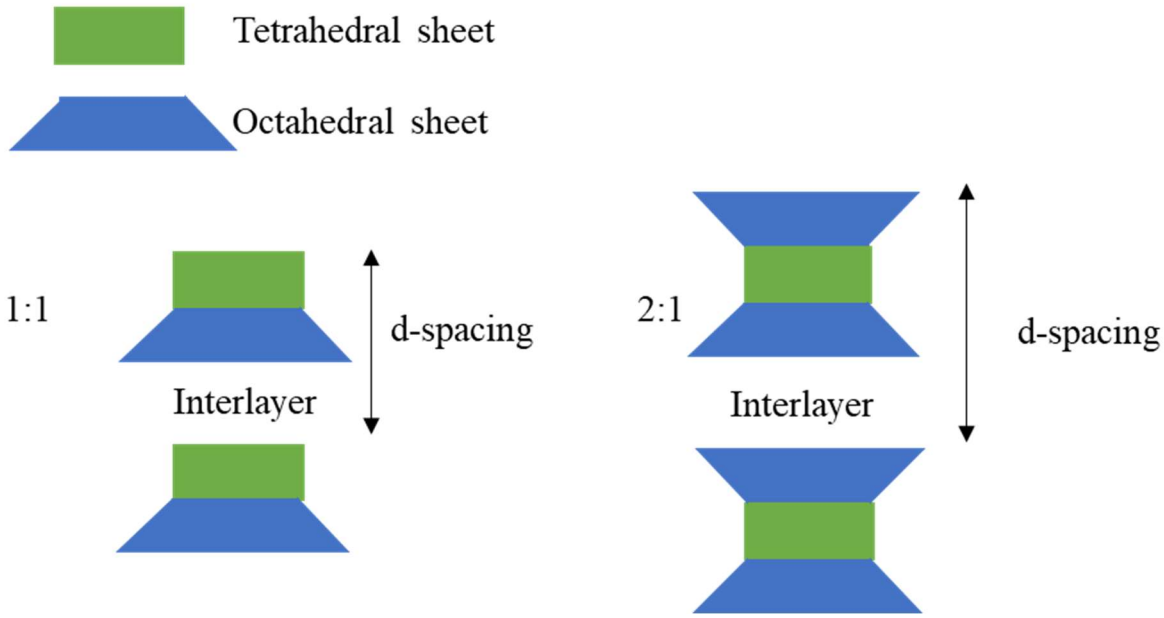

Figure 1.1. Layer stacking of a 1:1 clay mineral and a 2:1 clay mineral.

Kaolin group clay minerals can be classified as 1:1 dioctahedral clay minerals and are abundant in weathered rocks and soils around the world (Joussein *et al*., 2005). The four known kaolin subgroup minerals are kaolinite, halloysite, dickite and nacrite, the most studied being kaolinite. This thesis will focus on halloysite which was first identified by Berthier (1826) and is named after its discoverer, the Belgium geologist Jean-Baptiste d'Omalius d'Halloy.

Halloysite differs from other members of the kaolin group in that it occurs naturally with a monolayer of water molecules between the unit layers and has the ideal unit formula $Al_2Si_2O_5(OH)_4.nH_2O$ where n is between 0 and 2 depending on the state of hydration (Bailey, 1980). The naturally occurring, fully hydrated halloysite has a basal d-spacing of ~10 Å compared to ~7 Å for dehydrated halloysite, kaolinite, dickite and nacrite. As a result, the Nomenclature Committee for the Association Internationale pour l'Etude des Argiles (AIPEA) recommended in 1975 that the two end-member hydration states be officially named as halloysite (10 Å) and halloysite (7 Å), respectively. Halloysite occurs naturally in a variety of morphologies, the most common being tubular, but spheroidal and platy forms also exist. Due to their nanotubular shape, tubular halloysites are often referred to as halloysite nanotubes or

HNTs for short. Throughout this thesis, the nomenclature of halloysite nanotubes will be applied.

Pure halloysites are typically white in colour and have a hardness of 1-2 on Mohs scale (Mindat.org), as a result they are easy to crush for sample preparation. This white colour indicates that halloysites are effectively pure and display an ordered electronic structure with a large band gap. Whilst this is expected for Si-O and Al-O, it also suggests that little doping of other metal ions occurs within the halloysite structure, since any defect states in the structure would very likely be situated within the band gap and hence, result in visible light adsorption. Figure 1.2 is an example of a hand specimen of halloysite.

Figure 1.2. Example of a typical specimen of halloysite.

1.1.2 Occurrence and formation of halloysites

Halloysite is formed from a range of both igneous and non-igneous rocks and can be found worldwide in many weathered rocks and soils (Joussein *et al*., 2005). Halloysite has also been reported by Churchman and Lowe (2012) as being one of the most common secondary minerals formed from volcanic material and tephra where the occurrence of halloysite varies substantially between different geological environments. The formation conditions of halloysite by weathering necessitates a

hydrated environment and its formation is often noted in low pH environments (Cravero *et al*., 2014; Churchman *et al*., 2016).

The occurrence of halloysites worldwide has resulted in several commercially mined deposits. The main commercial halloysite deposits can be found in China, New Zealand, Japan, Turkey and the United States (Cravero *et al*., 2012; Wilson *et al*., 2016). These halloysite deposits are typically of high purity as supported by the analysis of multiple samples that have come through the commercial X-ray diffraction facilities at the James Hutton Institute for quantitative mineralogical analysis. These studies suggest that typical impurities, when present, include minerals such as kaolinite, quartz, anatase, alunite, iron-oxides, micas, and feldspars, for example. Since these impurities occur as separate phases, i.e. not within the crystal structure of the halloysite nanotubes, this is suggestive of a high lattice energy for the halloysite nanotubes which is also in agreement with apparently low doping observed for halloysites. One example of the low cost and facile mining of halloysite is The Dragon Mine in Utah, USA. The mine is owned by Applied Minerals and has an estimated measured resource of over two million tonnes of halloysite clay (www.appliedminerals.com), some *in situ,* and some from surface piles which had been formed through excavations by previous operators between 1949-1976. The fact that halloysite is a relatively low cost and easily mined mineral has resulted in its consideration for use in numerous technologies (Lvov *et al*., 2016).

1.1.3 Applications of halloysites

Halloysites are often considered as natural nanotubes and are attractive to industry as a non-toxic nanomaterial (Yuan *et al*., 2015), where several studies have verified the low toxicity of these materials (Vergaro *et al*., 2010; dos Santos *et al.,* 2017). Until around 2005 the main use of halloysite was as an alternative to kaolinite in ceramics (Wilson, 2004; Joussein *et al*., 2005). However, over the last 20+ years, there has been increasing interest in the different applications of the mineral. This can be seen in the exponential increase in publications on halloysite and the approximately equivalent number of patents which refer to halloysite (Churchman *et al.*, 2016).

In recent years, the tubular form of halloysite with its nanoscale central lumen, the term for the hole running through the centre of the halloysite nanotubes, along with other useful physical and chemical properties, such as high length to diameter ratio

and lack of toxicity, have been central to its increasing application in existing and emerging technologies such as drug delivery systems (Lvov *et al*., 2016; Massaro *et al*., 2017), as fillers in polymer nanocomposites and plastics (Du *et al*., 2008; Pasbakhsh *et al*., 2013; Yuan *et al*., 2015), flame retardant materials, catalysts (Levis and Desy, 2002) and in lithium sulphur batteries (Lin *et al*., 2017), amongst many others. This interest in halloysites in existing and emerging technologies emphasises that more needs to be understood surrounding the fundamentals of the surface chemistry of these materials.

1.2 HALLOYSITE STRUCTURE

1.2.1 Surface chemistry and crystallography of halloysites

As mentioned in Section 1.1.1 halloysites are 1:1 aluminosilicate clay minerals with the ideal chemical formula $Al_2Si_2O_5(OH)_4.nH_2O$ where n is between 0 and 2, depending on the hydration state of the halloysite (Bailey, 1980). The structure consists of a tetrahedral siloxane sheet and an octahedral alumina sheet which are connected by apical bridging oxygens (Al-O-Si) and interlayer hydrogen bonding holds the 1:1 unit layers together (Figure 1.3). The unit cell dimensions for halloysite (10 Å) as a ~ 5.1 Å, b ~ 8.9 Å, c ~ 10.2 Å whilst for halloysite (7 Å) they are a ~ 5.1 Å, b ~ 8.9 Å, c ~ 7.3 Å. For tubular halloysites, the long axis of the nanotube is most often coincident with the crystallographic b axis.

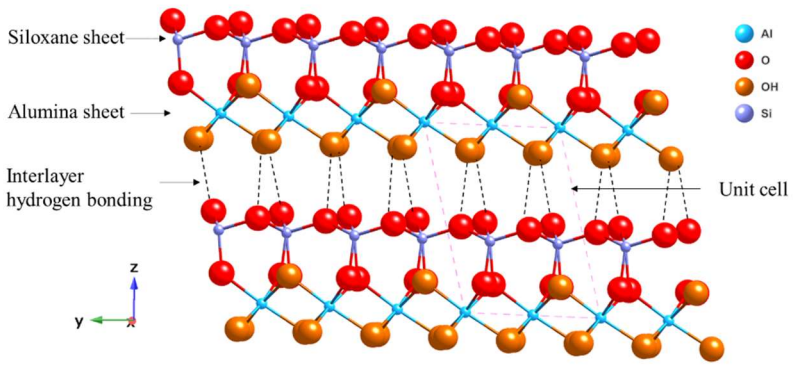

Figure 1.3. Labelled crystal structure of halloysite (7 Å) (n H_2O = 0) showing a tetrahedral siloxane sheet and octahedral alumina sheet which together comprise one unit 1:1 layer. Subsequent layers are held together by hydrogen bonding.

The Si-O-Si tetrahedral arrangement of basal sites in the siloxane sheet results in ditrigonal surface cavities (Figure 1.4). These 'holes' are surrounded by six sets of oxygen lone pair orbitals which can act as weak electron donors (Bache, 1990) and some authors have gone as far as to suggest that a permanent negative charge is present in these cavities (Davis & Kent, 1990; Peacock & Sherman, 2005). As will be discussed later in this chapter, and throughout the thesis, these sites are important in understanding the arrangement of interlayer water in halloysites.

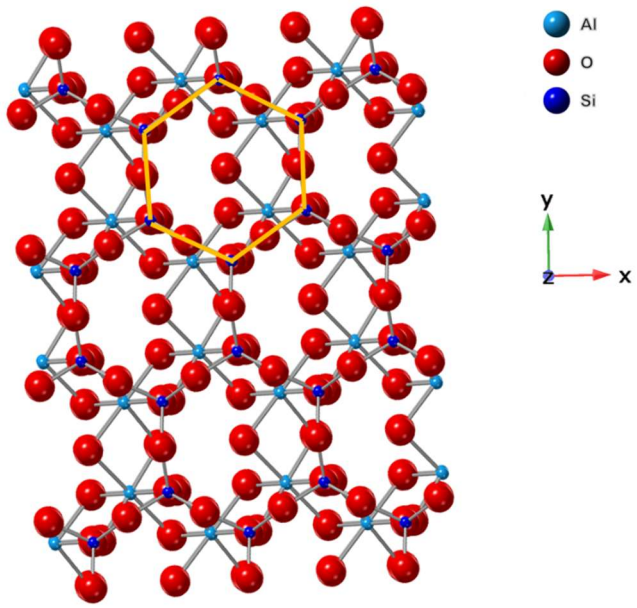

Figure 1.4. Diagram of the siloxane sheet arrangement that results in 'holes' surrounded by oxygen lone pair orbitals. The orange outline shows one such 'hole'.

In the alumina sheet, a 'gibbsite-like' surface arises along the ab plane since each aluminium is linked to two apical oxygens from the siloxane layer whilst the remaining four aluminium's in the octahedral arrangement share 4 hydroxyls with adjacent aluminium atoms. Three of these four bidentate $>Al_2OH$ are facing the external surface, the fourth is oriented towards the siloxane cavity and is positioned internal to the octahedral sheet. Figure 1.5 depicts the different orientations of these hydroxyl groups and this distinction in orientation of hydroxyls in the octahedral sheet has been observed by Fourier transform infrared (FTIR) analysis and will be referenced throughout this thesis.

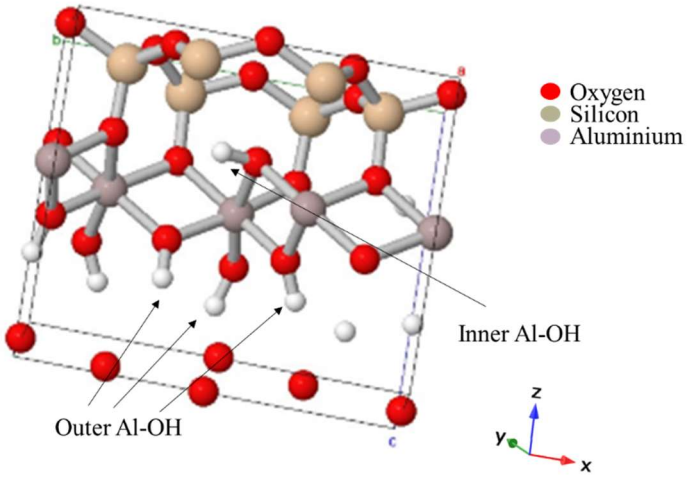

Figure 1.5. Orientation of the hydroxyl groups in the octahedral alumina sheet. Each aluminium atom shares four hydroxyl groups with adjacent aluminium atoms, three of which are orientated towards the external face of the layer and are labelled as 'outer Al-OH', whilst one is orientated towards the siloxane layer and is hence labelled as 'inner Al-OH.' Image sourced from Bish, D.L. (1993).

In the case of halloysite nanotubes, the siloxane sheet forms the outer surface whilst the inner lumen exposes the alumina sheet (Bates *et al*., 1950). Often, especially in studies of the application of halloysite in new technologies, these two surfaces are labelled as distinctly charged, with the outer siloxane surface exclusively negatively charged and the inner aluminol surface as positively charged (Bretti *et al*., 2016; Massaro *et al*., 2017). Studies on the surface charge of kaolinites have highlighted two distinct sources of charge; the in-plane basal sites in the tetrahedral sheet and the edge sites of both the octahedral and tetrahedral sheets, where charge is pH dependent (Zhou & Gunter, 1992; Brady *et al*., 1996; Gu & Evans, 2008). The permanent basal charge on the kaolinite siloxane sheet may arise due to isomorphic substitution of Al^{3+}/Fe^{3+} for Si^{4+}, although a study by Sposito (1984) suggested that the degree of ionic substitution is very small and the layer charge was estimated at <0.01 per $[(Si_4)(Al_4)O_{10}(OH)_8]$ formula unit. In the case of halloysites, Bailey (1990) proposed that they exhibit a small net negative charge in the siloxane sheet due to substitution of Si^{4+} for Al^{3+}, yet the isomorphous substitution of Fe^{3+} for Si^{4+} in the siloxane sheet has never been reported (Joussein *et al*., 2005). Although these substitutions of Al^{3+}/Fe^{3+} for Si^{4+} have been postulated to occur in the tetrahedral sheet (Bailey, 1990), there remains little firm evidence for their occurrence. Therefore, it is likely, as

predicted by Sposito (1984), that where substitution does occur it is to a small degree and contributes very little to the overall surface charge.

Further debate arises in understanding of the charge of the aluminol basal layer, which, in the case of halloysites forms the surface of the lumen. Fundamental surface studies on kaolin group minerals (Huertas *et al*, 1998; Tari *et al*, 1999; Levis and Deasy, 2002; Gupta and Miller, 2010) have used methods such as zeta potential and atomic force microscopy (AFM) to postulate that, at lower pH's, the alumina displays a positive charge, meaning it is protonated, whilst above approximately pH 4-6 the alumina basal sheet is negatively charged. In contrast, Han *et al*. (2016) suggested that the alumina sheet is positively charged over a large pH range. Given the importance of surface charge within the context of adsorption of ions, a key theme of this thesis, the surface charges on the halloysite nanotubes will be investigated in this thesis using zeta potential measurements (Chapter 3, Section 3.3.3).

It is widely accepted that the hydroxyl edge sites of both the aluminol and silanol sheets have a pH dependent charge. The edge sites of both alumina and siloxane sheets are both proton donor groups which can form complexes with metal cations as per the mechanism of proton transfer given below for amphoteric surface sites.

$$\equiv SOH_2^+ \leftrightarrow \equiv SOH + H^+$$

$$\equiv SOH \leftrightarrow \equiv SO^- + H^+$$

Where ≡ SOH is a surface binding site. Silica has a higher atomic charge than aluminium and so will have a less ionic hydroxyl group, resulting in shorter Si-OH bonds, which are harder to deprotonate. Therefore, silanol groups have a pKa(int) = -2 (Abendroth, 1970) compared to that of the aluminol edge sites (pKa ~ 4.5-8) (Huertas *et al.,* 1998) and so only the aluminol moieties (Al-OH) can act as proton acceptor groups for anion adsorption. In contrast, the protonated aluminol sites have been shown to be the sites of anion adsorption in kaolin group minerals (Theng *et al*., 1982; Van Emmerik *et al*., 2007; Han *et al.,* 2016), which will be investigated further in Chapters 3 and 5 of this thesis.

While there are fewer fundamental studies for the surface charge and behaviour of halloysites compared to number of surface studies of kaolinites, the investigations that have been conducted suggest that halloysites show a different behaviour despite being

composed of essentially the same building blocks. For example, Tari *et al*. (1999) showed that the zeta potential curves in the transformation of kaolinite to halloysite changed along with changes in their crystallinity. They concluded that the higher absolute zeta-potential in halloysite occurred due to the greater number of isomorphic substitutions in the halloysite, when compared to kaolinite. Furthermore, a brief comparison on the reported cation exchange capacities (CEC) of kaolinites (Ma and Eggleton, 1999; Borden and Giese, 2001) when compared to halloysites (Garrett and Walker, 1959; Joussein *et al*., 2005; Gray *et al.,* 2016) demonstrated that halloysites exhibited a higher CEC.

The reported values of CEC for halloysites range from 2 – 60 cmol+kg^{-1}, although the higher values have been suggested as perhaps due to the presence of other clays and and/or impurities (Joussein *et al*., 2005). The study by Gray *et al*. (2016) showed that the CEC of a range of halloysites was dependent upon the tubular morphology of the halloysite and measured the CEC of halloysites in the range of 2.9-9.3 cmol+kg^{-1}. In addition, Gray *et al*. (2016) estimated the ratio of variable charge sites to basal sites for halloysite (7 Å) as ~3:1, in contrast to ~6:1 as estimated previously for kaolinites (Gu and Evans, 2008). This implies that there are potentially a greater number of edge sites on halloysites when compared to kaolinites, from which it can be inferred that halloysites have a greater potential for surface reactions than kaolinites which is one of the reasons for the interest in these materials.

There are fewer studies on anion exchange and halloysites and those conducted are of narrower breadth. One such study looked at the adsorption of iodate (IO_3^-) on halloysite (10 Å) nanotubes and found the maximum adsorption capacity as 1.09 mg/g, where the adsorption showed a pH dependence (Yu *et al*., 2020). Two other very recent studies have looked at the anionic adsorption onto halloysite nanotubes with phosphate (PO_4^{3-}) anions (Almasri *et al*., 2019; Saki *et al.,* 2019) where the respective maximum phosphate anion adsorptions were 1.2 and 1.5 mg/g. Whilst these studies investigated the anion adsorption capacities of halloysite nanotubes, there was no reference to the morphology of the tubular halloysite and no specific attention was paid to the hydration state of the nanotubes.

In following on from previous work on the cation exchange of halloysites (Gray *et al.,* 2016), the anion exchange of two tubular morphologies of halloysite nanotubes, in

differing hydration states, has been investigated in this thesis and compared by using phosphate anions. This work is be outlined further in Chapter 3 of this thesis.

1.2.2 Morphology of halloysites

The morphology of the halloysites (i.e., tubular, platy or spheroidal) is widely reported as being related to their geological occurrence and crystallisation conditions upon formation (Joussein *et al.,* 2005), where halloysite nanotubes are often derived from other crystalline materials such as feldspars and micas (Bates, 1960; Singh and Gilkes, 1992; Churchman and Lowe, 2012).

Several authors have also reported on the relation between structural iron and the resultant morphology (Churchman and Theng, 1982; Bailey, 1990; Singh and Gilkes, 1992; Churchman, 2000; Joussein *et al.,* 2005), where the tubular morphology is typically low in iron whilst higher iron contents, caused by substitution in the octahedral layer, are noted in platy halloysites. Bailey (1990) related the amount of iron present as Fe_2O_3 to the curvature of the halloysites, where high iron resulted in the least curvature, i.e. platy halloysites. This can be rationalised by considering the larger ion size of Fe^{3+} compared to Al^{3+}. Hence, the reduced misfit between the octahedral and tetrahedral sheets reduces the need for layer rolling as a mechanism to accommodate the misfit. Spheroidal halloysites, by contrast, display a large range of iron contents suggesting that iron content has little effect on their formation (Joussein *et al*., 2005). Rather, Cravero *et al*. (2012) noted that the halloysite morphology can also be dependent on the texture of the primary rock source, where spheroidal halloysite was associated with low porosity rocks whilst tubular halloysite formed from high porosity primary rock sources.

The formation of halloysites into their nanotubular shape is not yet fully understood. Bates *et al.* (1950) proposed a rolling mechanism that arises due to a dimensional misfit between the tetrahedral and octahedral sheets, where the tetrahedral sheet is larger than the octahedral sheet, along with weak interlayer bonding (Bates *et al.,* 1950; Bailey, 1990). Singh (1996) suggested a different model which stated that the rolling occurred to reduce the Si-Si repulsion within the tetrahedral sheets, as opposed to tetrahedral rotation to account for the same misfit and applied the model to the rolling of planar kaolinites to form tubular halloysite.

In addition, the mechanism of layer rolling for halloysite nanotubes is, as of yet, undefined. The question as to whether they exist as nanotubes with concentric and separate sheets or or are instead formed by continuous rolling of the kaolin sheets is, as of yet, unclear (Chapter 4, Figure 4.9). Whilst this will not be directly answered in this thesis, the cross-section TEM analysis in Chapter 4 will address this question.

This thesis will focus on tubular halloysites, with particular attention being paid to the two identified tubular morphologies; cylindrical and polygonal prismatic, where the halloysite nanotubes have been shown to range in lengths from 170-950 nm and diameters of 50 – 160 nm (Hillier *et al*., 2016). The key distinction between the two morphologies is highlighted in the SEM images in Figure 1.6, whereby the cylindrical nanotubes are smaller with curved external surfaces whilst the polygonal prismatic samples are larger with flat external faces. Indeed, in the sample set studied by Hillier *et al.* (2016), the authors showed that those typically classed as cylindrical had cross section diameters of ~40-70 nm whilst those seen as prismatic were longer tubes with cross section diameters of up to 250 nm.

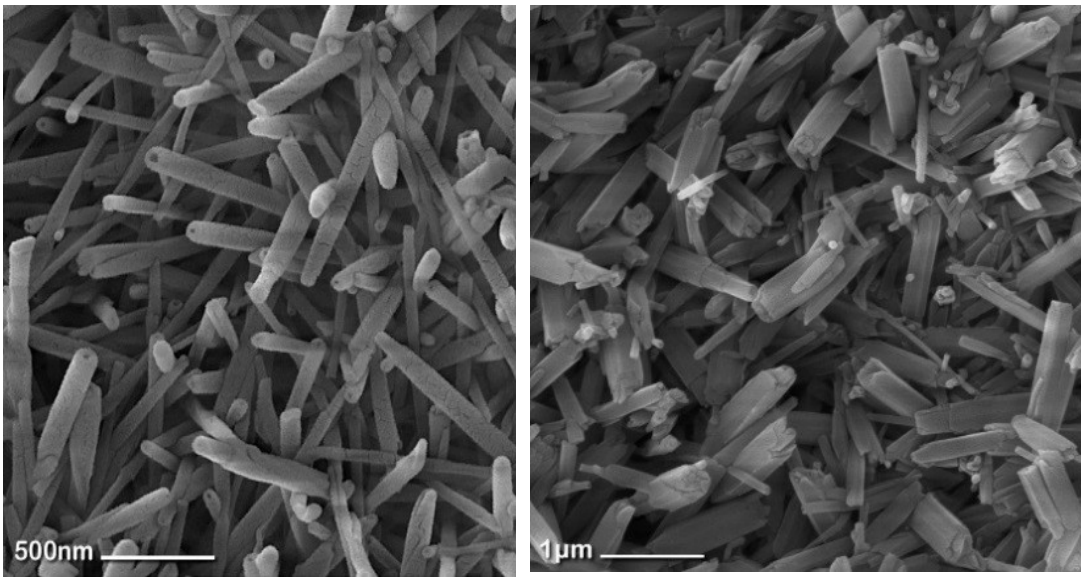

Figure 1.6. Scanning electron microscopy (SEM) images of the two morphologies of tubular halloysites. The image on the left is of a cylindrical sample whilst the image on the right is a polygonal prismatic sample. Image source Hillier et al. (2016).

The relation between the two tubular morphologies, cylindrical and prismatic, and the preference for one to form over another is also not yet settled. Kogure *et al*. (2013) suggested that the dehydration of halloysites results in flat kaolinite-like sector domains, and hence the creation of prismatic morphology. Alternatively, Hillier *et al.*

(2016) proposed that the prismatic halloysites form as a result of continued growth of the cylindrical nanotubular forms. The relation between the two will be discussed in greater detail in Chapter 4 (Sections 4.3.2 and 4.4) using cross sections studies of both morphologies by transmission electron microscopy (TEM).

Throughout this thesis, there are several references to the respective degree of ordering as a means to distinguish the two morphologies. In clay mineralogy, the degree of ordering refers mainly to the relationships between layers and their stacking arrangements. The degree of ordering can be identified using techniques such as Fourier transform infrared (FTIR) and X-ray powder diffraction (XRPD). For example, kaolinites are often referred to as either ordered or disordered. Well-ordered kaolinites have a regular layer stacking and for tubular halloysites elements of this are observed in the polygonal prismatic morphologies both by ordering of the (20,13) diffraction bands in XRPD patterns, and by the presence of extra 'ordered' bands in FTIR spectra, as will be discussed in more detail in Chapters 2 (Sections 2.2.1-2.2.2); 3 (Section 3.3.6) and 6 (Section 6.3.2).

Aside from their crystallography, the differences in behaviour between the two main tubular morphologies of halloysite have not been widely investigated, indeed recent papers by Gray *et al*. (2016) on the cation exchange capacity of halloysites and Hillier *et al*. (2016), which provided an overall picture of the distinctions between the two, are some of the only known works to tackle this issue, as was known at the time of writing this thesis. This thesis will aim to provide a more comprehensive review of the variations in phosphate adsorption behaviour (Chapter 3) and in-depth analysis of the varying surface features (Chapter 4) of the two morphologies, where the observed differences between them are highlighted throughout the thesis.

1.2.3 Interlayer water in halloysites

MacEwan (1947) was the first to propose that, like kaolinite, hydrated halloysites had a tetrahedral silica sheet and an octahedral aluminium sheet where the only structural difference between the two was the addition of interlayer water. This interlayer water, which is only found naturally in halloysites, occurs as a monolayer of water (~3 Å) and has been estimated at around 12.3 wt.% (Kohyama *et al*., 1978) which corresponds to two water molecules per formula unit, $Al_2Si_2O_5(OH)_4.2H_2O$, (Figure 1.7).

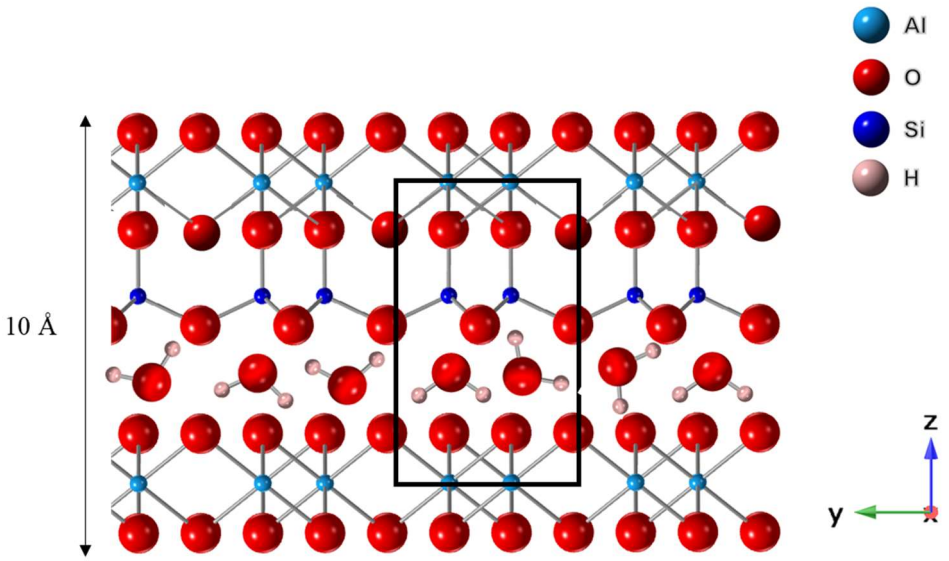

Figure 1.7. Structure of hydrated halloysite showing a monolayer of water molecules.

The interlayer water in halloysite is weakly held in the halloysite interlayers and so can rapidly and easily dehydrate (Alexander *et al.,* 1943), although the dehydration mechanism is dependent upon relative humidity and the physiochemical traits of the specific halloysite (Kohyama *et al.*, 1978; Joussein *et al.,* 2005; Joussein *et al*., 2006). There is now general agreement that the hydrated 10 Å form of halloysite is the primary form of all halloysites, and other forms have undergone some post formational degree of dehydration either in nature and or under laboratory or storage conditions. Indeed, this tendency for halloysite to dehydrate and loose its interlayer water under ambient laboratory conditions is a challenge for the study of the fully hydrated form.

Where halloysite is found in soils, it is typical to find dehydrated halloysite (7 Å) in the upper layers of soil, whilst hydrated halloysite (10 Å) is found in the lower layers, which are more likely to retain a higher moisture content. In soils with marked seasonal changes, the dehydration of halloysites is often driven by soil desiccation (Takahashi *et al.,* 1993). By contrast, Kautz and Ryan (2003) noted in perennially moist soils that the low rate of dehydration of halloysites suggests that the dehydration is controlled by kinetic factors. Joussein *et al.* (2006) used a series of dehydration experiments under varying relative humidity conditions to conclude that the dehydration of halloysites is heterogeneous and not subject to generalisation. Based upon this, and from general observation of the behaviour of the samples in the

laboratory timescale, time series XRPD analysis of the dehydration of several of the halloysites used in this thesis were conducted as outlined in Chapter 6.

The often rapid, relative humidity and temperature dependent (Joussein *et al.,* 2006), and irreversible dehydration of halloysite (10 Å) to the 7 Å form produces similar XRPD basal spacings to the other kaolin subgroup minerals, such that further tests such as scanning electron microscopy (SEM), Fourier transform infrared spectroscopy (FTIR) and intercalation with formamide are often required to distinguish between these minerals. These instrumental methods and their importance in clay mineral analysis are outlined in Chapter 2.

As mentioned earlier in this section, the layers of halloysite are either not thought to be permanently charged or to have a very low charge. As a result, unlike other clay minerals with a permanent layer charge such as smectites (Kaufhold and Dohrmann, 2013), halloysite does not contain any interlayer cations which serve the purpose of balancing out any negative layer charge. In the case of smectites, it is these interlayer cations which are believed to help facilitate rehydration (e.g. Derkowski *et al*., 2012) and so the lack of charge balancing interlayer cations may provide one explanation for the irreversible dehydration behaviour of halloysites. The absence of interlayer cations to act as a driving force for the rehydration of halloysite, raises the question as to the initial driving force or mechanism that results in the confinement of interlayer water in halloysite. The neutron scattering work outlined in Chapter 6 of this thesis hopes to begin to tackle this fundamental question through the study of the structure and dynamics of the interlayer water in halloysites.

It is not fully understood why the water is present in halloysites as opposed to the other kaolin polymorphs, although as stated earlier, halloysite forms naturally in the hydrated (10 Å) form and is formed in moist geological environments. Bailey (1990) argued that exchangeable cations in the tetrahedral sheet resulted in the introduction of the interlayer water which then acts as a stabiliser for the layer sequences, whilst Singh (1996) summarised that the interlayer water may be driven into the interlayer as a consequence of its activity and/or structural disorder. This suggests that the interlayer water has a role to play in the rolling of halloysite nanotubes, and as a result a greater understanding of this interlayer water is required. Fundamental research on the interlayer of water in halloysite nanotubes should also enable further understanding as

to whether the presence of interlayer water influences the reactions on the surface of halloysite when compared to kaolinite, since the interlayer water can be considered as effectively cleaving the two layers apart, hence exposing more of the surfaces to reactants. Finally, from a fundamental perspective, the interlayer water is the feature in halloysite that is least understood. To begin to answer the questions surrounding the interlayer water and gain more knowledge as to its features, and hence purpose, neutron scattering studies were conducted as part of this thesis. The neutron scattering studies are outlined in Chapter 6 of this thesis where the initial results are presented, and several experiments were conducted using neutron diffraction and scattering to study the structure and dynamics of the interlayer water.

1.2.4 Dehydration of halloysites

Whilst the dehydration of halloysite (10 Å) is irreversible under normal conditions, the halloysite may be rehydrated by first intercalating with organic molecules such as dimethyl sulfoxide (DMSO), or potassium acetate (Wada, 1961). Intercalation results in expansion along the *c* axis and so, if successful, can be readily detected by XRPD by observation of the basal spacings wherein the organic molecules expand the interlayer space, often to basal spacings of greater than 10 Å, and the reintroduction of water into the interlayer of halloysite occurs by their displacement (Costanzo and Giese, 1986), and subsequent collapse of the basal spacing to ~10 Å.

Churchman *et al*. (1972) concluded that halloysite (10 Å) and halloysite (7 Å) are the end members of the series of hydration states of halloysite, where interlayer water loss occurs in steps rather than in one transition (Churchman *et al*., 1972; Costanzo and Giese, 1985). Evidence of transition steps or intermediate structures in synthetically hydrated kaolinite has been observed by XRPD, as well as by FTIR (Costanzo and Giese, 1985). Some authors suggest interstratification of 10 Å /7 Å layers as an explanation for these intermediate peaks (Kautz and Ryan, 2003). Other work by Costanzo and Giese (1985) proposed an intermediate hydration complex at 8.6 Å due to two types of interlayer water. The first is ‘hole’ water which forms hydrogen bonds with the basal oxygens of the ditrigonal cavities highlighted in Figure 1.4 of this chapter. The second type of interlayer water is ‘associated’ ice-like water molecules which are located in the interlayer, interacting with the surface via hydrogen bonding and which have a high degree of mobility (Costanzo *et al*., 1982) and is dynamic at

temperatures of greater than -113 °C (Costanzo and Giese, 1985). Of the two types, the hole water is more strongly held in the interlayer due to the number of hydrogen bonds, this is reflected in the FTIR spectra of halloysite (10 Å) samples where the lower frequencies of the OH stretching bands for associated water, when compared to the 'hole' water (Costanzo *et al.,* 1984), indicate less H-bonding to their surroundings.

The fact that halloysite dehydrates to around 7.2 Å which is a slightly higher basal spacing than kaolinite (7.14 Å), even after heating to around 350 °C, suggests that some hole interlayer water may remain. It has been proposed that heating to 400 °C, and avoiding dehydroxylation, is required to fully dehydrate halloysite (10 Å) samples.

The literature presented so far has dealt with the fundamentals of the halloysite structure and its characteristic features. A further key aspect of halloysite nanotube studies is the modification of the structure for technological applications as will be outlined in the next section of this chapter.

1.3 HALLOYSITE SURFACE STUDIES AND THE INFLUENCE ON APPLICATION

1.3.1 Imaging of the surface of halloysite nanotubes

Whilst Pasbakhsh *et al.* (2013) concluded that optimisation of new products is possible when variations in the physical halloysite characteristics from different sources are taken into account when considering their application. However, halloysite nanotubes are often depicted as simple structures with a smooth outer siloxane surface and an inner alumina lumen surface (Yuan *et al*., 2015; Kim *et al*., 2017) as shown in Figure 1.8.

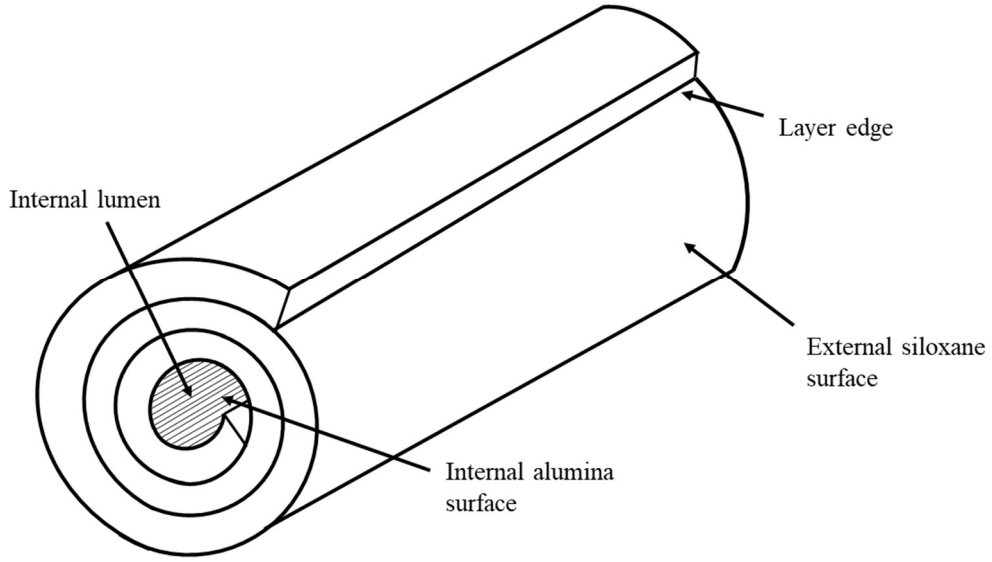

Figure 1.8. Simple depiction of halloysite nanotubes as is often applied for their technological uses.

Despite the often used and simple representation in Figure 1.8, a study by Yuan *et al.* (2008) suggested that there may be evidence of steps and edges on the surfaces of the nanotubes. The question of these surface features and their frequency is one that is tackled in Chapter 4 of this thesis where the work conducted was aimed at producing a potential updated depiction from the simplistic model of the halloysite nanotubes. It can be considered that the presence of extra steps and edges on halloysite nanotubes will influence their surface reactivity. New knowledge and understanding of the surface features of these nanotubes may also enable greater optimisation of procedures and selectivity of halloysites when halloysite nanotubes are functionalised for technological applications. Therefore, the research outlined in Chapter 4 used advanced microscopy techniques such as scanning electron microscopy (SEM), atomic force microscopy (AFM) and cross-section transmission electron microscopy (TEM) to conduct high resolution studies of the external surfaces of various halloysites nanotubes, from which conclusions as to the true depiction of the surfaces of these materials can be made.

1.3.2 Use of halloysite nanotubes for metal nanotag supports

Their small size and physical characteristics such as hollow lumen, high length to diameter ratio and high thermal stability have rendered halloysites a suitable material to consider in nanotechnology applications. In particular, some recent studies have examined their use as support materials for metal nanoparticles (Jana *et al.*, 2017;

Massaro *et al.,* 2018), where metal nanoparticles are used in a variety of technologies as antibacterial agents (Burridge *et al.,* 2010; Jana *et al.,* 2017), in electrochemical sensing devices (Cao *et al*., 2012) and as catalysts (Mallick *et al.,* 2006), amongst others. Chapter 5 of this thesis focuses on the use of gold and silver nanotags which were anchored to the halloysite surface with a variety of linkers, one of which had a phosphonic acid terminus group. By using imaging techniques such as TEM with the aim of visibly identifying the presence of the nanoparticles, Chapter 5 attempts to combine the results from the phosphate adsorption reactions in Chapter 3 with the imaging techniques from the surface studies outlined in Chapter 4. Hence, the overall aim of this work was to determine whether metal nanotags can be used to determine the locations of the phosphate adsorption onto the halloysite surface. In addition, the work was again conducted on tubular halloysites of the two morphologies, cylindrical and polygonal prismatic, to observe whether the differences in form influence the behaviour of the halloysites as metal nanotag supports.

1.4 ENVIRONMENTAL CONTEXT OF PHOSPHATE IN SOILS

1.4.1 Chemistry and occurrence of phosphorus and phosphate in environmental systems

As mentioned in the Section 1.2.1 above, one of the key aims of this thesis is to determine the anion adsorption of halloysites through the use of phosphate. While phosphate was used because of its anionic properties it was also selected due to its environmental significance.

Phosphorus is found throughout the Earth's crust, often in the form of apatite group minerals (Oelkers and Valsami-Jones, 2008), from where it undergoes physical and chemical weathering and enters natural ecosystems, such as marine, freshwater, and terrestrial. Within these ecosystems, phosphorus can act as a limiting nutrient to growth (Childers *et al*., 2011). Indeed, Kvatić *et al.* (2018) estimated that there is a current global restriction on production, between 22-55%, of temperate winter wheat, maize and rice due to insufficient phosphorus supply. On the other side, excess phosphate in natural systems, which may occur due to over fertilisation (Lu and Tian, 2017), results in substantial environmental problems such as eutrophication (Weng *et al.,* 2012) which causes multiple problems such as increased algal blooms and loss of

aquatic life (Carpenter *et al*., 1998). This thesis will focus on phosphorus in the form of phosphate anions (Figure 1.9), where it is most often found in soil systems in the forms HPO_4^{2-} and $H_2PO_4^-$ (Haygarth *et al*., 2013). It is worth bearing in mind that this is not the only labile from of phosphorus in the environment.

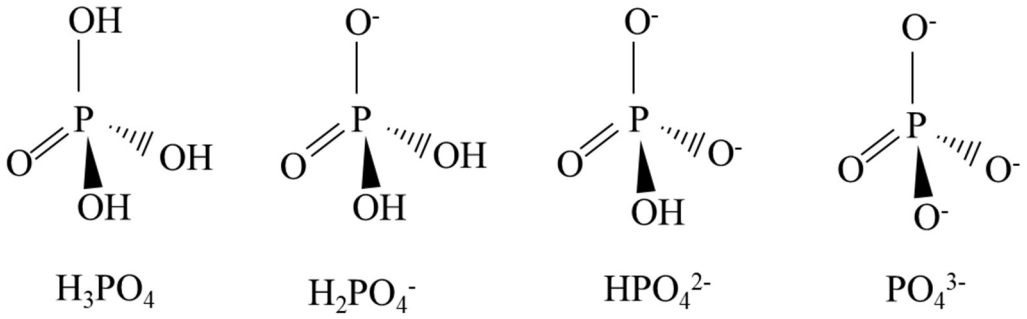

Figure 1.9. Chemical formulas and structures of different phosphate species, where HPO_4^{2-} and $H_2PO_4^-$ are most commonly found in soil systems (Haygarth et al., 2013).

Phosphate retention by clay minerals plays a vital role in the mobility of phosphate in the soil system (Gustafsson *et al*., 2012; Haygarth *et al*., 2013; Gérard, 2016). Whilst historically iron oxides were considered as the controlling minerals for phosphate mobility in soils, Gérard (2016) found through review that most soil clay minerals could be considered to have the same potential contribution to phosphate retention and hence, mobility. Halloysite is commonly found in rock and soils around the world (Joussein *et al.*, 2005) and is especially prevalent in highly weathered tropical soils (White & Dixon, 2002) and soils developed from volcanic ash (Dixon & McKee, 1974). Therefore, a greater understanding of the phosphate adsorption capacity of halloysite nanotubes may enable improved understanding of their contribution to the phosphate cycle in soils. As such, the phosphate adsorption capacity of halloysite nanotubes will be investigated in Chapter 3 of this thesis.

1.4.2 Adsorption mechanism of phosphates onto clay minerals

Adsorption is a partitioning process, which results in equilibrium between solvated and adsorbed species. This equilibrium can involve positively and negatively charged or potentially neutral species, both in solution and adsorbed to the halloysite. The precise nature of adsorption is influenced by the surface charge of both the adsorbent and the adsorbing molecule. There are two key types of adsorption that can occur, the first is

chemisorption, or inner sphere adsorption, which results in a chemical bond between the adsorbate and adsorbing molecule, and hence, can be considered as relatively stable, making it harder to desorb the adsorbing molecule. The second type of adsorption is physisorption, or outer sphere adsorption, where weaker, low energy, interactions such as Van der Waals forces associate the adsorbing molecule with the surface without resulting in a chemical bond. Due to its lower energy association, it is much easier to desorb molecules that are physisorbed to surfaces. In practice, adsorption is dynamic and under equilibrium, so adsorbates are likely to adsorb and desorb from surface until the lowest energy state is reached. In the context here of charged phosphate ions, charged surface sites are believed to be the most important once equilibrium is reached.

Adsorption reactions are often modelled using adsorption isotherms to understand more about the nature of adsorption onto material surfaces. In this thesis (Chapter 3, Section 3.3.1) the Langmuir adsorption isotherm is applied. The Langmuir adsorption model assumes that adsorption occurs as a monolayer with localised adsorption and that each adsorption site can only accommodate one adsorbate molecule. It further assumes that the binding energy of each molecule is independent of occupation of nearby sites and that the surface coverage (θ) is directly proportional to the rate of desorption from the surface (Equation 1.1). The model further assumes that the system is at equilibrium.

Equation 1.1: $\theta = \frac{q}{qm} = \frac{b\mathrm{Ce}}{(1+bCe)}$

Where b=k_a/k_d (k_a, k_d = rate constants for adsorption and desorption respectively), C_e = equilibrium concentration of adsorbate (mg/l), q = amount of adsorbate (mg/g), q_m = maximum amount of adsorbate (mg/g).

This model has successfully been applied to adsorption reactions on soils and clay minerals in multiple studies (Edzwald *et* al., 1976; Singh and Gilkes, 1992; Wisawapipat *et al*., 2009; He *et* al., 2017; Almasri *et al*., 2019; Saki *et al*., 2019; Yu *et al*., 2020).

1.4.3 Removal of phosphates from wastewaters and water bodies

The aims of phosphate removal from systems, such as wastewater, may be two-fold. Either with the purpose of reducing eutrophication (Kamiyango *et al*., 2009) or to improve the recycling of phosphate as it is a limited resource (Loganathan *et al.,* 2013). This is especially important since, as of yet, there is no available chemical or

technological substitute for phosphorus within natural ecosystems, where it is a key macronutrient in cellular vitality, formation of bones and teeth in vertebrates and is an essential component of DNA and RNA, amongst others (Childers *et al*., 2011).

Chemical precipitation techniques are often applied for phosphate removal and incur high costs, due to the metal salts used and unwanted waste sludge (Liu *et al*., 2016) and often they are also not efficient at low phosphate concentrations (He *et al*., 2017). As a result, multiple studies have investigated the use of adsorbent materials for the recovery of phosphate from wastewater systems, with another advantage being the recyclability potential of adsorbents (Loganathan *et al.,* 2013; Trimme *et al.,* 2017). Therefore, the desorption of phosphate from halloysite nanotubes was also investigated in this thesis (Chapter 3, Section 3.3.8) with the aim of considering the potential of halloysite nanotubes as recyclable materials for phosphate remediation.

1.5 SUMMARY

To summarise, this thesis will focus on halloysite nanotubes of two different morphologies, cylindrical and polygonal prismatic, with the aim of increasing the understanding of their surface features. Whilst the fundamental surface features of kaolinites have been extensively studied, at this time, there are fewer such studies which focus on tubular halloysites. Chapter 3 of this thesis will focus on the adsorption of phosphate anions by halloysite nanotubes, where the phosphate anions are used as a probe to understand more about the surface chemistry and behaviour of these materials. Additionally, the aim was to further understand the behaviour of anion exchange on the surface of halloysite nanotubes, of varying morphology, which is complementary to earlier work published on cation exchange capacity of halloysite nanotubes. As well as the use of phosphate as a chemical probe for the surface behaviour, by attaching gold and silver nanotags to a combination of linkers with varying functional groups in Chapter 5, it is hoped to use imaging techniques such as TEM to visibly observe the reactive sites for anionic adsorption on the surfaces of these nanotubes.

Through use of advanced microscopy techniques, further explorations of the physical traits and characteristics of the inner and outer surfaces of the two morphologies of tubular halloysites will be presented in Chapter 4 of this thesis. This work aims to

examine, on the atomic scale, the surface features of the two halloysites which should hence provide a guide as to the efficacy of their use in technologies, especially when considered in contrast to the simplistic model often employed and as depicted in Figure 1.8. Cross-section TEM analysis of the halloysite nanotubes of both cylindrical and polygonal prismatic morphologies was also conducted in an attempt to understand more about the relationship between the two, where, as mentioned in this literature review, this relationship is currently debated and not fully understood.

As described in detail in this chapter, halloysite occurs naturally with interlayer water and yet the exact nature of the interlayer water and why it occurs in halloysite remains unknown. Use of neutron scattering and diffraction as first steps to study the structure and dynamics of this interlayer water is outlined in Chapter 6 of the thesis. Whilst only the initial results are presented, they are the beginning of a series of experiments being undertaken to answer this fundamental question about the purpose and effect of the interlayer water on the halloysite minerals.

Despite being studied for many years and an increasing number of publications and interest in halloysite in the last 20 years, there remains several fundamental questions relating to the structure and surface chemistry of these minerals. The work presented in this thesis throughout Chapters 3-6 aims to contribute towards the discussion of some the research questions that have been outlined in this literature review.

1.6 REFERENCES

www.appliedminerals.com

Abendroth, R.P. (1970) Behavior of a pyrogenic silica in simple electrolytes. *Journal of Colloid and Interface Science*, **34**, 591-596.

Alexander, L.T., Faust, G.T., Hendricks, S.B., Insley, H. & McMurdie, H.F. (1943) Relationship of the clay minerals halloysite and endellite. *American Mineralogist*, **28**, 1-18.

Almasri, D.A., Saleh, N.B., Atieh, M.A., McKay, G. & Ahzi, S. (2019) Adsorption of phosphate on iron oxide doped halloysite nanotubes. *Scientific Reports*, **9**, 3232.

Bache, B.W. (1990) G. Sposito 1989. The chemistry of soils. Xiii + 277 pp. New York, Oxford: Oxford university press. Isbn 0 19 504615 3. *Geological Magazine*, **127**, 190-191.

Bailey, S.W. (1980) Summary of recommendations of AIPEA nomenclature committee. *Clays and Clay Minerals*, **28**, 73-78.

Brindley. (1990) Halloysite- a critical assessment. *Sciences Geologiques-Memoires*, **86**, 89-98.
Bates, T.F. (1960) Halloysite and gibbsite formation in Hawaii, *Clays and Clay Minerals*, **9**, 315-328.
Bates, T.F., Hildebrand, F.A. & Swineford, A. (1950) Morphology and structure of endellite and halloysite. *American Mineralogist*, **35**, 463-484.
Berthier, P. (1826) Analyse de l'halloysite. *Ann. Chim. Phys*, **32**, 332-335.
Bish, D.L. (1993) Rietveld refinement of the kaolinite structure at 1.5 k. *Clays and Clay Minerals*, **41**, 738-744.
Borden, D. & Giese, R.F. (2001) Baseline studies of the clay minerals society source clays: Cation exchange capacity measurements by the ammonia-electrode method. *Clays and Clay Minerals*, **49**, 444-445.
Brady, P.V., Cygan, R.T. & Nagy, K.L. (1996) Molecular controls on kaolinite surface charge. *Journal of Colloid and Interface Science*, **183**, 356-364.
Bretti, C., Cataldo, S., Gianguzza, A., Lando, G., Lazzara, G., Pettignano, A. & Sammartano, S. (2016) Thermodynamics of proton binding of halloysite nanotubes. *The Journal of Physical Chemistry C*, **120**, 7849-7859.
Burridge, K., Johnston, J. & Borrmann, T. (2011) Silver nanoparticle–clay composites. *Journal of Materials Chemistry*, **21**, 734-742.
Cao, H., Sun, X., Zhang, Y. & Jia, N. (2012) Electrochemical sensing based on gold nanoparticle-decorated halloysite nanotube composites. *Analytical Biochemistry*, **430**, 111-115.
Churchman, G.J., Aldridge, L.P. & Carr, R.M. (1972) The relationship between the hydrated and dehydrated states of an halloysite. *Clays and Clay Minerals*, **20**, 241-246.
Churchman, G.J. & Lowe, D.J. (2012) Alteration, formation and occurence of minerals in soils. Pp. 20.21-20.72. In P.M. Huang, Y. Li, and M.E. Sumner, Eds. *Handbook of soil sciences. Properties and processes, second edition*,CRC Press, Boca Raton, Florida
Churchman, G.J., Pasbakhsh, P. & Hillier, S. (2016) The rise and rise of halloysite. *Clay Minerals*, **51**, 303-308.
Costanzo, P.M. & Giese, R.F. (1985) Dehydration of synthetic hydrated kaolinites: A model for the dehydration of halloysite (10 Å). *Clays and Clay Minerals*, **33**, 415-423.
Costanzo, P.M., Giese, R.F., Lipsicas, M. & Straley, C. (1982) Synthesis of a quasi-stable kaolinite and heat capacity of interlayer water. *Nature*, **296**, 549-551.
Costanzo, P.M. & Giesse, R.F. (1986) Ordered halloysite; dimethylsulfoxide intercalate. *Clays and Clay Minerals*, **34**, 105-107.
Cravero, F., Fernández, L., Marfil, S., Sánchez, M., Maiza, P. & Martínez, A. (2016) Spheroidal halloysites from patagonia, argentina: Some aspects of their formation and applications. *Applied Clay Science*, **131**, 48-58.
Cravero, F., Maiza, P.J. & Marfil, S.A. (2012) Halloysite in Argentinian deposits: Origin and textural constraints. *Clay Minerals*, **47**, 329-340.
Davis, J.A. & Kent, D.B. (1990) Surface complexation modeling in aqueous geochemistry. *Reviews in Mineralogy and Geochemistry*, **23**, 177-260.
Derkowski, A., Drits, V.A. & McCarty, D.K. (2012) Rehydration of dehydrated-dehydroxylated smectite in a low water vapor environment. *American Mineralogist*, **97**, 110-127.
dos Santos, E.C., Rozynek, Z., Hansen, E.L., Hartmann-Petersen, R., Klitgaard, R.N., Løbner-Olesen, A., Michels, L., Mikkelsen, A., Plivelic, T.S., Bordallo,

H.N. & Fossum, J.O. (2017) Ciprofloxacin intercalated in fluorohectorite clay: Identical pure drug activity and toxicity with higher adsorption and controlled release rate. *RSC Advances*, **7**, 26537-26545.

Du, M., Guo, B., Lei, Y., Liu, M. & Jia, D. (2008) Carboxylated butadiene–styrene rubber/halloysite nanotube nanocomposites: Interfacial interaction and performance. *Polymer*, **49**, 4871-4876.

Edzwald, J.K., Toensing, D.C. & Leung, M.C.-Y. (1976) Phosphate adsorption reactions with clay minerals. *Environmental Science & Technology*, **10**, 485-490.

Garrett, W. & Walker, G. (1959) The cation-exchange capacity of hydrated halloysite and the formation of halloysite-salt complexes. *Clay Minerals Bull*, **4**, 75-80.

Gray, N., Lumsdon, D.G. & Hillier, S. (2016) Effect of pH on the cation exchange capacity of some halloysite nanotubes. *Clay Minerals*, **51**, 373-383.

Gu, X.Y. & Evans, L.J. (2008) Surface complexation modelling of Cd(II), Cu(II), Ni(II), Pb(II) and Zn(II) adsorption onto kaolinite. *Geochimica Et Cosmochimica Acta*, **72**, 267-276.

Gupta, V., Hampton, M.A., Nguyen, A.V. & Miller, J.D. (2010) Crystal lattice imaging of the silica and alumina faces of kaolinite using atomic force microscopy. *Journal of Colloid and Interface Science*, **352**, 75-80.

Han, Y., Liu, W., Zhou, J. & Chen, J. (2016) Interactions between kaolinite aloh surface and sodium hexametaphosphate. *Applied Surface Science*, **387**, 759-765.

He, Y., Lin, H., Dong, Y. & Wang, L. (2017) Preferable adsorption of phosphate using lanthanum-incorporated porous zeolite: Characteristics and mechanism. *Applied Surface Science*, **426**, 995-1004.

Hillier, S., Brydson, R., Delbos, E., Fraser, T., Gray, N., Pendlowski, H., Phillips, I., Robertson, J. & Wilson, I. (2016) Correlations among the mineralogical and physical properties of halloysite nanotubes (HNTs). *Clay Minerals*, **51**, 325-350.

Huertas, F.J., Chou, L. & Wollast, R. (1998) Mechanism of kaolinite dissolution at room temperature and pressure: Part 1. Surface speciation. *Geochimica Et Cosmochimica Acta*, **62**, 417-431.

Huggett, J.M. (2005) Clay minerals. Pp. 358-365. In R.C. Selley, L.R.M. Cocks, and I.R. Plimer, Eds. *Encyclopedia of geology*, Elsevier, Oxford.

Jana, S., Kondakova, A.V., Shevchenko, S.N., Sheval, E.V., Gonchar, K.A., Timoshenko, V.Y. & Vasiliev, A.N. (2017) Halloysite nanotubes with immobilized silver nanoparticles for anti-bacterial application. *Colloids and Surfaces B: Biointerfaces*, **151**, 249-254.

Joussein, E., Petit, S., Churchman, J., Theng, B., Righi, D. & Delvaux, B. (2005) Halloysite clay minerals - a review. *Clay Minerals*, **40**, 383-426.

Joussein, E., Petit, S., Fialips, C.-I., Vieillard, P. & Righi, D. (2006) Differences in the dehydration-rehydration behavior of halloysites: New evidence and interpretations. *Clays and Clay Minerals*, **54**, 473-484.

Kaufhold, S. & Dohrmann, R. (2013) The variable charge of dioctahedral smectites. *Journal of Colloid and Interface Science*, **390**, 225-233.

Kautz, C.Q. & Ryan, P.C. (2003) The 10 Å to 7 Å halloysite transition in a tropical soil sequence, Costa Rica. *Clays and Clay Minerals*, **51**, 252-263.

Kim, T., Kim, S., Lee, D.K., Seo, B. & Lim, C.-S. (2017) Surface treatment of halloysite nanotubes with sol–gel reaction for the preparation of epoxy composites. *RSC Advances*, **7**, 47636-47642.
Kogure, T., Mori, K., Drits, V.A. & Takai, Y. (2013) Structure of prismatic halloysite. *American Mineralogist*, **98**, 1008-1016.
Kohyama, N., Fukushima, K. & Fukami, A. (1978) Observation of the hydrated form of tubular halloysite by an electron microscope equipped with an environmental cell. *Clays and Clay Minerals*, **26**, 25-40.
Levis, S.R. & Deasy, P.B. (2002) Characterisation of halloysite for use as a microtubular drug delivery system. *Int J Pharm*, **243**, 125-134.
Lin, Y., Wang, X., Liu, J. & Miller, J.D. (2017) Natural halloysite nano-clay electrolyte for advanced all-solid-state lithium-sulfur batteries. *Nano Energy*, **31**, 478-485.
Lvov, Y., Wang, W., Zhang, L. & Fakhrullin, R. (2016) Halloysite clay nanotubes for loading and sustained release of functional compounds. *Advanced Materials*, **28**, 1227-1250.
Ma, C. & Eggleton, R.A. (1999) Cation exchange capacity of kaolinite. *Clays and Clay Minerals*, **47**, 174-180.
MacEwan, D. (1947) The nomenclautre of the halloysite minerals. *Mineralogical Magazine and Journal of the Mineralogical Society*, **28**, 196.
Mallick, K., Witcomb, M. & Scurrell, M. (2006) Silver nanoparticle catalysed redox reaction: An electron relay effect. *Materials Chemistry and Physics*, **97**, 283-287.
Massaro, M., Lazzara, G., Milioto, S., Noto, R. & Riela, S. (2017) Covalently modified halloysite clay nanotubes: Synthesis, properties, biological and medical applications. *Journal of Materials Chemistry B*, **5**, 2867-2882.
Pasbakhsh, P., Churchman, G.J. & Keeling, J.L. (2013) Characterisation of properties of various halloysites relevant to their use as nanotubes and microfibre fillers. *Applied Clay Science*, **74**, 47-57.
Peacock, C.L. & Sherman, D.M. (2005) Surface complexation model for multisite adsorption of copper(II) onto kaolinite. *Geochimica Et Cosmochimica Acta*, **69**, 3733-3745.
Saki, H., Alemayehu, E., Schomburg, J. & Lennartz, B. (2019) Halloysite nanotubes as adsorptive material for phosphate removal from aqueous solution. *Water*, **11**, 203.
Singh, B. (1996) Why does halloysite roll?—a new model. *Clays and Clay Minerals*, **44**, 191-196.
Singh, B. & Gilkes, R.J. (1992) An electron optical investigation of the alteration of kaolinite to halloysite. *Clays and Clay Minerals*, **40**, 212-229.
Sposito, G. (1984) *The surface chemistry of soils*. Pp. 234. Oxford University Press, New York,.
Takahashi, T., Dahlgren, R. & van Susteren, P. (1993) Clay mineralogy and chemistry of soils formed in volcanic materials in the xeric moisture regime of Northern California. *Geoderma*, **59**, 131-150.
Tarì, G., Bobos, I., Gomes, C.S.F. & Ferreira, J.M.F. (1999) Modification of surface charge properties during kaolinite to halloysite-7 Å transformation. *Journal of Colloid and Interface Science*, **210**, 360-366.
Theng, B.K.G., Russell, M., Churchman, G.J. & Parfitt, R.L. (1982) Surface properties of allophane, halloysite, imogolite. *Clays and Clay Minerals*, **30**, 143-149.

Van Emmerik, T.J., Sandström, D.E., Antzutkin, O.N., Angove, M.J. & Johnson, B.B. (2007) ^{31}P solid-state nuclear magnetic resonance study of the sorption of phosphate onto gibbsite and kaolinite. *Langmuir*, **23**, 3205-3213.

Vergaro, V., Abdullayev, E., Lvov, Y.M., Zeitoun, A., Cingolani, R., Rinaldi, R. & Leporatti, S. (2010) Cytocompatibility and uptake of halloysite clay nanotubes. *Biomacromolecules*, **11**, 820-826.

Wada, K. (1961) Lattice expansion of kaolin minerals by treatment with potassium acetate. *American Mineralogist*, **46**, 78-91.

Wilson, I. & Keeling, J. (2016) Global occurrence, geology and characteristics of tubular halloysite deposits. *Clay Minerals*, **51**, 309-324.

Wilson, I.R. (2004) Kaolin and halloysite deposits of China. *Clay Minerals*, **39**, 1-15.

Wisawapipat, W., Kheoruenromne, I., Suddhiprakarn, A. & Gilkes, R.J. (2009) Phosphate sorption and desorption by Thai upland soils. *Geoderma*, **153**, 408-415.

Yu, W., Xu, H., Tan, D., Fang, Y., Roden, E.E. & Wan, Q. (2020) Adsorption of iodate on nanosized tubular halloysite. *Applied Clay Science*, **184**, 105407.

Yuan, P., Southon, P.D., Liu, Z., Green, M.E.R., Hook, J.M., Antill, S.J. & Kepert, C.J. (2008) Functionalization of halloysite clay nanotubes by grafting with γ-aminopropyltriethoxysilane. *The Journal of Physical Chemistry C*, **112**, 15742-15751.

Yuan, P., Tan, D. & Annabi-Bergaya, F. (2015) Properties and applications of halloysite nanotubes: Recent research advances and future prospects. *Applied Clay Science*, **112-113**, 75-93.

Zhou, Z. & Gunter. William, D. (1992) The nature of the surface charge of kaolinite. *Clays and Clay Minerals*, **40**, 365-368.

Chapter 2

Materials and Methods

The aim of this chapter is to provide further details and characteristics of the halloysite materials used, as well as describing the background theory and specific details for the instrumental methods that were employed throughout the thesis to analyse the samples. While none of the details and theory presented here are new, they provide an overview of the importance of understanding the limitations of analytical techniques for the identification and characterisation of halloysite clay minerals.

2.1 MATERIALS

As described in detail in the Introduction (Chapter 1), halloysite nanotubes are naturally occurring aluminosilicate clay minerals. The halloysites employed in this thesis have been sourced from multiple sites across the world (Table 2.1) and have been collected and stored at the James Hutton Institute in Aberdeen, with the aim of using them for future research projects, such as this one. Where the halloysites have been stated as hydrated (halloysite (10 Å)), they have been maintained in this state either by full emersion in water or by maintaining a humid atmosphere in the storage containers by using damp tissues and ensuring a full seal (Figures 2.1 and 2.2). This has been stated by Giese (1988) as an effective storage method for hydrated halloysites.

Typically, halloysites are soft friable materials that break apart easily with slight pressure in a mortar and pestle. No further purification of the samples or treatment was applied before analysis, unless otherwise identified in the experimental procedure. Additionally, a list of all of the chemicals used throughout this thesis are provided in Table 2.2.

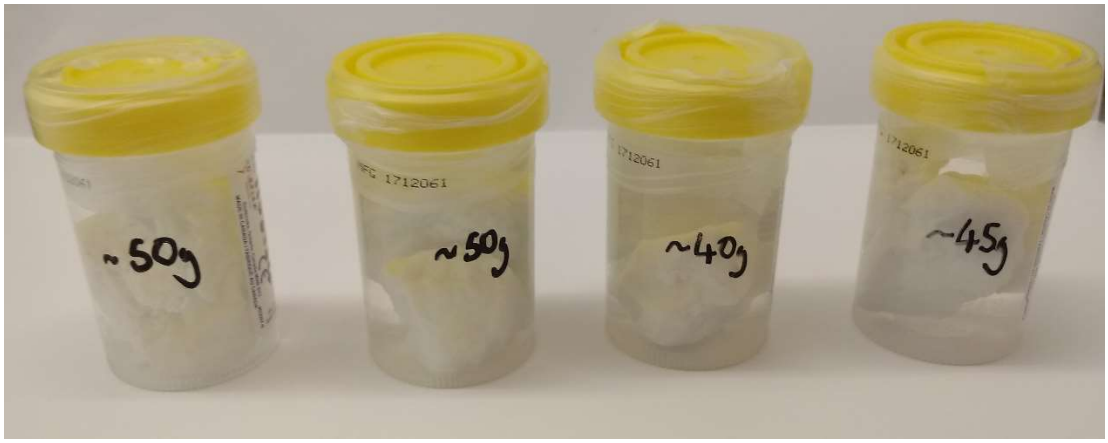

Figure 2.1. Halloysite (10 Å) stored under water.

Figure 2.2. Halloysite (10 Å) stored in humid atmosphere.

Table 2.1. Overview of halloysite and kaolinite samples used in this thesis.

Kaolin ID	Location of Deposit	Dominant Morphology	Hydration state	BET Specific Surface Area (m^2/g)	% of halloysite by X-ray powder diffraction
4Ch[a]	Defang, China	Cylindrical	Dehydrated	80.4	98.5
5Ch[a]	Bifa, China	Cylindrical	Hydrated	68.5	99.8
6Ch[a]	Wanjiar, China	Cylindrical	Hydrated	90.6	100
11Sc[a]	Elgin, Scotland	Prismatic	Dehydrated	15.5	99.4
12Tu[a]	Turkey	Cylindrical	Dehydrated	60.7	88.0
17US[a]	Dragon Mine, USA	Prismatic	Dehydrated	30.0	99.0
21US[a]	Bovill Deposit, USA	Prismatic	Dehydrated	28.0	93.5
22US	Wagon Wheel Gap, USA	Prismatic	Dehydrated	N/A	98.0**
23US	Dragon Mine, USA	Prismatic and some cylindrical	Hydrated	57.7	86.9**
24US	Dragon Mine, USA	Prismatic and some cylindrical	Hydrated	53.8	98.1**
KGa-2	Georgia	Platy kaolinite	Dehydrated	23.5[b]	96[c*]

[a] Hiller *et al*. (2016)
[b]Martin (1979)
[c]Chipera and Bish (2001)
[*]Percent of kaolinite given as determined by XRPD
[**]As reported in private commercial reports from the James Hutton Institute

Table 2.2. List of chemicals used throughout the thesis.

Chemical	Source	Purity
Sodium hydroxide	Fischer Scientific	98.6%
Hydrochloric acid	Fischer Scientific	37%
Sodium chloride	Sigma Aldrich	99%
Sodium dihydrogen orthophosphate 1-hydrate pellets	Sigma Aldrich	N/A
Calgon	Supermarket brand	N/A
Embedded 812 Resin	Electron Microscopy Sciences	N/A
Ethanol	Fischer Scientific	98.98%
Lemix L029 resin	TAAB	N/A
Nitric acid	Sigma Aldrich	70%
Acetone	Fischer Scientific	99.98%
Dodecanthiol	Alfa Aesar	98%
11-mercaptoudodecanoic acid	Alfa Aesar	97%
12-mercaptodpdecylphosphonic acid	Alfa Aesar	95%
Tert-butylamine-borane	Alfa Aesar	98%
Chloro(triphenylphosphine)gold(I)	Sigma Aldrich	99%
Silver nitrate	Sigma Aldrich	>99%
Dimethylformamide	Alfa Aesar	99%
Polyvinylpyrrolidone	Alfa Aesar	N/A
Deuterated water	Sigma Aldrich	99.8%

2.2 METHODS

Multiple analytical methods have been employed throughout this thesis at a variety of laboratory sites. Primarily, analysis was conducted in the laboratories in the James Hutton Institute in Aberdeen, whilst work was also carried out at Swansea University Bay Campus, Durham University Campus and the Leeds Electron Microscopy and Spectroscopy Centre (LEMAS) at the University of Leeds. Neutron spectroscopy and diffraction work was conducted at the ISIS Neutron and Muon Source, Rutherford Appleton Laboratory of the Science and Technology Facilities Council in Oxfordshire.

2.2.1 X-Ray Powder Diffraction (XRPD)

XRPD has primarily been used throughout this thesis to verify the purity of the samples used throughout this thesis (Table 2.1) where the purity here is defined as the weight percent of halloysite in the sample, typical 'impurities' were present as small weight percent's and were minerals such as quartz, feldspars and iron oxides. Additionally, XRPD was used to study the rate of dehydration from halloysite (10 Å) to halloysite (7 Å), as detailed in Chapter 6 (Section 6.3.1). XRPD detects long range order of a material, making it an effective tool for studying crystalline minerals (Brindley and Brown, 1980). XRPD works according to Braggs Law (Equation 2.1) whereby the planes of electron density within the crystal are of a spacing close enough to the wavelength of an X-ray to act as a diffraction grating. Where the diffracted radiation satisfies Braggs law, then constructive interference occurs, and an increased intensity is observed. (Figure 2.3). The angle at which the X-rays diffract is related to the distance between the lattice planes and, hence, a characteristic fingerprint spectra of the unit cell arrangement can be obtained.

Equation 2.1: $n\lambda = 2d\sin\theta$

Where n = integer, λ = incident wavelength, d = spacing between the atomic planes, θ = angle of diffraction.

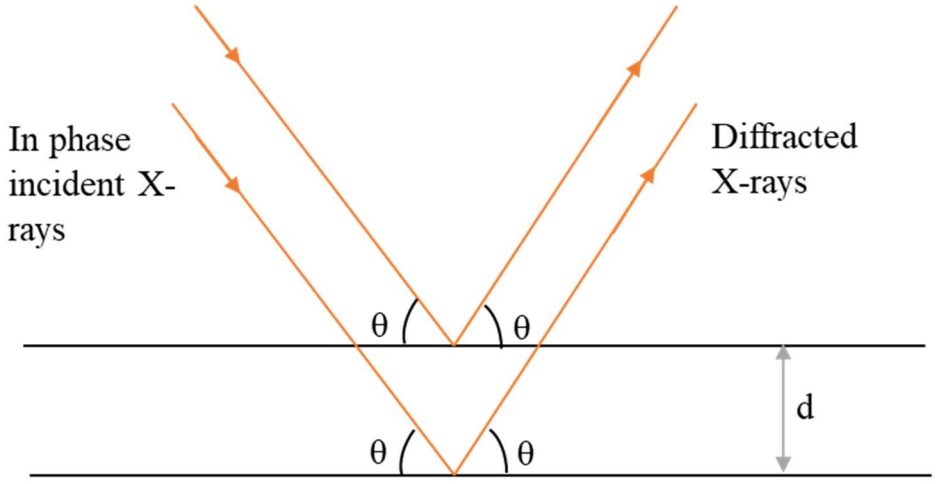

Figure 2.3. Schematic of Braggs Law for a crystalline material showing in plane constructive interference between the incident X-rays and the crystal lattice planes.

Frequently, XRPD is employed as a rapid tool to identify the hydration state of a halloysite, or to distinguish between a sample of kaolinite or halloysite. To distinguish

between kaolinite and halloysite, both of which have a basal spacing of around 7 Å (Chapter 1, Section 1.1.1), a simple test using formamide can be used. Formamide can rapidly intercalate into the interlayers of halloysite causing it to swell to a 001 basal spacing of around 10 Å (Churchman and Theng, 1984), whilst no change is observed within a short timescale of around 4 hours in the basal spacing of kaolinite.

To prepare the samples for quantitative bulk analysis by XRPD, (3 g) of sample was McCrone milled in ethanol for 12 minutes and spray dried at 60 °C to obtain a random powder (Hillier, 1999). The benefit of this method over grinding alone is that the random powder consists of spheres which will display no preferred orientation when packed into the sample holder for analysis. This allows for much greater accuracy in quantitative analysis since preferred orientation of a certain mineral or phase results in an overestimation of the presence of that particular phase and underestimation of phases whose planes are not oriented with respect to the incident X-ray beam. Where only limited sample was available, or where the initial hydration state of the samples was being investigated, the samples were hand ground as a powder and gently packed into the sample holder or dusted onto a silicon wafer for analysis. Quantitative analysis was conducted using a full pattern fitting method (Omotoso *et al*., 2006) which uses real diffraction patterns from multiple standards to simulate the experimental pattern as a weighted mixture of component patterns.

Samples were analysed on one of three instruments, where there was little difference between the three aside from X-ray source. In addition, in the ranges studied here this has little effect on the data. A Siemens D5000, a Panalytical X-pert Pro and a D8 Advance were used where the Siemens D5000 and D8 Advance both had cobalt as an X-ray source whilst the Panalytical X-pert Pro used copper. Cobalt was selected as the X-ray source because, if samples are high in iron, the use of a copper X-ray source can result in a high background due to fluorescence. This issue did not arise with the halloysite samples used throughout the thesis since they had little to no iron mineral impurities. The instrument used for each analysis in this thesis was primarily chosen depending on availability. As an example, the set-up of the D8 Advance Diffractometer is shown in Figure 2.4.

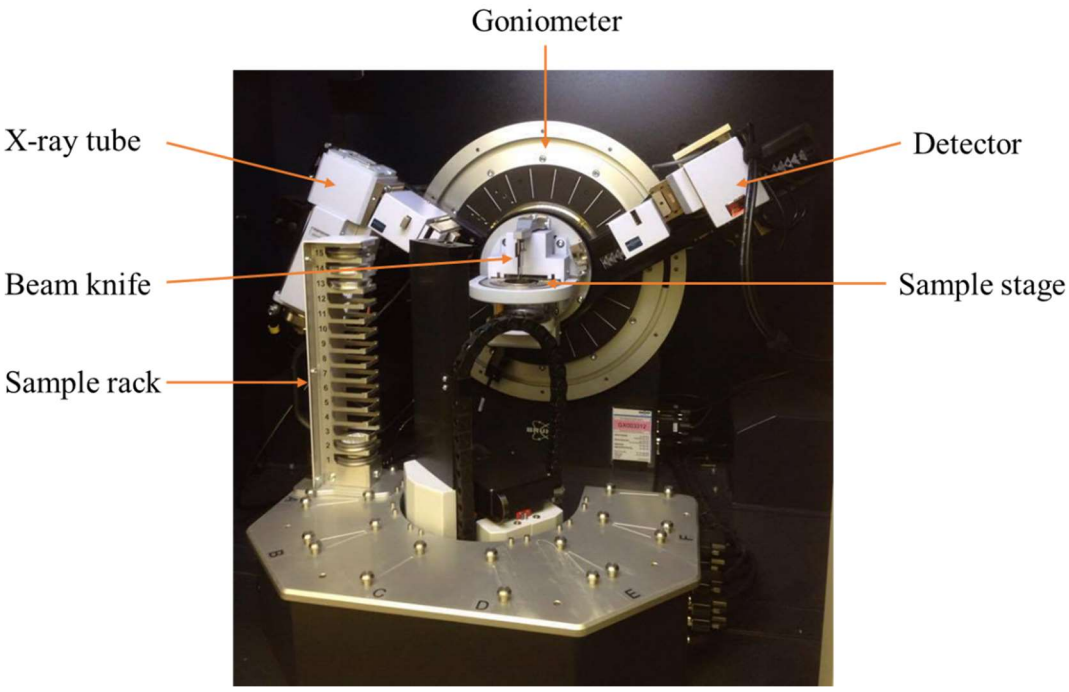

Figure 2.4. Labelled diagram of inside the D8 Advance Diffractometer.

As discussed previously, XRPD can be a powerful tool for interpreting subtle changes in the crystallinity and hence structure of a halloysite. From this, distinctions between the two morphologies of tubular halloysite, cylindrical and polygonal prismatic, can be inferred (Hillier *et al*., 2016). This is demonstrated in Figure 2.5 where the polygonal prismatic trace (red) shows a greater degree of ordering in the (20,13) bands than the cylindrical trace (black) which occur at between 33-38 2θ. Typically, in crystallography diffraction bands are given as three *hkl* indices, however in the case of clay minerals some diffraction bands may arise due to *hk* reflections only. This is due to the stacking formation of clay minerals (See Introduction Chapter 1, Figure 1.1, 1.3) where, for non-basal bands, there is no order in the c-direction, i.e. between different layers of the clay mineral. The extent of modulation of these bands can be used to construct the 'CP' (cylindrical-prismatic) index (Hillier *et al*., 2016) where the index is defined as background-subtracted minimum/(minimum+maximum) intensities of the band, as illustrated in Figure 2.5. From this the tubular morphology of the samples can be inferred since the greater the value of the CP index indicates a reduction in modulation, hence, cylindrical character of the halloysite. The 'CP' index values of the halloysites used throughout this thesis are provided in Chapter 4, Table

4.1.

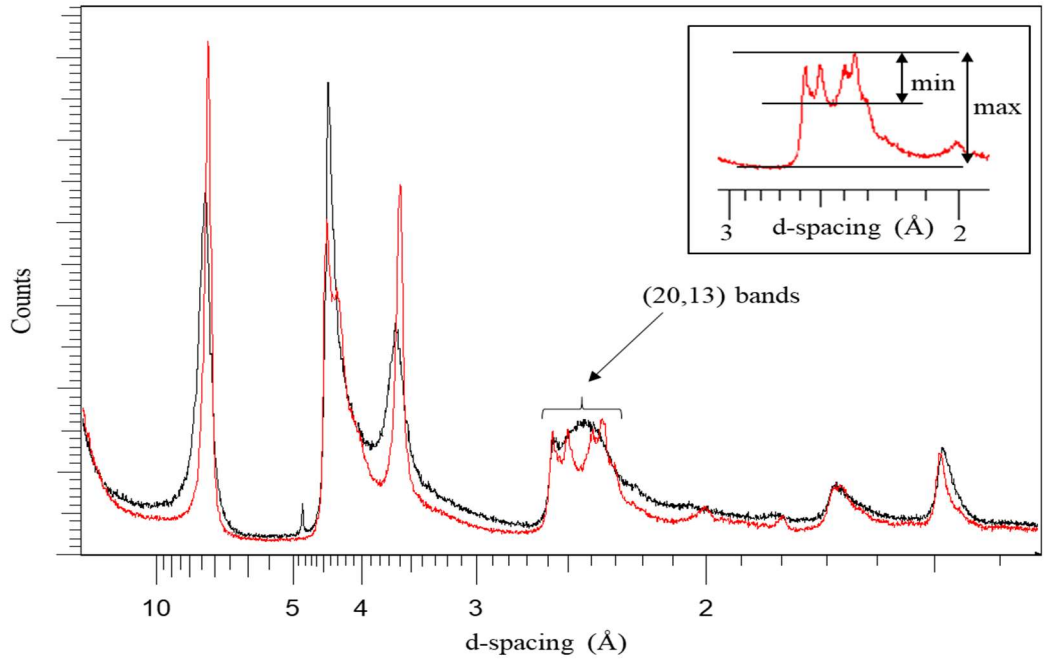

Figure 2.5. Comparison of XRPD traces of a polygonal prismatic halloysite, 17US (red) and cylindrical halloysite, 4Ch (black). The insert illustrates the maximum and minimum intensities of the (20,13) band used to calculate the CP index for a polygonal prismatic sample.

2.2.2 Attenuated Total Reflectance - Fourier Transform infrared spectroscopy (ATR-FTIR)

FTIR is a rapid and non-destructive analytical tool that is widely used in clay science. Like XRPD, FTIR can be diagnostic in identifying the specific tubular morphology of halloysite samples where the characteristic bands for distinguishing between the two morphologies are highlighted in Figure 2.7. Additionally, FTIR was used to attempt to understand the adsorption mechanism of phosphate onto the halloysite surface (Chapter 3, Section 3.3.7). The extent of deuteration of the hydrated halloysite samples was also studied using FTIR for the neutron scattering work (Chapter 6, Section 6.3.2). Hand ground samples were oven dried at 105 °C over two days to remove residual water and infrared spectra were measured on a Bruker Vertex 70 Fourier Transform Infrared (FTIR) Spectrometer in the mid infrared region of 4000 to 400 cm^{-1} with 200 scans per sample. The FTIR spectrometer was dry-air purged to prevent interference

in the spectra from water vapour and carbon dioxide and the spectra were analysed using the OMNIC^{TM} software.

A typical FTIR spectrum of halloysite (7 Å) is shown in Figure 2.6 with each of the characteristic bands identified. It has been shown that the polygonal prismatic samples (17US and 23US in Figure 2.7) have up to two additional bands in the hydroxyl stretching region (Farmer, 1974; Hillier *et al*., 2016). These peaks, found at around 3670 and 3653 cm^{-1} have been assigned as the out of phase stretching which arises due to imperfect three-fold symmetry of the samples (Farmer, 1974) and are also found in kaolinite samples. By contrast disordered cylindrical samples (4Ch in Figure 2.7) show only two bands in this region at around 3690 and 3620 cm^{-1}.

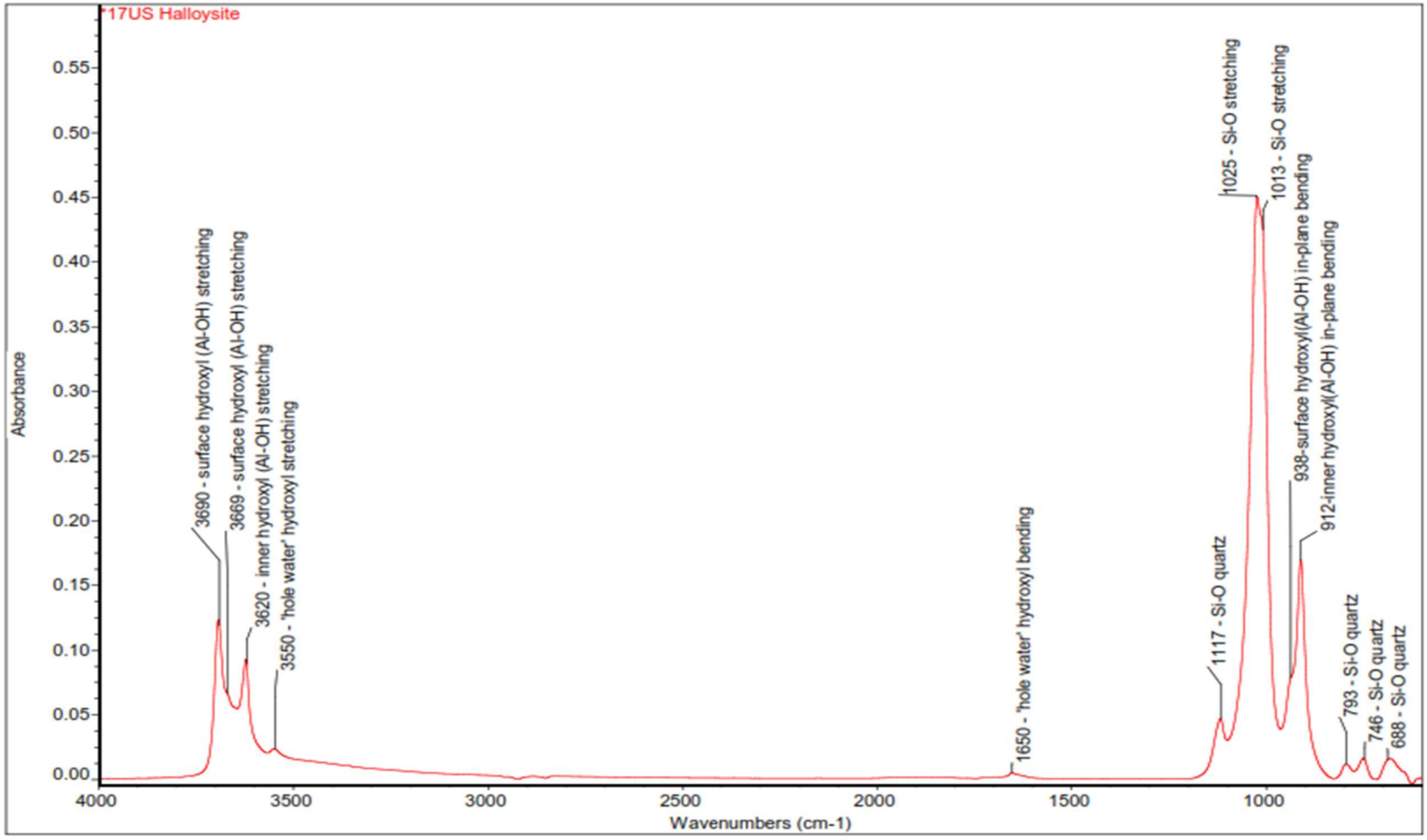

Figure 2.6. Labelled FTIR spectra of a polygonal prismatic halloysite (17US). N. B. trace of quartz impurity detected.

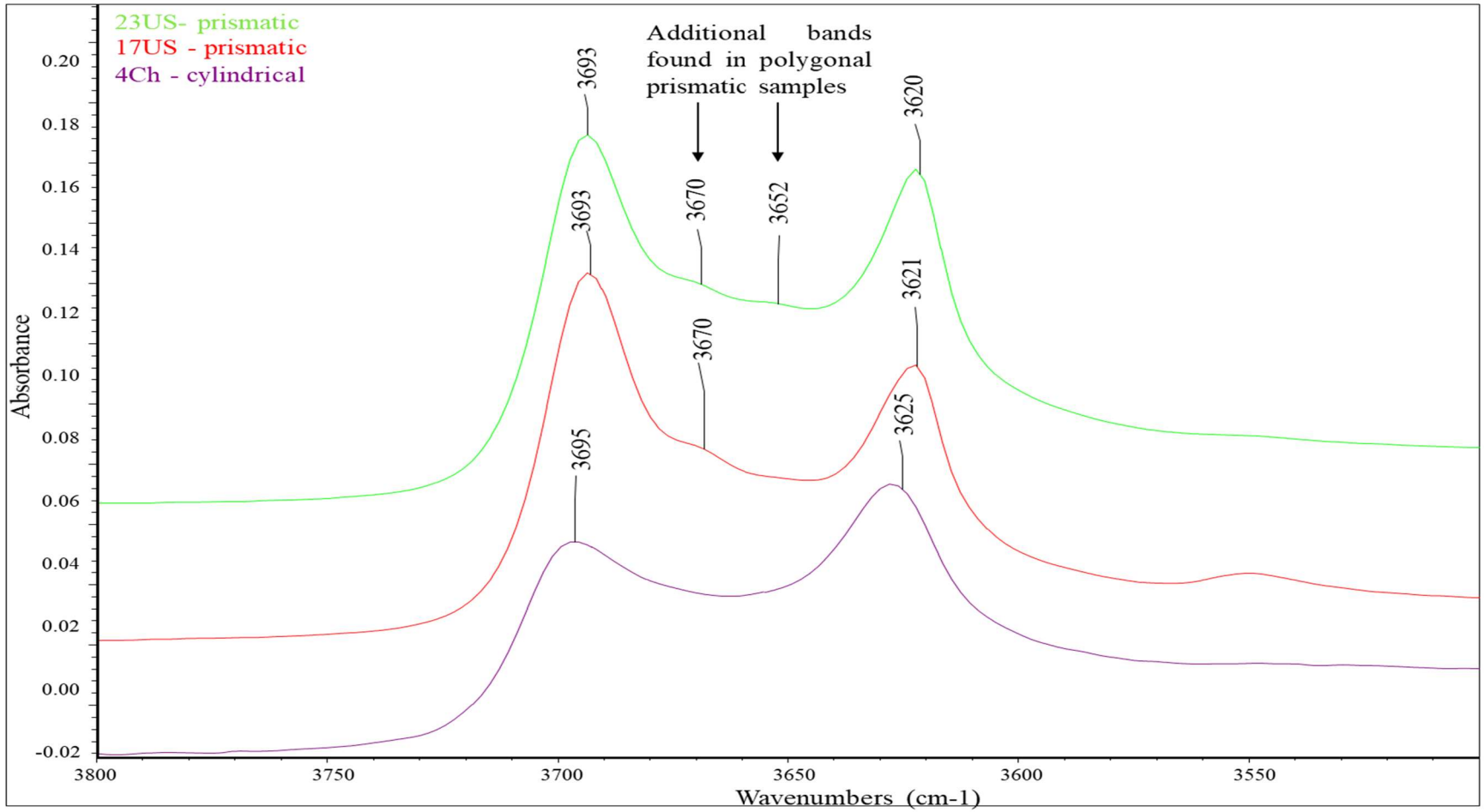

Figure 2.7. Comparison of disorder of cylindrical and polygonal prismatic halloysite nanotubes in FTIR in the characteristic hydroxyl stretching region between 3500-3800 cm^{-1}.

2.2.3 Field emission gun scanning electron microscopy (FEG-SEM)

FEG-SEM (hereafter referred to as SEM) is a powerful tool for studying clay minerals since it can capture images of the surfaces of materials on the nanometre scale at ultrahigh resolution by using a focused beam of low energy electrons to probe the sample surface. SEM analysis of tubular halloysite samples can be used to verify their tubular nature as well as identify their specific tubular morphology, i.e. cylindrical or polygonal prismatic as will be described in greater detail in Chapter 4 (Section 4.3.1). Some examples of SEM images of the halloysites used throughout this PhD are shown in Figure 2.8.

Samples were prepared for analysis by one of two methods, depending on the final use of the images. For some samples available as intact pieces, the preparation simply involved drying out of the sample in an oven at 105 °C for several days before breaking the piece to reveal a fresh surface which was platinum coated before analysis.

The second method involved initial gentle crushing and homogenisation of the intact or powdered sample. To do this, approximately 10 mg of which was weighed out into a beaker to which 100 ml of deionised water was added along with two drops of Calgon, to aid dispersion. The suspension was sonicated for 5 minutes to encourage dispersion of the nanotubes and a single drop of this suspension was then deposited on a silicon wafer supporting a 3.05 mm nickel grid. The grid aided a more even distribution of particles across the surface of the silicon wafer. Once dry, the samples were platinum coated to reduce charging in the SEM. SEM images for both types of sample preparation were taken using a Carl Zeiss Sigma VP Field Emission Scanning Electron Microscope (FEG-SEM) where the instrumental analysis was conducted by Evelyne Delbos and Laura-Jane Strachan at the James Hutton Institute.

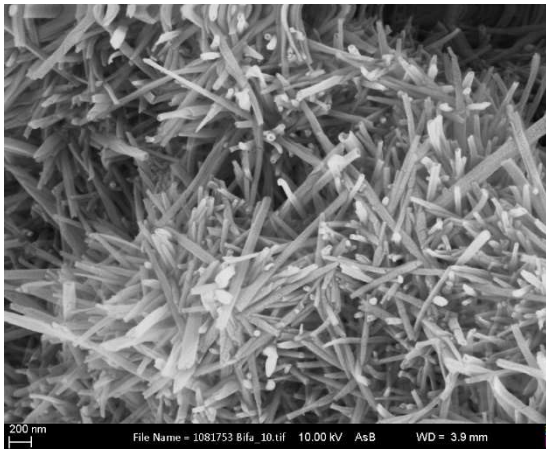

a) 5Ch – piece - cylindrical

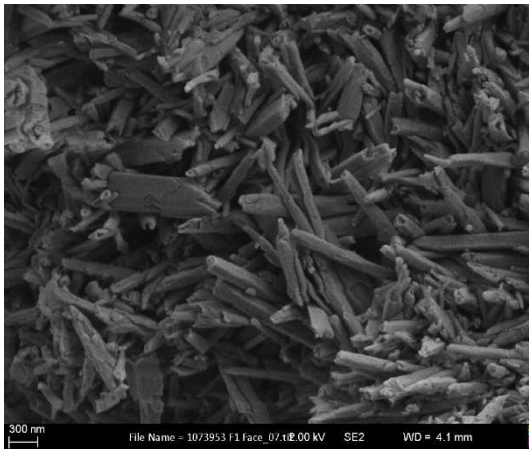

b) 23US – piece - prismatic

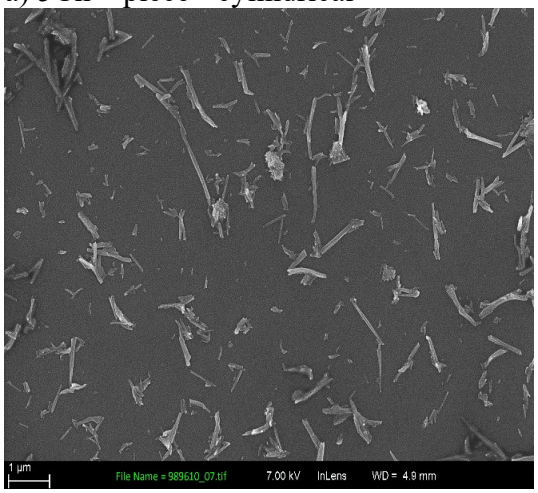

c) 4Ch – grid - cylindrical

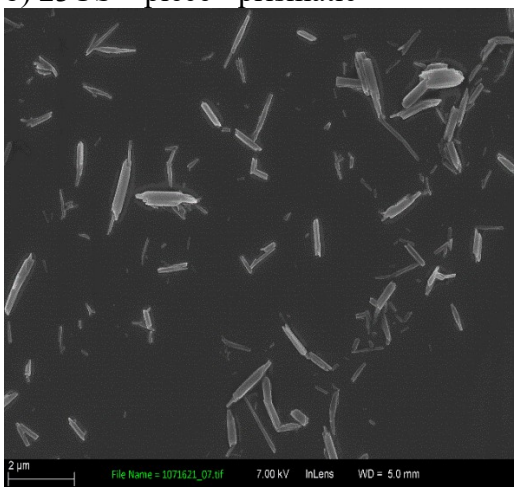

d) 17US – grid - prismatic

Figure 2.8. Examples of FEG-SEM images of some of the halloysites used in this thesis.

2.2.4 Atomic force microscopy (AFM)

AFM analysis was conducted over three visits to Durham University with Dr Pablo Cubillas. AFM analysis was conducted as AFM can provide a much more representative and more detailed picture of the surface features and topography of the halloysites nanotubes when compared to SEM and was used in Chapter 4 of this thesis to study the steps and edges on the external faces of the halloysite nanotubes. AFM is a type of scanning probe microscopy which works by measuring the surface force changes between a cantilever tip and a sample, wherein the local attractive or repulsive forces between the tip of the cantilever and sample surface is converted into a deflection of the cantilever, which then changes the angle of the reflected laser. This change in reflected signal to the photodetector is measured and used to calculate the deflection signal. A simple depiction of this mechanism is shown in Figure 2.9.

Two different instruments were used for the analysis: a Bruker JPK AFM and a Multimode AFM. The JPK AFM is a tip scanning AFM that is equipped with quantitative imaging (QI) mode, making it suitable for analysis of nanoparticles. QI mode is based on force volume mode, where the sample surface is mapped by changing the force between the sample and surface as the tip scans the sample, where QI mode can achieve much faster scanning speeds. The multimode AFM was operated in PeakForce^{TM} scanning mode which allows extreme tip-to-sample force control, again making it suitable for the nanoparticle size of the halloysites. Details of the sample preparation are given in Chapter 4 (Section 4.3.2). Data analysis was conducted using a combination of the programmes JPKSPM Data Processing, Nanoscope Analysis 1.5 and ImageJ (Schneider *et al.,* 2012).

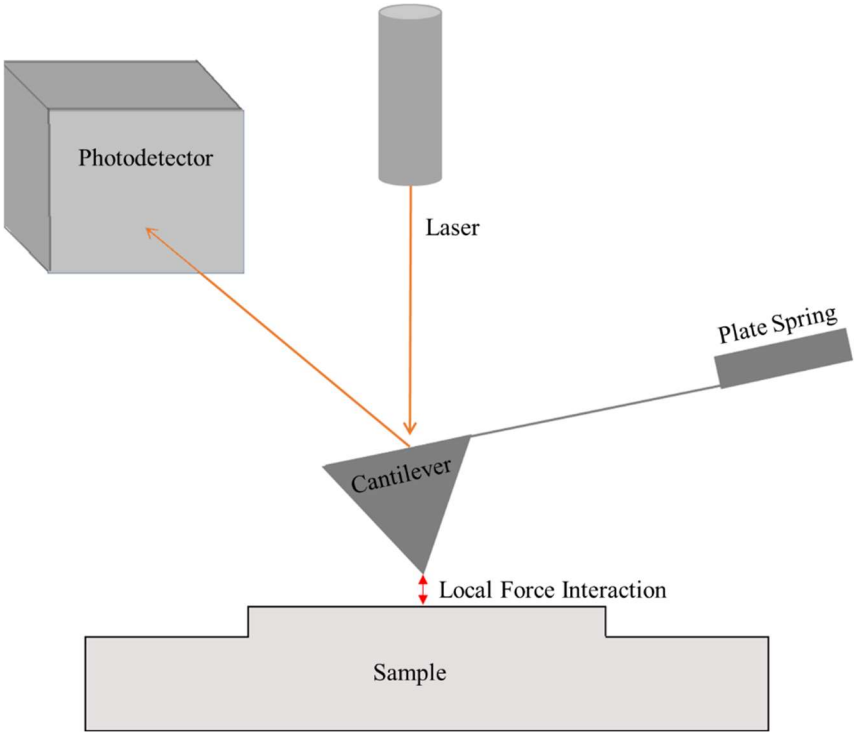

Figure 2.9. Typical depiction of an AFM instrument. Modified and redrawn from a combination of images in the JPK Instruments manual.

2.2.5 Transmission electron microscopy (TEM)

TEM analysis was conducted at the Leeds Electron Microscopy and Spectroscopy Centre (LEMAS) at the University of Leeds with Dr Zabeada Aslam over two visits. TEM analysis enables atomic scale analysis of materials to a much greater resolution than SEM. Historically TEM has been used to study the crystal structure of halloysites

as described in Chapter 4 (Section 4.4) whilst more recently it has been used to verify the use of tubular halloysites as supports for metal nanoparticles as detailed in Chapter 5 (Section 5.1). For this thesis, TEM analysis was used to obtain high resolution images of the nanoparticle cross sections of the tubular halloysites (Chapter 4, Section 4.3.2). The TEM instrument used also is able to generate images that have sufficient contrast to clearly identify metal nanoparticles 1-2 nm in diameter on the surface of the halloysites nanotubes (Chapter 5, Section 5.4.3).

TEM uses an electron beam to probe the samples and the electrons pass directly through the sample onto a phosphor screen where an image is generated. The contrast of the image is determined by the number of electrons that pass through the sample and the electron/sample interaction. Electron diffraction was also conducted where the diffracted electrons were focused into an image of the electron diffraction pattern by the objective lens.

The halloysites were prepared for TEM analysis by one of two ways;

1) For the observation of gold nanoparticles the samples were prepared by dispersion and deposition onto a 3 mm copper grid mounted onto an amorphous carbon film.
2) For the cross-section analysis of the halloysite nanotubes the samples were set in resin (as outlined in Chapter 4, Section 4.2.4) and thin sections made at Leeds University by Martin Fuller. The thin sections were cut using a Diatome diamond knife on a Reichert-Jung Ultracut-E ultramicrotome. The sections were cut to around 100 nm thick and placed on 200 mesh, thin bar copper TEM grids for TEM imaging. The TEM analysis was conducted on a FEI: Titan Themis instrument as shown in Figure 2.10. The TEM was operated at 300 kV and is fitted with a monochromator which allowed control over the electron dose during imaging, an important feature due to the beam sensitive nature of the halloysite samples.

Energy dispersive spectroscopy (EDS) data was collected using the Super-X EDX system with 4-windowless design and then processed using Velox. The TEM images were collected on a Gatan Oneview 16-megapixel CMOS digital camera Data analysis of the TEM images was conducted in ImageJ (Schneider *et al.,* 2012).

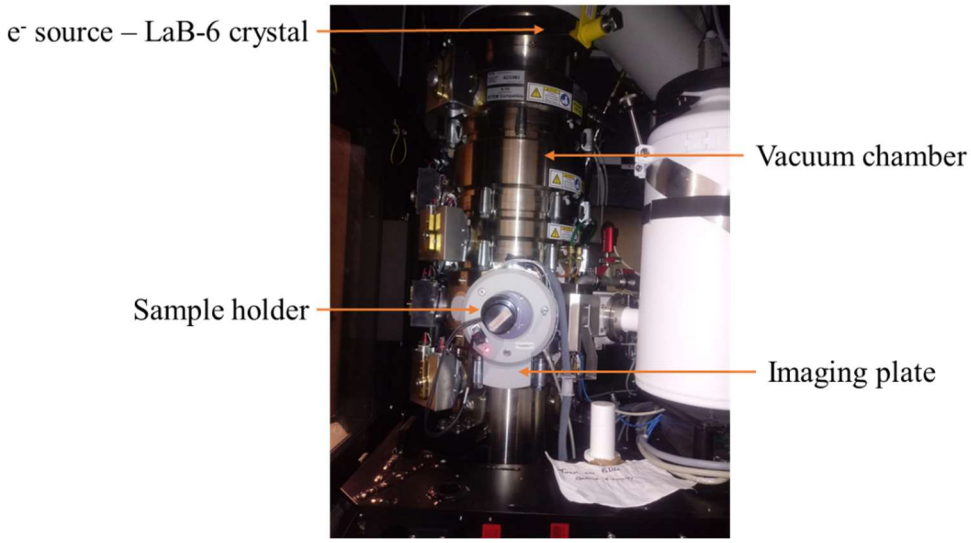

Figure 2.10. Labelled diagram of FEI-Themis transmission electron microscope.

2.2.6 Optical Microscopy

Optical microscopy was conducted at Swansea University on the samples used for gold nano-tagging as described in Chapter 5 on a KEYENCE VHX Digital Microscopy Lens Z20:X50. By using a narrow focus on the agglomerated halloysite nanotube clusters combined with the stepped microscope sample stage, it was possible to obtain high quality colour images by optical microscopy. The images also produce a more stereoscopic image than the other microscopy methods so far employed in the thesis because the depth of focus was effectively increased by the microscope taking images at fixed heights before the software "stitched" these data together into a single image.

2.2.7 X-Ray Photoelectron Spectroscopy (XPS)

XPS analysis was conducted and the results analysed at Swansea University by Dr James Mcgettrick and Christopher Kershaw on a KRATOS AXIS SUPRA instrument using a monochromated Al K_α source and a beam footprint of 700 µm on the x-axis and 300 µm on the y-axis. XPS was used in this thesis to determine the presence of gold and silver for the nano-tagging work presented in Chapter 5. Data was recorded using a charge neutraliser to limit differential charging and elemental binding energies were calibrated to the main hydrocarbon peak at 284.8 eV. XPS is a surface analysis technique that can probe around 10 nm into a sample whereby the surface is irradiated with X-rays and ejected electrons are counted over a range of kinetic energies. The kinetic energy associated with ejected electrons can be used to determine the element

from which the electron was emitted as well provide information on the orbital and chemical environment. XPS data was analysed using the CasaXPS© programme.

2.2.8 Scanning thermal analysis (STA), thermogravimetric analysis (TGA) and differential scanning calorimetry (DSC)

Scanning thermal analysis (STA) was conducted on a Perkin-Elmer STA 6000 at Swansea University by Lee Price. These methods were used as outlined in Chapter 5 to study the loss transitions on the halloysites with gold nanotags. The instrument was regularly calibrated to the melting points of indium and silver and the samples were run under an air gas flow rate of 19.8 ml/min in a continuous run from 30-600 °C with temperature increases of 10 °C/min. DSC analysis measures the difference in energy inputs between a sample and reference material using a controlled temperature programme. Power-compensation DSC curves result in an upward displacement of the curve with endothermic peaks and a downward displacement of the curve with exothermic peaks. TGA curves are integral curves which measure the mass of the sample with increasing temperature. In order to clearly see any mass loss transitions a first derivative of the data, derivative thermogravimetric curve (DTG) was created.

2.2.9 Inductively coupled plasma spectroscopy and spectrometry (ICP)

ICP instrument analysis was conducted in the analytical laboratory at the James Hutton Institute, Aberdeen by Fiona Sturgeon and Carol Curran on either a Perkin Elmer Optima 5300DV ICP-OES or an Agilent 7700 ICP-MS. Both ICP-OES (Optical Emission Spectroscopy) and ICP-MS (Mass Spectrometry) were carried out, the method used depended on the chemical element being looked for and is highlighted in the appropriate section of this thesis (Chapter 3). For ICP-MS the plasma ionised elements are separated and detected according to their charge/mass whilst for ICP-OES the plasma atomised atoms release photons with wavelengths characteristic of the atomic energy levels of the emitting atom.

For the ICP-OES analysis, two standards were made up; a 50 mg/L Al standard and a 20 mg/L Si and P standard in a 0.1 M NaCl matrix and run with a pump flow rate of 0.6 mL/min and 15 L/min for the plasma. ICP-OES was used to determine Al and Si where their limits of detection were 0.006 mg/L and 0.009 mg/g respectively. As is standard practice in the commercial ICP laboratory at The James Hutton Institute where multiple jobs may be run at once, for the ICP-MS analysis two standards were

made up; a 1 mg/L As, Cd, Ni, Zn, Hg, Se, Sc, V, Cr, Co, Cu, Ga, Pb, Sr, Y, Zr, Nb, Mo, Sn, Cs and Ba standard and a 1 mg/L Th, La, Ce, Nd, Sn, Er, Lu, Hf, Ta, W, Ti, Rb and U standard in a $LiBO_2$/2 M HNO_3 matrix. The samples were run with a pump flow rate of 0.60 revolutions per second and an integration time of 0.10 seconds. This method was primarily used to detect P, where the limit of detection of P in this method was 0.009 mg/L.

To prepare the samples for ICP analysis, the samples were oven dried overnight at 105 °C before undergoing lithium metaborate fusion using a Katanax X-3000 fusion instrument. The molten samples were dissolved in 10 % nitric acid and made up to volume in a 100 ml volumetric flask as outlined in the methods section of Chapter 3.

2.2.10 BET specific surface area (SSA)

Surface area measurements of the halloysite samples were carried out at the James Hutton Institute, Aberdeen on a Beckman Coulter SA3100 (Figure 2.11). The Brunauer-Emmett-Teller (BET) models multilayer adsorption of the adsorbing gas, nitrogen, onto a solid surface to calculate the specific surface area of the solid. The specific surface area (SSA) is defined as the total surface area of a material per unit mass (m^2/g). Each sample was oven dried at 105 °C overnight, accurately weighed and outgassed before analysis for 60 minutes at 100 °C.

Figure 2.11. Beckman Coulter Specific Surface Area instrument with nitrogen as the adsorbing gas.

2.2.11 Neutron Scattering Experiments

Neutron spectroscopy and neutron diffraction experiments were conducted at the ISIS Neutron and Muon Source, Rutherford Appleton Laboratories to study the structure and dynamics of the interlayer water in halloysite nanotubes as outlined in Chapter 6 of this thesis. This work was conducted in collaboration with a group from University College London, led by Professor Neal Skipper as outlined in Chapter 6 of this thesis. The benefits of neutron analysis are multiple. For example, they have a smaller attenuation coefficient than X-rays which enables them to penetrate deeper into the samples and unlike other methods such as X-ray diffraction it is possible to easily detect hydrogen using neutron scattering which makes it suitable for water analysis.

The equipment and set up of the site were complex but can be simplified into four stages:

1: Injector: The injector consists of an ion source, producing H^- ions which are separated into bunches or pulses using a Radio Frequency Quadrupole before being accelerated to travelling at 37% the speed of light.

2: Synchrotron: The H^- ions enter the synchrotron which consists of a ring 163 m in circumference. Tellurium thin film strips the ions of their electrons resulting in a beam of protons which are focused around the synchrotron using strong magnets. The protons circumvent almost 10,000 revelations of the synchrotron, resulting in their separation into two bunches travelling at 84% the speed of light.

3: Target Station: There are two target stations at ISIS. In each station neutrons are produced as focused pulses using spallation of a tungsten target. The neutrons can then be slowed using a variety of moderators and directed towards the appropriate instrument. The image in Figure 2.12 is from Target Station 2 and was taken during the neutron spectroscopy experiments.

4: Instrument: The instruments will have a sample positioned for analysis and the neutrons are directed towards the sample and analysed according to their interaction with the sample.

Figure 2.12. Target Station 1, neutrons are released via spallation and syphoned off to each instrument.

2.2.12 Neutron spectroscopy

Neutron spectroscopy experiments were conducted on the OSIRIS instrument to study the dynamics of the interlayer water of halloysite as outlined in Chapter 6. OSIRIS is a time of flight pulsed neutron source, where the neutron source was a tantalum target. Incident wavelength of the neutrons was kept fixed at 6.5 Å with an energy of 1.845 meV by pyrolytic graphite. Additionally, graphite moderators were also used to control the neutron speed. Whilst the exact experimental procedure and background theory is described in detail in Chapter 6, as a summary, the halloysite sample was loaded into an aluminium holder, sealed and placed into the instrument. Incident neutrons were scattered by the sample and, where neutron scattering occurred, the change in the momentum of the scattered neutrons was energy analysed by a diffractometer according to their Bragg scattering. This was measured and by using further data analysis in the programme Mantid (Arnold *et al*., 2014; Mukhopadhyay

et al., 2019) information on the diffusional behaviour of the interlayer water molecules was gained.

2.2.13 Neutron diffraction

Neutron diffraction experiments were also conducted at the ISIS Neutron and Muon Source, Rutherford Appleton Laboratories on the NIMROD (Near and Intermediate Range Order Diffractometer) instrument. Whilst present for the on-site experiments, the data interpretation and analysis is being conducted by our collaborators at UCL. For these experiments, as detailed in Chapter 6, neutron diffraction was used to study the structure of the interlayer water molecules with respect to the halloysite layers. The results are analysed using a programme called Gudrun and will be compared to simulations run using the Empirical Potential Structure Refinement (EPSR) models and Monte Carlo simulations.

2.3 REFERENCES

Arnold, O., Bilheux, J.C., Borreguero, J.M., Buts, A., Campbell, S.I., Chapon, L., Doucet, M., Draper, N., Ferraz Leal, R., Gigg, M.A., Lynch, V.E., Markvardsen, A., Mikkelson, D.J., Mikkelson, R.L., Miller, R., Palmen, K., Parker, P., Passos, G., Perring, T.G., Peterson, P.F., Ren, S., Reuter, M.A., Savici, A.T., Taylor, J.W., Taylor, R.J., Tolchenov, R., Zhou, W. & Zikovsky, J. (2014) Mantid—data analysis and visualization package for neutron scattering and μ sr experiments. *Nuclear Instruments and Methods in Physics Research Section A: Accelerators, Spectrometers, Detectors and Associated Equipment*, **764**, 156-166.

Chipera, S.J. & Bish, D.L. (2013) Fitting full X-ray diffraction patterns for quantitative analysis: A method for readily quantifying crystalline and disordered phases. *Advances in Materials Physics and Chemistry*, **3**, 47-53.

Churchman, G.J. & Theng, B.K.G. (1984) Interactions of halloysites with amides; mineralogical factors affecting complex formation. *Clay Minerals*, **19**, 161-175.

Farmer, V.C. & Farmer, V.C. (1974) The layer silicates. Pp. 0. *The Infrared Spectra of Minerals*, **4**, Mineralogical Society of Great Britain and Ireland.

Giese, R.F. (1988) Kaolin minerals; structures and stabilities. *Reviews in Mineralogy and Geochemistry*, **19**, 29-66.

Hillier, S. (1999) Use of an air brush to spray dry samples for X-ray powder diffraction. *Clay Minerals*, **34**, 127-135.

Hillier, S., Brydson, R., Delbos, E., Fraser, T., Gray, N., Pendlowski, H., Phillips, I., Robertson, J. & Wilson, I. (2016) Correlations among the mineralogical and physical properties of halloysite nanotubes (HNTs). *Clay Minerals*, **51**, 325-350.

Martin, R.T. (1980) Data handbook for clay materials and other non-metallic minerals. *Clays and Clay Minerals*, **28**, 160-160.
Mukhopadhyay, S., Hewer, B., Howells, S. & Markvardsen, A. (2019) A modern approach to QENS data analysis in Mantid. *Physica B: Condensed Matter*, **563**, 41-49.
Omotoso, O., McCarty, D.K., Hillier, S. & Kleeberg, R. (2006) Some successful approaches to quantitative mineral analysis as revealed by the 3rd reynolds cup contest. *Clays and Clay Minerals*, **54**, 748-760.
Schneider, C.A., Rasband, W.S. & Eliceiri, K.W. (2012) Nih image to ImageJ: 25 years of image analysis. *Nature Methods*, **9**, 671-675.

Chapter 3

Phosphate Adsorption on Halloysite Nanotubes

3.1 INTRODUCTION

3.1.1 Phosphorus in agricultural soil systems

Phosphate minerals, such as those from the apatite group ($Ca_5(PO_4)_3(F,OH,Cl)$), can be found worldwide in igneous rocks (Oelkers & Valsami-Jones, 2008). These primary minerals subsequently release phosphorus into the soil system via various physical and chemical weathering processes. Labile phosphorus is an important component in the soil and plant growth cycle and in soil systems, often occurs in the dissolved ionic form HPO_4^{2-} and $H_2PO_4^-$ (Haygarth *et al*., 2013). Deficiency of phosphorus and phosphates in agricultural systems can limit terrestrial plant growth (Vitousek & Howarth, 1991; Smith *et al.*, 1999) and biological productivity (Oelkers and Valsami-Jones, 2008). As such, when available phosphorus or phosphate minerals are present in trace amounts or have a low solubility, this results in the need for phosphate fertilisers to improve crop production (Oelkers & Valsami-Jones, 2008). The use of phosphate fertilisers has increased significantly in Asia, where Southern Asia has a 91% contribution to global phosphate fertiliser use increase over the last 50 years (Lu & Tian, 2017). At the same time Lu and Tian (2017) found that the amount used decreased in Europe, where this decrease was in part due to concern over watercourse pollution. Excess phosphorus can be leached from soil into groundwater either as orthophosphate, organic and inorganic phosphorus or solution mineral species, as well as from food chain losses and household and human waste (Haygarth *et al*., 2013). These processes can result in significant environmental problems such as eutrophication (Weng *et al.*, 2012), which can cause loss of aquatic life, increased algal blooms and oxygen depletion of the water (Carpenter *et al.*, 1998). The use of phosphate fertilisers worldwide is dependent on population and agricultural demands, yet, phosphate is a finite resource and phosphorus extraction and recycling from waste systems is one way of efficiently using current resources (Valsami-Jones, 2005; Oelkers & Valsami-Jones, 2008).

3.1.2 Phosphate and clay minerals

Clay minerals are present in soil systems worldwide and due to both their bulk properties and surface functionalities they are the most reactive inorganic components in soils (Churchman, 2018). Phosphate retention by clay minerals plays an important role in the mobility of phosphate in the soil system (Gustafsson *et al*., 2012; Haygarth *et al*., 2013; Gérard, 2016). Historically studies on the adsorption of anions such as phosphate on minerals in the soil have focused on iron oxides/oxyhydroxide such as goethite (Golberg, 1985; He *et al*., 1997; Kubicki *et al*., 2012; Krumina *et al*., 2016), aluminium trihydroxides, such as gibbsite (Van Emmerik *et al*., 2007) and clay minerals such as kaolinite (Van Emmerick *et al*., 2007; Kamiyango *et al.*, 2009), montmorillonite and illite (Manning and Goldberg, 1996).

Halloysite is commonly found in rocks and soils around the world (Joussein *et al.*, 2005) and is especially prevalent in highly weathered tropical soils (White & Dixon, 2002) and soils developed from volcanic ash (Dixon & McKee, 1974). A greater understanding of the conditions of adsorption of phosphate onto the halloysite surface may help to contribute towards the understanding of the role and functionalities of halloysite in soils. As discussed in detail in Chapter 1, halloysite is commonly found in soil systems in its hydrated form, halloysite (10 Å). Previous studies (Grim, 1968; Norrish, 1995) have suggested that for cation exchange capacity halloysite (10 Å) has a higher cation adsorption than halloysite (7 Å). Due to the difficulties in maintaining halloysite in the 10 Å state, there are no such studies comparing the anion exchange capacity between the two hydration states of halloysite, at least according to detailed literature searching at the time of this thesis. For this reason, the phosphate adsorption will also be studied on three halloysite (10 Å) samples to determine the effect of hydration state on the anion adsorption capacity.

It is hoped that increasing the fundamental understanding of the behaviour of halloysite in soil towards phosphate adsorption and retention will contribute to the much larger discussion of the phosphate cycle.

3.1.3 Halloysite in technology

In recent years, halloysite nanotubes have found increasing application in existing and emerging technologies as discussed in Chapter 1 (Section 1.1.3), with their nanoscale central lumen, along with other useful physical and chemical properties such as high

length to diameter ratio and low toxicity (Vergaro *et al*., 2010;dos Santos *et al.*, 2017). Many of the technological applications of halloysite nanotubes rely on surface functionalisation with specific anions and cations, effectively making the halloysites anchors for functional groups. Such work requires an in-depth understanding of the surface chemistry and available reactive sites on the surfaces of the halloysites. Additionally, as a study by Pasbakhsh *et al*. (2013) highlighted, it is important to fully understand the physical characteristics of different halloysites in order to select the appropriate sample depending on the application requirements. Hence, an understanding of whether the type of tubular morphology selected makes a difference in the adsorption may allow for increased yields and efficiency when used in technology. In this context, it is hoped that phosphate anions can be used as a probe to understand more about the surface functionalities of the two morphologies of tubular halloysites and their respective anion adsorption capacities.

3.1.4 Adsorption mechanism on halloysite nanotubes

Adsorption is a partitioning process which results in an equilibrium between solvated and adsorbed species, both in solution and adsorbed to the halloysite surface.

The surface properties of halloysite may often be considered as similar to those of kaolinite. Yet, halloysite is initially formed with an interlayer of water and primarily occurs in nanotubular form compared to the exclusively planar form of kaolinite (Figure 3.1). Previous studies have emphasised differences in the adsorption behaviour of halloysite with respect to kaolinite, e.g. the higher cation exchange capacity of halloysite, reported at between 2.9-9.3 $cmol{+}kg^{-1}$ (Gray *et al*., 2016) compared to kaolinite, 2.8 – 5.0 $cmol{+}kg^{-1}$ (Ma and Eggleton, 1999), where the higher CEC for halloysite was credited to higher surface area, hence, more available edge sites for adsorption (Gray *et al.,* 2016). A study by Tarì *et al.* (1999) found a higher zeta potential of halloysites compared to kaolinites, suggestive of variations in surface charge, and therefore surface chemistry between the two polytypes, where these authors attributed the change due to a higher degree of isomorphic substitution and hence increase in permanent charge of halloysites.

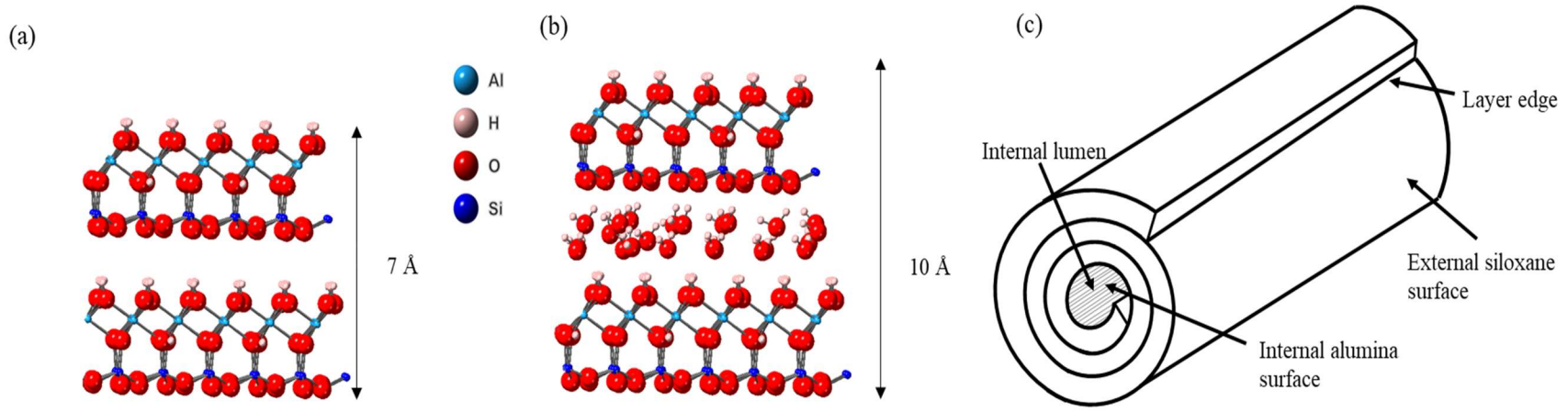

Figure 3.1a. Layer structure of halloysite (7 Å) b. Layer structure halloysite (10 Å) c. Assumed simplistic diagram of a tubular halloysite.

Whilst kaolinite has been regularly studied for its phosphate adsorption properties (Edzwald *et al*., 1976; He *et al*., 1997; Gimsing and Borggaard, 2002; Kamiyango *et al*., 2009; Gérard, 2016) there are, by contrast, very few studies on halloysite. Recent studies include those by Saki *et al*. (2019) and Almasri *et al*. (2019) who reported phosphate adsorption on the Al-OH sites at the tube edge and inner lumen of halloysites with adsorption capacities of 1.2 mg/g and 1.5 mg/g, respectively. A study by Theng *et al.* (1982) highlighted the importance of morphology on adsorption capacity for halloysite when they reported the maximum phosphate adsorption as 10 μmol/g (2.58 mg/g) for tubular halloysites and ≤ 50% of this for spheroidal morphologies. This dramatic drop in adsorption for spheroidal halloysites was attributed to there being fewer edge sites on the spheroidal morphology.

3.1.5 Clay minerals in remediation

Multiple studies have been conducted on the removal of phosphates from waste water systems using materials such as natural and modified zeolites (Uzunova & Mikosch, 2016; He *et al*., 2017; Andrés *et al*., 2018) ochre (Heal *et al*., 2003), kaolinite (Kamiyango *et al*., 2009), goethite (Ioannou *et al*., 2013; Wei *et al*., 2014), hematite (Borgaard, 1983) and bentonite systems (Ioannou *et al*., 2013), where after normalisation to specific surface area the most effective adsorbents were the iron oxide, hematite, (0.34 mg/g) and modified zeolite (0.326 mg/m^2). The desorption of phosphate from these materials was not always investigated. The potential use of halloysite for such methods has only recently been considered (Almasri *et al*., 2019) and is such identified as an area that requires further research. In order to increase the feasibility of a material for use in phosphate remediation it is necessary to consider the recyclability of the materials (Loganathan *et al.,* 2013), hence, as well as adsorption, the desorption of phosphate from halloysite nanotubes will also be considered in this chapter.

3.1.6 Summary

The adsorption behaviour of the phosphate anion can be used as a useful reference molecular probe of the surface chemistry characteristics of halloysite nanotubes. This chapter aims to document the characteristics of phosphate adsorption on halloysite nanotubes, and to highlight the effects of varying morphology and surface area of halloysite nanotubes on the resulting phosphate adsorption capacity. In addition, the

work outlined in this chapter will briefly touch upon a comparison of the phosphate adsorption behaviour between halloysite (10 Å) and halloysite (7 Å), as well as looking at the desorption of phosphate from halloysite (7 Å).

3.2 MATERIALS AND METHODS

3.2.1 Kaolin samples

Batch adsorption reactions were conducted to determine the effect of pH, varying background electrolyte ionic strength, phosphate concentration and hydration state on the phosphate anion adsorption behaviour of the kaolin group minerals, with particular focus on whether the morphology of the halloysite nanotubes affected the adsorption behaviour.

Two well-characterised dehydrated halloysite (7 Å) samples (Hillier *et al.*, 2016) were used for this study: one from China (4Ch) and one from Utah, USA (17US) some tests were conducted on the disordered and well-studied (He *et al.*, 1997; Gimsing and Borggard, 2002; Van Emmerick *et al*., 2007) kaolinite KGa-2 from the Clay Minerals Society Source Clays Repository. Additionally, three halloysite (10 Å) samples: two of cylindrical morphology from China (5Ch and 6Ch) and one prismatic sample from Dragon Mine, USA (23US), where the physical properties of each are given in Chapter 2, Table 2.1.

All three dehydrated clay samples (17US, 4Ch and KGa-2) were prepared for analysis by sieving to <53 μm, sodium saturated with excess NaCl and repeatedly washed with deionised water until they were verified as salt free by silver nitrate testing which took around 3-4 days. The samples were then freeze dried. The halloysite (10 Å) samples were prepared by wet sieving through a < 53 μm sieve, the wet mix was then transferred to dialysis tubing and saturated with excess NaCl to monosaturate the surface and remove another cations that may be present, before being washed with deionised water until verified as salt free by silver nitrate testing. The halloysite (10 Å) samples were transferred as the wet suspension to plastic sample bottles for storage until analysis. As an additional check a portion from each sample was dried down and run by X-ray powder diffraction (XRPD) as hand ground powders.

Multiple experiments were run as part of the work for this chapter as are outlined in the simplified flow diagram in Figure 3.2 below.

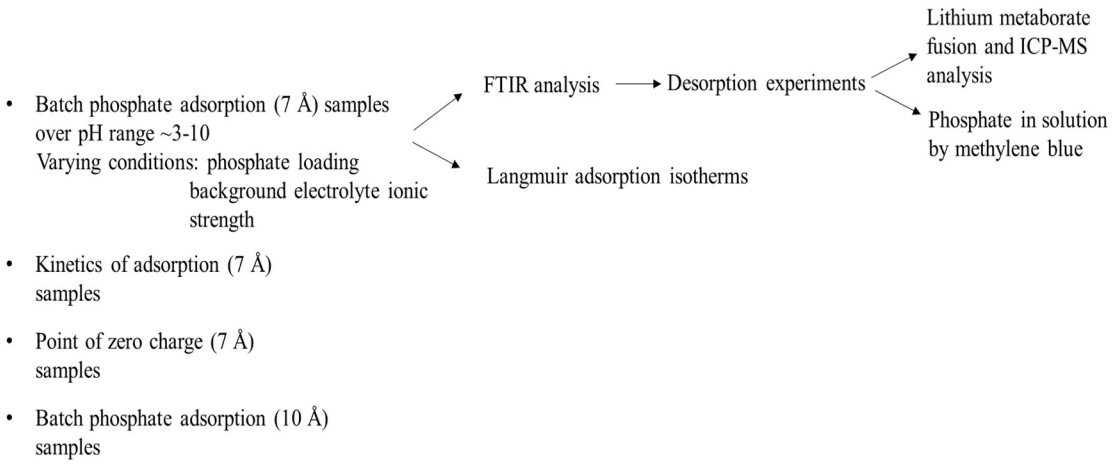

Figure 3.2. Simplified flow diagram of the experimental procedures conducted as part of this chapter.

3.2.2 Batch equilibrium experiments on dehydrated kaolin minerals (4Ch, 17US and KGa-2)

Batch equilibrium systems were used to measure the phosphate adsorption onto the clay minerals over a pH range. For this, 0.1 g of clay was oven-dried at 105 ˚C overnight and mixed with 28 ml of varying concentrations of background electrolyte, NaCl, varying from 0.001 M to 0.1 M. The varying concentration of NaCl provides information of the type of adsorption, i.e., chemisorption or physisorption as discussed further in Section 3.4.3. The resulting suspensions were pH adjusted to a range of around pH 3-10 using 1 ml of differing concentrations of HCl (standardised against Na_2CO_3) or NaOH (standardised and carbonate free) before being shaken for 24 hours in a box shaker. The varying pH values were to determine the effect of pH on the adsorption. 1 ml of a known concentration of sodium dihydrogen (ortho)phosphate 1-hydrate ($NaH_2PO_4.H_2O$) was added to the samples and they were shaken for 16 hours. The initial phosphate concentration ranged from 2.5-8 mg/l. The maximum and minimum concentrations of phosphate required for monolayer saturation was initially estimated from previous work that calculated the ratio of permanent negatively charged surface sites to pH dependent edge sites as 1:3 (Gray *et al*., 2016) and from reference to literature (Theng *et al*. 1982). Avoidance of supersaturation of the surface

by excess phosphate was employed to minimise, where possible, excess precipitation of phosphate in the solution with dissolved kaolin at low pH (Section 3.3.) and multilayer adsorption.

The pH for each sample was measured using a HACH HQ440d pH meter and recorded after 5 minutes with constant stirring. The samples were centrifuged before filtering through 0.45 µm Nylon® filters and stored in a cold room for analysis. Due to their small size, they rapidly blocked up the filter paper and so significant pressure was often required to force the samples through the syringe. Supernatant phosphate concentrations were determined using the molybdenum blue method on a Konelab Discrete Analyser, which measures phosphorus in the form of phosphate ($P\text{-}PO_4$) to give phosphate concentrations by colorimetry. Dissolved aluminium and silicon in the filtrate were measured by inductively coupled plasma-optical emission spectroscopy (ICP-OES) on a Perkin Elmer Optima 5300DV ICP-OES in a 0.1 M NaCl matrix with a pump flow rate of 0.6 mL/min and 15 L/min plasma. Each experiment was run in triplicate along with a control blank.

3.2.3 Batch equilibrium experiments on hydrated (10 Å) halloysites (5Ch, 6Ch and 23US)

Phosphate adsorption on three halloysite (10 Å) samples was also studied. The slurries were transferred to large beakers under continual stirring and 2 ml of suspension (halloysite (10 Å) and deionised water) was weight recorded and mixed with 27 ml of 0.01 M NaCl background electrolyte. The resulting suspensions were pH adjusted using 1 ml of differing concentrations of HCl (standardised against Na_2CO_3) or NaOH (standardised and carbonate free) and shaken for 24 hours in a box shaker. 1 ml of a known concentration of sodium dihydrogen (ortho)phosphate 1-hydrate, 10 mg/l phosphate, was added to the samples and they were shaken for 48 hours. The remainder of the method was the same as for the halloysite (7 Å) samples as outlined in Section 3.2.2.

To reduce potential errors in calculating the amount of phosphate adsorbed per mass of halloysite three 2 ml aliquots of each sample were dried down in the oven to obtain an average density. From this is was determined that the average mass of halloysite in 2 ml was 0.1 g, to correspond with the mass used in the dehydrated batch equilibrium experiments.

3.2.4 Kinetic experiments of phosphate adsorption

Halloysite (7 Å) (0.1 g) was mixed with 28 ml of 0.01 M NaCl, the pH was adjusted to around pH 6 using weak sodium hydroxide base. The samples were shaken for 24 hours in a box shaker at between 150-200 rpm. After 24 hours of shaking, 1 ml of ~8 mg/l phosphate was added to the suspension and the samples were shaken using the same settings described above for a range of times between 1 hour and 10 days. The pH of the suspension was measured before centrifugation, filtration and remaining phosphate analysis, as described in the batch equilibration method in Section 3.2.2. All experiments were conducted in triplicate with control blanks.

3.2.5 Point of zero charge (PZC) measurements

Point of zero charge measurements were conducted on the halloysite (7 Å) and KGa-2 samples according to the salt addition method (Holliman *et al.*, 2008) wherein aliquots of 0.01 M NaCl were added to ten individual centrifuge tubes, each containing 0.1 g clay and the initial pH was adjusted and recorded to vary from ~2 to 11 using varying concentrations of HCl and NaOH. The samples were thoroughly mixed and shaken for 24 hours in a box shaker and the final pH was measured after 24 hours. The difference between the initial and final pH (ΔpH) was plotted against the initial pH. The PZC is described as the point at which the change in pH is zero with respect to the initial pH.

3.2.6 Langmuir adsorption isotherms

Data from the phosphate loading results obtained in the batch adsorption experiments for the halloysites at four approximate pH values (3, 6, 7.5 and 10) were fitted to the linearized form of the Langmuir equation (as rearranged in Parfitt, 1978) as shown in equation 3.1 below:

Equation 3.1: $\frac{c}{x} = \frac{1}{Ky} + \frac{c}{y}$

Where c is the concentration of phosphate in solution (mg/l), x is the amount of phosphate adsorbed onto the kaolin surface (mg/g), y is the Langmuir sorption maximum (mg/g) and K is a Langmuir coefficient related to the bonding energy. The Langmuir adsorption model assumes that adsorption occurs as a monolayer with localised adsorption and that each adsorption site can only accommodate one

adsorbate molecule. It further assumes that the binding energy of each molecule is independent of occupation of nearby sites. The data for each sample was plotted on a graph of c/x vs x and when a straight line with slope equal to 1/y and intercept equal to 1/Ky was obtained for the samples, then the Langmuir isotherm was seen to be satisfied.

3.2.7 Fourier transform infrared spectroscopy (FTIR)

ATR-FTIR can be used to identify changes in the nature of chemical bonds in clay minerals, and hence, by comparison of pure clay samples and samples with adsorbed species on the surface the adsorption sites can be inferred. Hand ground samples were oven dried at 105 ˚C over two days and infrared spectra were measured on a Bruker Vertex 70 Fourier Transform Infrared (ATR-FTIR) spectrometer in the mid infrared region from 4000 to 400 cm^{-1} with a scan rate of 200 scans per spectra and a resolution of 4 cm^{-1}. 200 scans were run for each sample to improve the signal to noise ratio. A germanium ATR disk was used to reduce penetration depth into the sample to determine the changes on the surface more clearly. The FTIR spectrometer is dry-air purged to prevent interference in the spectra from water vapour and carbon dioxide. Due to the difficulties in detecting changes in the FTIR spectra from the batch adsorption experiments the samples were saturated with 215 mg/l phosphate to determine whether a change could be noted in the FTIR spectra.

3.2.8 Desorption experiments

Desorption experiments were conducted on the samples which had been saturated with 215 mg/l phosphate after FTIR analysis. The samples were dried down after analysis by purging with nitrogen gas. The dried down samples were then subjected to two types of washing. The first used acetone to remove physisorbed phosphate and the second involved washing with 0.1 M NaOH to remove chemisorbed phosphate, where NaOH has been shown as effective in removing phosphonates from galvanised steel (Hill *et al*., 2019). Desorption experiments were carried out by mixing the samples with combinations of acetone alone or acetone and then 0.1 M sodium hydroxide. Once the acetone/NaOH was added, the samples were hand shaken for 5 minutes and centrifuged at 2000 rpm for 15 minutes before being filtered through 0.45 µm Nylon® filters. The filtered supernatant was stored in a cold room until analysis for desorbed phosphate was conducted using the molybdenum blue method on a Konelab Discrete

Analyser. In a new method for desorption reactions the solid material was dried down under nitrogen after the respective washing where a portion of dried down material then underwent treatment by lithium metaborate fusion and Inductively Coupled Plasma Mass Spectrometry (ICP-MS) chemical analysis (outlined in section 3.2.9 below). ICP-MS was conducted on an Agilent 7700 ICP-MS in a $LiBO_2$/2 M HNO_3 matrix with a pump flow rate of 0.60 revolutions per second and an integration time of 0.10 seconds. The limit of detection of P in this method was 0.009 mg/l. In addition, FTIR analysis was conducted on any remaining material.

3.2.9 Lithium metaborate fusion and Inductively Coupled Plasma-Mass Spectrometry analysis

Borate fusion reactions are often used for the dissolution of geological materials due to the efficacy in dissolving most silicates, carbonates and sulphates for trace element analysis (Croudace *et al*., 1998; Mounteney *et al*., 2018), and hence such a method has been adapted and applied here. From this, it was deemed a suitable method for dissolution of the solid halloysite samples for elemental analysis by ICP-MS.

Analysis was conducted on samples that had been dried overnight at 105 ˚C. The hand ground sample (100 mg) was weighed into a platinum crucible. To each crucible 1 g of lithium metaborate flux was added and care was taken to ensure that the flux covered the sample evenly. The samples were placed in the Katanax X-3000 fusion machine as shown in Figure 3.3. Nitric acid (8 ml, 10%) was added to each of the corresponding PTFE beakers along with a stirrer and the fusion method was initiated as a ten-minute heating stage programme which heats the samples to 1000 °C. The molten samples in the platinum cups were automatically poured into the PTFE beakers containing nitric acid. The PTFE beakers were removed from the instrument and placed onto stirring plates with magnetic stirrers for a full ten minutes to aid in full dissolution of material. From this the samples are transferred to 100 ml volumetric flasks and made up to volume with Millipore water for analysis by ICP-MS.

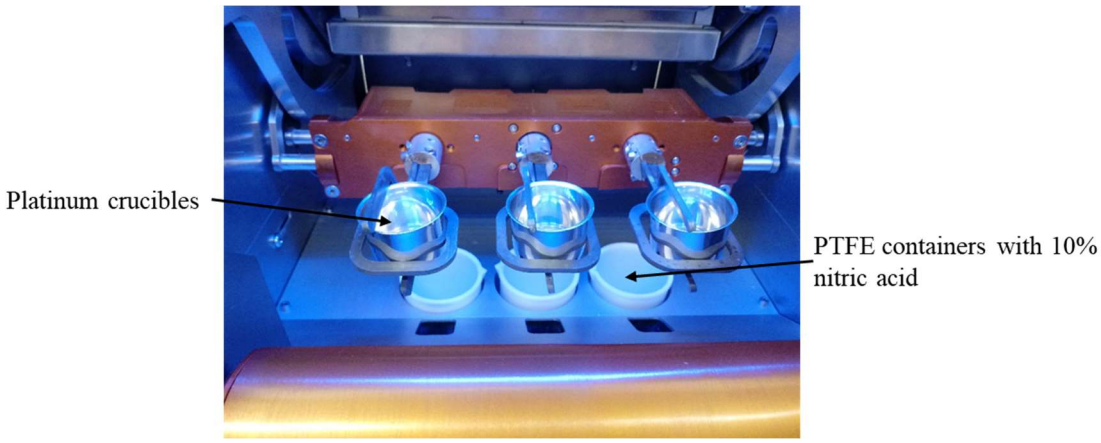

Figure 3.3. Platinum crucibles in the Katanax X-3000 fusion instrument.

3.3 RESULTS

3.3.1 Batch adsorption experiments and kinetic studies

Kinetic adsorption experiments conducted over a time period of 30 minutes to 10 days showed that, for both halloysites, the adsorption of phosphate was rapid and the initial adsorption occurred within hours (Figure 3.4). This is particularly noticeable in the prismatic halloysite 17US. From Figure 3.4 it is apparent that the cylindrical halloysite (4Ch) displays the greatest phosphate adsorption (ca. 42 µmol/g: 1.3 mg/g) compared to the polygonal prismatic 17US halloysite (ca 15 µmol/g: 0.5 mg/g) after 10 days equilibration.

The batch adsorption experiments for this study were therefore conducted after a minimum of overnight shaking (*ca*. 16 hours). Phosphate adsorption curves over a large pH range and under varying conditions of background electrolyte ionic strength and initial phosphate loading all show a similar parabolic shape with maximum adsorption at around pH 6 and a steady decrease in adsorption with increasing pH (Figures 3.5 and 3.6).

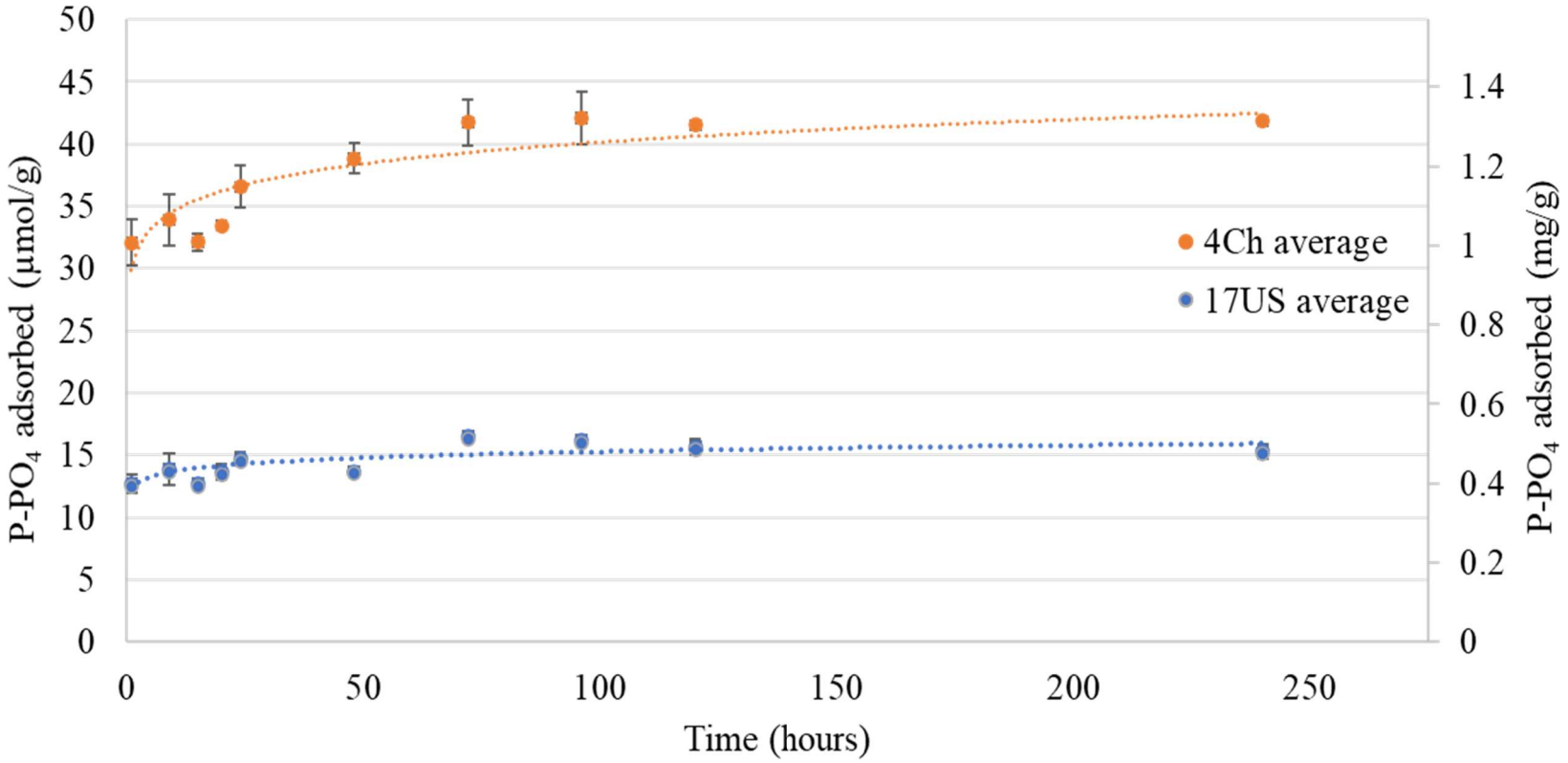

Figure 3.4. Graph showing a comparison of the kinetics of adsorption for 17US and 4Ch halloysite (7 Å) samples at ambient pH (approximately pH 5- 6). The phosphate (P-PO_4) adsorbed to the surface of each sample was measured from a timescale of between 30 minutes and 10 days.

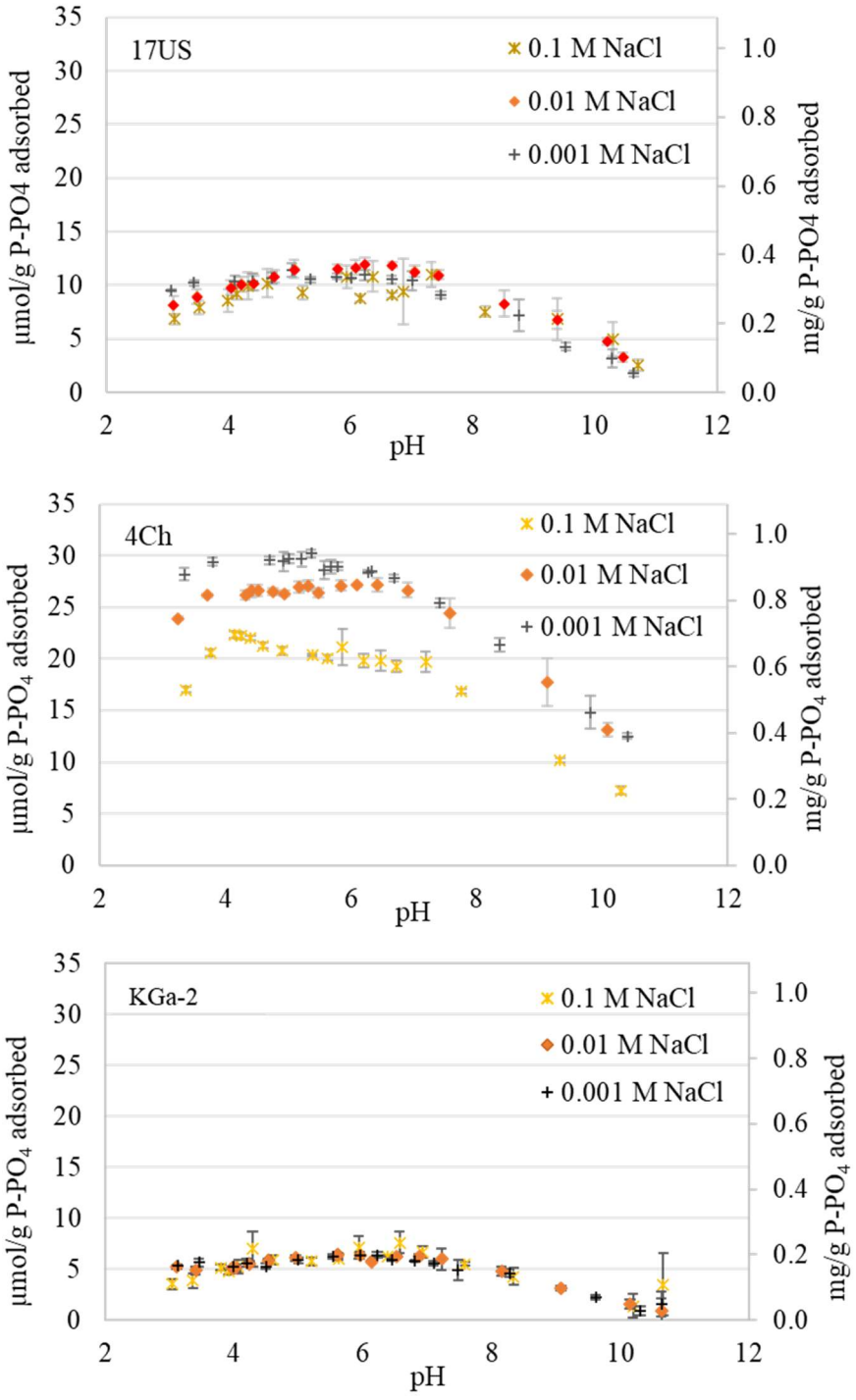

Figure 3.5. The effect of background electrolyte ionic strength on kaolin adsorption for the two halloysite (7 Å) samples and the kaolinite sample. The initial phosphate ($P\text{-}PO_4$) loading for each sample was 4 mg/l. Each analysis was conducted in triplicate and the error bars are shown on each graph.

For the two halloysite (7 Å) samples the amount of phosphate adsorbed is seen to be dependent on the initial concentration of phosphate, where the maximum phosphate

added in this experimental series was 10 mg/l as shown in Figure 3.6. From these graphs the maximum adsorption for 17US and 4Ch was 0.45 mg/g and 1.1 mg/g respectively.

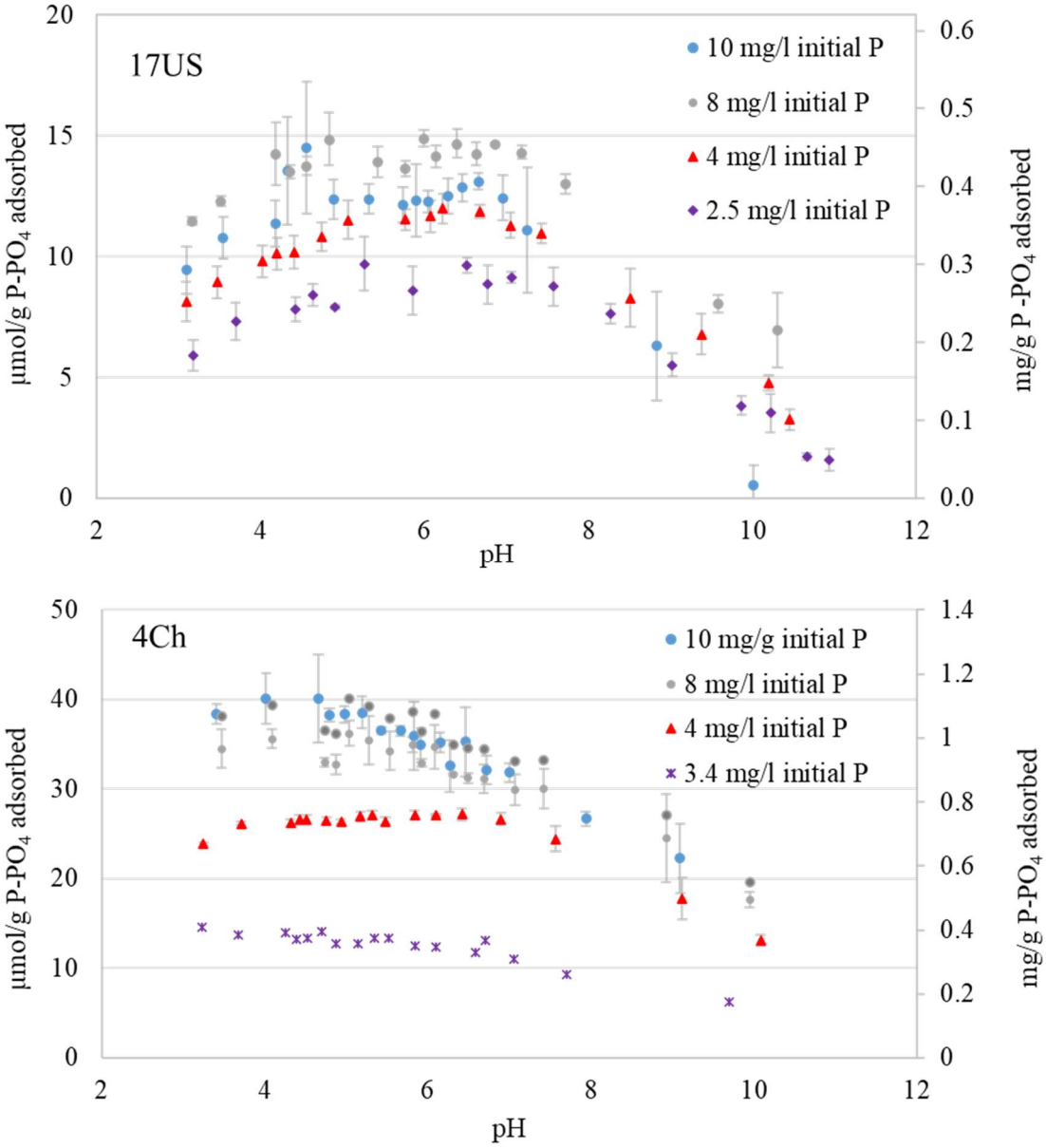

Figure 3.6. The effect of initial phosphate loading on phosphate (P-PO_4) adsorption for the two halloysite (7 Å) samples over a pH range of ~3-10 with a NaCl concentration of 0.01 M. The maximum adsorption for 17US and 4Ch was 0.45 mg/g and 1.1 mg/g respectively. Each analysis was conducted in triplicate and the error bars are shown on each graph.

The phosphate adsorption data with varying initial phosphate concentrations was applied to the data at approximate pH points of 3, 6, 7.5 and 10. The resulting graphs (Figures 3.7 and 3.8) show that the 17US halloysite fits a linear Langmuir isotherm equation (R^2 = 0.9165-0.9395) for the lower pH's whilst a poor fit was obtained at pH 10 (R^2 = 0.4902). The linear Langmuir equation gave a maximum phosphate adsorption of 0.45 mg/g at pH 6 under these experimental conditions for the 17US sample. In contrast, the 4Ch data did not fit to a Langmuir isotherm (R^2 = 8 x 10^{-6} – 0.5226).

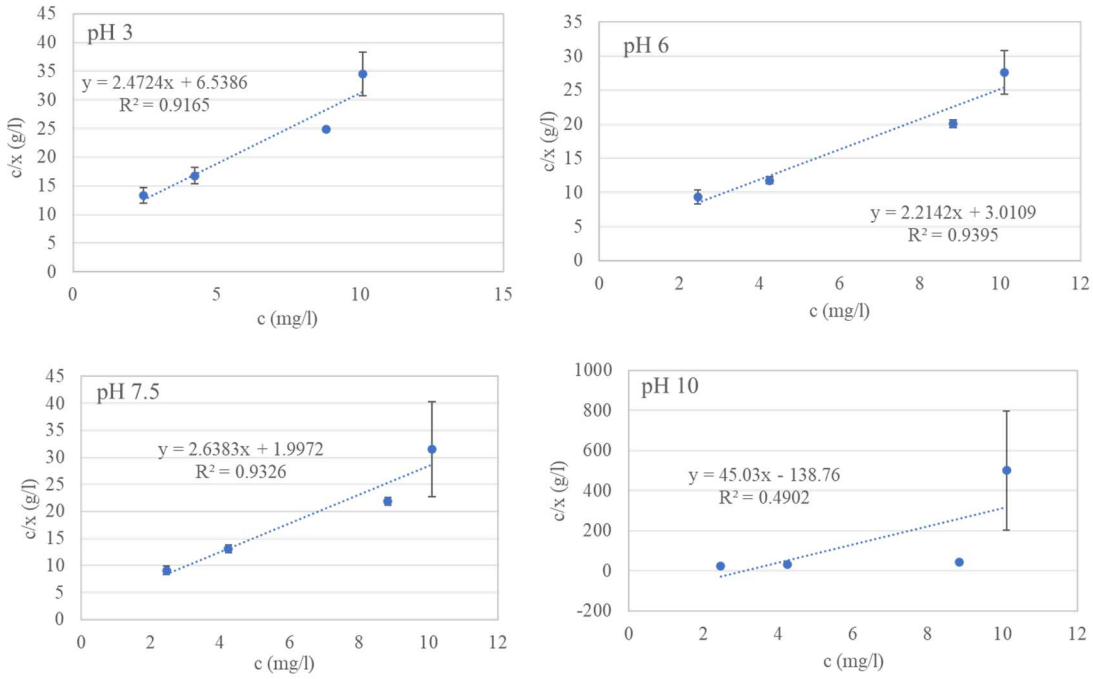

Figure 3.7. Linear Langmuir isotherms at fixed pH's for polygonal prismatic 17US. A good fit was observed for pH's 3, 6, and 7.5 as shown by the R^2 values on the respective graphs. From the graphs a maximum phosphate adsorption of 0.45 mg/g at pH 6 was estimated.

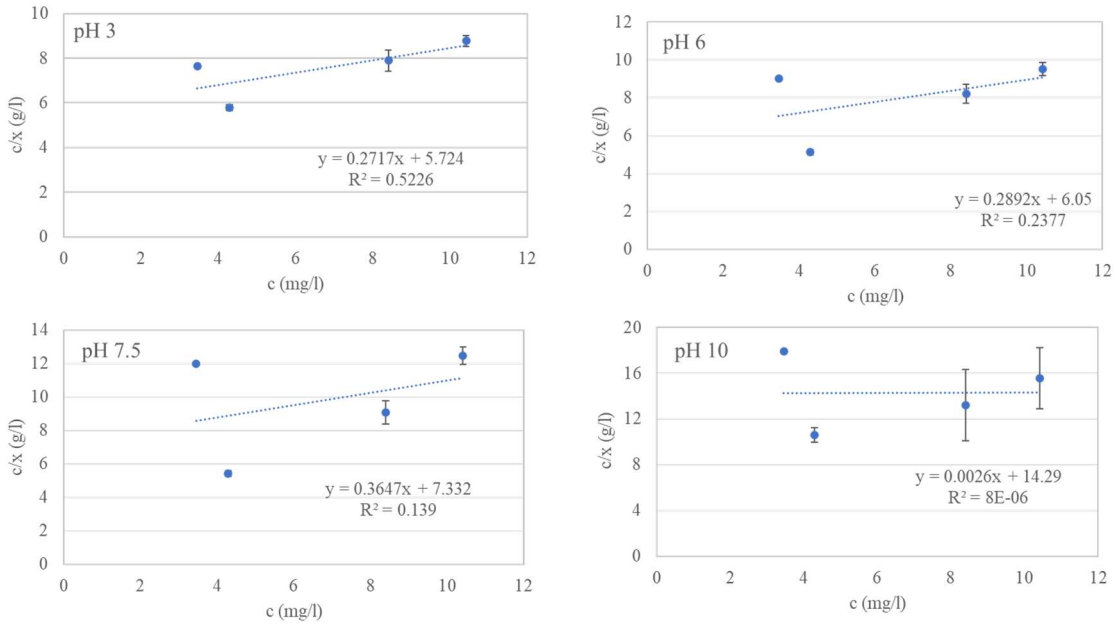

Figure 3.8. Linear Langmuir isotherms at fixed pH's for cylindrical 4Ch.The calculated R^2 values on the graphs indicate that the sample does not fit to the Langmuir model for phosphate adsorption at the pH's shown.

3.3.2 Halloysite (10 Å) batch adsorption results

Batch adsorption experiments were conducted on three hydrated halloysite (10 Å) samples, of differing morphologies, one polygonal (23US) and two cylindrical (5Ch and 6Ch). The parameters such as changing background electrolyte strength and varying phosphate loadings for these adsorption reactions were not investigated, instead 10 mg/l initial phosphate was added using 0.01 M NaCl to determine if the hydrated halloysites showed higher or comparable phosphate adsorption to the halloysite (7 Å) samples that were run under the same conditions. The results for the three replicates of each adsorption curve over a pH range are shown in Figure 3.9 for the halloysite (10 Å) samples and Figure 3.10 for the halloysite (7 Å) samples.

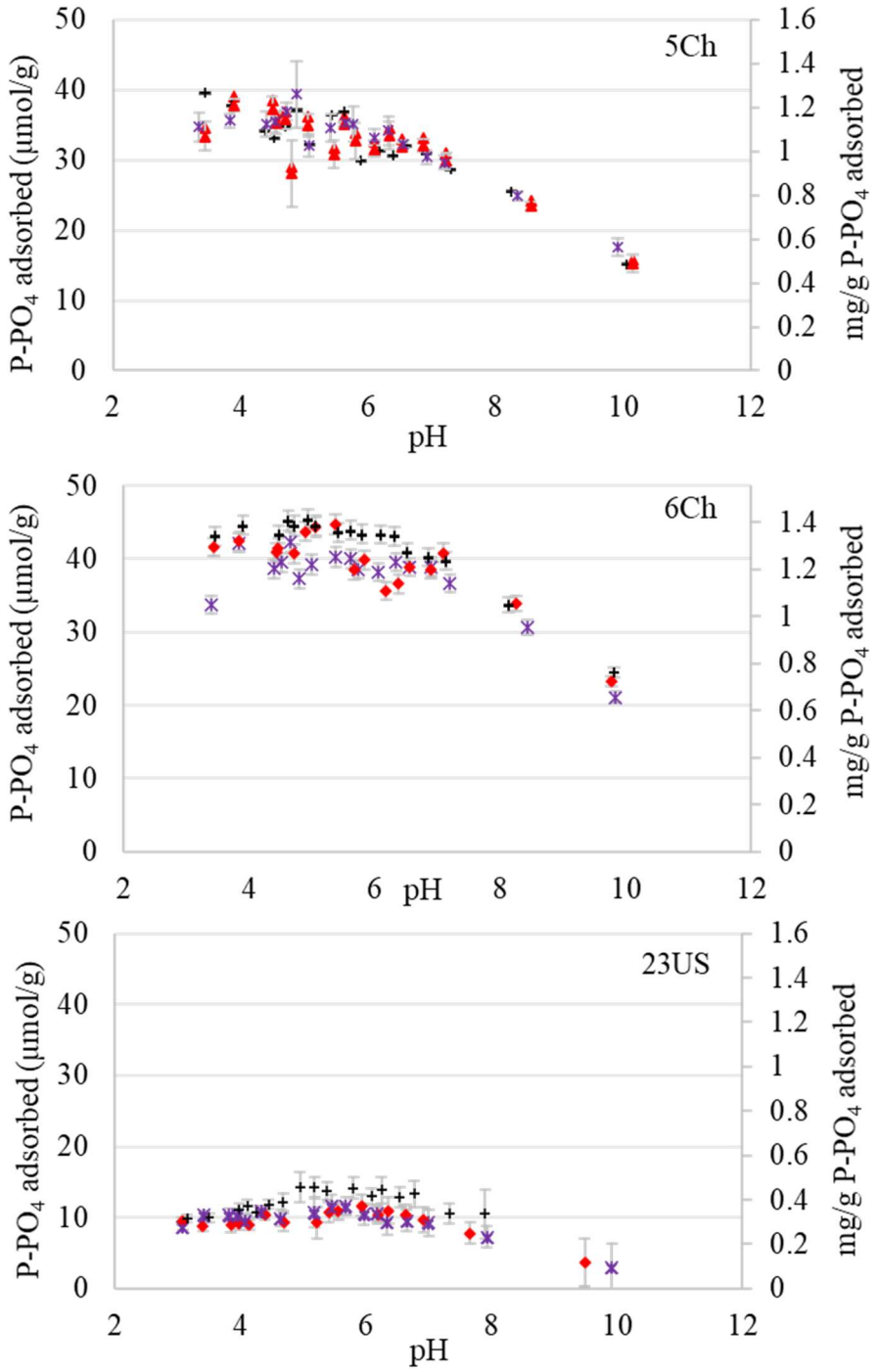

Figure 3.9. Graphs showing phosphate (P-PO_4) adsorption over a pH range of ~3-10 for three repeats of three halloysite (10 Å) samples (5Ch, 6Ch and 23US). The initial phosphate loading for each sample was 10 mg/l and equilibrium time was 48 hours. The error bars are shown on each graph.

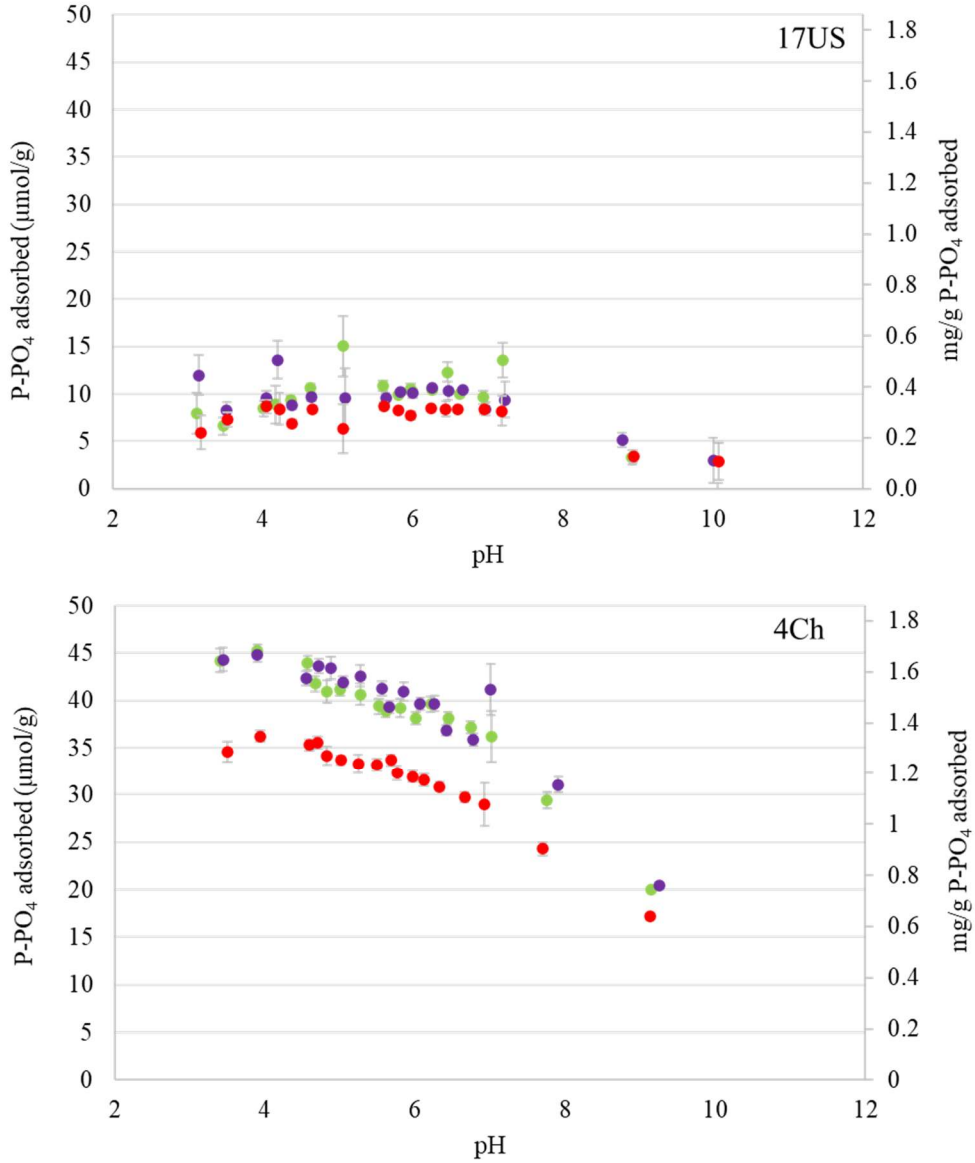

Figure 3.10. Graphs showing phosphate ($P\text{-}PO_4$) adsorption over a pH range of ~3-10 for the three repeats of two halloysite (7 Å) samples. The initial phosphate loading for each sample was 10 mg/l and equilibrium time was 48 hours. The error bars are shown on each graph.

A comparison of the results between the halloysite (10 Å) samples and the halloysite (7 Å) samples indicates that there is no considerable variation between the two when their morphologies and possible mass errors due to the use of a suspension for the halloysite (10 Å) samples are considered. The maximum adsorption of 1.3 mg/g, 1.4 mg/g and 0.4 mg/g were seen for the hydrated halloysite (10 Å) 5Ch, 6Ch and 23US respectively, whilst the dehydrated halloysite (7 Å) 4Ch and 17US adsorbed

maximums of around 1.6 mg/g and 0.4 mg/g respectively. An interesting aside notes that the hydrated 6Ch cylindrical sample adsorbs slightly higher phosphate than the hydrated 5Ch cylindrical halloysite, suggesting that even within the same morphology and identical treatments, further small differences in the samples such as surface area and particle size may result in different adsorptions.

3.3.3 Point of zero charge results

The further understand the surface charge on the halloysites the point of zero charge (PZC) is the pH at which the charge density on the surface of the clay is zero. The graphs describing ΔpH as a function of pH (Figure 3.11) for PZC determination show notably similar trends across the three minerals investigated. The measured PZC values for the three samples were 5.65 (4Ch), 4.85 (17US) and 5.90 (KGa-2).

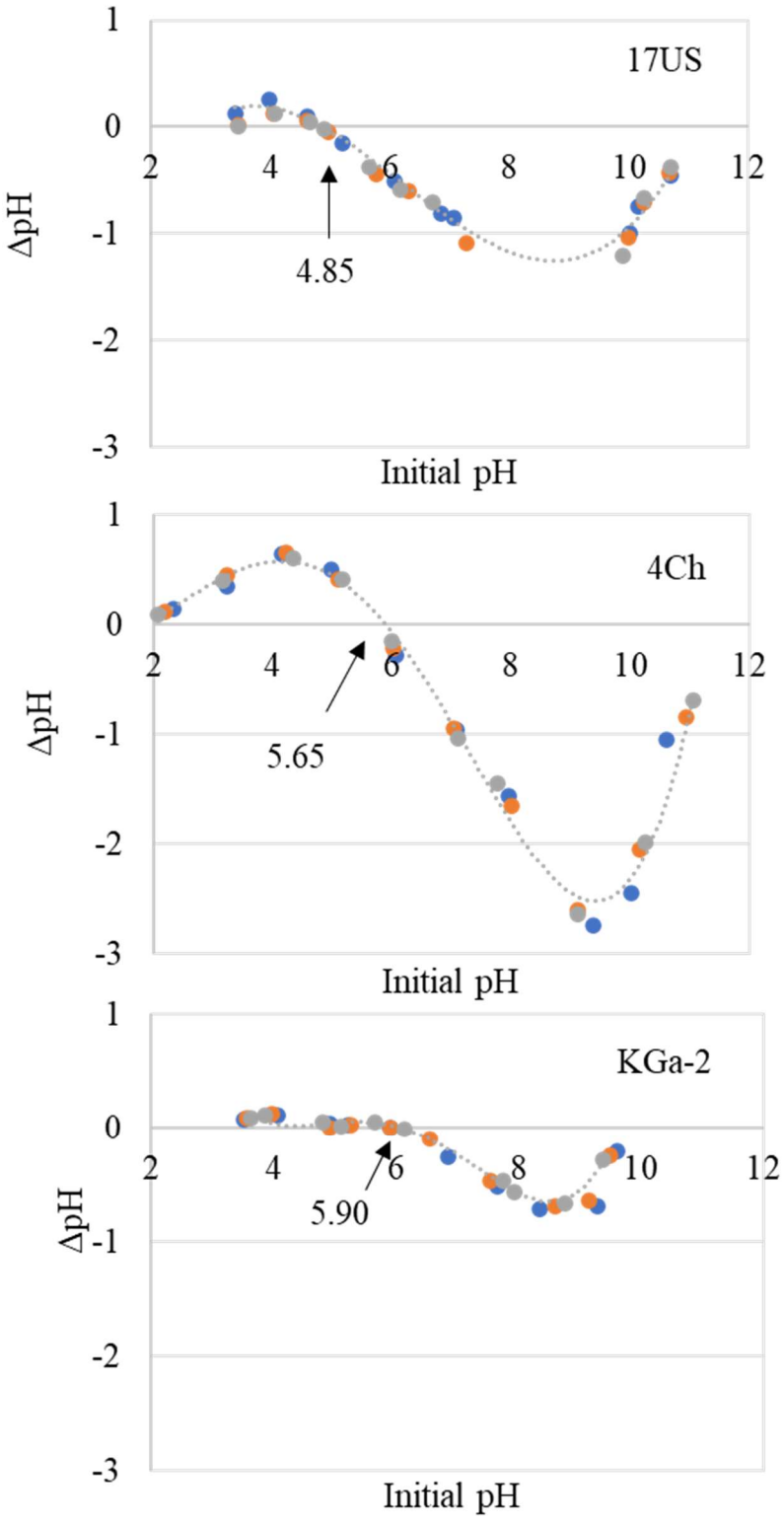

Figure 3.11. Point of zero charge measurements for the three repeats of the two halloysite (7 Å) samples and the disordered kaolinite. The PZC values were measured as 4.85 for 17US, 5.65 for 4Ch and 5.90 for KGa-2 as labelled on the graphs.

3.3.4 Effect of morphology on anion adsorption

As shown in Chapter 2, Table 2.1, cylindrical halloysites typically have a greater surface area (approximately 60-90 m^2/g) than polygonal prismatic halloysites (approximately 15-30 m^2/g), this is due to their smaller particle size. To determine the effect of tubular morphology on the phosphate adsorption the kaolin group minerals were normalised to their specific surface area. In the case of the halloysite (7 Å) samples (Figure 3.12), the normalised adsorption curves for kaolinite and cylindrical halloysite 4Ch are closely matched whilst the polygonal prismatic 17US displays a small increase in adsorption levels between pH 5 and 7. The general convergence of the data points after normalisation to the specific surface area effectively demonstrates the importance of this feature on the phosphate adsorption capacity.

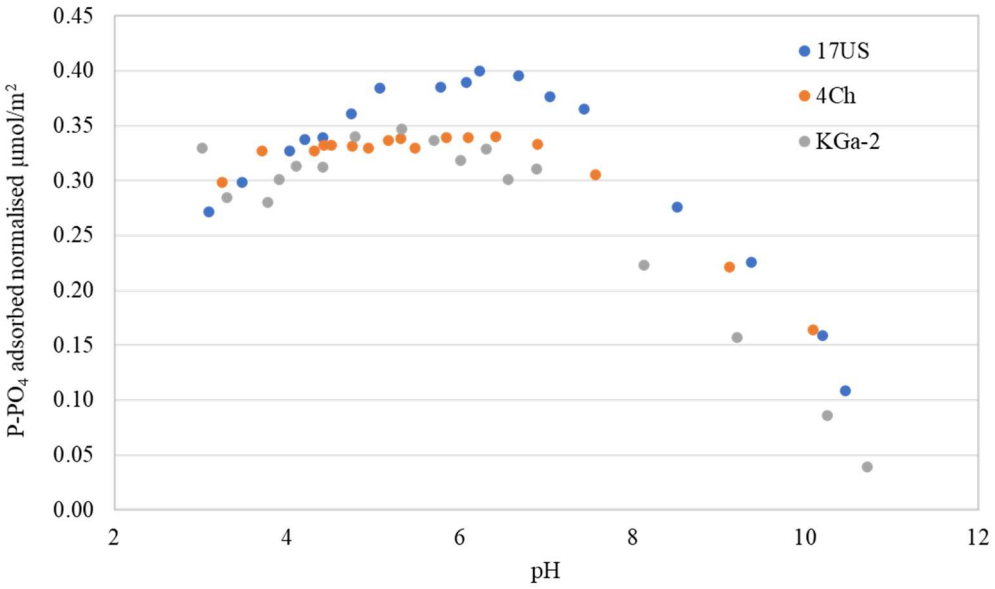

Figure 3.12. Normalisation of adsorption curves to surface area for the halloysite (7 Å) samples with a phosphate loading of 4 mg/l where a general convergence of data points can be observed with the maximum adsorption at around pH 6.

By contrast, the halloysite (10 Å) samples do not show the same behaviour after normalisation to surface area (Figure 3.13). The two cylindrical samples (5Ch and 6Ch) converge upon normalisation whilst the normalised adsorption for the polygonal prismatic sample (23US) is seen to drop significantly.

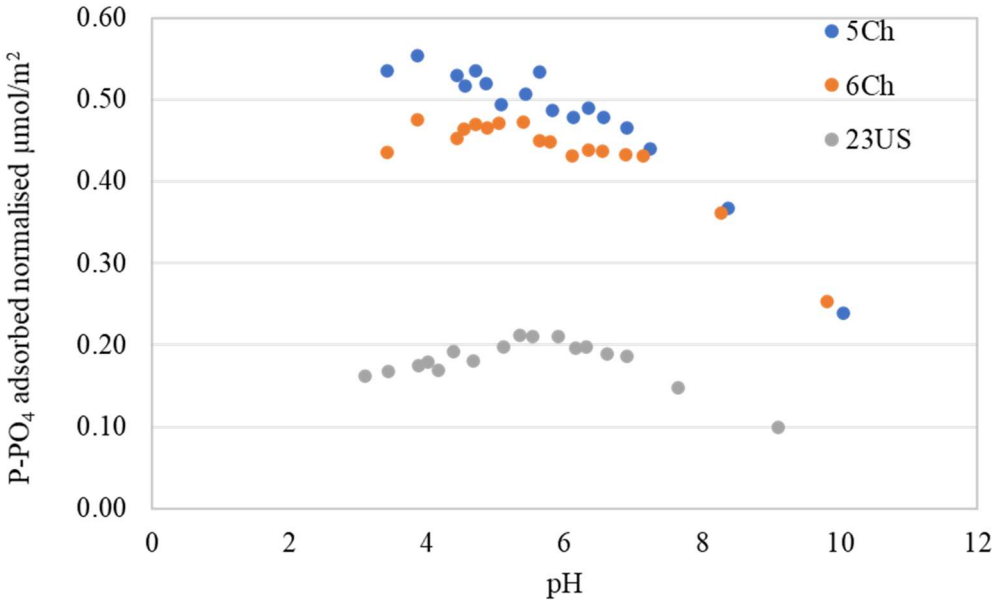

Figure 3.13. Normalisation of adsorption curves to surface area for the halloysite (10 Å) samples where a convergence of the data points can be observed for the cylindrical samples 5Ch and 6Ch.

Some further observations of the samples were made during the batch adsorption experiments by examining their Tyndall effect. The Tyndall effect is a visual representation of the scattering of light by particles in a suspension, from which the stability of the suspension can be inferred. In this instance, a red or green laser pen was shone through the samples after continuous stirring for 5 minutes during the pH measurements, and the scattering of the light was noted after 1 minute, 5 minutes and 10 minutes of settling time. The results are presented in Table 3.1. For the polygonal prismatic 17US sample at low pH (~3) the change in scattering of light over times is suggestive of an unstable suspension (Figure 3.14). Whilst at pH ~10-11 the suspension was stable for up to 30 minutes. In the case of the cylindrical 4Ch it could be seen that at all pH's there was no scattering of the light, this suggests that the cylindrical sample rapidly flocculated in comparison to the polygonal prismatic sample.

Table 3.1. Tyndall Effect observations on the two halloysite (7 Å) samples at a variety of pH's and timescales.

Sample ID	pH	Time (minutes)	Observation
17US	~3	1	Small scattering
	~3	5	No scattering
	~3	10	No scattering
	~5	1	No scattering
	~5	5	No scattering
	~5	10	No scattering
	~10-11	1	High scattering, no passage of beam through sample
	~10-11	5	High scattering, no passage of beam through sample
	~10-11	10	High scattering, no passage of beam through sample
	~10-11	30	High scattering, no passage of beam through sample
4Ch	~3	1	No scattering
	~3	5	No scattering
	~3	10	No scattering
	~5	1	No scattering
	~5	5	No scattering
	~5	10	No scattering
	~10-11	1	No scattering
	~10-11	5	No scattering
	~10-11	10	No scattering

Figure 3.14. Tyndall Effect observations for the 17US prismatic sample at three different time points. The sample solutions are approximately pH 3.

3.3.5 Phosphate speciation curves

Phosphate speciation curves were calculated from first principles using the speciation of phosphoric acid, which is a triprotic acid. The dissociation of phosphoric acid can be expressed as a series of dissociation constants as shown below:

$H_3PO_4 \leftrightarrow H_2PO_4^- + H^+$ $\quad \log_{Ka1} = -2.148$

$H_3PO_4 \leftrightarrow HPO_4^{2-} + 2H^+$ $\quad \log_{\beta 2} = -9.346,\ \beta_2 = K_{a1} \times K_{a2}$

$H_3PO_4 \leftrightarrow PO_4^{3-} + 3H^+$ $\quad \log_{\beta 3} = -21.721,\ \beta_3 = K_{a1} \times K_{a2} \times K_{a3}$

Where K_a = Individual steps formation constant and β = combined stepwise formation constant.

The speciation constants are also given in Table 3.2 and the calculated solution speciation curves for phosphonic acid with varying pH (Figure 3.15) show increasing charge of the phosphate species with increasing pH.

Table 3.2. Thermodynamic constants used in the calculation of the solution speciation of phosphoric acid.

K_{a1}	7.11×10^{-3}	K_{a2}	6.44×10^{-8}	K_{a3}	4.22×10^{-13}
pK_{a1}	2.148	pK_{a2}	7.191	pK_{a3}	12.375

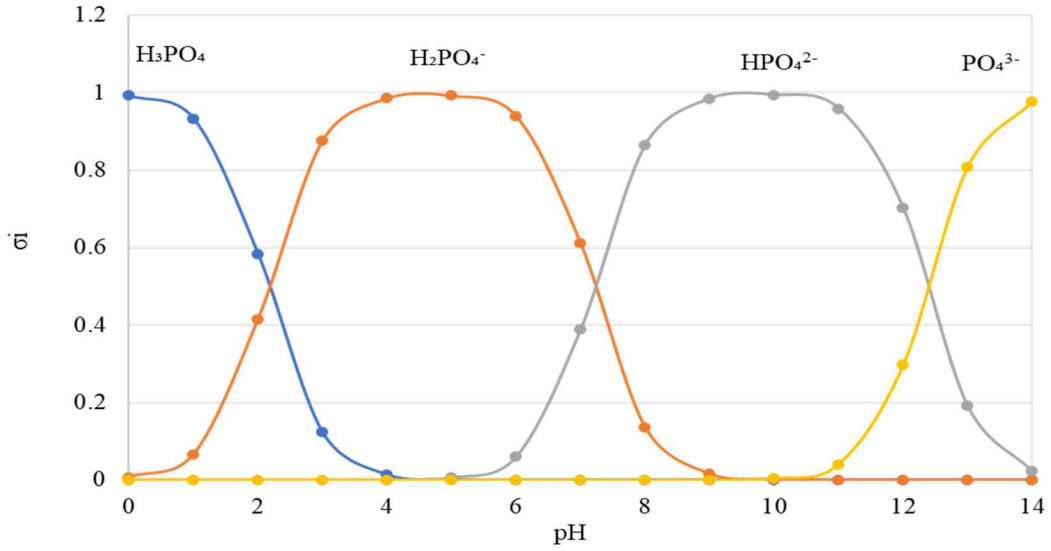

Figure 3.15. Calculated solution speciation curve for phosphonic acid as derived from thermodynamic first principles using the constants provided in Table 3.2. σ_i is the proportion of each species.

To understand more about the interaction between the phosphate and the halloysite surface a comparison of the charge on the phosphate as determined by the speciation curve (Figure 3.15) with the amount of phosphate adsorbed on the 17US and 4Ch samples is shown in Figure 3.16.

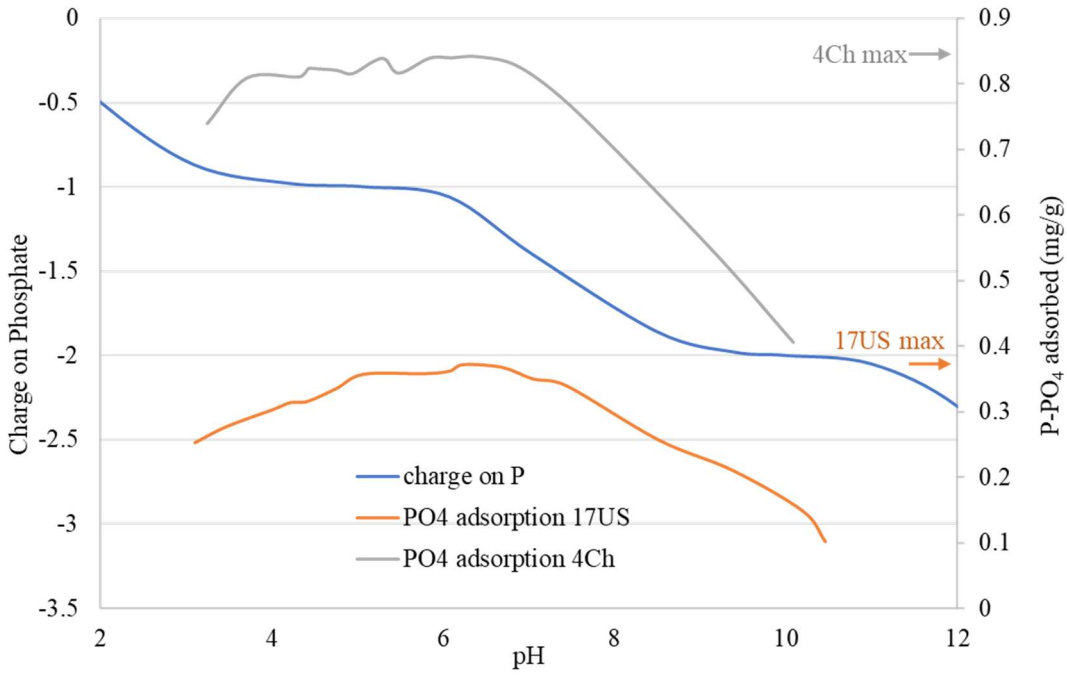

Figure 3.16. Charge on phosphate compared to adsorption curves. Original data used was from a batch adsorption process with the conditions 4 mg/l initial phosphate and 0.01 M NaCl as shown in Figures 3.5 and 3.6.

By correlating the expected charge on the phosphate with the adsorption curves, the type of adsorption onto the surface can be inferred. For example, from Figure 3.17 which shows the distribution of charge on the phosphate anion, adsorption of the monoanion $H_2PO_4^-$ would suggest monodentate adsorption onto the surface whilst the triply charged PO_4^{3-} species could potentially adsorb to between 1 and 3 positively charged surface sites on the halloysite nanotubes.

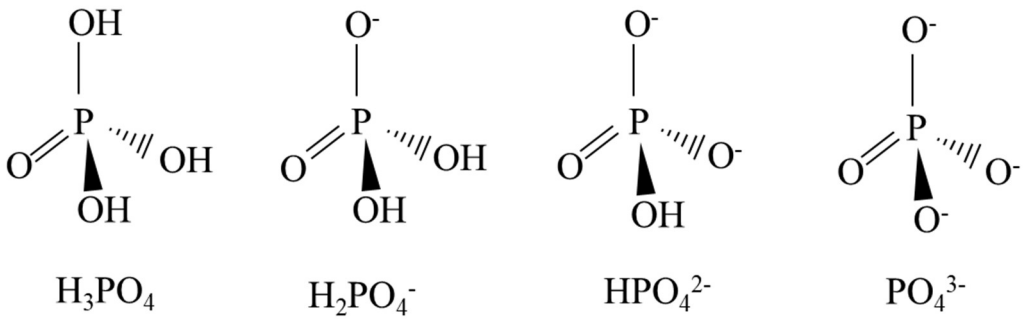

Figure 3.17. Chemical structures and formulas of the different phosphate species predicted over the pH range of the adsorption curves studied in the batch adsorption experiments.

3.3.6 Inductively coupled plasma - optical emission spectroscopy (ICP-OES) results

One of the main assumptions of this method is that after equilibrium had been reached the phosphate remaining in solution was free and available to react with the surface of the mineral. ICP-OES analysis of the remnant solutions across the pH range shows that below pH 4 the amount of aluminium in solution increases rapidly, as shown in Figure 3.18, suggesting that at these pH levels some aluminium and silica is free to form soluble complexes with phosphate.

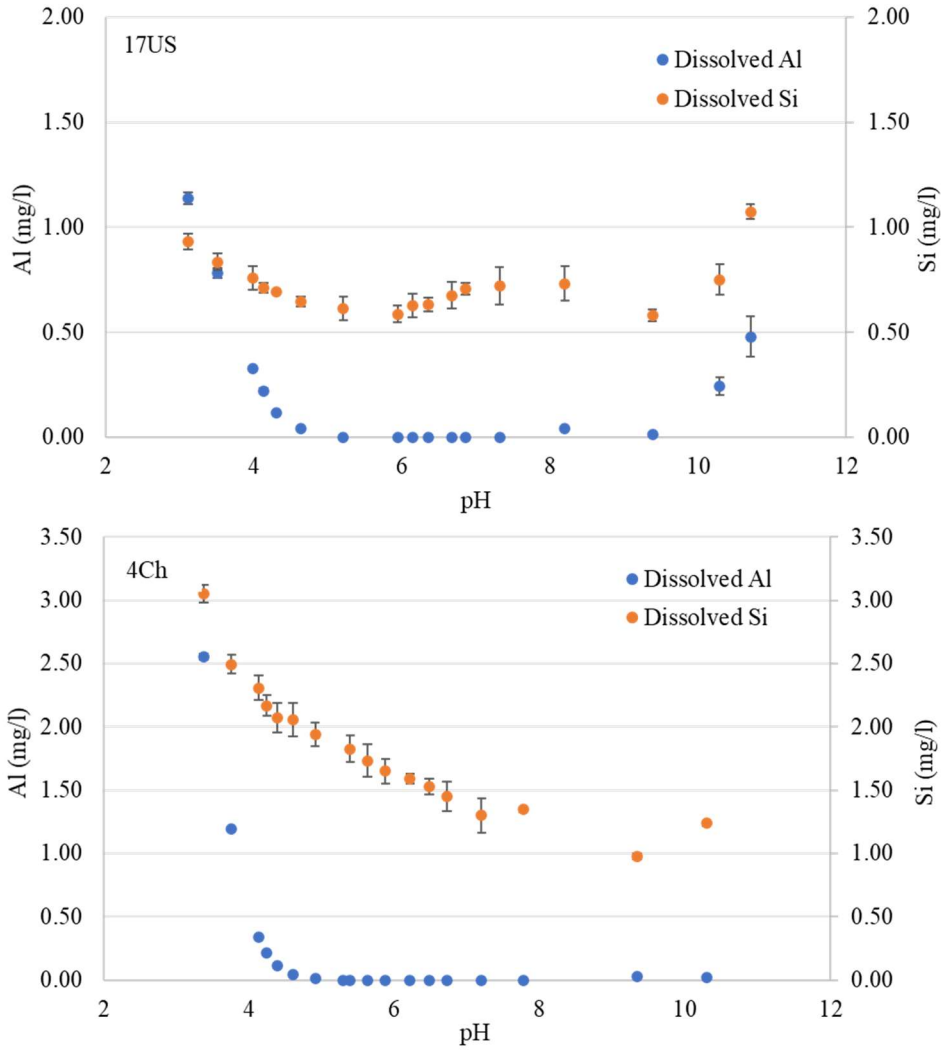

Figure 3.18. ICP-OES analysis of dissolved aluminium and silica in the remnant solution from the two halloysite (7 Å) samples after phosphate adsorption (0.1 M NaCl and 4 mg/l P-PO_4). Each analysis was conducted in triplicate and the error bars are shown on each graph.

3.3.7 Fourier transform infrared spectroscopy (FTIR) results

ATR-FTIR was employed in an attempt to gain information on the sites of adsorption of the phosphate onto the halloysite nanotubes. The OH-stretching region in kaolinite and halloysite is between 3800-3500 cm^{-1} and can be diagnostic for the degree of ordering and morphology of the kaolin (Hillier *et al*., 2016). Kaolinite and the more ordered polygonal prismatic morphologies often have two prominent bands at around 3620 and 3690 cm^{-1}, where the higher frequency band is more intense. In addition, they have two weak bands at around 3670 and 3650 cm^{-1} which, in the case of halloysite, is assigned to out-of-phase Al-OH stretching due to imperfect 3-fold

symmetry (Farmer, 1974) as explained in Chapter 2, Figure 2.7. ATR-FTIR analysis was conducted on several of the samples with adsorbed phosphate. Initially, FTIR analysis was not sensitive enough to detect changes in the spectra after phosphate adsorption, even when using a germanium disk instead of diamond in the spectrometer, where the germanium disk results in lower penetration into the sample and so is more suitable for surface studies. Therefore, several batch adsorption experiments were run with halloysite clay that had been saturated with 215 mg/l phosphate with the theory that a higher amount of phosphate would result in more adsorption, hence, a bigger and more visible change in the FTIR spectra.

Comparison of the FTIR spectra of 17US with and without phosphate adsorption display a subtle reduction in intensity of the 3670 cm^{-1} Al-OH stretching band after phosphate adsorption, indicating that these edge and lumen sites are the most likely sites of adsorption (Figure 3.19). This decrease in intensity was estimated from peak area measurements as decreasing the Al-OH stretching band at 3670 cm^{-1} cm peak area by approximately one third. Due to the very small peak areas this is an estimation of peak area loss only. The cylindrical 4Ch sample shows only two bands in the OH-stretching region at 3625 and 3690 cm^{-1}, where the lower frequency band is of higher intensity. Due to the lack of out of phase stretching bands in 4Ch, no change was noted after phosphate adsorption (See Chapter 2, Figure 2.7).

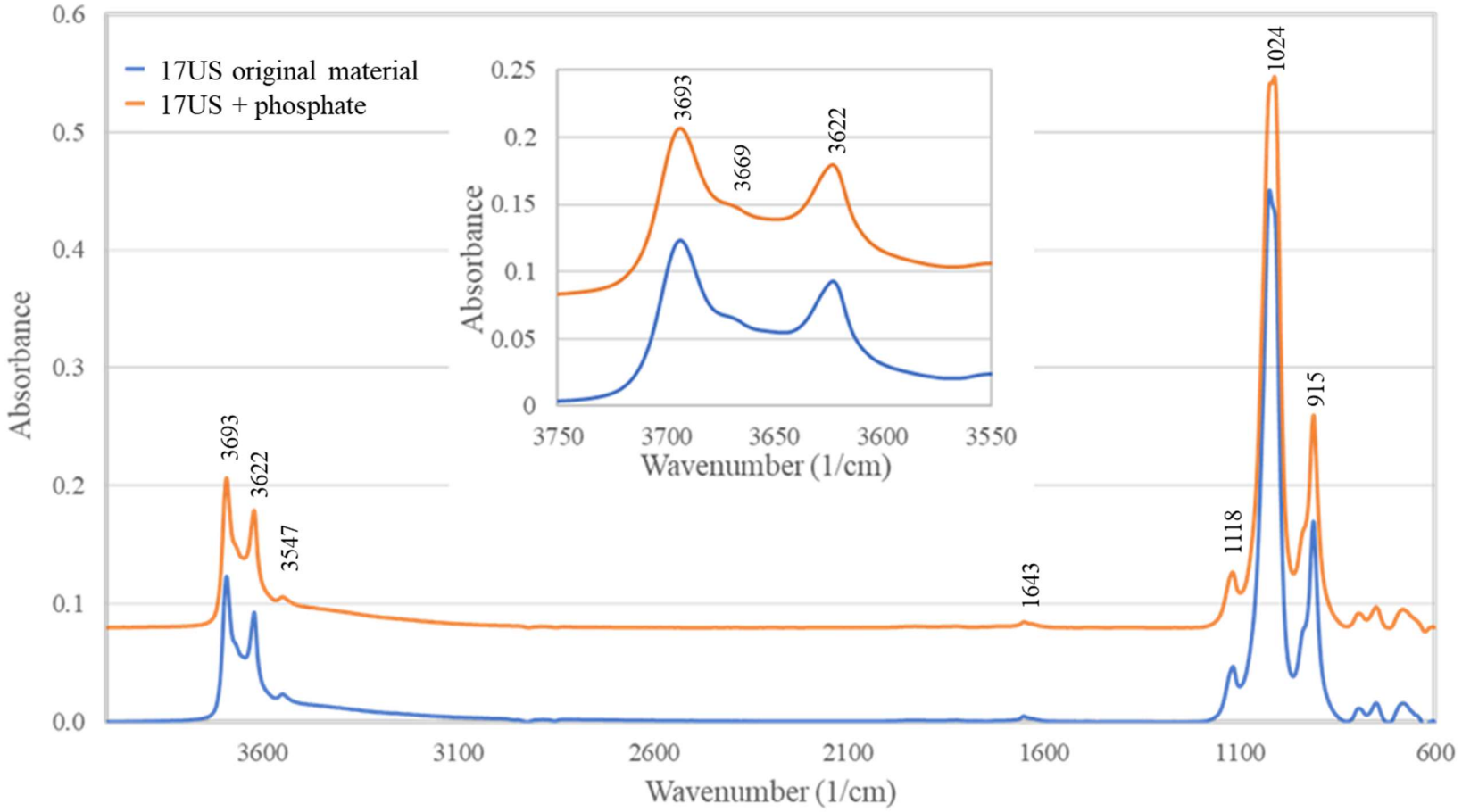

Figure 3.19. FTIR analysis of adsorbed phosphate on prismatic halloysite (17US) where the inset displays a clearer image of the characteristic Al-OH stretching bands.

3.3.8 Desorption experiments

The 17US, 4Ch and KGa-2 samples which had been saturated with 215 mg/l P-PO_4 were analysed by lithium metaborate fusion and inductively coupled plasma mass spectroscopy (ICP-MS) after various states of washing to determine the amount of phosphate left on the halloysite (7 Å)/kaolinite sample. After the fusion process, each sample was duplicated *in situ* for ICP-MS analysis. Duplicates of the pure halloysite and kaolinite clays were also run through the fusion process as controls to verify that no phosphate could be detected on these samples. The results from the phosphate desorption experiments can be summarised as inconclusive and slightly conflicted as shown in Table 3.3, where poor reproducibility arises between the duplicates of some of the samples. Similar variations in results were seen for other elements, such as Si, which were also analysed at the same time by ICP-MS. This suggests that there may be some issues with the fusion method when dealing with these materials, as will be discussed further in Section 3.4.8 of this chapter.

Table 3.3. ICP-MS results from the desorption experiments where the samples were washed with either acetone or a combination of acetone and sodium hydroxide. The samples were dissolved using a high temperature fusion method before analysis by ICP-MS to detect the remaining phosphate on the halloysites after their respective washings.

Sample ID	Initial phosphate on surface (mg/l)	Phosphate remaining on sample (mg/l)		Phosphate desorbed (mg/l)		Standard error between duplicates	% phosphate desorbed (mg/l)	
		Run 1	Run 2	Run 1	Run 2		Run 1	Run 2
17US + phosphate	17.06	1.03	1.06	16.04	16.00	0.02	93.99*	93.76*
17US + phosphate acetone washed	13.55	0.88	1.45	12.67	12.10	0.29	93.53	89.30
17US + phosphate acetone and NaOH washed	12.71	1.11	0.63	11.60	12.07	0.24	91.26	95.00
4Ch + phosphate	34.65	1.82	1.75	32.83	32.90	0.04	94.74*	94.96*

Sample ID	Initial phosphate on surface (mg/l)	Phosphate remaining on sample (mg/l)		Phosphate desorbed (mg/l)		Standard error between duplicates	% phosphate desorbed (mg/l)	
		Run 1	Run 2	Run 1	Run 2		Run 1	Run 2
4Ch +phosphate acetone washed	34.37	2.56	2.69	31.82	31.68	0.07	92.57	92.18
4Ch + phosphate acetone and NaOH washed	31.20	1.49	0.68	29.71	30.53	0.41	95.23	97.83
KGa-2 + phosphate	35.88	1.07	1.38	34.80	34.49	0.16	97.01*	96.15*
KGa-2 + phosphate acetone washed	10.63	1.36	0.92	9.27	9.71	0.22	87.20	91.31
KGa-2 + phosphate acetone and NaOH washed	41.88	<0.50	<0.50	N/A	N/A	N/A	N/A	N/A

*These samples were not washed in any way to remove the phosphate from the material.

In addition, the % loss values highlighted with an asterix (*) were not washed in any way to remove the phosphate from the kaolin mineral. These are the unwashed kaolin samples which after phosphate adsorption were dried down under N_2 and underwent the fusion method. From this it would be expected that they would have little to no loss of phosphate, instead we see values of 93.76-97.01% phosphate loss for these samples.

Another method of desorption was attempted wherein the amount of phosphate removed from the surface into solution was measured using the Konelab Discrete Analyser. Due to the volatility of acetone, it was not feasible to run the acetone-only washed samples through the instruments, instead only the samples subsequently washed with sodium hydroxide were analysed. From this it could be seen that the amount of phosphate removed by the combination of acetone and sodium hydroxide for 17US was 30 ± 0.88% (n=2), 4Ch was 20 ± 1.17% (n=2) and KGa-2 was 31 ± 0.98% (n=2). Unfortunately, there is no indication of the removal ratio of each method. From these initial results is interesting to note that the two ordered samples (17US and KGa-2) displayed similar desorption rates whilst the cylindrical sample desorbs two thirds less phosphate.

3.4 DISCUSSION

The phosphate adsorption curves all display a parabolic shape with a maximum adsorption observed at around pH 6 (Figures 3.4 and 3.5) with adsorption showing a gentle sloping off at lower pH's and a steady decrease in adsorption with pH > 6. This parabolic shape is similar to those seen by other authors studying phosphate adsorption onto kaolinites (Edzwald *et al.*, 1976; Manning & Goldberg, 1996).

3.4.1 Batch adsorption experiments and the influence of morphology

Under the experimental conditions for the batch adsorption experiments performed, the maximum phosphate adsorptions observed are 0.45 mg/g and 1.1 mg/g for the polygonal prismatic 17US and cylindrical 4Ch respectively. The adsorption obtained for the cylindrical 4Ch sample is in line with the values recently reported by Almasri *et al*. (2019) and Saki *et al*. (2019), 1.5 mg/g and 1.2 mg/g respectively, although their results were obtained under different experimental conditions and varying equilibrium

times. Where Almasri *et al*. (2019) reported 3 hours equilibration and Saki *et al*. (2019) employed 24 hours equilibration time. This suggests that, while not specified, the halloysite sample they were using was of cylindrical morphology.

The variable phosphate loading data at fixed pH values were plotted as shown in Figures 3.7-3.8. The data can be described as fitting the linearized Langmuir equation when a plot of c/x vs c gives a straight line. The good Langmuir fits for the polygonal prismatic 17US sample at each pH suggests that single site adsorption is occurring. From what is known about their pH dependency and from previously reported work such as that by Van Emmerick *et al*. (2007) who proposed that the singly coordinated Al-OH edge sites in kaolinite actively bind phosphate, these adsorption sites can be postulated as the Al-OH edge sites (Figure 3.20). The cylindrical 4Ch sample did not fit to the linear Langmuir equation, suggesting at least two distinct adsorption sites on this sample or multilayer adsorption. Only by conducting further trials at additional loadings will it be possible to say for certain that the two halloysites behave in a different manner when fitting the data to a Langmuir isotherm. This is because upon close examination of the Langmuir graphs for the 4Ch sample it appears that it is one data set that skews the lines off being linear for each pH studied. Without a bigger dataset it cannot be said for certain whether this is a real effect that is being observed.

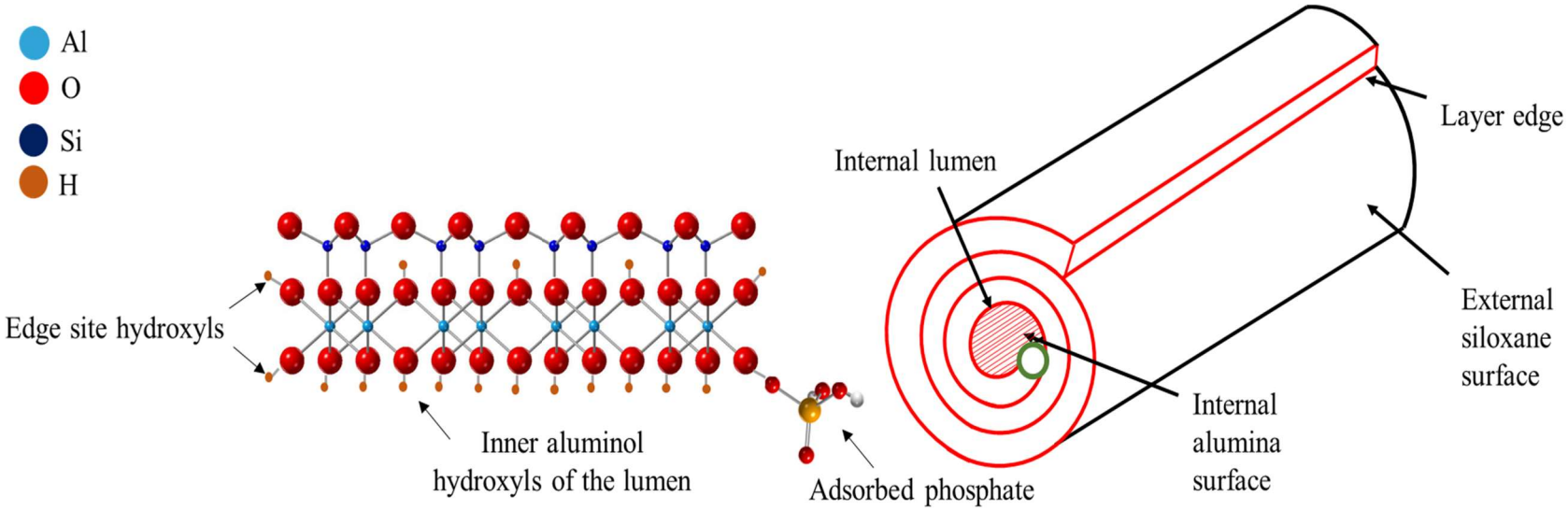

Figure 3.20. Single layer of halloysite nanotube. The areas highlighted in red show the inner aluminol hydroxyls which would line the inner lumen and the edge site hydroxyls which are situated at the terminus of the nanotubes, as highlighted by the green circle in the halloysite nanotube diagram on the right-hand side of the figure.

The difference in adsorption capacity at equilibrium between the cylindrical and polygonal prismatic halloysite is shown in the kinetic adsorption experiments (Figure 3.4), where the cylindrical halloysite (4Ch) has an adsorption just over 2.5 times greater than the polygonal prismatic halloysite (17US). Kinetic adsorption experiments, conducted over a time frame of 30 minutes to 10 days, demonstrated that adsorption was rapid and that a maximum adsorption was achieved between 24 hours for 17US and 48 hours for 4Ch. Initially it appears that the 4Ch sample has a slower rate of uptake than 17US, yet, given that the cylindrical sample adsorbs 2.5 times more phosphate than the polygonal prismatic sample, the actual rate in terms of phosphate uptake is higher in the timescale given. For both samples, a slight dip was noted at around 20 hours equilibration followed by a recovery which follows the trendline of adsorption with increasing time. This feature occurred during all repeats of the experiments and so may be postulated as symptomatic of the adsorption mechanism, such as possible rearrangement of phosphate on the surface, as opposed to due to experimental error. Given this and previous reported equilibration times (Theng *et al*., 1982), 16 hours was chosen for the batch equilibration experiments conducted here. It is most likely that the kinetics of adsorption of phosphate on the halloysite nanotubes is driven by mass transfer, where the mass transfer most strongly influenced by the variable charges on the halloysite surfaces. A similar mechanism can be seen for use of halloysites in lithium sulphur batteries (Lin *et al*., 2017) where they proposed that the oppositely charged halloysite surfaces split the lithium salts into lithium ions, hence creating a 3D structure for lithium-ion transport. In the case of the environment, at ambient pH (~pH 6) the halloysites may be seen to act as a soil phosphate 'batteries' where the phosphate anions are adsorbed into the positively charged inner lumen of the halloysites.

Typically, adsorption experiments have been considered to be at equilibrium in under 24 hours (Theng *et al*., 1982; Ioannou & Dimirkou, 1997) and continued reaction times could result in further sorption processes such as multilayer adsorption or, after periods of several days to a few weeks, surface precipitation (Gérard, 2016). This is in contrast with other non-clay materials such as industrial by-products where Habibiandehkordi *et al*. (2014) showed that a minimum equilibration period of 5 days is required for maximum phosphate adsorption. By contrast, the kinetic experiments conducted here

on timescales of up to 10 days showed no significant increase in adsorption after 48 hours.

The Tyndall Effect observations (Table 3.1) show that in the instance of the prismatic halloysite (7 Å), 17US, sample at high pHs there is a high dispersion of the nanotubes. This is in line with previous research by Joo *et al*. (2013). It is interesting to note, however, that the cylindrical halloysite (7 Å), 4Ch, did not disperse in the same manner, even at high pHs. The ease of the 17US sample for dispersion when compared to 4Ch has been noted in several of the experiments outlined in this thesis (Chapter 5, sections 5.5.3 and 5.5.6; Chapter 6, section 6.4). While the reason for this cannot be fully explained it would be rational to consider that it may be due in part to the different surface charges of the two halloysites, as highlighted by their difference in ZPC.

3.4.2 Proposed anion adsorption sites of halloysite nanotubes

Previous work has hypothesised that anion adsorption occurs primarily on the pH dependent edge sites of the halloysite nanotubes (Theng *et al*., 1982). FTIR analysis is a useful tool in identifying clay minerals and can be used in adsorption reactions to identify mechanisms of adsorption. While the results are subtle, the 17US and KGa-2 samples show a small decrease in intensity in the 3670 cm^{-1} Al-OH stretching band after phosphate adsorption. This result is in line with previous studies which suggested that the aluminol edge groups are the sites with anion exchange potential (Theng *et al.*, 1982; Han *et al.*, 2016). Due to their subtle nature, the slight changes in the Al-OH stretching bands in the FTIR spectra (Figure 3.19) before and after phosphate adsorption cannot be regarded as fully conclusive. While no change was noted for 4Ch the lack of visible change may be considered in part as due to the lack of peak at 3659 cm^{-1} and hence, is not indicative of lack of adsorption to the surface. Future work such as ^{31}P NMR may be required to verify the adsorption mechanism.

The difference in adsorption between the two morphologies may be rationalised by considering that the cylindrical halloysite nanotubes are much smaller with a higher specific surface area, hence, more Al-OH edge sites are available for adsorption reactions. Results reported in a study of the cation exchange capacity (CEC) of seven different halloysites (Gray *et al*., 2016) showed that in general cylindrical halloysites had a slightly higher CEC than the polygonal prismatic halloysites although this difference was reduced after normalisation to surface area. After normalisation of the

data for the dehydrated halloysites (Figure 3.12) the slightly elevated levels of phosphate adsorption per m^2 for 17US compared to 4Ch and KGa-2 may be explained by a greater number of steps and edges, and hence edge reaction sites, on the larger prismatic tubes of 17US halloysite. Further work, such as atomic force microscopy (AFM) studies, to verify this theory will be discussed in Chapter 4.

3.4.3 Mechanism of phosphate adsorption onto the halloysite nanotube surface

Information on the type of adsorption to the surface of a mineral can be inferred by the response of adsorption to changing background electrolyte concentration (Hayes and Leckie, 1987). For example, physisorption, otherwise known as outer sphere adsorption, where a weak intermolecular bond exists (around 2 kJ/mol for a Van der Waals interaction) between the mineral surface and adsorbing species, can be seen to reduce with increased concentration of background electrolyte. This is most likely due to adsorption reactions between the electrolyte and adsorbing species. This can also be compared to kT (the amount of available energy at a given temperature) which is *ca.* 2 kJ $mole^{-1}$ at ambient temperature meaning that the desorption of physisorbed species will not be energy limited at ambient temperature. In contrast, chemisorption, or inner sphere adsorption, where the attraction between the mineral surface and adsorbing species results in a strong covalent bond, is unaffected by changes in background electrolyte. The covalent bond formed in the chemisorption can be estimated at around 33 kJ/mol for monodentate adsorption and 208 kJ/mol for bidentate adsorption from previous work which studied the adsorption of phosphate on an alumina surface (Ren *et al*., 2012). A comparison of the two adsorption mechanisms is shown in Figure 3.21.

The strength of chemisorption interactions suggests they are not reversible at ambient temperature unless the equilibrium is disturbed (e.g., chemically by the addition of base). Indeed, He *et al*. (1997) studied phosphate adsorption onto kaolinite (KGa-2) with varying ionic strengths and noted that the ionic strength had little effect on phosphate adsorption, rather it was pH that had the most significant effect, with maximum adsorption occurring at around pH 6. From Figure 3.5 where little effect on adsorption was observed with changing ionic strength, it can be suggested that predominantly inner sphere chemisorption may be taking place. Yet, in the instance of 4Ch a slight decrease in adsorption can be seen with the increased NaCl molarity

0.1 M) suggesting that the presence of some outer sphere physisorption reactions occurring between the mineral and phosphate in solution should not be ruled out.

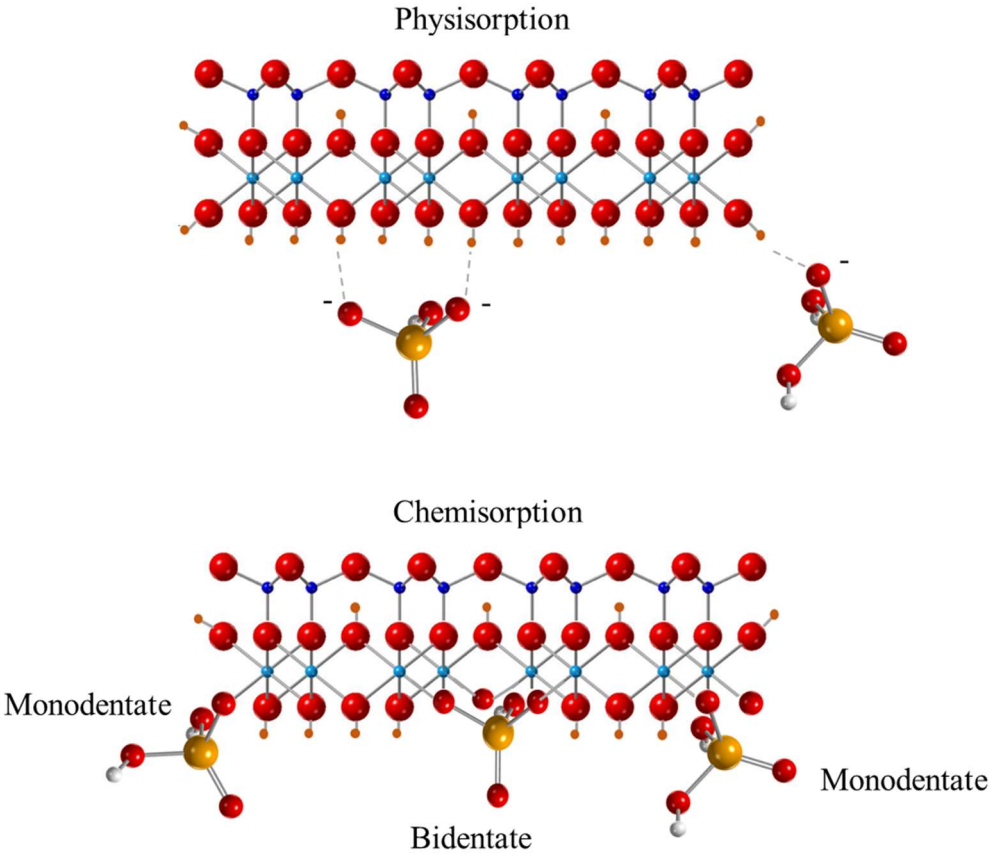

Figure 3.21. Graphical depiction of the two potential types of surface adsorption, chemisorption and physisorption. The adsorbing phosphate anions are of mono and bidentate charge resulting in assumed mono/bidentate adsorption onto the halloysite surface with chemisorption.

Where chemisorption occurs, it is theorised to be via a ligand exchange mechanism as shown in the reactions below for monodentate adsorption of the two phosphate species found at a pH range of 2-12 (Figure 3.15).

Reaction on a neutral edge site (pH = PZC):

$\equiv Al\text{-}O\text{-}H + H_2PO_4^- \leftrightarrow \equiv Al\text{-}O\text{-}PO_3H_2 + OH^-$

$\equiv Al\text{-}O\text{-}H + HPO_4^{2-} \leftrightarrow \equiv Al\text{-}O\text{-}PO_3H^+ + H_2O$

Reaction on a positively charged edge site (pH < PZC):

$\equiv Al\text{-}O\text{-}H_2^+ + H_2PO_4^- \leftrightarrow \equiv Al\text{-}O\text{-}PO_3H_2 + H_2O$

$\equiv Al\text{-}O\text{-}H_2^+ + HPO_4^{2-} \leftrightarrow \equiv Al\text{-}O\text{-}PO_3H^+ + H_2O$

Reaction on a negatively charged edge site (pH > PZC): Surface repulsion occurs:

$\equiv Al\text{-}O^- + H_2PO_4^- \leftrightarrow \equiv Al\text{-}O^- + H_2PO_4^-$

In addition, the fitting to the linearized Langmuir adsorption isotherms for the 17US polygonal prismatic halloysite infers chemisorption to the halloysite surface. Whilst the linear Langmuir isotherm did not fit the data for the 4Ch sample, it can be considered that the similar surface groups of the two halloysites results predominantly in chemisorption for the 4Ch cylindrical sample as well.

3.4.4 Effect of hydration state on the adsorption of phosphate on halloysite nanotubes

In contrast to the normalised results for the dehydrated halloysite (7 Å) samples, the hydrated halloysite (10 Å) sample (Figure 3.13) showed that after normalisation to surface area a significant difference in adsorption was maintained, where the cylindrical samples (5Ch and 6Ch) displayed 2.5 times greater adsorption than the polygonal prismatic sample (23US). The exact cause of this difference is unknown, as is the reason for the divergence from the trend shown in the dehydrated samples and several possible reasons can be proposed. Initially, it can be noted that the associated experimental errors for the hydrated samples are expected to be slightly higher in calculating the phosphate adsorption since a slurry was used instead of an exact and measured weight of sample. This may introduce a small degree of uncertainty into the calculation of g/l halloysite in each sample vial, although this would be expected to have only a small effect on the overall adsorption calculated and hence, cannot explain the difference observed after normalisation for the hydrated halloysites. Additionally, the polygonal prismatic halloysite (10 Å) sample 23US is of slightly lower purity at 86.9 % halloysite than the cylindrical halloysite (10 Å) samples at 99.8 and 100% purity (Chapter 2, Table 2.1), the lower purity would result in a lower contribution to the adsorption of phosphate by the halloysite nanotubes which would subsequently affect the normalisation of the data.

With respect to the pre-normalised data presented here there is little substantial difference between the phosphate adsorption capacity for halloysite (10 Å) and halloysite (7 Å) samples of the same morphology (Figures 3.9 and 3.10). In contrast, by comparison of the normalised data of the halloysite (10 Å) and halloysite (7 Å)

samples it can be seen that the two cylindrical halloysite (10 Å) samples had a higher phosphate adsorption capacity (~0.50 μmol/m^2) compared to the cylindrical and prismatic halloysite (7 Å) samples (~0.35-0.40 μmol/m^2). In the case of cation exchange some authors (Grim, 1968; Norrish, 1995) have proposed that halloysite (10 Å) samples have a larger cation exchange capacity than their dehydrated halloysite (7 Å) counterparts. Although the reasons for this were not understood, this could suggest that there are some additional differences between the two hydration states. As will be discussed in more detail in Chapter 4, there remains some debate as to whether the structure of the halloysite nanotubes changes depending on the hydration state. From what is known about the reactivity of halloysites, it seems unlikely that the presence of interlayer water would facilitate interlayer ion adsorption. However, it may be considered that the interlayer water in halloysite (10 Å) samples results in greater accessibility of the edge sites to adsorbing ions. For cation exchange, in particular, this edge site adsorption can occur on both the siloxane and aluminol edge sites (Gray *et al*., 2016) and so may be one explanation for the variations in anion and cation adsorption between the hydration states. The study of a larger dataset of halloysites and more direct comparisons between the same halloysite in both hydration states with varying anions and cations would be required before any further conclusion could be drawn.

3.4.5 Effect of pH on the dissolution of the halloysite nanotubes

Van Emmerik *et al*. (2007) studied phosphate adsorption on kaolinite and gibbsite by ^{31}P NMR and found evidence of a partially crystalline $AlPO_4$ phase at low pH's. The authors inferred that the Al-OH edge sites where anion adsorption occurs play a role in the formation of a surface precipitate, which at low pH's would reduce the available sites for anion adsorption. It can be seen from the ICP-OES analysis in this current study that labile aluminium is present in solution at these lower pH's (Figure 3.18). The presence of such phases could provide one explanation for the observed reduction in phosphate adsorption at lower pH's wherein the labile aluminium could complex with the phosphate. This would also result in a change in the surface charge and available Al-OH sites for adsorption, where the phosphates are increasingly protonated with decreasing pH (Figure 3.15). In addition, Huang *et al*. (2009) proposed a model for Al-oxides that suggested the decrease in phosphate sorption at

pH < 4 was due to the absence of proton reactive but phosphate non-reactive triply-coordinated surface hydroxyls in the alumina sheet, and used these groups to distinguish between Al and Fe oxides and their adsorption curves.

3.4.6 Influence of halloysite surface charge on phosphate adsorption

The adsorption of phosphate on the halloysite nanotubes was observed to be dependent upon pH across all batch adsorption conditions. It is therefore prudent to consider the influence of both the halloysite and phosphate surface charges on adsorption, since they will vary with pH.

The maximum adsorption at around pH 6 is seen to be just above the PZC values measured for these materials (Figure 3.11). The reduction in adsorption with an increasingly basic solution can be rationalised by considering that at higher pH, the edge sites are deprotonated and so display a net negative charge which would electrostatically repel the phosphate anions. In contrast, at pH's below the PZC the surface is positively charged and hence would be expected to adsorb some phosphate anions. Almasri *et al*. (2019) reported a PZC of 2.5 for halloysites which is in the range of zeta potential reported by Vergaro *et al*. (2010) although it is substantially lower than the values found in our study. The value of 5.9 for kaolinite KGa-2 in 0.1 M NaCl found in this study is slightly higher than previously reported values for kaolinite: KGa-2 = 5.4 (Schroth & Sposito, 1997); China kaolinite = 4.1 (Wei *et al*., 2014); and Linthipe kaolinite = 5.1 (Kamiyango *et al*., 2009). Variations between reported results may arise due to differences in background ionic strength, kaolinite crystallinity and experimental methods. In the case of the halloysites, the higher pH for the point of zero charge (PZC) of the cylindrical 4Ch suggests that it has more positively charged surface sites than the polygonal prismatic 17US sample which may be explained by the higher surface area of cylindrical halloysites. In addition, previous work by Gray *et al.* (2016) found via proton titration experiments that the cylindrical halloysite, 4Ch, had slightly more permanent charged sites per unit cell (0.07) than the polygonal prismatic, 17US, halloysite (0.06). In contrast to the halloysite (7 Å) samples, where the PZC is around the pH of the maximum observed phosphate adsorption, the point of zero charge for goethite is around pH 9 (Van Emmerik *et al*., 2007), the pH at which the adsorption of phosphate on goethite is at its lowest. Consequently, while PZC is an effective measurement for understanding some of the surface chemistry of the

mineral, anion adsorption on minerals is not considered to be related to the PZC but rather is surface area dependent (Gérard, 2016).

3.4.7 Effect of the surface charge of phosphate

The charge on phosphate with varying pH when compared to the phosphate adsorption for 17US and 4Ch (Figure 3.16) indicates that the most likely species of phosphate involved in the adsorption reactions are the species found around the adsorption maxima at pH 6; primarily $H_2PO_4^-$ with a potential contribution from HPO_4^{2-}. From this it can be inferred that mono or bidentate adsorption is most likely on the surface of the nanotubes, as shown in Figure 3.21. Whilst the solution speciation curve for phosphonic acid indicates the behaviour of the phosphate in solution, some authors have suggested that this cannot be taken as a direct link between the speciation of phosphate in solution and the speciation of phosphate on the surface (Goldberg and Sposito, 1984), as such further work such as density function theory modelling is required to obtain the favoured adsorptions onto the surface. However, in using the solution speciation curves as a guideline for available phosphate species they are determined as the same species of phosphate expected to be found as labile and hence, soluble, anions in soils (Haygarth *et al*., 2013). At low pH, the halloysite surface is protonated and so is positively charged, at these lower pH's the phosphate is a monoanion and hence would be expected to have high uptake. There can be seen a slight plateau until just after pH 6 as the phosphate is moving towards being a dianion. As the pH is increased further the halloysite surface switches to a negative charge, which has far less affinity for the anions, in addition to this the phosphate anion would be of higher charge in solution resulting in stronger repulsion with the negatively charged surface.

3.4.8 Desorption of phosphate from the kaolin minerals

Desorption of phosphate from soils and clay minerals is known to be influenced by pH (Gustafsson *et al*., 2012; Krumina *et al*., 2016). The methods of desorption employed included washing the kaolin samples with acetone and 0.1 M NaOH. The sodium hydroxide wash increased the pH to around pH 13, resulting in a negative charge on the surface of the mineral. This increase in pH would be expected to shift the equilibrium and result in more phosphate in solution than adsorbed to the surface

from the adsorption curves (Figures 3.5 and 3.6) since at high pH's the amount of phosphate on the surface of the clays decreases dramatically.

As mentioned in the results section (3.3.8), it appeared that the desorption results obtained after lithium metaborate fusion and ICP analysis contained multiple errors. One possible explanation for this may be that, whilst it appeared by eye that the halloysite samples had completely dissolved in the nitric acid during the fusion method, it may have been that some smaller particles were still in suspension. Indeed, any such nanoparticles < 20 nm in size would be invisible to the naked eye. The variations in results may also suggest that the phosphate remains attached to any undissolved halloysite, even after heating to 1000 °C and reaction with nitric acid which infers that the halloysite is not easily desorbed from the surface.

The second method which measured the desorption using colorimetry appeared more successful. Despite that, it is complicated to ascertain whether the calculated phosphate removal from the halloysite (7 Å) samples in this study is accurate, where the desorption was measured as 30% (17US), 20% (4Ch) and 31% (KGa-2). Typically studies on phosphate adsorption/desorption focus on soil systems as a whole and not individual clay mineral types. While desorption from hydroxide surfaces is expected to be reversible (Gustafsson *et al*., 2012), in the case of Fe, Al oxides and kaolinite it was shown that adsorbed P was difficult to remove (He *et al*., 1994) and in some soil systems a large proportion of phosphate does not desorb after 24 hours (Wisawapipat *et al*., 2009). The same authors also found that soils with lower clay mineral contents had higher rates of desorption suggesting that adsorption onto the surface of clay minerals is not easily reversible. One of the main reasons that phosphate does not fully and easily desorb is the inner-sphere sorption mechanism is difficult to reverse using diffusion or simple ion exchange (He *et al*., 1990; He *et al*., 1994). He *et al* (1994) found that their kaolinite desorbed 17% phosphate after washing with anion exchange resins, suggesting that a 30% removal of phosphate from the polygonal prismatic halloysite and kaolinite in our study is high. While there was no information on the type of kaolinite used by He *et al*. (1994), future comparisons could show that perhaps order/disorder in kaolinite also makes a difference to the desorption capacity of these materials.

3.5 APPLICATIONS IN PHOSPHATE REMEDIATION

3.5.1 Comparison with other materials

As discussed in the introduction to this chapter, phosphate pollution is of great environmental significance and hence, the use of natural materials as scavengers is widely researched for phosphate pollution remediation studies. To understand the efficacy of halloysite nanotubes and their potential use in phosphate remediation the phosphate adsorption capacities as measured in the experiments presented throughout this chapter are presented in Table 3.4, along with the data recorded from other material studies as a comparison.

Table 3.4. Comparison of phosphate adsorption on halloysite nanotubes and other reported materials. To compare datasets the values have been normalised to the specific surface area of each material.

Material	Phosphate adsorbed (mg/g)	Phosphate adsorbed normalised to specific surface	Specific surface area in literature (m^2/g)	Reference
La-zeolite	17.20	0.33	52	He *et al*., 2017
Zeolite	0.30	0.00	243	Andrés *et al*., 2018
Montmorillonite	0.16	0.01	20	Gimsing and Borggaard, 2002
Illite	0.23	0.01	43	Gimsing and Borggaard, 2002
Gibbsite	4.90	0.11	45	Gimsing and Borggaard, 2002
Goethite	5.60	0.14	40	Gimsing and Borggaard, 2002
Goethite	7.10	0.21	32	Ioannou *et al*., 2013

Material	Phosphate adsorbed (mg/g)	Phosphate adsorbed normalised to specific surface area	Specific surface area in literature (m^2/g)	Reference
Goethite 1	3.02	0.19	16	Borggaard, 1983
Goethite B	19.19	0.23	82	Borggaard, 1983
Hematite	5.27	0.38	14	Borggaard, 1983
Hematite	21.56	0.34	64	Borggaard, 1983
Goethite	10.00	0.20	51	Wei *et al*., 2014
Kaolinite	1.60	0.10	16	Wei *et al*., 2014
Kaolinite (KGa- 2)	0.18	0.01	23	He *et al*., 1997
Kaolinite (KGa- 2)	0.33	0.02	22	Gimsing and Borggaard, 2002
Soil Kaolinite	0.65	0.01	53	Singh and Gilkes, 1992
Cylindrical halloysite (4Ch)	1.30	0.02	80	This study
Polygonal prismatic halloysite (17US)	0.50	0.02	30	This study
Kaolinite (KGa- 2)	0.27	0.01	23	This study
Granular Halloysite	1.20	0.05	25	Saki *et al*., 2019
Powdered Halloysite	~1.10	~0.04	25	Saki *et al*., 2019

Material	Phosphate adsorbed (mg/g)	Phosphate adsorbed normalised to specific surface area	Specific surface area in literature (m^2/g)	Reference
Cylindrical halloysite 6 Ch (10 Å)	1.30	0.01	91	This study
Prismatic halloysite 23 US (10 Å)	0.35	0.01	58	This study
Halloysite + Lanthanum oxycarbonate	130.40	2.03	64	Wei *et al*., 2019

While a direct comparison between the studies is not possible due to their different experimental methods, results of each material have been normalised to their specific surface area as one way to compare the data. From this the halloysite data generated in this study, when compared with the data given in Table 3.4, indicates that halloysite nanotubes have the potential to adsorb more phosphate than certain montmorillonites, illite and unmodified zeolite. Despite this, the halloysites are observed to adsorb significantly less phosphate than the iron oxide minerals, although the initial findings of the desorption experiments presented here suggest that they may have higher recyclability potential than iron oxide materials. Further work would be required to verify this. The data presented in Table 3.4 demonstrates that although halloysites may not act as the most efficacious phosphate traps or sinks in soil systems, the work conducted here, along with further studies using modified and unmodified halloysite nanotubes, demonstrates that these minerals may have some impact on the phosphate removal and transport through soil systems. As such, they have the potential for use in industrial phosphate removal, especially after surface modification. With respect to information learned in these experiments and its application to the technological applications of halloysite nanotubes this work has identified that the morphology of

nanotube used in adsorption experiments on a weight-by-weight basis affects the potential phosphate adsorption (and hence anion adsorption) capacity.

3.6 CONCLUSION

The experiments outline in this chapter have aimed to understand more about the fundamentals of phosphate adsorption onto halloysite nanotubes of varying morphology and hydration state, as well as beginning to explore the desorption of phosphate from halloysite. By using batch adsorption experiments the results presented in this chapter have investigated the phosphate adsorption capacities of tubular halloysites where their morphology, and hence surface area, was seen to greatly influence the phosphate adsorption capacity. The 4Ch cylindrical halloysite has a higher adsorption than the polygonal prismatic halloysite, presumably due to their higher surface area, leading to a greater number of available Al-OH edge sites for reaction. Additionally, a noticeable difference in behaviour between the two morphologies was observed in the Langmuir isotherm fits, where the 17US sample adhered to a linear Langmuir isotherm whilst the 4Ch did not.

With respect to the effect of hydration state on the phosphate adsorption it was noted that after normalisation to surface area, the phosphate adsorption for the cylindrical halloysite (10 Å) samples was higher than that for the cylindrical (7 Å) samples. This is a significant result since it infers a change in availability of adsorbent sites with differing hydration states on the atomic scale. The effect of interlayer water on reactions of halloysite nanotubes is not one that is regularly studied due to the difficulties that arise in maintaining the hydration state of the halloysites. The fundamental question about the function and purpose of this interlayer water is approached further in Chapter 6.

The adsorption of phosphate onto kaolin group clay minerals shows a high dependency on pH. The maximum adsorption for both halloysites and kaolinite occurs around pH 6, which is slightly higher than, or around their PZC, and similar to the pH of many aquatic and soil systems. In terms of applying this knowledge to understanding the behaviour of halloysites in soil towards phosphate adsorption this can be seen as convincing that in soils with significant halloysite present the phosphate may be able to act as phosphate traps or sinks in the soil system. This can also be applied to

considerations of halloysite nanotubes in phosphate remediation studies where comparison of the normalised phosphate adsorption capacities of halloysites with other clay minerals such as montmorillonite, illite and kaolinite suggests that the halloysites have a slightly higher phosphate adsorption capacity. This contrasts with adsorption of phosphate by iron oxides which can be seen to be greater than that of clay minerals by a factor of at least 10. The desorption experiments presented in this chapter can be summarised as inconclusive, where it could be seen that halloysites bear the potential for semi-reversable phosphate adsorption at a minimum. Further desorption experiments of greater reproducibility is an avenue which should be explored in the future on a variety of halloysites of both tubular morphologies as well as on halloysite (10 Å) samples with adsorbed phosphate.

As found for kaolinite, the adsorption of anions onto the surface of halloysite nanotubes is governed by pH dependent aluminol edge sites on the halloysite nanotubes. The relationships between adsorption, morphology and surface area imply that these sites must exist on the external surfaces of the halloysite nanotubes and that the model of the halloysite tubular structure, as often assumed in technological applications with a uniform external siloxane surface is too simplistic. Despite the curved layers of many halloysites and the surface structural differences that would be a consequence of interlayer water, the adsorption behaviour of phosphate onto tubular halloysite appears to reflect its adsorption onto platy kaolinite. Future work outlined in Chapter 4 is aimed at more direct ways to examine the surface of halloysite nanotubes. From this it is intended to document the true structure of the external surface, which is fundamental to understanding the attempts and results of halloysite nanotube functionalisation in emerging technological applications and the role of halloysite in adsorption processes in soils.

3.7 REFERENCES

Almasri, D.A., Saleh, N.B., Atieh, M.A., McKay, G. & Ahzi, S. (2019) Adsorption of phosphate on iron oxide doped halloysite nanotubes. *Scientific Reports*, **9**, 3232.

Andrés, E., Araya, F., Vera, I., Pozo, G. & Vidal, G. (2018) Phosphate removal using zeolite in treatment wetlands under different oxidation-reduction potentials. *Ecological Engineering*, **117**, 18-27.

Borggaard, O.K. (1983) Effects of surface area and mineralogy of iron oxides on their surface charge and anion-adsorption properties. *Clays and Clay Minerals*, **31**, 230-232.

Carpenter, S.R., Caraco, N.F., Correll, D.L., Howarth, R.W., Sharpley, A.N. & Smith, V.H. (1998) Nonpoint pollution of surface waters with phosphorus and nitrogen. *Ecological Applications*, **8**, 559-568.

Churchman, G.J. (2018) Game changer in soil science. Functional role of clay minerals in soil. *Journal of Plant Nutrition and Soil Science*, **181**, 99-103.

Croudace, I., Warwick, P., Taylor, R. & Dee, S. (1998) Rapid procedure for plutonium and uranium determination in soils using a borate fusion followed by ion-exchange and extraction chromatography. *Analytica Chimica Acta*, **371**, 217-225.

Dixon, J.B. & McKee, T.R. (1974) Internal and external morphology of tubular and spheroidal halloysite particles. *Clays and Clay Minerals*, **22**, 127-137.

dos Santos, E.C., Rozynek, Z., Hansen, E.L., Hartmann-Petersen, R., Klitgaard, R.N., Løbner-Olesen, A., Michels, L., Mikkelsen, A., Plivelic, T.S., Bordallo, H.N. & Fossum, J.O. (2017) Ciprofloxacin intercalated in fluorohectorite clay: Identical pure drug activity and toxicity with higher adsorption and controlled release rate. *RSC Advances*, **7**, 26537-26545.

Edzwald, J.K., Toensing, D.C. & Leung, M.C.-Y. (1976) Phosphate adsorption reactions with clay minerals. *Environmental Science & Technology*, **10**, 485-490.

Farmer, V.C. & Farmer, V.C. (1974) The layer silicates. Pp. 0. *The infrared spectra of minerals*, **4**, Mineralogical Society of Great Britain and Ireland.

Gérard, F. (2016) Clay minerals, iron/aluminum oxides, and their contribution to phosphate sorption in soils — a myth revisited. *Geoderma*, **262**, 213-226.

Gimsing, A.L. & Borggaard, O.K. (2002) Competitive adsorption and desorption of glyphosate and phosphate on clay silicates and oxides. *Clay Minerals*, **37**, 509-515.

Golberg, S. (1985) Chemical modeling of anion competition on goethite using the constant capacitance model. *Soil Science Society America*, **49**, 851-856.

Gray, N., Lumsdon, D.G. & Hillier, S. (2016) Effect of pH on the cation exchange capacity of some halloysite nanotubes. *Clay Minerals*, **51**, 373-383.

Grim, R.E. (1968) *Clay mineralogy*. New York.

Gustafsson, J.P., Mwamila, L.B. & Kergoat, K. (2012) The pH dependence of phosphate sorption and desorption in swedish agricultural soils. *Geoderma*, **189**, 304-311.

Habibiandehkordi, R., Quinton, J.N. & Surridge, B.W.J. (2014) Effect of equilibration time on estimates of the maximum phosphorus sorption capacity of industrial by-products using the langmuir model. *Journal of Soils and Sediments*, **14**, 1818-1828.

Han, Y., Liu, W., Zhou, J. & Chen, J. (2016) Interactions between kaolinite AlOH surface and sodium hexametaphosphate. *Applied Surface Science*, **387**, 759-765.

Hayes, K.F. & Leckie, J.O. (1987) Modeling ionic strength effects on cation adsorption at hydrous oxide/solution interfaces. *Journal of Colloid and Interface Science*, **115**, 564-572.

Haygarth, P.M., Bardgett, R.D. & Condron, L.M. Nitrogen and phosphorus cycles and their management. Pp. 132-159. *Soil conditions and plant growth*.

He, L., W. Zelazny, L., C. Martens, D., Baligar, V. & D. Ritchey, K. (1997) Ionic strength effects on sulfate and phosphate adsorption on γ-alumina and kaolinite: Triple-layer model. *Soil Science Society of America Journal - SSSAJ*, **61**.

He, Y., Lin, H., Dong, Y. & Wang, L. (2017) Preferable adsorption of phosphate using lanthanum-incorporated porous zeolite: Characteristics and mechanism. *Applied Surface Science*, **426**, 995-1004.

He, Z.L., Yang, X., Yuan, K.N. & Zhu, Z.X. (1994) Desorption and plant-availability of phosphate sorbed by some important minerals. *Plant and Soil*, **162**, 89-97.

Heal, K.V., Younger, P.L., Smith, K.A., Glendinning, S., Quinn, O. & Dobbie, K.E. (2003) Novel use of ochre from mine waste treatment plants to reduce point and diffuse phosphorus pollution. *Land Contamination and Reclamation*, **11**, 145-152.

Hill, D., Holliman, P.J., Jones, E.W., McGettrick, J., Worsley, D.A., Appleman, M. & Chatterjee, P. (2019) Desorption of carboxylates and phosphonates from galvanized steel: Towards greener lubricants. *Surface and Interface Analysis*, **51**, 934-942.

Hillier, S., Brydson, R., Delbos, E., Fraser, T., Gray, N., Pendlowski, H., Phillips, I., Robertson, J. & Wilson, I. (2016) Correlations among the mineralogical and physical properties of halloysite nanotubes (HNTs). *Clay Minerals*, **51**, 325-350.

Holliman, P.J., Vaca Velasco, B., Butler, I., Wijdekop, M. & Worsley, D.A. (2008) Studies of dye sensitisation kinetics and sorption isotherms of direct red 23 on titania. *International Journal of Photoenergy*, **2008**.

Huang, X., Foster, G.D., Honeychuck, R.V. & Schreifels, J.A. (2009) The maximum of phosphate adsorption at pH 4.0: Why it appears on aluminum oxides but not on iron oxides. *Langmuir*, **25**, 4450-4461.

Huertas, F.J., Chou, L. & Wollast, R. (1998) Mechanism of kaolinite dissolution at room temperature and pressure: Part 1. Surface speciation. *Geochimica Et Cosmochimica Acta*, **62**, 417-431.

Ioannou, A. & Dimirkou, A. (1997) Phosphate adsorption on hematite, kaolinite, and kaolinite–hematite (k–h) systems as described by a constant capacitance model. *Journal of Colloid and Interface Science*, **192**, 119-128.

Ioannou, Z., Dimirkou, A. & Ioannou, A. (2013) Phosphate adsorption from aqueous solutions onto goethite, bentonite, and bentonite–goethite system. *Water, Air, & Soil Pollution*, **224**, 1374.

Joo, Y., Sim, J.H., Jeon, Y., Lee, S.U. & Sohn, D. (2013) Opening and blocking the inner-pores of halloysite. *Chemical Communications*, **49**, 4519-4521.

Joussein, E., Petit, S., Churchman, J., Theng, B., Righi, D. & Delvaux, B. (2005) Halloysite clay minerals - a review. *Clay Minerals*, **40**, 383-426.

Kamiyango, M.W., Masamba, W.R.L., Sajidu, S.M.I. & Fabiano, E. (2009) Phosphate removal from aqueous solutions using kaolinite obtained from linthipe, Malawi. *Physics and Chemistry of the Earth, Parts A/B/C*, **34**, 850-856.

Krumina, L., Kenney, J.P.L., Loring, J.S. & Persson, P. (2016) Desorption mechanisms of phosphate from ferrihydrite and goethite surfaces. *Chemical Geology*, **427**, 54-64.

Kubicki, J.D., Paul, K.W., Kabalan, L., Zhu, Q., Mrozik, M.K., Aryanpour, M., Pierre-Louis, A.-M. & Strongin, D.R. (2012) ATR-FTIR and density

functional theory study of the structures, energetics, and vibrational spectra of phosphate adsorbed onto goethite. *Langmuir*, **28**, 14573-14587.
Lin, Y., Wang, X., Liu, J. & Miller, J.D. (2017) Natural halloysite nano-clay electrolyte for advanced all-solid-state lithium-sulfur batteries. *Nano Energy*, **31**, 478-485.
Loganathan, P., Vigneswaran, S., Kandasamy, J. & Bolan, N.S. (2014) Removal and recovery of phosphate from water using sorption. *Critical Reviews in Environmental Science and Technology*, **44**, 847-907.
Lu, C. & Tian, H. (2017) Global nitrogen and phosphorus fertilizer use for agriculture production in the past half century: Shifted hot spots and nutrient imbalance. *Earth Syst. Sci. Data*, **9**, 181-192.
Manning, B.A. & Goldberg, S. (1996) Modeling arsenate competitive adsorption on kaolinite, montmorillonite and illite. *Clays and Clay Minerals*, **44**, 609-623.
Mounteney, I., Burton, A.K., Farrant, A.R., Watts, M.J., Kemp, S.J. & Cook, J.M. (2018) Heavy mineral analysis by ICP-AES a tool to aid sediment provenancing. *Journal of Geochemical Exploration*, **184**, 1-10.
Norrish, K. (1995) *An unusual fibrous halloysite*. Pp. 275-284. CSIRO Publishing, Melbourne, Australia.
Oelkers, E.H. & Valsami-Jones, E. (2008) Phosphate mineral reactivity and global sustainability. *Elements*, **4**, 83-87.
Pasbakhsh, P., Churchman, G.J. & Keeling, J.L. (2013) Characterisation of properties of various halloysites relevant to their use as nanotubes and microfibre fillers. *Applied Clay Science*, **74**, 47-57.
Parfitt, R.L. (1979) Anion adsorption by soils and soil materials. *Advances in Agronomy*, **30**, 1-50.
Ren, X., Yang, S., Tan, X., Chen, C., Sheng, G. & Wang, X. (2012) Mutual effects of copper and phosphate on their interaction with γ-Al_2O_3: Combined batch macroscopic experiments with DFT calculations. *Journal of Hazardous Materials*, **237-238**, 199-208.
Saki, H., Alemayehu, E., Schomburg, J. & Lennartz, B. (2019) Halloysite nanotubes as adsorptive material for phosphate removal from aqueous solution. *Water*, **11**, 203.
Schroth, B.K. & Sposito, G. (1997) Surface charge properties of kaolinite. *Clays and Clay Minerals*, **45**, 85-91.
Singh, B. & Gilkes, R.J. (1992) An electron optical investigation of the alteration of kaolinite to halloysite. *Clays and Clay Minerals*, **40**, 212-229.
Tarì, G., Bobos, I., Gomes, C.S.F. & Ferreira, J.M.F. (1999) Modification of surface charge properties during kaolinite to halloysite-7 Å transformation. *Journal of Colloid and Interface Science*, **210**, 360-366.
Theng, B.K.G., Russell, M., Churchman, G.J. & Parfitt, R.L. (1982) Surface properties of allophane, halloysite, imogolite. *Clays and Clay Minerals*, **30**, 143-149.
Uzunova, E.L. & Mikosch, H. (2016) Adsorption of phosphates and phosphoric acid in zeolite clinoptilolite: Electronic structure study. *Microporous and Mesoporous Materials*, **232**, 119-125.
Valsami-Jones, E. (2005) *Phosphorus in environmental technology: Principles and applications*. IWA Publishing.
Van Emmerik, T.J., Sandström, D.E., Antzutkin, O.N., Angove, M.J. & Johnson, B.B. (2007) ^{31}P solid-state nuclear magnetic resonance study of the sorption of phosphate onto gibbsite and kaolinite. *Langmuir*, **23**, 3205-3213.

Vergaro, V., Abdullayev, E., Lvov, Y.M., Zeitoun, A., Cingolani, R., Rinaldi, R. & Leporatti, S. (2010) Cytocompatibility and uptake of halloysite clay nanotubes. *Biomacromolecules*, **11**, 820-826.

Vitousek, P.M. & Howarth, R.W. (1991) Nitrogen limitation on land and in the sea: How can it occur? *Biogeochemistry*, **13**, 87-115.

Wei, S., Tan, W., Liu, F., Zhao, W. & Weng, L. (2014) Surface properties and phosphate adsorption of binary systems containing goethite and kaolinite. *Geoderma*, **213**, 478-484.

Weng, L., Van Riemsdijk, W.H. & Hiemstra, T. (2012) Factors controlling phosphate interaction with iron oxides. *J Environ Qual*, **41**, 628-635.

White, G.N. & Dixon, J.B. (2002) Kaolin-serpentine minerals. *Soil Science Society America*, **7**, 367-388.

Wisawapipat, W., Kheoruenromne, I., Suddhiprakarn, A. & Gilkes, R.J. (2009) Phosphate sorption and desorption by Thai upland soils. *Geoderma*, **153**, 408-415.

Chapter 4

Use of Advanced Microscopy Methods to Study the Internal and External Features of Halloysite Nanotubes

4.1 INTRODUCTION

Advanced microscopy imaging techniques, such as scanning electron microscopy (SEM), transmission electron microscopy (TEM) and atomic force microscopy (AFM) have been used extensively in clay mineral research due to their ability to investigate the microscopic surface structure of these materials at the nanoscale (Sirentanu *et al.,* 2016; Zhang *et al*., 2017). Zbik and Smart (1998) used comparative studies of both SEM and AFM to identify and distinguish differences in nanomorphology and surface features of kaolinites of varying crystallinity, where multiple steps were observed on the poorly crystalline sample. Additionally, Sirentanu *et al.* (2016) observed multiple defects on the surface of the minerals gibbsite, kaolinite, illite and montmorillonite through use of AFM analysis, although they noted that it was difficult to precisely identify the nature of the defects. TEM analysis has also been used frequently in clay science to examine the atomic structure and layer arrangements of clay minerals, for example, in estimations of layer periodicity (Kohyama *et al.,* 1978; Guthrie Jr and Veblen, 1989; Kogure *et al*., 2013) and particle thickness measurements (Hooshiar *et al*., 2010).

Several authors have studied halloysites using some, or all, of the above microscopy techniques (Dixon and McKee, 1974; Kohyama *et al*., 1978; Kogure *et al*., 2011; Kogure *et al.* 2013). In pioneering microscopy work, Dixon and McKee (1974) conducted a TEM study of a tubular and a spheroidal halloysite including some cross-sectional analysis of particles bound in epoxy resin. In this work, they observed that tubes with smaller cross sections were more nearly circular whereas larger tubular particles displayed flattened and planar features. However, in previous studies, difficulties have been encountered when attempting to take high resolution images of halloysite samples primarily due to their beam sensitivity (Kogure *et al.,* 2011) and small (nm-range) particle size.

As outlined in the introductionary Chapter 1, and shown in Figure 4.1, the most widely presented structure of halloysite is rather simple with a smooth external siloxane surface and an inner alumina surface, which forms the nanotube lumen (Yuan *et al.*, 2015; Kim *et al.*, 2017; Massaro *et al.*, 2017).

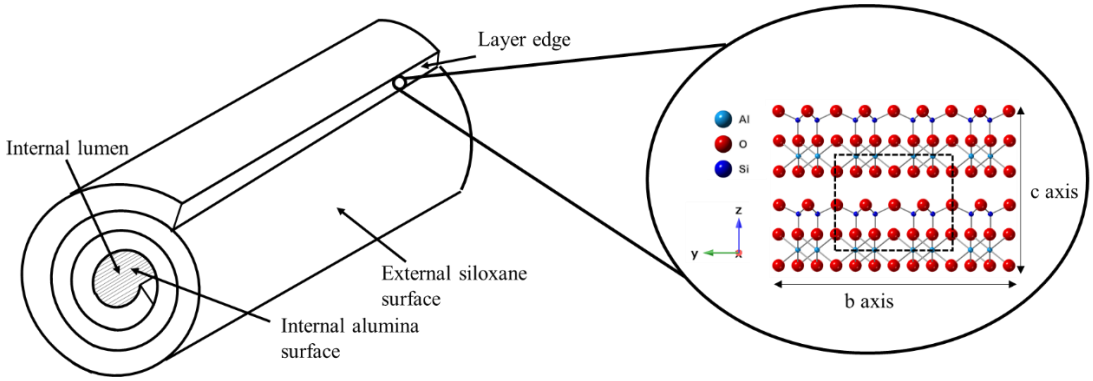

Figure 4.1. Simple schematic of a halloysite nanotube with magnified inset showing the crystal structure orientated along the (100) plane or b-axis. The unit cell is highlighted using the dotted rectangle and has the parameters a = 5.14 Å, b = 8.93 Å and c = 7.37 Å, where the a-axis is orientated directly into the page.

Although this simplistic model of halloysite (Figure 4.1) has been assumed in a multitude of studies, there is evidence that the outer surface of the halloysite nanotube should not simply be considered as a smooth, continuous, siloxane surface, but is more complex. For example, Yuan *et al.* (2008) observed defects on the surface of halloysite by AFM and noted that these could account for extra surface hydroxyl sites available for reaction. Following on from the observations made by Yuan *et al*. (2008), it can be surmised that understanding more about the internal and external surface features of the nanotubes will aid in understanding the chemical reactions at these surfaces.

Hence, the over-arching aim of this chapter is to use high resolution microscopy studies to study the surface features of tubular halloysites. As is the case throughout the thesis the two tubular morphologies, cylindrical and polygonal prismatic, were studied to determine whether they displayed variations in surface features.

4.2 MATERIALS AND METHODS

Nine samples of halloysite nanotubes originating from a variety of localities in the United States, China, Turkey and Scotland were studied (Table 4.1) where their

properties are outlined Chapter 2, Table 2.1. The samples were selected to cover a range of polygonal prismatic and cylindrical morphologies and have been referenced throughout this thesis. The halloysites were all run in their dehydrated 7 Å state for the analysis in this chapter to ensure consistency.

Table 4.1. List of halloysites used in this chapter where the dominant morphology is noted along with the 'CP' (cylindrical-prismatic) index, as outlined in Hillier *et al*. (2016).

Halloysite ID	Location	Dominant Morphology	CP index
4Ch	Defang, China	Cylindrical	0.354
5Ch	Bifa China	Cylindrical	0.326
11Sc	Elgin, Scotland	Polygonal prismatic	0.083
12Tu	Turkey	Cylindrical	0.339
17US	Dragon Mine, USA	Polygonal prismatic	0.213
21US	Bovill Deposit, USA	Polygonal prismatic	0.172
22US	Wagon Wheel Gap, USA	Polygonal prismatic	0.149
23US	FI Face, USA	Polygonal prismatic (considerable cylindrical)	0.293
24US	Hal in water, USA	Polygonal prismatic (considerable cylindrical)	0.317

As outlined in Chapter 2 (Section 2.2.1, Figure 2.5) the 'CP' index can be calculated from the modulation of the (20,13) diagnostic bands in XRPD patterns, from which the tubular morphology can be inferred.

Whilst the analytical methods used in this chapter are outlined in Chapter 2, the precise details are provided below as a recap, along with some specific details relating to the methods used only in this chapter.

4.2.1 Field emission gun scanning electron microscopy (FEG-SEM)

The halloysite samples were prepared for FEG-SEM analysis by one of two methods. For some samples, which were kept as intact pieces, the preparation simply involved drying out of the sample in an oven at 105 °C for several days before cleaving the sample to reveal a fresh surface, which was then platinum coated before analysis.

The second method which was looking at individual nanotubes involved initial gentle crushing and homogenisation of the intact or powdered sample. Then, approximately 10 mg of this was weighted out into a beaker to which 100 ml of deionised water was added along with two drops of Calgon, to aid dispersion. The suspension was sonicated for 5 minutes to ensure even dispersion and a single drop deposited on a silicon wafer supporting a 3.05 mm nickel grid. The grid assured that the droplet dried in a way to aid in more even distribution of particles across the surface of the silicon wafer. Once dry, the samples were platinum coated to reduce charging in the electron beam of the microscope. SEM images for both types of sample preparation were taken using a Carl Zeiss Sigma VP Field Emission Scanning Electron Microscope (FEG-SEM). To reduce the effects of beam damage, the silicon wafer samples were analysed using a low voltage and the thin layer of platinum deposited on the samples minimised charging. For the cleaved surface analysis, the samples were analysed under variable pressure conditions, i.e. under N_2 gas, again to reduce beam charging.

4.2.2 Atomic force microscopy (AFM)

Samples were prepared for AFM analysis by two methods. The first was dispersion of the halloysite in Milli-Q water. The suspension was then dispersed using a sonic probe (QSonica-Q125) at 20% amplitude for a total of 14 minutes sonication time (with a 2 second to 5 second sonication to rest cycle). After sonication, a droplet of the solution was pipetted onto a mica surface and placed in an oven to dry at 70 °C. The second method involved preparing a dispersed solution of halloysite in the same manner and then placing a drop of the suspension into partially dried Embedded 812 resin (sourced from Electron Microscopy Sciences). The resin was used with the aim of partially embedding the halloysite nanotubes to hold them stable during analysis.

Two different AFM instruments were used. The first, a Nanowizard 3 AFM (JPK-Bruker model). This instrument is a tip scanning AFM and is equipped with the quantitative imaging (QI) mode for delicate and small samples. QI mode was used to analyse the samples were QI is based on force-volume mode but can achieve much faster scanning speeds. The second instrument utilised was a Bruker Multimode 8 AFM, equipped with a Nanoscope V controller. The instrument was operated in PeakForce^{TM} scanning mode which allowed extreme tip-to-sample force control,

making it ideal for small crystals and soft samples. For both instruments under ideal scanning conditions the vertical resolution is 1 Å.

Measurements and analysis of the AFM images were made using ImageJ (Schneider *et al.*, 2012), JPK SPM Data Processing Analyser Version 6.1.79 and NanoScope Analysis 1.5.

4.2.3 Transmission electron microscopy (TEM)

TEM analysis was conducted on a FEI: Titan Themis instrument at Leeds University. For all the TEM analysis, because halloysites are known to be highly beam sensitive, the beam current was dropped to around 0.5 nAmp to minimise beam damage. The TEM was operated at 300 kV and is fitted with a monochromator which allowed control over the electron dose during imaging, an important feature due to the beam sensitive nature of the halloysite samples.

EDS data was collected using the Super-X EDX system with 4-windowless design and then processed using Velox. The TEM images were collected on a Gatan Oneview 16-megapixel CMOS digital camera.

4.2.4 Cross-sectional analysis of the halloysite nanotubes

Samples of cylindrical and polygonal prismatic halloysite nanotubes were embedded in Lemix L029 resin (sourced from TAAB) for cross sectional analysis by TEM. Around 50 mg of hand ground sample was mixed with 2.5 ml of Lemix A and the samples gently sonicated. The dispersion was then mixed with 5.5 ml Lemix B, 0.2 ml Lemix C and 2 ml Lemix D and the material thoroughly shaken and gently sonicated. The samples were then hand shaken and syringed into modified pipette tips which had an area cut out to allow for air flow and cured overnight at 70 °C (Figure 4.2). As there was excess material, some was also pipetted into Eppendorf vials that were cured with their lids open. No change was noted in the quality of the TEM images from the cured resin cross-sections from either the pipette tips or Eppendorf vials.

The cured resin samples were prepared as thin sections for analysis by TEM at Leeds University wherein the blocks were trimmed with a razor blade and the thin sections cut using a Diatome diamond knife on a Reichert-Jung Ultracut E-ultramicrotome.

The cut sections were around 100 nm thick and were placed on 200 mesh, thin bar copper TEM grids in preparation for TEM analysis.

Image analysis and measurements of the TEM images were conducted using ImageJ software (Schneider *et al.,* 2012).

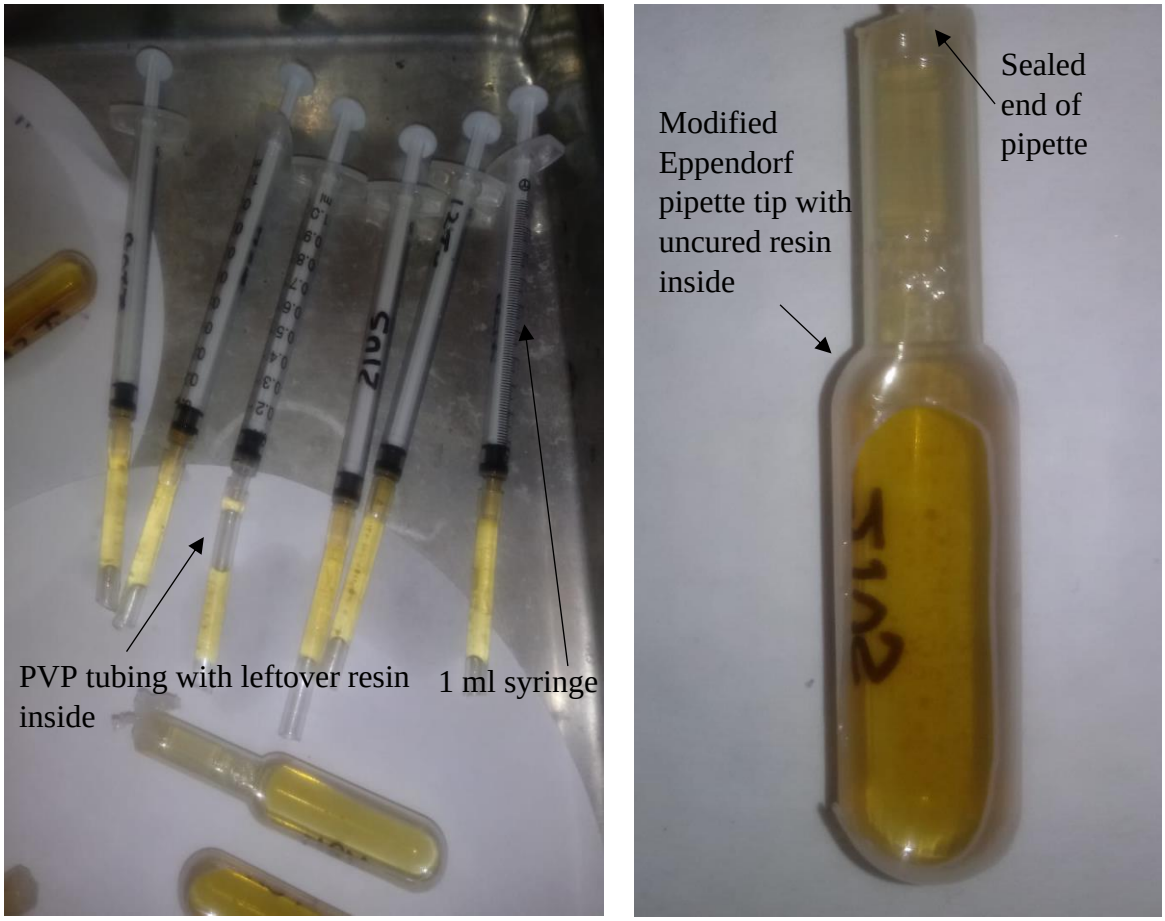

Figure 4.2. Syringe set up and modified pipette tip with uncured resin. The modified pipette tip was made by slicing off and sealing the long end of an Eppendorf pipette and cutting open a whole in the top length of the pipette bulb to allow access for air during the curing process.

4.3 RESULTS

4.3.1 Field emission gun scanning electron microscopy (FEG-SEM) results

SEM analysis revealed a clear distinction in the size and shape between the two tubular morphologies as shown in Figure 4.3. The cylindrical samples are much smaller, both

in total diameter and length, with curved external faces whilst the polygonal prismatic samples are generally larger with blocky external faces which run as flat faces along the elongation length of the nanotubes. Previous analysis of SEM images of some of these samples, and additional samples, calculated the mean nanotube lengths as ranging from between 40 – 12,700 nm and mean tube diameters of 20 - 600 nm (Hillier *et al.*, 2016). The nanotube highlighted in Figure 4.3a suggests a 5-sided polygon for the prismatic samples, although this is often a feature that is hard to discern using SEM due to difficulties in tube alignment relative to the electron beam and detector. Many of the prismatic samples show staggered layering leading to terracing at the terminus of the tube ends (Figures 4.3 d, e, h) and a rolling effect around the elongated (b-axis) edge of the nanotube (Figure 2d, g, h, i). This rolling effect is also observed and highlighted in Figure 4.3b in a cylindrical halloysite.

As can be seen most clearly in Figures 4.3e-g, the samples are not homogeneous in their morphology and while each sample may be predominantly either cylindrical or polygonal prismatic, a mixture of the two morphologies is always seen to occur, a feature of their natural occurrence and suggestive of a link between the two morphologies. This feature also verifies the 'CP' index as shown in Table 4.1, where the two polygonal prismatic samples 23US and 24US, in particular, were estimated to contain considerable quantities of cylindrical nanotubes.

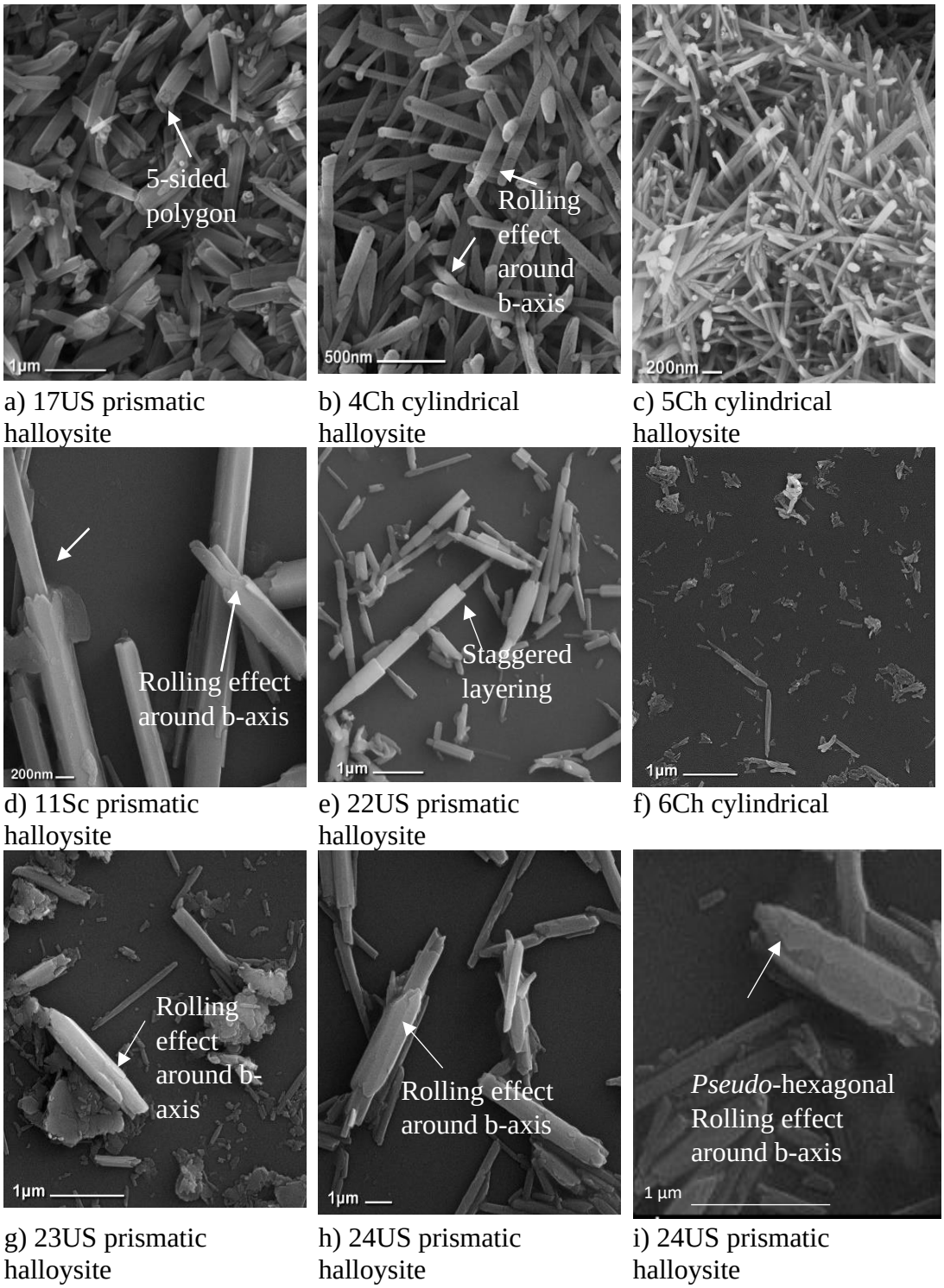

a) 17US prismatic halloysite

b) 4Ch cylindrical halloysite

c) 5Ch cylindrical halloysite

d) 11Sc prismatic halloysite

e) 22US prismatic halloysite

f) 6Ch cylindrical

g) 23US prismatic halloysite

h) 24US prismatic halloysite

i) 24US prismatic halloysite

Figure 4.3. SEM images of prismatic (a, d, e, g, h, i) and cylindrical (b, c, f) halloysite nanotubes, where the labelled arrows in each image show features of interest.

4.3.2 Atomic force microscopy (AFM) results

Like with the SEM images, the distinguishing features between the cylindrical and polygonal prismatic tubular morphologies can be identified by AFM (Figure 4.4). The polygonal prismatic nanotubes are distinguished by their characteristic rectangular flat faces which run along the elongated length of the nanotube, with adjacent faces separated by defined sharp edges. Curved outer faces were observed on the cylindrical nanotubes, although primarily due to their smaller size it was much harder to obtain clearer images of these samples. As with the SEM analysis, both morphologies were observed together in the same sample. The terminus of the polygonal prismatic tubes regularly displays staggered ends (Figure 4.4 a-c) showing a tube shortening with the addition of successive layers.

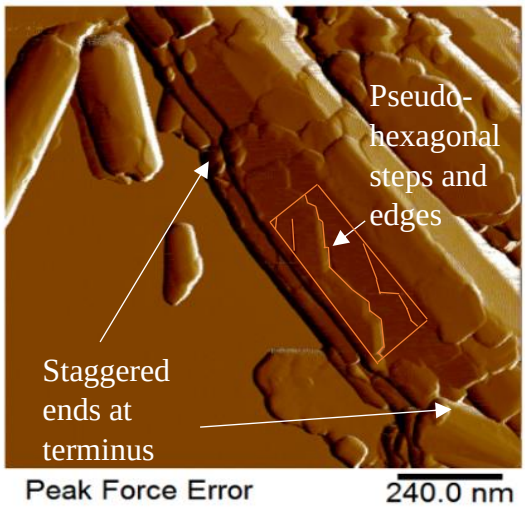

a) 17US – polygonal prismatic

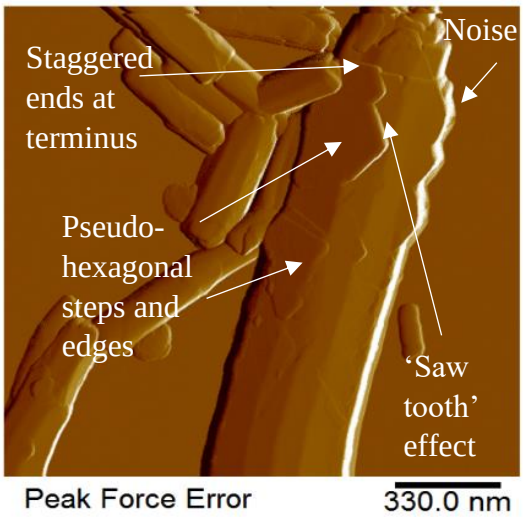

b) 17US – polygonal prismatic

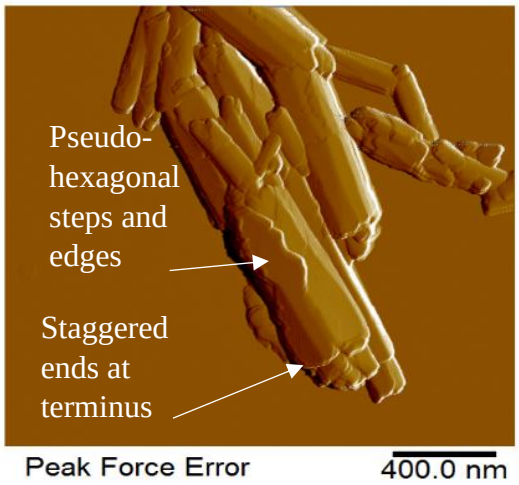

c) 17US – polygonal prismatic

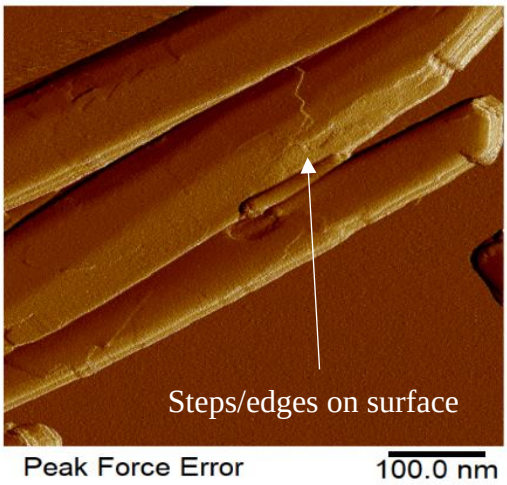

d) 23US – polygonal prismatic

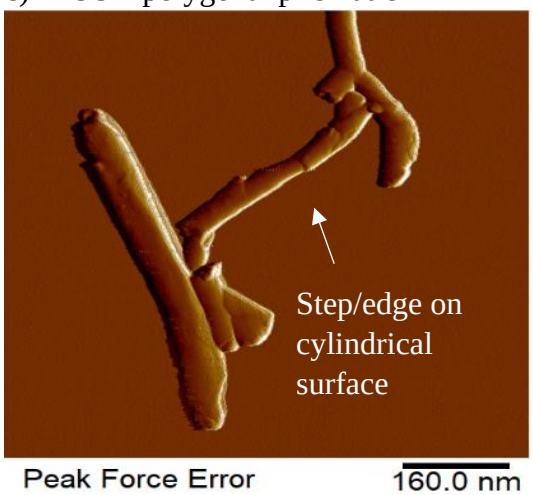

e) 4Ch - cylindrical

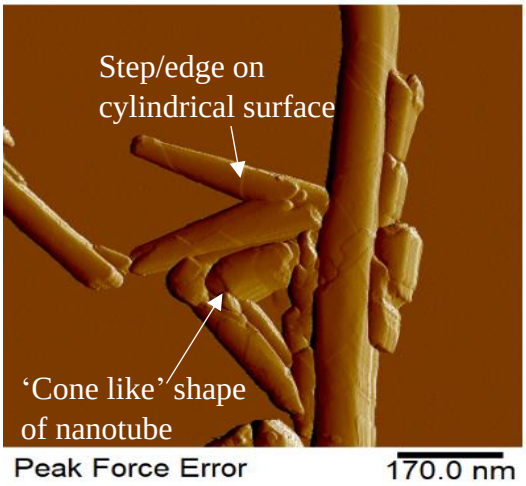

f) 5Ch - cylindrical

Figure 4.4. AFM peak force error images of prismatic (a-d) halloysite nanotubes and cylindrical (e-f) halloysite nanotubes. The key features of each image are labelled in the figure. The orange rectangle in image a indicates one area from which measurements of steps and edges were taken.

The greater topographic detail observed in the AFM images when compared to the SEM images revealed a number of steps and edges on the external faces of the prismatic nanotubes, which often appear to overlap and grow around the length of the crystal in a *pseudo*-hexagonal shape (Figure 4.4 a-c). These overlapping edges display a 'saw tooth' like appearance. These saw tooth features occur at angles of approximately 122° ± 4 ° (n=6) and are orientated in a perpendicular direction in relation to the underlying b-axis of the nanotube (Figure 4.4 a-c). Additionally, the number of steps and edges on the polygonal prismatic external faces per given surface area was calculated where the results of five measurements made on different nanotubes from the same polygonal prismatic sample, 17US, are shown in Table 4.2 and Figure 4.4a. Care was taken when making such measurements to ensure that none were taken at the edges of the nanotubes where effects such as distortion of the shape and noise were observed, which is a common feature with AFM analysis (as indicated in Figure 4.4b).

Table 4.2. Measurements of additional steps and edges within a selected area of the flat faces of the prismatic nanotube, 17US. Five separate measurements were taken of five individual nanotubes.

Sample ID	Total area (nm^2)	Total length of steps and edges (nm)
17US, nanotube 1	72335.8	1053.8
17US, nanotube 2	105740.5	769.4
17US, nanotube 3	69973.2	415.7
17US, nanotube 4	91774.5	543.1
17US, nanotube 5	66573.3	583.4

Using the JPK Data Processing software, it was possible to make further measurements of the steps on the surfaces of both morphologies. For the prismatic nanotubes, 33 measurements were made in total with step sizes ranging from 4.2 to 24.9 nm, the majority at either just over 7 or 14 nm (Figure 4.5), with an average step height of 11.8 ± 5.9 nm. The unit layer thickness of a dehydrated halloysite (7 Å) layer is around 0.72 nm so it can be assumed that the larger size of the majority of steps, often by a factor of 10, indicate that the steps and edges of the surface of the halloysite are features of around 10 unit layers or more thick, although the full range can be calculated as between 6 to 35 layers with a d-spacing of 0.72 nm. Despite the lower quality of images due to the smaller size of the cylindrical tubes, some steps and edges

are still clearly visible on the surface of these nanotubes (Figure 4.4 e-f) with those that were measured indicating step sizes of approximately 7 nm, i.e. around 10 layers. For the most part, the edges observed traverse the surface of the cylindrical tubes at an average angle of 54 ± 15° (n=26) in a clockwise direction with respect to the tube axis, though other angles are also apparent for example, where the tube form is distorted towards that of a cone as labelled in Figure 4.4f. These conical tubes showed an average of 56° ± 10° (n=3). As with the polygonal prismatic tubes, edges or steps parallel to the tube b-axis, as depicted in the schematic of Figure 4.1 are not apparent.

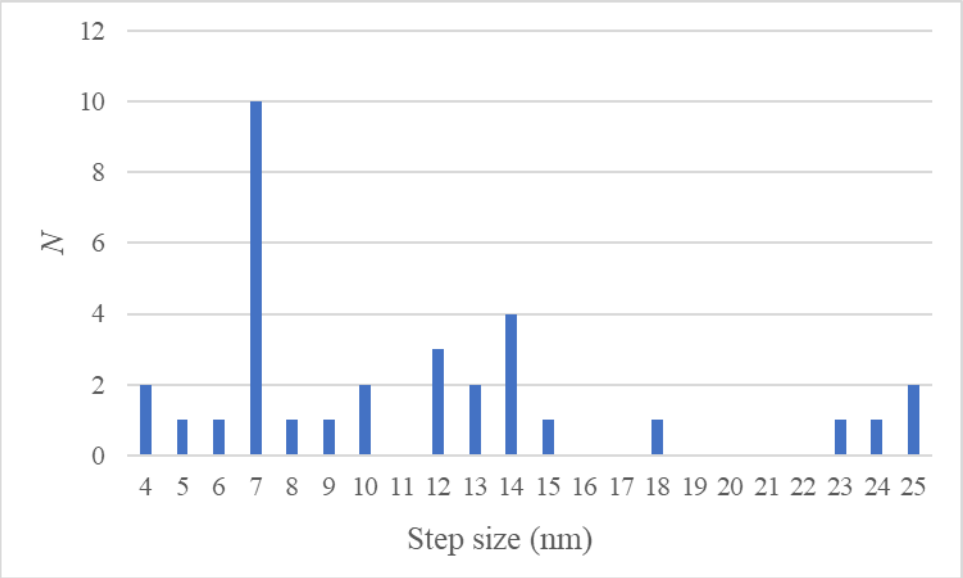

Figure 4.5. Measured step sizes from atomic force microscopy images of 3 different prismatic samples. Total n = 33.

4.3.3 Transmission electron microscopy (TEM) results

TEM analysis of the cross sections of a range of polygonal prismatic and cylindrical halloysites resulted in the successful acquisition of many useful images, some of which are displayed in Figures 4.6 and 4.7. As with both AFM and SEM analysis, it was clear that while the samples were predominantly cylindrical or polygonal prismatic in morphology, all the samples contained examples of both morphologies. Using ImageJ, measurements of the lumen diameters averaged out at 12.1 ± 4.1 nm (n=24) for the polygonal prismatic samples compared to 12.3 ± 2.7 nm (n=25) for the cylindrical halloysites. Whilst the external diameters varied significantly with an average diameter of 135.2 ± 97.8 nm (n=25) for the polygonal prismatic cross sections, the largest measured having an external diameter of 420.3 nm and the smallest 43.6

nm. By contrast the cylindrical nanotubes had an average external diameter of 57.5 nm (n=26) where these features are labelled in Figure 4.6a.

From Figure 4.6, showing a cross-section for selected cylindrical halloysites, it is apparent that these nanotubes are relatively simple in terms of their features. They display a seemingly continuous and even layer spacing of layers with few intervening pores within the structure, where the pores can be considered as disruptions to the interlayer spacings. It is unclear from the cross-section images how the nanotubes begin to roll, i.e. via a concentric or spiralling mechanism of the layers. One feature that can be noted from Figures 4.6 d-e is that the continued growth of the cylindrical forms seems to occur from a single point by a thickening block of successive layers. It may also be argued that the morphology of the cross-section in Figure 4.6c is unclear and appears to have some polygonal prismatic character as labelled in the figure.

TEM analysis was also conducted on the polygonal prismatic samples and one of the first observations that can be made from the polygonal prismatic cross-section TEM images is that several appear to have a cylindrical core at the centre of the nanotube (Figures 4.7 a, b, c). The exact formation mechanism of the nanotubular shape remains unclear from the cross-section images, for example whether the tubular shape occurs by growth of concentric layers of rolling of layers as simplified in Figure 4.9.

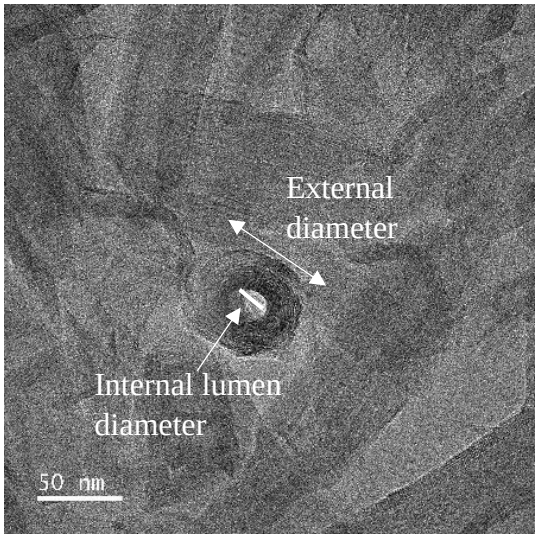

a) 4Ch halloysite

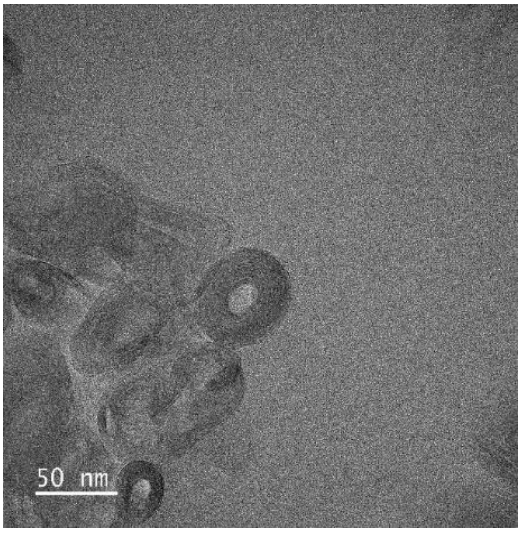

b) 5Ch halloysite

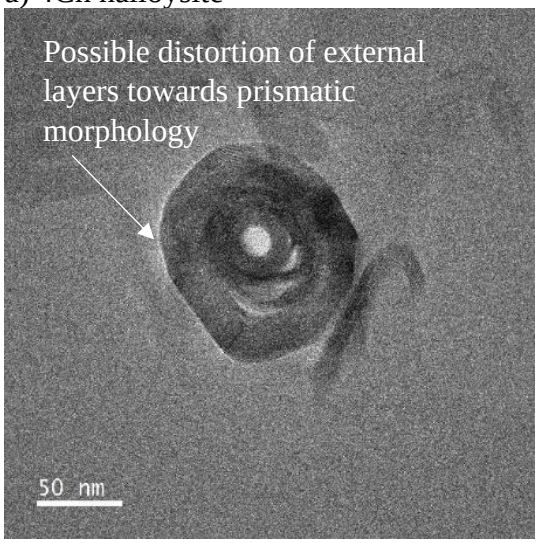

c) 22US halloysite

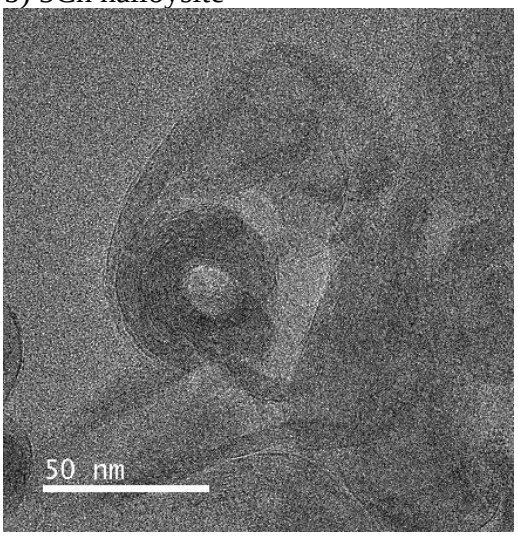

d) 21US halloysite

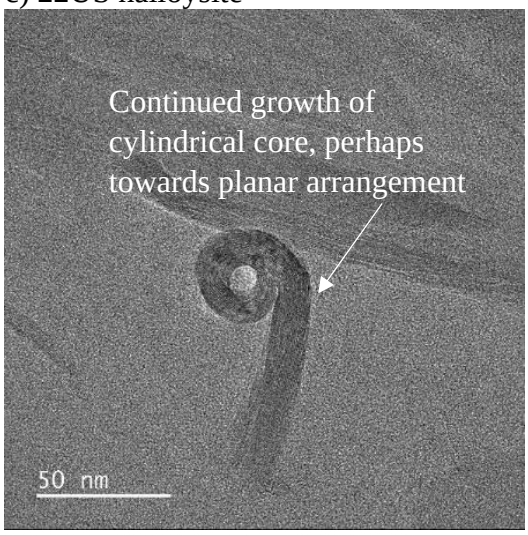

e) 4Ch halloysite

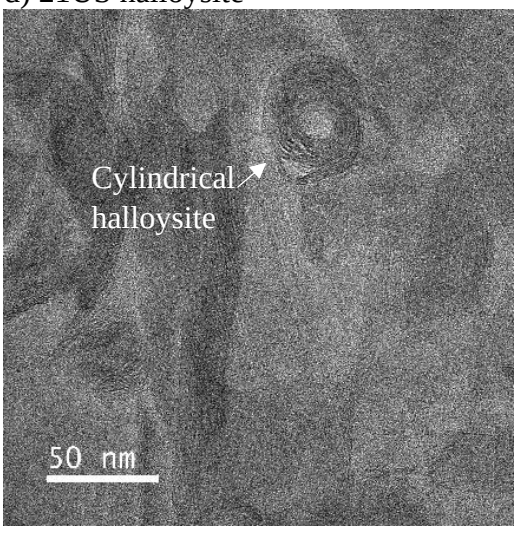

f) 12Tu halloysite

Figure 4.6. TEM images of the cross section of a variety of cylindrical halloysites with the key features labelled.

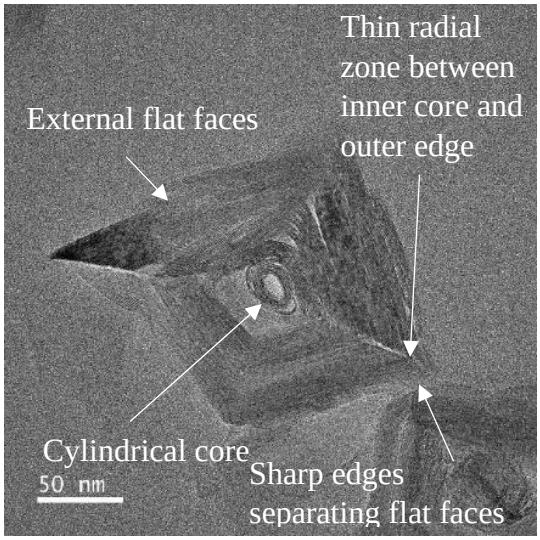

a) 21US halloysite

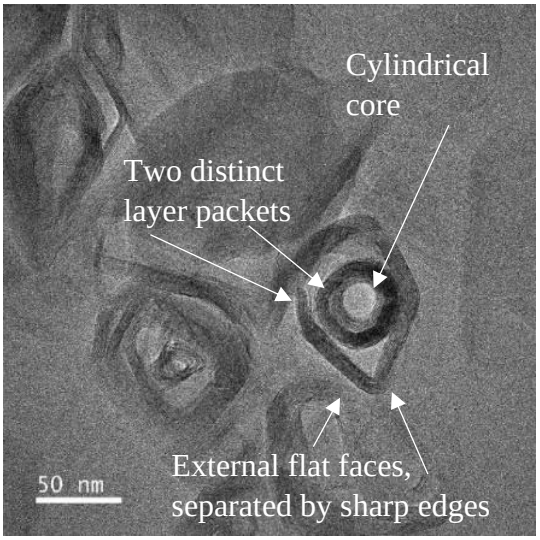

b) 22US halloysite

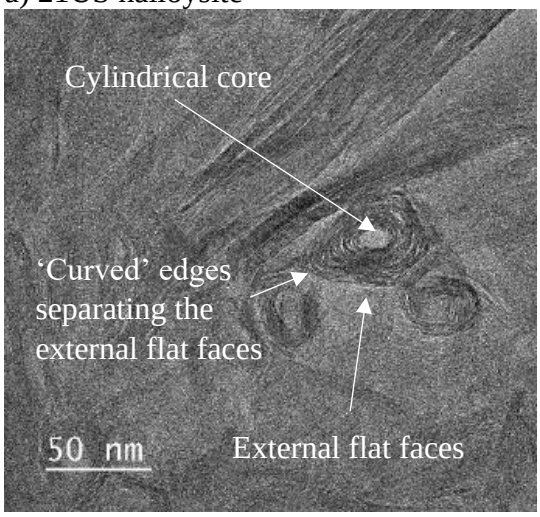

c) 12Tu halloysite

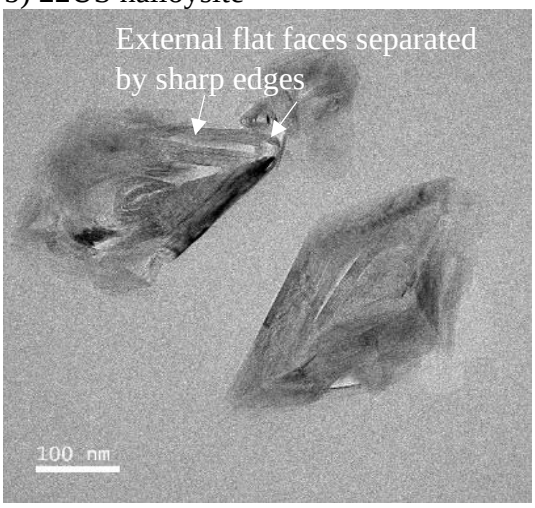

d) 11Sc halloysite

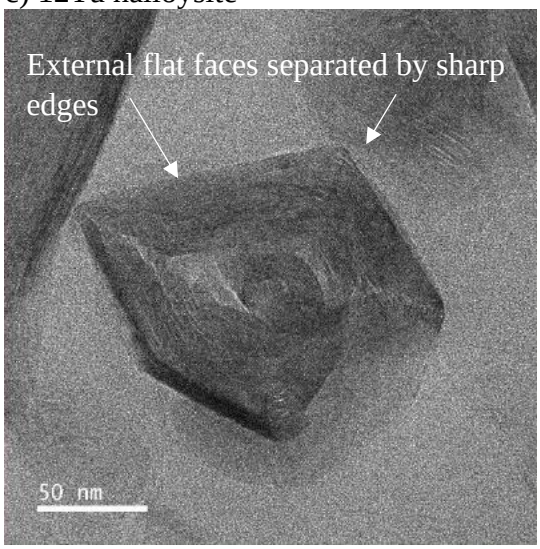

e) 17US halloysite

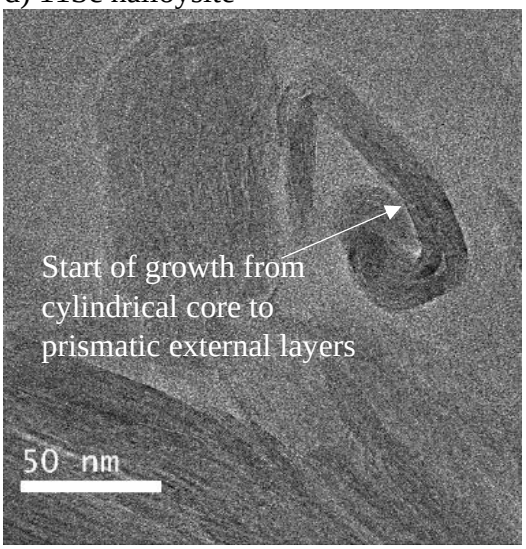

f) 21US halloysite

Figure 4.7. TEM images of the cross section of a variety of polygonal prismatic halloysites with the key features labelled.

From Figure 4.7 of a selection of the polygonal prismatic cross-sections, the external flat faces separated by sharp edges are apparent. These edges often appear as thin radial junction zones (as labelled in Figure 4.7a) between the outer edge and the inner core of the nanotubes and vary from being sharp junctions as in Figures 4.7a, d, and e to often more curved in nature as in Figure 4.7c. The diversity of the samples and clarity of the images enabled counting of the number of external faces on the prismatic forms. Out of 45 individual nanotubes counted, 30 had 5 sides, 13 had 4 sides and, because the distinction between some sides was unclear, two were judged to be between 4-5 sides. This lack of distinction may be a result of distortion during sectioning or amorphization of the sample by electron beam damage, where beam damage was observed to occur several times during the TEM analysis if the beam was focused on a sample spot for a prolonged period. To counteract this, the images were taken rapidly. Additionally, the angles of intersection between sides were measured (Figure 4.8) and range from an acute angles of 57° to an obtuse angle of 159°, with a mean of 117° and a mode of 122°, where a schematic of the angle of intersection is shown in Figure 4.9.

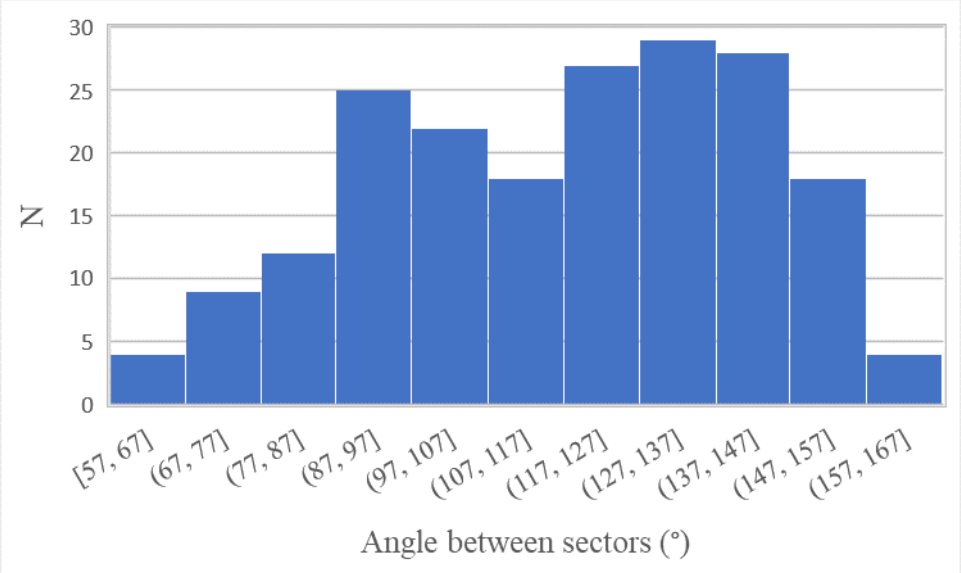

Figure 4.8. Angle distribution between adjacent sides in polygonal cross sections. N = 196.

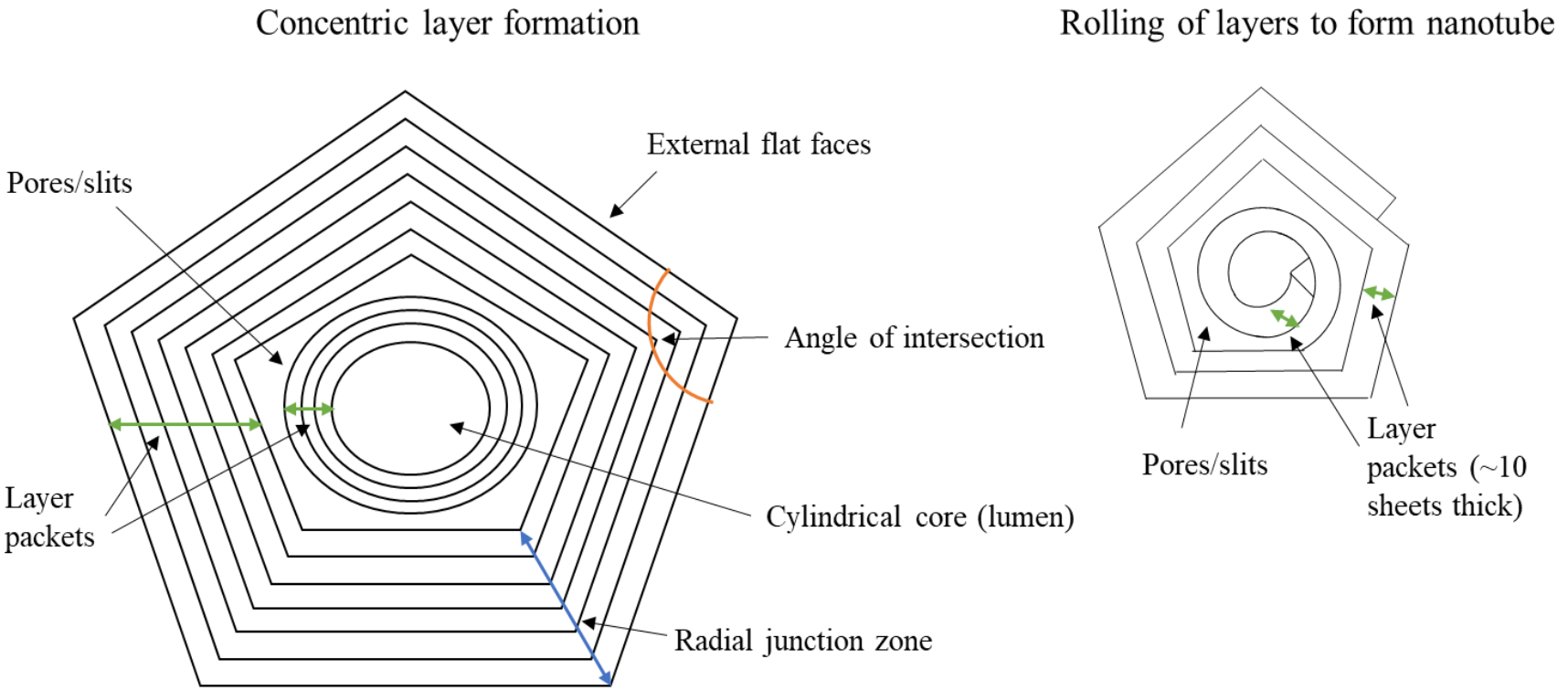

Figure 4.9. Simplified schematics depicting the angle of intersection on an assumed perfectly symmetrical prismatic nanotube with a hollow cylindrical core. In addition, layer packets are identified which can be observed as distinct segments of groups of layers separated by a change in morphology or by slits/pores. The two hypotheses of cylindrical to polygonal formation are shown, the larger diagram is that of concentric layer formation, the smaller of rolling of layers to form a nanotube.

The polygonal prismatic cross-sections were also observed as being divided into packets of layers wrapping around the nanotube centre which are separated by slits or triangular shaped pores (Figure 4.7). Analysis of seventeen polygonal prismatic nanotubes across the range of samples shows that the average number of layers in each packet is 39 ± 23.2 (n=17) (Table 4.3). A layer packet was observed as distinct segments of halloysite layers starting from the cylindrical core that are separated by a change in morphology or the slit like pores or voids in the structure (Figure 4.7b, 4.9).

Table 4.3. Layer packet measurements taken from TEM cross sections, where n refers to the number of measurements made.

Tubular Morphology	Layer Position	n	Average Number of Layers	Standard Deviation
Cylindrical	All	15	15	3.8
Prismatic	Average total layers	17	39	23.2
Prismatic	Inner layer packet	17	12	3.9
Prismatic	First outer layer packet	14	19	10.1
Prismatic	Second outer layer packet	6	19	4.2
Prismatic	Third outer layer packet	2	41	8.0
Prismatic	No distinction between layers	2	18	5.5

*layer packets are defined as distinct segments of halloysite nanotube growth separated by a change in morphology/slit like pores or voids in the structure.

The pores that occur between the packets in prismatic samples measured between 0.88 and 18.1 nm in diameter, with an average pore width of 4.5 nm (n = 15) and they occur most commonly at the boundary between the cylindrical inner core layers and the polygonal prismatic ‘outer’ packets of layers. Two of the of polygonal prismatic tubes had outlying pore widths of 16.8 nm and 18.1 nm respectively, highlighting the large variation in void size that may occur. Cross-section analysis revealed the occurrence

of pores in all the polygonal prismatic samples which suggests that they are a common feature in polygonal prismatic morphologies of halloysite nanotubes.

4.4 DISCUSSION

4.4.1 Optimising sample preparation

During the sample preparation for AFM analysis some issues arose with the samples mounted into resin wherein it was unclear if certain features that were observed were true surface features or resin impurities on the surface. The resin method also resulted in dense aggregation of the halloysite nanotubes with several of them sticking straight out of the surface of the resin. For these reasons, the data analysis presented here and imaging of the halloysites primarily focused on the samples mounted onto mica sheets.

In the sample preparation for the cross-section analysis by TEM, it took several attempts to perfect the method for curing the samples in resin. Initially it had been hoped to align the halloysite nanotubes for cross-section by gently syringing the uncured material through long strips of PVC tubing and placing the tubing in the oven overnight at 70 °C to cure. This did not result in successful curing, as the samples were found to be too soft for slicing by thin section. After several adjustments to the method to determine the source of the problem, it was concluded that air flow over the resin was required for curing. For this reason, the final samples were slowly syringed through shorter segments of PVC tubing into modified pipette tips, where the top had been cut off the pipette bulb and the end sealed to prevent leakage of uncured material (Figure 4.2).

As mentioned in the introduction to this chapter (Section 4.1), halloysite nanotubes are known to be susceptible to beam damage during high resolution imaging analysis. There were several ways in which this was circumvented, primarily by ensuring that in the SEM and TEM analysis the images were taken rapidly so that the focused beam was not held onto the sample for longer than required. Both methods also used low accelerating voltages and beam currents. Where beam damage did arise, this was apparent by a distortion of the image and an obvious blurring of the features over the time taken to process the image.

4.4.2 Distinctions between the two tubular morphologies as observed by the three microscopy techniques

Careful inspection of images from all three microscopy methods of both morphologies revealed that while a sample may be classified as predominately either polygonal prismatic or cylindrical, the samples are not exclusively of one morphological type and examples of polygonal prismatic forms can be found in predominantly cylindrical samples and vice versa. Indeed, this can be noted by observing the 'CP' index in Table 4.1, in particular for the samples 23US and 24US, where this is a measure of the disorder of the halloysites as determined by XRPD with a larger CP value suggesting lower disorder and hence cylindrical morphology. The disorder observed in the (20,13) bands is reflective of the tubular morphology.

Microscopy analysis confirmed that the major distinction between the two morphologies is their average tubular diameter, as was most clearly shown by the varying scale bars in the SEM images (Figure 4.3) and observed when undergoing AFM analysis. From TEM cross section measurements the cylindrical nanotubes have an average outer diameter of 57.5 nm compared to 135.2 nm for the polygonal prismatic samples.The same finding was also emphasised in Hillier *et al.* (2016) and is similar to measurements made by Bates and Comer (1957) who reported nanotube diameters ranging from 44 -175 nm (n=5200). Despite the large distinction in cross-sectional diameters between the two morphologies, measurements of the cross-sectional images of the lumen revealed little distinction in size and shape between the two. Indeed, the lumen shape varied between circular and oval for both where it was unclear whether the oval shape is real or an artifact as a result of the cross-section not being at an angle of 90 ° to the elongated axis of the nanotubes. An additional verification of the lumen measurements was made in Chapter 5 from images taken along the elongated lengths of the nanotubes where the lumen diameters were measured as 11.4 ± 2.8 nm (n=34) for the polygonal prismatic samples and 12.0 ± 3.0 (n=43) for the cylindrical samples. The comparable results between the different methods for lumen size measurements verifies the data obtained for the lumen diameters via their cross-section analysis.

The TEM analysis of the cross section indicates that the halloysites appear to grow in sections or packets of layers (Figure 4.9) which are grouped together in distinct

segments, separated by a change in morphology or slit like gaps and pores in the structure. For the cylindrical halloysites with only one 'layer packet' an average of 15 layers is observed, which corresponds to the 10-15 layers often quoted in literature with reference to cylindrical halloysites (Lvov *et al*., 2016) whilst being slightly larger than those observed by Dixon and McKee (1974) who noted thin packets of 5 layers each for circular cross-sectioned nanotubes. Polygonal prismatic nanotubes were shown to consist of up to 4 distinct layer packets, with the inner cylindrical core an average of 12 layers thick and the outer layer packets varying in average thickness from 19 to 41 layers thick. This is similar to previous estimations by Dixon and McKee (1974) who observed thicker tubes in cross section analysis that showed similar planar features to kaolinite and were between 27-38 layers thick. Whilst the polygonal prismatic nanotubes were not observed as growing with more than four separate layer packets, it may be considered that continued growth beyond this becomes energetically unfavourable. This is one potential theory which may explain why halloysites are found in nature as nanotubes. Further research such as modelling the constraints and thermodynamics of halloysite growth would be required to confirm this hypothesis.

4.4.3 Formation of the pores/slits in polygonal prismatic nanotubes

Slit like pores often separate the layer packets in the prismatic samples and have been previously noted in halloysite samples when studied by TEM (Dixon and McKee, 1974; Kohyama *et al*., 1975; Churchman *et al*., 1995; Pasbakhsh *et al.,* 2013). In those studies, the presence of pores in the prismatic samples was attributed to layer packing or the shrinkage of the halloysite layers upon transformation of hydrated (10 Å) halloysite to dehydrated (7 Å) halloysite. Berthonneau *et al.* (2015) used TEM on a spheroidal halloysite (10 Å) and (7 Å) to ascertain that pores were only observed in the halloysite (7 Å) samples, supporting the theory that the pores are formed upon natural dehydration and hence, result in a mismatch between the layers. Churchman *et al.* (1995) showed that the presence of such micro and mesopores could be detected by nitrogen gas adsorption and desorption isotherms. The size of several of the pores observed in the samples studied here (Figure 4.7b) may suggest that some the pores are formed during growth of the nanotubes, as opposed to solely being attributed to shrinkage upon dehydration. From the size of the pores and their accessibility it can be tentatively suggested that they may act as additional sites of anion adsorption of

small molecules, since the exposed aluminol and silanol groups may be accessible on the outer and inner walls of these pores respectively. Additionally, even if they are all formed during dehydration, they will undoubtedly be of some importance for most technological applications of halloysite nanotubes since the raw halloysite materials typically consist of refined and dried material. Future work is therefore required to fully understand the formation and significance of these pores in prismatic halloysites.

4.4.4 External surface features of the cylindrical and polygonal prismatic nanotubes

The SEM images of the cylindrical examples shown here (Figure 4.3 b, c) display smoother outer surfaces although some overlapping of layers was apparent on the external surfaces, as indicated by the arrows in Figure 4.3b. The SEM images demonstrate that the prismatic samples do not grow in a uniform shape and several effects such as the stepped back terminus of the tubes (Figure 4.3d) and growths or folds around the nanotubes occur (4.3 d, g, h, i). These folds appear as a type of 'wrapping around' of layers, indicating that crystal growth appears to occur around the elongated b-axis edge of the nanotubes, although the mechanism of growth is, as of yet, unknown. The stepped and broken edges at the terminus of the nanotubes is much more defined in the polygonal prismatic AFM images than in the SEM images, where the continued layer growth occurs in a wrapping or folding mechanism around the elongated length of the polygonal prismatic nanotubes (Figure 4.4 a-c). The edges of these features can be seen to be sharp and pointed in shape in many instances and may be described as *pseudo*-hexagonal which is similar to previous observations made for kaolinite. Indeed, Brindley and Comer (1955) noted that for a kaolinite material studied using electron microscopy several surface features with hexagonal outlines could be distinguished.

From the AFM analysis edge step sizes were measured across a variety of prismatic samples and ranged from 4.2 to 24.9 nm (Figure 4.5), with an average step height of 11.8 ± 5.9 nm. The cylindrical nanotubes appeared by eye to have fewer steps and edges on the external surface of the nanotube, particularly those which grow around the elongation length of the nanotube. While it was harder to accurately measure these steps due to the lower quality of the images, the attempts that were made estimated them as around 7 nm, suggesting steps that are 10 layers thick, since each halloysite unit cell is around 0.7 nm. The range and magnitude of step sizes suggests that the

layers are assembled in packets around the circumference of tubes, a feature that was also first noted by Dixon and McKee (1974) and was observed in the cross sectional TEM images here. The presence of smaller steps not identified by the AFM analysis should not be ruled out, indeed although the AFM resolution is 1 Å, this is under ideal conditions which were not obtained for all of these samples due to their small sample size. Further work would be required to verify that small steps and edges are not present on the external surfaces of these nanotubes.

The sharp and pointed edges regularly appear as a 'saw tooth effect' on the outer surfaces of prismatic nanotubes in the AFM images. The re-entrant angles of the 'teeth' at an average of 122 ° suggest crystal structure controlled orientation of the faces with respect to the long axis of the tubes (typically the b-axis) and the rolling direction, as confirmed by Drits *et al.* (2018), suggest by analogy with kaolinite, that the edges observed correspond to faces indexed as (110) and ($1\bar{1}0$). Additionally, the layers with the saw tooth edges are seen to extend around the arrangement of planar sectors, they do not just represent *pseudo*-hexagonal plates topotactically arranged on one planar sector, though such plates have also often observed in some samples, particularly in SEM images (Figure 4.3i). For the cylindrical halloysites, the angles on the edges can be seen to be 54°, suggesting that they also correspond to the (110) and ($1\bar{1}0$) faces. While the root cause of the saw tooth shape is not investigated further in this thesis, it can be postulated that it may be a feature of twinning of the a,c plane although further study is required to verify this.

The significance of these angles of intersection or rolling around the halloysite nanotubes can be explained by a closer look at the crystal planes. Typically, as depicted in Figure 4.1, it is assumed that the edge site runs in line with the elongated length of the halloysite nanotube, exposing the (100) face to adsorption reactions. As observed in the AFM images presented in this chapter and the angle measurements made, it appears instead that is the (110) and ($1\bar{1}0$) faces that are exposed. A comparison of the two is shown in Figure 4.10. Where it may be considered that the different spacial arrangement of the (110), ($1\bar{1}0$) faces may result in a change in the type of adsorption, i.e., mono/bi/tri-dentate occurring at the available hydroxyl edge groups due to their different steric arrangement. By a similar argument the edges that are normal to the end of the tubes forming the terraced ends, i.e. those at the terminus

of the tubes with (100) planes along the b-axis, are assumed to correspond to (010) faces. Together with the prism faces described above, the two forms (110) and (100) correspond to the typical faces that are developed on *pseudo*-hexagonal plates of kaolinite (Flegmann *et al*., 1971).

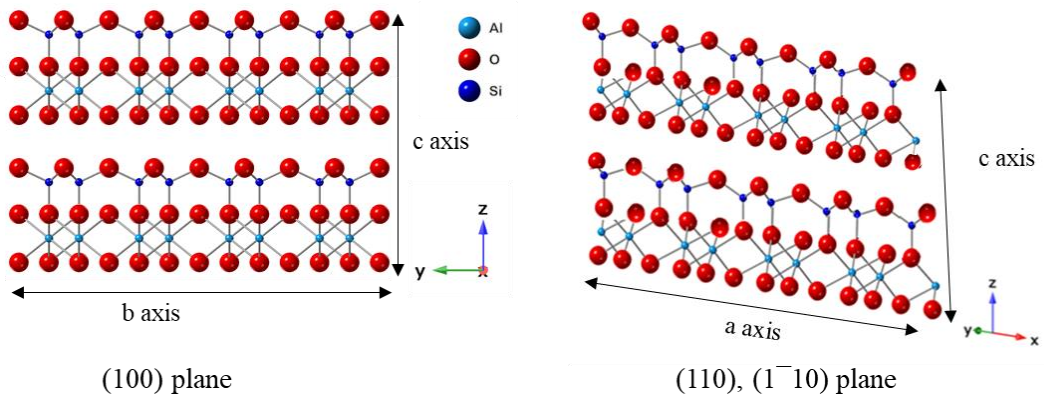

Figure 4.10. Comparison of the two exposed planes along elongated halloysite edge.

Previous work that has compared the difference edge faces on kaolinite surfaces have calculated that the (010) and (110) edges are structurally equivalent with an edge surface area of 295 Å, whilst the (1¯10) surface has an edge surface area of 213 Å (Pouvreau *et al.*, 2019). This smaller surface area would be expected to result in different steric effects for phosphate adsorption to this surface. Future, focused, in depth modelling would be required to quantify the true nature of the effect of the different surface exposures.

4.4.5 Effect of the additional edge sites on anion adsorption

Yuan *et al.* (2008) suggested these edge sites on the external surface may provide additional adsorption sites. It was also proposed in Chapter 3 that the polygonal prismatic nanotubes had a slightly higher phosphate adsorption capacity than the cylindrical nanotubes after normalisation to surface area, potentially due to the hypothetical presence of these additional pH dependent edge adsorption sites. The total number of clearly visible additional edge sites per area were measured for five polygonal prismatic nanotubes from the same sample (17US) as shown in Table 4.2. From this the additional edge site contribution can be estimated by using the average step height of the layers (11.8 nm) and calculating this as a total percentage of the initial area being measured. The average of the 5 measurements results in an additional

10% surface area. It is worth considering that this value may also be an underestimate as there are likely additional steps and edges on the surface that have not been detected by AFM. Despite this, the estimation of an additional 10% steps and edges on the surface suggests that these polygonal prismatic nanotubes may have more available edge sites of adsorption reactions than would be considered by evaluation of surface area measurements only. These extra sites have been studied and attempts to quantify them made for kaolinite. For example, Zbik and Smart (1998) studied a poorly crystalline kaolinite and estimated that the extra steps and edges on the surface resulted in an additional 6% edge site contribution, whilst Brady *et al*., (1996) estimated this an extra 5% edge site contribution. From this initial comparison of the results for kaolinite and halloysite it can be considered that the halloysites may have a greater number of steps and edges on their external surfaces, especially if there are additional steps present below the resolution of the AFM images that have been acquired.

This work suggests that the simplistic figure of the halloysite nanotube as presented in Figure 4.1 should be revised to include the more complex surface and the presence of pores that are additional to the central lumen, particularly in the case of prismatic nanotubes a schematic of which is shown in Figure 4.11.

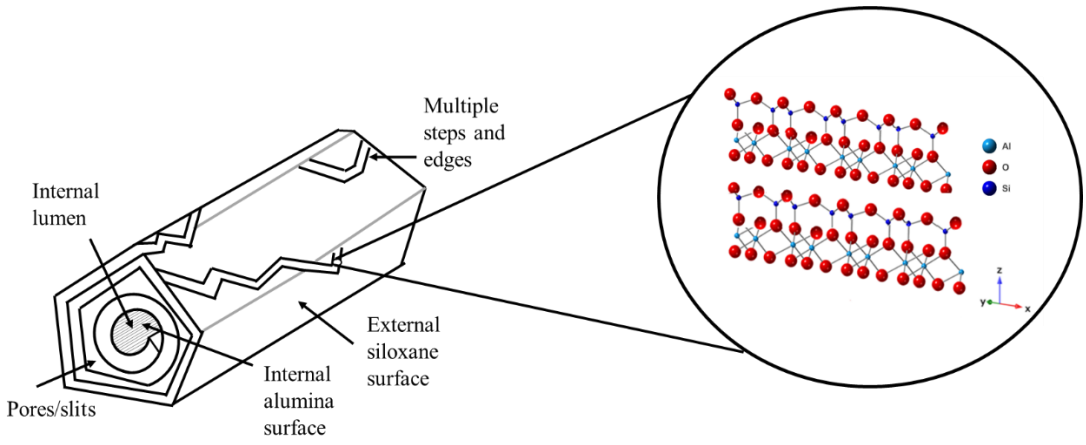

Figure 4.11. Suggested and simplified figure outlining the complexity of the surface of halloysite nanotubes where the (110), (1¯10) plane is exposed at the edge sites. The figure depicts a prismatic halloysite which has grown from a cylindrical core.

4.4.6 Observations of the shape of the polygonal prismatic nanotubes as identified by cross-section TEM analysis

From the cross-sectional TEM analysis, the polygonal nanotubes can be identified by their flat layers where the bending of sheets connects adjacent sides. The angle at which the adjacent sides connect is seen to vary within each individual nanotube, highlighting that they are not uniform in shape (Figure 4.8). There is a certain degree of caution regarding these measurements from the cross sections. Indeed, Berthonneau *et al.* (2015) stressed that since TEM images are projections of the sample, shifts in the alignment of the sample may result in a distorted view of observed angles. There is also the possibility that the thin sectioning for cross-section analysis resulted in some distortion of the nanotubes. However, given the number of samples imaged and compared in these experiments (>100) it can be said with some degree of certainty that the measurements made are real and not artifacts.

Bearing the above caution in mind, cross-section TEM analysis indicated that the prismatic halloysite nanotubes display a tendency towards a 5-sided polygon shape. This is in line with the report by Kogure *et al.* (2013) who obtained cross section images of prismatic HNTs where four-five major sectors were noted in some prismatic tubes and one nanotube which contained 18 sectors as verified using selected area electron diffraction (SAED). These results show a similarity to other cylindrical minerals, such as serpentines where 15-30 sectored polygons have been observed (Cressey and Zussman, 1976; Yada and Liu, 1987; Baronnet *et al*., 1994). The analogous results between previous studies and the work presented in this chapter reinforces the quality and robust nature of the data obtained. It can be noted that the polygonal blocky sides that are often uneven in length and connecting angles, particularly when they are 5-sided (Figure 4.7 b, c, d, e), whilst the 4 sided-polygons appear to be more evenly spaced (Figure 4.7a). While not every single sample analysed displayed a clear distinction in the number of sides, this is perhaps an interesting route for future research to examine this aspect further, especially since 5- fold symmetry is usual in crystallography.

4.4.7 Relationship between cylindrical and polygonal prismatic nanotubes

It is well documented and has been observed in our sample sets that both tubular morphologies can occur together in nature. Kogure *et al.* (2013) used high resolution transmission electron microscopy (HRTEM) analysis of the layer structure of tubular halloysites to propose that prismatic nanotubes are formed upon dehydration from cylindrical nanotubes. By contrast, Hillier *et al.* (2016) proposed that at some critical point in the continued growth of cylindrical halloysites it becomes more energetically favourable to switch to planar layers, hence prismatic nanotubes start off as cylindrical nanotubes and the cylindrical inner layer then acts as a template around which subsequent layers grow. Hillier *et al.* (2016) also referred to XRPD data to show that the typical disorder observed in prismatic halloysites, as shown by the 'CP' index, is observed in both halloysite (10 Å) and halloysite (7 Å) traces. Both the cylindrical and polygonal prismatic nanotubes have been shown in this chapter to have similar inner lumen diameters (of around 12 nm), supporting the theory by Bates *et al.* (1950) who hypothesised that the lumen size is regulated by the structural misfit between the tetrahedral and octahedral sheets upon curvature. Analysis of the cross-sections of tubular halloysites in this study show that some of the polygonal prismatic halloysites have a purely cylindrical core (Figure 4.7). Additionally, the smaller average total nanotube diameters observed for the cylindrical halloysites support this hypothesis. This phenomenon of an inner cylindrical core surrounded by blocky polygon layers has been observed in other tubular minerals such as some serpentines (Middleton and Whittaker, 1976). Baronnet *et al.* (1994) also noted that polygonal serpentine fibres are almost always found in the presence of smaller cylindrical fibres, suggesting that the larger polygonal fibres were grown from the smaller cylindrical fibres, although the precise mechanism of growth remains largely unknown (Baronnet *et al.*, 1994).

4.5 CONCLUSION

Nine different halloysites were investigated in this study that were a mix of both cylindrical and polygonal prismatic morphologies. Despite their small size and beam sensitivity, which often rendered them difficult to image using methods such as AFM and TEM, multiple measurements were made of the nanotubes. From the SEM and AFM analysis, multiple steps and edges were established as present on the external surface of the nanotubes, in contrast to the simplistic model of halloysite nanotubes

often presented. From measurements made from the AFM analysis it can be surmised that these *pseudo*-hexagonal steps on the surface of the polygonal prismatic nanotubes occur as multilayer thick steps, an observation that was also noted by the packets of layers in the TEM cross-sections, although the presence of smaller and undetected steps and edges can only be ruled out by further AFM analysis. Difficulties in imaging the smaller cylindrical nanotubes hinder this being a definite conclusion for the cylindrical nanotubes, although they displayed some surface defects and breaks over the outer edges of the tube to a lower degree than the larger polygonal prismatic samples. The angles at which the edge sites intersect on both the cylindrical and prismatic nanotubes suggest that it is the (110) plane that would be 'visible' for additional reactions on the external surface, as opposed to the (100) single plane often depicted. The estimation of an additional 10% of adsorption sites on the external surfaces of the polygonal prismatic halloysites was made. These steps and edges will have a substantial effect on the external surface chemistry of the halloysites and, hence, facilitate additional adsorption reactions at these sites. This work was further explored in Chapter 5 with the use of gold nano-tagging.

All three advanced microscopy methods highlighted the contrast in size of the nanotubes, where the polygonal prismatic nanotubes were significantly larger and also displayed a large variability in their size. Despite the large range in total diameters, both cylindrical and polygonal prismatic nanotubes showed an average inner lumen diameter of around 12 nm, suggesting a common origin of the two morphologies. In several of the cross-section TEM images of the polygonal prismatic halloysites it appears that the layer packets switch from cylindrical to tubular at a certain point of growth, seen here to be around 12 layers or at diameters of 33.9 ± 7.0 nm. These results strengthen the arguments made by Hillier *et al.* (2016) that the continued growth of cylindrical halloysites results in the polygonal prismatic morphology.

The regular appearance of pores and slits in the prismatic nanotubes along with their preference to grow as irregular 5-sided polyhedrons was noted in the cross-sectional TEM analysis. Further TEM work is planned to understand more about the potential for morphological changes between tubular halloysite (10 Å) and halloysite (7 Å). This work plans to use a sealed vessel which would maintain the halloysite samples in their hydrated state for TEM then allow dehydration of the samples and observation

of any changes. It is hoped that this work will enable verification of the XRPD data that the polygonal prismatic morphology occurs in the halloysite (10 Å) state, rather than just upon dehydration. Additionally, the work will examine whether the presence of slits and pores are observed in the prismatic halloysite (10 Å) samples. *In situ* electron diffraction imaging will be employed to verify the state of hydration of the samples.

4.6 REFERENCES

Baronnet, A., Mellini, M. & Devouard, B. (1994) Sectors in polygonal serpentine. A model based on dislocations. *Physics and Chemistry of Minerals*, **21**, 330-343.

Berthonneau, J., Grauby, O., Jeannin, C., Chaudanson, D., Joussein, E. & Baronnet, A. (2015) Native morphology of hydrated spheroidal halloysite observed by environmental transmission electron microscopy. *Clays and Clay Minerals*, **63**, 368-377.

Brady, P.V., Cygan, R.T. & Nagy, K.L. (1996) Molecular controls on kaolinite surface charge. *Journal of Colloid and Interface Science*, **183**, 356-364.

Brindley, G.W. & Comer, J.J. (1955) The structure and morphology of a kaolin clay from Les Eyzies (France). *Clays and Clay Minerals*, **4**, 61-66.

Churchman, G.J., Davy, T.J., Aylmore, L.A.G., Gilkes, R.J. & Self, P.G. (1995) Characteristics of fine pores in some halloysites. Pp. 89. *Clay Minerals*, 30.

Cressey, B.A., & Zussman, J. (1976) Electron microscopic studies of serpentines. *Canadian Mineralogist*, ***14**, 307-313.*

Dixon, J.B. & McKee, T.R. (1974) Internal and external morphology of tubular and spheroidal halloysite particles. *Clays and Clay Minerals*, **22**, 127-137.

Drits, V.A., Sakharov, B.A. & Hillier, S. (2018) Phase and structural features of tubular halloysite (7 å). *Clay Minerals*, **53**, 691-720.

Flegmann, A.W., Love, G. & Scott, V.D. (1971) Electron-optical study of the prism surfaces of kaolinite microcrystals. *Clay Minerals*, **9**, 245-249.

Guthrie, G.D. & Veblen, D.R. (1989) High-resolution transmission electron microscopy of mixed-layer illite/smectite: Computer simulations. *Clays and Clay Minerals*, **37**, 1-11.

Hillier, S., Brydson, R., Delbos, E., Fraser, T., Gray, N., Pendlowski, H., Phillips, I., Robertson, J. & Wilson, I. (2016) Correlations among the mineralogical and physical properties of halloysite nanotubes (HNTs). *Clay Minerals*, **51**, 325-350.

Hooshiar, A., Uhlík, P., Kaminsky, H.W., Shinbine, A., Omotoso, O., Liu, Q., Ivey, D.G. & Etsell, T.H. (2010) High resolution transmission electron microscopy study of clay mineral particles from streams of simulated water based bitumen extraction of athabasca oil sands. *Applied Clay Science*, **48**, 466-474.

Kim, T., Kim, S., Lee, D.K., Seo, B. & Lim, C.-S. (2017) Surface treatment of halloysite nanotubes with sol–gel reaction for the preparation of epoxy composites. *RSC Advances*, **7**, 47636-47642.

Kogure, T., Mori, K., Drits, V.A. & Takai, Y. (2013) Structure of prismatic halloysite. *American Mineralogist*, **98**, 1008-1016.
Kogure, T., Mori, K., Kimura, Y. & Takai, Y. (2011) Unraveling the stacking structure in tubular halloysite using a new tem with computer-assisted minimal-dose system. *American Mineralogist*, **96**, 1776-1780.
Kohyama, N., Fukushima, K. & Fukami, A. (1978) Observation of the hydrated form of tubular halloysite by an electron microscope equipped with an environmental cell. *Clays and Clay Minerals*, **26**, 25-40.
Lvov, Y., Wang, W., Zhang, L. & Fakhrullin, R. (2016) Halloysite clay nanotubes for loading and sustained release of functional compounds. *Advanced Materials*, **28**, 1227-1250.
Massaro, M., Lazzara, G., Milioto, S., Noto, R. & Riela, S. (2017) Covalently modified halloysite clay nanotubes: Synthesis, properties, biological and medical applications. *Journal of Materials Chemistry B*, **5**, 2867-2882.
Middleton, A.P. & Whittaker, E.J.W. (1976) The structure of povlen-type chrysotile. *The Canadian Mineralogist*, **14**, 301-306.
Pasbakhsh, P., Churchman, G.J. & Keeling, J.L. (2013) Characterisation of properties of various halloysites relevant to their use as nanotubes and microfibre fillers. *Applied Clay Science*, **74**, 47-57.
Pouvreau, M., Greathouse, J.A., Cygan, R.T., Kalinichev, A.G. (2019) Structure of hydrated kaolinite edge surfaces: DFT results and further development of the ClayFF Classical Force Field with Metal-O-H angle bending terms. *Journal of Physical Chemistry C*, **123**, 11628-11638.
Schneider, C.A., Rasband, W.S. & Eliceiri, K.W. (2012) Nih image to imagej: 25 years of image analysis. *Nature Methods*, **9**, 671-675.
Siretanu, I., van den Ende, D. & Mugele, F. (2016) Atomic structure and surface defects at mineral-water interfaces probed by in situ atomic force microscopy. *Nanoscale*, **8**, 8220-8227.
Yada, K & Lui, W. (1987) Polygonal microstructures of Polven chrysotile observed by high resolution electron microscopy. Sixth Meet. Europ. Clay. Group (Seville, Spain), 596-597.
Yuan, P., Southon, P.D., Liu, Z., Green, M.E.R., Hook, J.M., Antill, S.J. & Kepert, C.J. (2008) Functionalization of halloysite clay nanotubes by grafting with γ-aminopropyltriethoxysilane. *The Journal of Physical Chemistry C*, **112**, 15742-15751.
Yuan, P., Tan, D. & Annabi-Bergaya, F. (2015) Properties and applications of halloysite nanotubes: Recent research advances and future prospects. *Applied Clay Science*, **112-113**, 75-93.
Zbik, M. & Smart, R.S.C. (1998) Nanomorphology of kaolinites: Comparative SEM and AFM studies. *Clays and Clay Minerals*, **46**, 153-160.
Zhang, S., Liu, Q., Gao, F., Li, X., Liu, C., Li, H., Boyd, S.A., Johnston, C.T. & Teppen, B.J. (2017) Mechanism associated with kaolinite intercalation with urea: Combination of infrared spectroscopy and molecular dynamics simulation studies. *The Journal of Physical Chemistry C*, **121**, 402-409.

Chapter 5

Gold Nanoparticle Decoration of the Halloysite Surfaces

5.1 INTRODUCTION

Nanoparticles can be defined as between 1-100 nm in size (2011/696/EU) and the area of nanoscience is one that has rapidly expanded in recent years. For example, it has been shown for metals that the formation of nanoparticles can drastically change the physical and chemical properties due to their large surface-to-volume ratio (Zhang *et al*., 2016), hence opening up a range of new and available technologies and uses for these materials. Gold and silver nanoparticles are currently used in a myriad of nanotechnologies as antibacterial (Burridge *et al.,* 2010; Jana *et al*., 2017), antiviral and anti-inflammatory agents (Zhang *et al*., 2016), as well as in catalytic reactions (Mallick *et al*., 2006), as optical devices (Qu *et al*., 2002; Rao *et al*., 2019) and electrochemical sensing applications (Cao *et al*., 2012), amongst many others. Whilst nanoparticles such as gold nanoparticles are hailed as having high thermal stability and efficient catalytic behaviours (Massaro *et al*., 2018), they often display a tendency to agglomerate into clusters when attractive forces exist between the surfaces of the nanoparticles, which lowers their potential catalytic activity. A commonly used method to overcome this is to apply the nanoparticles to stable support materials, such as zeolites, fullerenes and carbon nanotubes, etc., and more recently to halloysite nanotubes (Burridge *et al*., 2010; Jana *et al*., 2017; Massaro *et al*., 2018). The use of these stable supports can also aid in lowering the loading of the expensive metals without reducing their efficacy whilst potentially introducing secondary interactions which can further improve the activity.

The interest in this rapidly developing field has resulted in a variety of synthesis routes for metal nanoparticles, where, like the properties of quantum dots, the functionalities of the metal nanoparticles can be adapted by tailoring their size and shape (Wiley *et al.*, 2005). The most common method of metal nanoparticle synthesis is the chemical reduction of metal salts (Pillai *et al*., 2003) to their respective metal atoms which nucleate into nanoparticles. These nanoparticles can then be attached to the substrate surface via pre-adsorbed linkers (Burridge *et al*., 2010; Jana *et al*., 2017., Massaro *et*

al., 2018). Other methods such as layer-by-layer depositions have also been reported (Burridge *et al*., 2010) and stabilisers such as organic molecules and polymers can be used to control the growth and prevent agglomeration of the nanoparticles (Pillai *et al*., 2004). Further work by Vinokurov *et al*. (2017) used halloysites as a template for Ru clusters by modifying the halloysites with furfuraldehyde based Schiff bases to enable loading of the metal ions in the lumen and interlayers of the halloysites, before using reduction reactions to form metal Ru clusters.

Halloysites can be considered as potential support materials, especially for biomedical purposes, due to their low toxicity (Vergaro *et al.,* 2010; dos Santos *et al*., 2017) and relative low cost (Lvov *et al.,* 2016). An additional benefit often touted for the use of halloysite nanotubes has been the two different surfaces available for reaction, i.e., the inner positively charged alumina surface and outer negatively charged siloxane surface, where these distinct surfaces are viewed as beneficial to allow for selective functionalisation (Yuan *et al.,* 2015; Kim *et al*., 2017; Massaro *et al*., 2018). The simplistic model of halloysite nanotubes has been discussed in detail throughout this thesis and, whilst the surfaces do indeed have different functionalities, the results presented in Chapters 3 and 4 highlighted the variations in behaviour and external surface features between different morphologies of tubular halloysites.

Several of the previously reported publications for halloysites as stable supports, attached the metal nanoparticles to the surface of the halloysite using pre-adsorbed linker chain molecules (Burridge *et al*., 2010; Jana *et al*., 2017; Massaro *et al*., 2018). Imaging techniques such as transmission electron microscopy (TEM) and scanning electron microscopy (SEM) were then used to show that the metal nanoparticles adhered to the halloysite nanotubes, the theory being that these nanoparticles were attached to the surface via the linker chain molecules (Burridge *et al*., 2010; Cao *et al*., 2012; Jana *et al*., 2017).

In contrast, the work outlined in this chapter first synthesised the metal nanoparticles which were then reacted with the linker chain molecules before mixing with the halloysite nanotubes. The work undertaken in this chapter used a selection of linker molecules with different chemical moieties at their terminus to study the surface site functionalisation of the halloysite nanotubes by high resolution imaging techniques. Three linker molecules were used where each one was selected for their different

functional groups: phosphonic acid, carboxylic acid and a methyl group. Phosphonic acids contain the R-CPO$(OH)_2$ functional group and have previously been reported to covalently adsorb to the inner lumen of halloysites via an Al-O-P mechanism (Taroni *et al*., 2019), where it was suggested that the adsorption may be via bi and tridentate binding modes. The carboxylate terminated linker (R-COOH) has been proposed as adsorbing to the surface of the halloysite nanotubes via hydrogen bonding with the hydroxyls and oxygen atoms on the Si-O-Si external surface, where the hydrogen bonding also improves dispersion of the nanotubes (Du *et al*., 2008) although an ester linkage should also be considered. In comparison, the methyl group (CH_3) has not yet been shown to have an affinity for the surface of halloysite.

The aim of these experiments was firstly to determine whether it is possible to tag the two different halloysite morphologies with gold and silver nanoparticles (hereafter referred to as nanotags), where previous studies using halloysite nanotubes have not investigated the effect of tubular morphology with metal nano-tagging. A secondary aim was to determine if imaging techniques, such as TEM, can be used to study the nanotag adsorption on the surfaces of halloysite and specify where this adsorption might be taking place. Finally, the influence of the linker molecules with different functional groups was investigated to determine whether this affects the type of adsorption onto the halloysite surfaces. This is a route that, as yet, has not been explored when using halloysites as stable support materials.

5.2 EXPERIMENTAL OUTLINE

Two separate experiments were run over two separate time periods, as outlined in Table 5.1, using the same set of the halloysites used throughout this thesis whose physical characteristics are detailed in Chapter 2 (Table 2.1). The first exploratory experiments (Experimental Set 1) focused on using gold nanotags of one size with two different 12-carbon chain linkers, one terminated with phosphonic acid ($C_{12}H_{27}O_3PS$), the other with methyl ($C_{12}H_{26}S$), for halloysites 4Ch (cylindrical) and 17US (polygonal prismatic), to determine the location of the functional sites on the halloysite surfaces. In addition, two further samples, one of each halloysite, were prepared by reaction with excess phenyl phosphonic acid, as this has been used in previous adsorption studies with halloysites (Breen *et al*., 2002). The success of the adsorption

of the gold nanotags onto the surfaces of the halloysite nanotubes was determined through the use of techniques such as X-ray photoelectron spectroscopy (XPS), Fourier transform infrared (FTIR), scanning thermal analysis (STA), optical microscopy and transmission electron microscopy (TEM).

It can be expected that successful reaction would occur via the phosphonic acid terminated group and the hydroxyl surface sites of the halloysites via a condensation reaction, resulting in an ester link, as shown below:

$\equiv Al\text{-}OH + R\text{-}PO(OH)_2 \leftrightarrow \equiv Al\text{-}O\text{-}PO(OH)\text{-}R + H_2O$

Once it was established that the mechanism and experiments from Experimental Set 1 were successful a second experiment was designed, and the parameters expanded. The second set of experiments (Experimental Set 2) used a wider range of six halloysites of both tubular morphologies; 4Ch, 17US, 5Ch, 6Ch, 23US and 24US with two distinct anionic linkers, one phosphonic acid terminated and one carboxylate anion terminated, and either gold or silver nanotags of varying size. The silver nanotag diameters were estimated at between 5-10 nm and the gold nanotag diameters were estimated at around 0.9 nm and 3.3 nm. The overall aim of the second set of experiments was to verify whether broadening the range of halloysites across the two tubular morphologies and varying the size and type of metal nanotag would have any effect on the functionalisation of the halloysite nanotubes as observed by multiple analysis including FTIR, XRPD, XPS and TEM analysis.

The three different types of linker used across both experimental sets were dodecanthiol (thiol), 12-mercaptododecylphosphonic acid (phosphonic acid) and 11-mercaptoudodecanoic acid (carboxylate) as shown in Figure 5.1 and outlined in Table 5.1. All three linkers contain a thiol functional group which has a strong affinity for gold and silver nanoparticles through the formation of metal-sulphur bonds (Wiley *et al*., 2005).

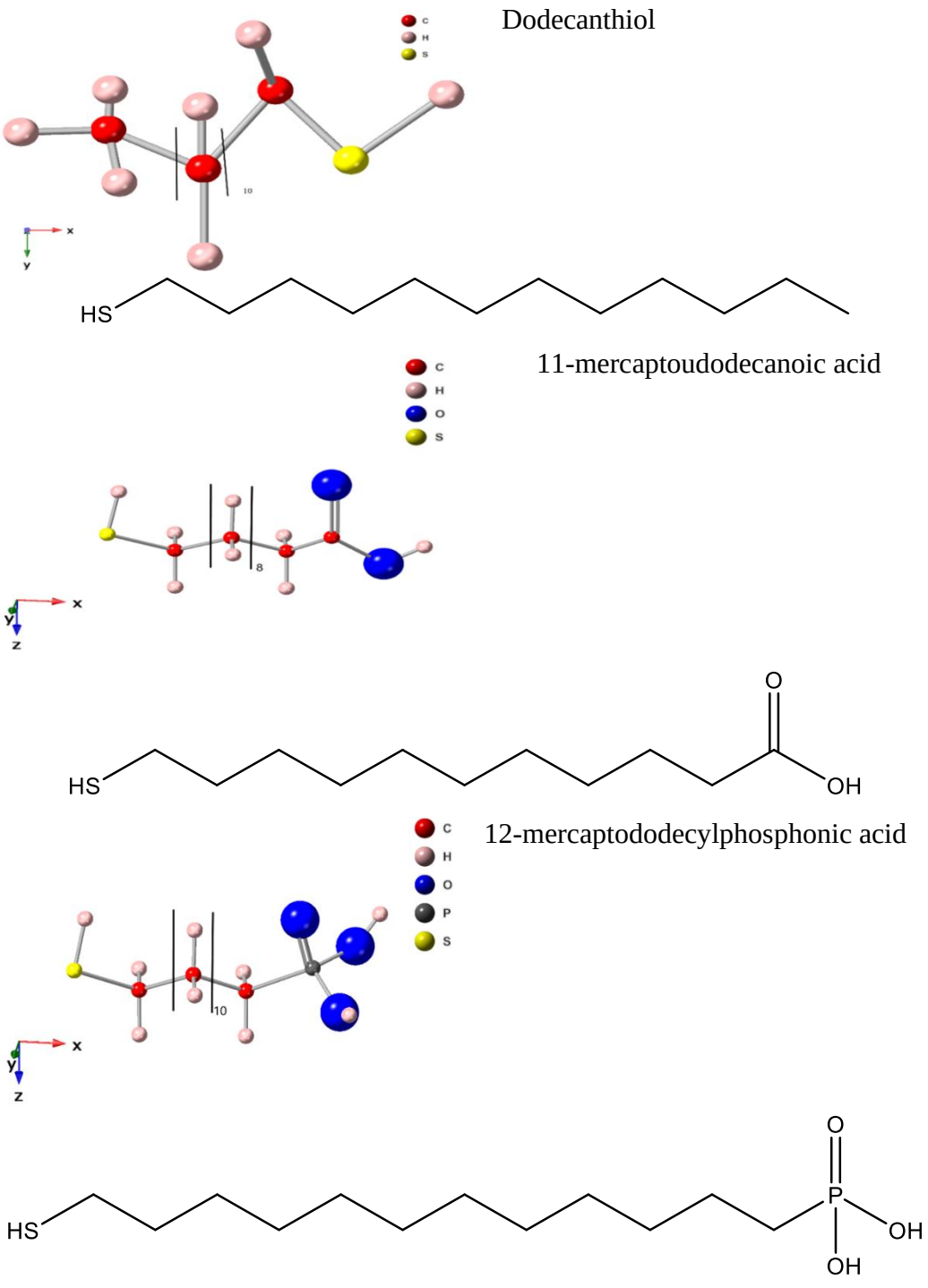

Figure 5.1. Chemical structures of the three linkers used throughout the experiments shown as the simplified chemical structure and as ball and stick chemical diagrams where the parallel lines followed by a number, n, denotes the number of CH_2 units.

Table 5.1. Experimental outlines for Experimental Sets 1 and 2.

Experimental Set 1				
Halloysite ID	Hydration State	Functional group at terminus of linker	Nanotag	Nanotag size (approx. nm)
4Ch	Dehydrated	Methyl	Au	1-2
4Ch	Dehydrated	Phosphonic acid	Au	1-2
17US	Dehydrated	Methyl	Au	1-2
17US	Dehydrated	Phosphonic acid	Au	1-2
4Ch	Dehydrated	Phenyl phosphonic acid	-	-
17US	Dehydrated	Phenyl phosphonic acid	-	-
Experimental Set 2				
23US	Dehydrated	Carboxylate	Au	0.9
23US	Dehydrated	Carboxylate	Au	3.3
23US	Dehydrated	Carboxylate	Ag	5-10
23US	Dehydrated	Phosphonic acid	Au	0.9
23US	Dehydrated	Phosphonic acid	Au	3.3
23US	Dehydrated	Phosphonic acid	Ag	5-10
5Ch	Hydrated	Carboxylate	Au	0.9
5Ch	Hydrated	Carboxylate	Au	3.3
5Ch	Hydrated	Carboxylate	Ag	5-10
5Ch	Hydrated	Phosphonic acid	Au	0.9
5Ch	Hydrated	Phosphonic acid	Au	3.3
5Ch	Hydrated	Phosphonic acid	Ag	5-10
6Ch	Hydrated	Carboxylate	Au	0.9
6Ch	Hydrated	Carboxylate	Au	3.3
6Ch	Hydrated	Carboxylate	Ag	5-10
6Ch	Hydrated	Phosphonic acid	Au	0.9
6Ch	Hydrated	Phosphonic acid	Au	3.3
6Ch	Hydrated	Phosphonic acid	Ag	5-10
24US	Hydrated	Carboxylate	Au	0.9
24US	Hydrated	Carboxylate	Au	3.3
24US	Hydrated	Carboxylate	Ag	5-10
24US	Hydrated	Phosphonic acid	Au	0.9
24US	Hydrated	Phosphonic acid	Au	3.3
24US	Hydrated	Phosphonic acid	Ag	5-10
4Ch	Dehydrated	Carboxylate	Au	0.9
4Ch	Dehydrated	Carboxylate	Au	3.3
4Ch	Dehydrated	Carboxylate	Ag	5-10
4Ch	Dehydrated	Phosphonic acid	Au	0.9
4Ch	Dehydrated	Phosphonic acid	Au	3.3
4Ch	Dehydrated	Phosphonic acid	Ag	5-10
17US	Dehydrated	Carboxylate	Au	0.9
17US	Dehydrated	Carboxylate	Au	3.3
17US	Dehydrated	Carboxylate	Ag	5-10
17US	Dehydrated	Phosphonic acid	Au	0.9
17US	Dehydrated	Phosphonic acid	Au	3.3
17US	Dehydrated	Phosphonic acid	Ag	5-10

5.3 METHODS

5.3.1 Experimental Method: Set 1

Two halloysite samples, 4Ch and 17US, were gold nanoparticle tagged following the gold nanotag synthesis method outlined by Li *et al*. (2012). Two separate routes were undertaken for the gold nano-tagging (Figure 5.2). The first method involved reacting a thiol group linker with the gold nanoparticle with a methyl terminated 12-carbon chain (dodecanthiol, $C_{12}H_{26}S$). The second method involved reacting a thiol group linker to the gold nanoparticle with a phosphonic acid terminated 12-carbon chain (12-mercaptododecyl phosphonic acid, $C_{12}H_{27}O_3PS$). The initial steps for both routes were the same: 0.375 moles of $AuClPPh_3$ was added to a two-necked round bottom flask to which 21 ml of ethanol was added under rapid stirring. A reducing agent, tert-butylamine-borane (TBAB, 0.3263 g; 3.75 mol), was added to the mix and the samples stirred. After 30 minutes, 0.2 mol of the required linker, dodecanthiol or 12-mercaptododecylphosphonic acid, was added via syringe. Aliquots of each of these gold nano-tagged linkers were mixed with around 100 mg of the halloysite samples. The reaction was conducted at room temperature and atmosphere.

The time between adding tert-butylamine-borane and the linker was an essential step for controlling the size of the gold nanoparticle. In this instance the time was 30 minutes, which resulted in gold nanoparticles of around 1-2 nm in size as confirmed by UV-Vis spectroscopy. The size of the nanotags was measured on a Perkin Elmer Lambda 35 UV/Vis spectrometer with a scan range of 250-700 nm and after heating the UV lamps for 15 minutes.

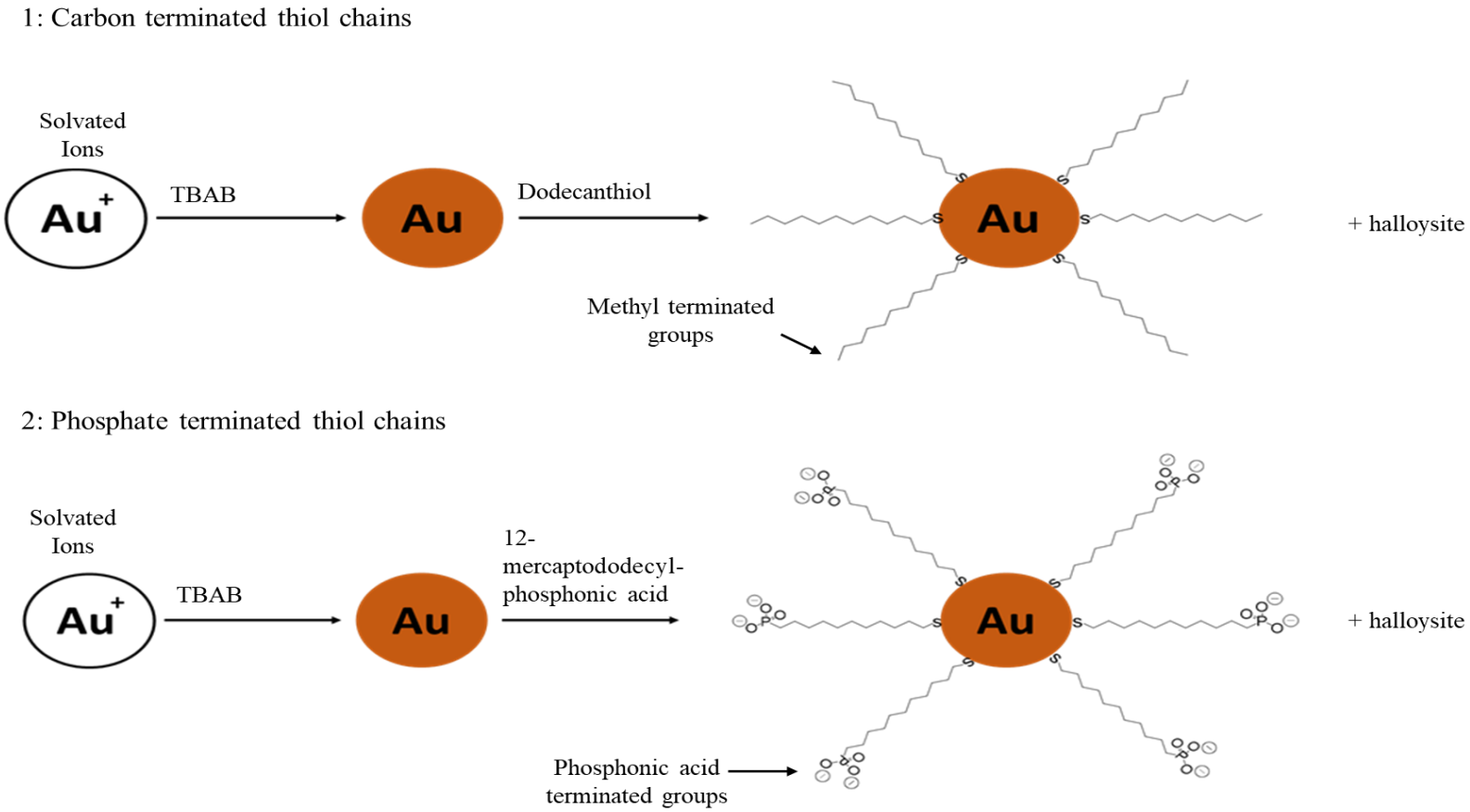

Figure 5.2. Schematic for Experimental Set 1 showing the two experimental set ups. The first uses the linker molecule dodecanthiol to obtain methyl terminated groups attached to the gold nanoparticle; the second uses 12-mercaptododecylphosphonic acid to obtain phosphonic acid terminated groups on the gold nanotag.

The gold nano-tagged samples were analysed using X-ray photoelectron spectroscopy (XPS), thermogravimetric analysis (TGA), Fourier transform infrared spectroscopy (FTIR), optical microscopy and transmission electron microscopy (TEM).

5.3.2 Experimental Method: Set 2

For the synthesis of the silver nanotags, polyvinylpyrrolidone (PVP, 8.61 g, 3.44 mol) and dimethylformamide (DMF, 200 ml) were mixed together in a round bottomed flask flask. To this, 2.5 g (0.015 mol) $AgNO_3$ was added and samples were heated under reflux in an oil bath at 90 °C for 6 hours until the solution turned a deep yellow.

1 ml of the yellow solution was pipetted into an Eppendorf centrifuge tube and to this 0.2 ml of acetone was added. The samples were centrifuged for 30 seconds, the supernatant was decanted away and replaced with 1 ml of ethanol. The suspension was then hand shaken. Two separate round bottomed flasks were set up. To each flask, the solution from 20 Eppendorf tubes containing the yellow ethanolic suspension were added. The Eppendorf tubes were lightly rinsed with ethanol to remove all of the suspension and the solution in the round bottom flask was diluted by a further 20 ml of ethanol. Linkers were then added to each flask as follows. Flask one contained the phosphonic acid linker, 12-mercaptododecylphosphonic acid (0.0303 g; 1.07 mmol, $C_{12}H_{27}O_3PS$), and flask two contained the carboxylate linker, 11-mercaptoundecanoic acid (0.0227 g; 1.04 mmol, $C_{11}H_{22}O_2S$). Flasks one and two were left stirring for 15 minutes before being stoppered until they were ready to add to the halloysite.

Two separate syntheses were carried out for the gold nanotags to obtain their two sizes as will be discussed later on in this chapter (Section 5.5). The preparation routes were identical except for one condition; the larger nanotags were left stirring for 36 hours whilst the smaller nanotags were given 30 minutes reaction time.

The source of gold, chloro(triphenylphosphine)gold(I) ($AuClPPH_3$, 0.1864 g; 0.377 mmol), was mixed with 21 ml ethanol and stirred rapidly in a round bottom flask. To this borane tert-butyl amine (TBAB, 0.3263 g; 3.75 mmol) was added and an immediate colour change to yellow was noted (Figure 5.3). The solution was stirred for either 36 hours or 30 minutes after which the necks were stoppered. Each solution was diluted with 21 ml of ethanol and split equally between two flasks, resulting in 2 flasks containing large gold nanotags and 2 flasks containing small gold nanotags. To one flask of each size of nanotag, 12-mercaptododecylphosphoric acid (0.0303 g; 1.07

mmol) was added whilst to the remaining 2 flasks, one of each gold nanotag size, was added 11-mercaptoundecanoic acid (0.0224 g; 1.04 mmol). The four flasks were stirred for 15 minutes, transferred to sample vials and stoppered until ready for addition to the halloysites.

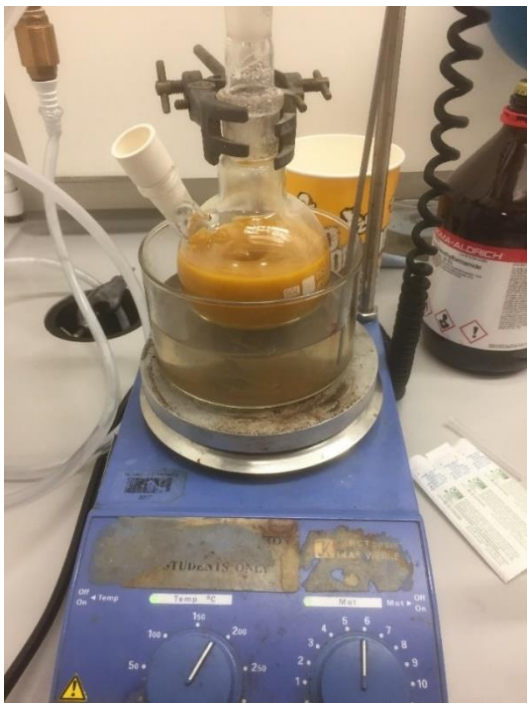

Figure 5.3: Gold nanotag synthesis where the flask contains 12-mercaptododecylphosphonic acid, chloro(triphenylphosphine)gold(I) and borane tert-butyl amine in an ethanol solution.

The nanotag synthesis routes described above resulted in six different solutions where small Au nanotag refers to an assumed small gold nanotag linker and the large Au nanotag refers to an assumed larger gold nanotag linker based on the reaction times allowed for each one respectively:

Solution 1: Small Au nanotag with carboxylate terminated linker

Solution 2: Large Au nanotag with carboxylate terminated linker

Solution 3: Ag nanotag with carboxylate terminated linker

Solution 4: Small Au nanotag with phosphonic acid terminated linker

Solution 5: Large Au nanotag with phosphonic acid terminated linker

Solution 6: Ag nanotag with phosphonic acid terminated linker

Each of these solutions was then mixed with each of the six different halloysites as outlined in Table 5.1. For the dehydrated (7 Å) halloysites, 100 mg of each was weighed out and mixed with 3 ml of Solution 1-6 above along with 3 ml ethanol. For the hydrated (10 Å) halloysites, 2 ml of suspsended halloysite in water was mixed with 3 ml of Solution 1-6 above along with 3 ml ethanol. This resulted in a total of 36 samples. Each sample was sonicated in a sonic bath at room temperature for 10 minutes and left to settle overnight. The following day the samples were sonicated for a further 10 minutes and centrifuged. Initially, the first few samples were filtered through Whatmann® 55 mm filters but this proved extremely time consuming and so the samples were centrifuged. All samples were then dried under vacuum ready for futher analysis.

Due to the large number of samples prepared, only selected samples from the second experimental set were analysed by XPS and XRPD and a select few were awaiting analysis by TEM when this thesis was submitted, where the samples were selected to represent the three different nanotags, one silver and two gold of different sizes and the two morphologies of halloysite. All samples were analysed by FTIR as described below.

5.3.3 X-ray photoelectron spectroscopy (XPS)

XPS was used to verify the surface elemental composition of the samples and to determine whether adsorption of the linker and nanotage was successful. XPS analysis was conducted on a KRATOS AXIS SUPRA using a monochromated Al K_α source. The samples were loaded as powders onto carbon strips which were evacuated in the instrument before analysis. The beam footprint was 700 µm on the x-axis and 300 µm on the y-axis. Long scans of 8 seconds per count were conducted for the phosphorus peak since the levels were determined as close to the limit of detection. Data was recorded using a charge neutraliser to limit differential charging and elemental binding energies were calibrated to the main hydrocarbon peak at 284.8 eV.

The following peaks were analysed: C 1s, Al 2p, Si 2p, O 1s, P 2p, Na 1s, Ag 3d and Au 4f. The results are calculated using the programme CASAXPS© programme.

5.3.4 Scanning thermal analysis (STA): thermogravimetric analysis (TGA) and differential scanning calorimetry (DSC)

Scanning thermal analysis (STA) was used to determine whether the transition loss features could be correlated with groups adsorbed onto the surface. STA was conducted on a Perkin-Elmer STA 6000 which had been calibrated to the melting points of indium and silver. An air gas flat rate of 19.8 ml/min was used for a continuous run from 30-600 °C with ramps of 10 °C/min.

5.3.5 Transmission electron microscopy (TEM)

To visually observe the gold nanotags on the halloysite nanotubes TEM analysis was conducted on a FEI: Titan Themis instrument at Leeds University for both the pure halloysite samples and the gold nano-tagged samples. The samples were prepared by dispersion in methanol before being dropped onto a 3 mm copper grid mounted onto an amorphous carbon film. Due to the sensitivity of halloysite nanotubes to the electron beam and to avoid amorphitisation of the tubes, the beam strength was kept at around 0.5 nA. The TEM was operated at 300 kV and was fitted with a monochromator which allowed control over the electron dose during imaging. Energy dispersive spectroscopy (EDS) analysis was carried out on some of the gold nano-tagged samples to confirm that the observed features were the nanoparticles. EDS data was collected using the Super-X EDX system with 4 windowless design and then processed using Velox. The TEM images were collected on a Gatan Oneview 16-megapixel CMOS digital camera. In addition, *in situ* selected area electron diffraction patterns (SAEDP) were conducted to observe the hydration state and layer ordering of the nanotubes.

5.3.6 Fourier transform infrared spectroscopy (FTIR)

In order to identify if the metal nanotags and linkers were present in the samples after adsorption FTIR analysis was conducted on the vacuum dried samples. Infrared spectra were measured on a Bruker Vertex 70 Fourier Transform Infrared (ATR-FTIR) spectrometer in the mid-infrared region from 4000 to 400 cm^{-1} with a scan rate of 200 scans per spectra. During analysis the FTIR spectrometer was dry-air purged to prevent interference in the spectra from water vapour and carbon dioxide.

5.3.7 Optical Microscopy

A further visual comparison of the samples after reaction between the nanotags and halloysite nanotubes used optical microscopy on the four samples from Experimental Set 1. A KEYENCE VHX Digital Microscopy Lens Z20:X50 was used. By using a narrow focus on the agglomerated halloysite nanotube clusters combined with the stepped microscope sample stage, it was possible to obtain high quality colour images by optical microscopy.

5.3.8 X-ray powder diffraction

XRD was also used as an analytical tool to identify whether the nanotages were observed in the spectra after adsorption. Six samples were run on a Panalytical X-pert Pro diffractometer as hand ground powders from 3-80 °2θ with a step size of 0.017 °2θ and the total time per step at 99.69 seconds. Each scan took just over one hour. Due to the low sample mass, it was not possible to prepare the samples by spray drying. Instead, they were lightly hand ground and dispersed onto a silica holder by gentle tapping of a suspended paintbrush which had been dipped into the powder. The six samples were chosen to compare a cylindrical and polygonal prismatic sample set with both gold and silver nanotags, where the cylindrical sample (6Ch) was initially in the halloysite (10 Å) form whilst the polygonal prismatic sample (23US) was in the halloysite (7 Å) form.

5.4 RESULTS

5.4.1 X-ray photoelectron spectroscopy (XPS) results

XPS analysis was conducted on the samples from Experimental Set 1 and selected samples from Experimental Set 2 (Tables 5.2 and 5.3). In order to more accurately compare the two sets of XPS data (Tables 5.2 and 5.3) the data was normalised for the removal of carbon which is present as an impurity. The normalised results are presented in Tables 5.4 and 5.5.

Both gold and silver were detected by XPS as shown in the data from Experimental Set 2 (Table 5.5). This infers that the use of both phosphonic acid and carboxylate

terminated linkers resulted in the presence of metal nanotags on the surface of the halloysites.

In addition, for quality control, some of the samples from Chapter 3 of phosphate adsorbed onto 4Ch and 17US were included in the analysis. Some issues arose during the XPS analysis, primarily that the intensity of the phosphorus peaks was of the order of 0.06 - 0.1%, which is around the level of detection for this technique. It was observed for Experimental Set 1 that the phosphorus appeared to be in two separate chemical environments, M-phosphonic acid and a less oxidised phosphorus, which matched either a metal coordinated PR3 organic species or a phosphonic acid that had reacted, oxidised and then formed a new bond. The samples with methyl terminated linkers showed very low gold levels (0.02, 0.07%) whilst the phosphonic acid terminated linkers had higher amounts of gold present (ca. 1.3%).

Table 5.2. XPS results from Experimental Set 1.

Sample ID	Aluminium 2p %	Gold 4f %	Carbon 1s %	Sodium 1s %	Oxygen 1s %	Oxygen -organic 1s %	Phosphorus - M-phosphonic acid 2p %	Phosphorus - PX3 organic? 2p %	Sulphur - thiol-Au 2s %	Silicon - SiO_4 – 2p %	Total
17US Control	9.3	0.0	34.8	0.4	38.6	6.5	0.0	0.0	0.0	10.4	100
17US + P-PO_4	14.3	0.0	5.6	0.8	60.4	3.0	0.1	0.0	0.0	15.8	100
17US + P-PO_4 (repeat)	14.8	0.0	5.7	0.5	59.7	3.1	0.1	0.0	0.0	16.1	100
4Ch Control	14.3	0.0	5.6	0.4	57.9	6.7	0.0	0.0	0.0	15.2	100
4Ch + P-PO_4	15.8	0.0	6.0	0.8	57.9	2.7	0.1	0.0	0.0	16.7	100
4Ch + P-PO_4 (repeat)	14.9	0.0	6.1	1.0	59.5	2.6	0.1	0.0	0.0	15.8	100
4Ch + Au-methyl	16.0	0.0	6.5	0.1	57.6	2.6	0.0	0.0	0.0	17.1	100
4Ch + Au-phosphonic acid	13.9	1.0	17.7	0.1	45.9	5.4	0.4	0.3	0.2	15.0	100
17US + Au-methyl	14.6	0.1	6.4	0.0	59.3	3.6	0.0	0.0	0.0	16.0	100
17US + Au-phosphonic acid	10.3	1.1	23.7	0.0	45.2	6.7	0.3	0.6	0.2	11.8	100

Table 5.3. XPS data of selected samples from Experimental Set 2.

Sample ID	Aluminium 2p %	Silver 3d %	Gold 4f %	Carbon 1s %	Iron 2p %	Nitrogen 1s %	Sodium 1s %	Oxygen 1s %	Phosphorus 2p %	Sulphur 2s %	Silicon 2p %	Total
6Ch Hydrated small Au nanotag and carboxylate linker	12.2	-	0.5	15.8	-	0.3	-	57.8	0.1	0.1	13.2	100
6Ch Hydrated Ag nanotag and carboxylate linker	13.0	1.0	-	11.2	0.2	0.6	-	60.0	-	0.4	13.6	100
6Ch Hydrated small Au nanotag and phosphonic acid linker	12.7	-	1.1	16.0	-	-	-	55.6	0.6	0.2	13.7	100
6Ch Hydrated Ag nanotag and phosphonic acid linker	11.1	0.6	-	23.6	0.1	0.6	-	52.1	0.1	0.1	11.7	100
24US Hydrated large Au nanotag and phosphonic acid linker	14.1	-	0.5	9.7	0.0	0.4	-	59.9	0.2	0.2	15.0	100
23US Dehydrated Original Material	14.5	-	-	3.2	0.7	-	0.8	64.8	-	-	15.9	100

Table 5.4. Normalised XPS results from Experimental Set 1.

Sample	Aluminium	Gold	Sodium	Oxygen Mox	Oxygen -organic	Phosphorous - M-phosphate	Phosphorous - PX3 organic?	Sulfur - thiol-Au	Silicon - SiO4	*Total*
17US Control	14.3	0.0	0.6	59.2	10.0	0.0	0.0	0.0	16.0	100
17US + P-PO_4	15.2	0.0	0.8	64.0	3.2	0.1	0.0	0.0	16.7	100
17US + P-PO_4 (repeat)	15.7	0.0	0.5	63.3	3.3	0.1	0.0	0.0	17.1	100
4Ch Control	15.1	0.0	0.4	61.3	7.1	0.0	0.0	0.0	16.1	100
4Ch + P-PO_4	16.8	0.0	0.9	61.6	2.9	0.1	0.0	0.0	17.8	100
4Ch + P-PO_4 (repeat)	15.9	0.0	1.1	63.4	2.8	0.1	0.0	0.0	16.8	100
A – 4Ch + Au-methyl	17.1	0.0	0.1	61.7	2.8	0.0	0.0	0.0	18.3	100
B – 4Ch + Au-phosphonic acid	16.9	1.3	0.1	55.8	6.6	0.5	0.4	0.2	18.2	100
C – 17US + Au-methyl	15.6	0.1	0.0	63.4	3.8	0.0	0.0	0.0	17.1	100
D – 17US + Au-phosphonic acid	13.5	1.4	0.0	59.3	8.8	0.4	0.8	0.3	15.5	100

Table 5.5. Normalised XPS data of selected samples from Experimental Set 2.

Sample ID	Aluminium 2p %	Silver 3d %	Gold 4f %	Iron 2p %	Nitrogen 1s %	Sodium 1s %	Oxygen 1s %	Phosphorus 2p %	Sulfur 2s %	Silicon 2p %	Total
Wanjiar Hydrated small Au nanotag and carboxylate linker	14.5	-	0.6	-	0.3	-	68.7	0.1	0.2	15.7	100
Wanjiar Hydrated Ag nanotag and carboxylate linker	14.7	1.1	-	0.2	0.7	-	67.6	-	0.4	15.3	100
Wanjiar Hydrated small Au nanotag and phosphonic acid linker	15.2	-	1.3	-	-	-	66.2	0.7	0.3	16.3	100
Wanjiar Hydrated Ag nanotag and phosphonic acid linker	14.5	0.7	-	0.2	0.7	-	68.2	0.2	0.2	15.4	100
Hal in water Hydrated large Au nanotag and phosphonic acid linker	15.6	-	0.6	0.0	0.4	-	66.4	0.2	0.2	16.6	100
Fi Face Dehydrated Original Material	15.0	-	-	0.7	-	0.8	67.0	-	-	16.5	100

Labelled spectra of two of the samples from Experimental Set 2 are shown in Figures 5.4 and 5.5 where the gold and silver peaks appear as doublets due to spin orbit splitting.

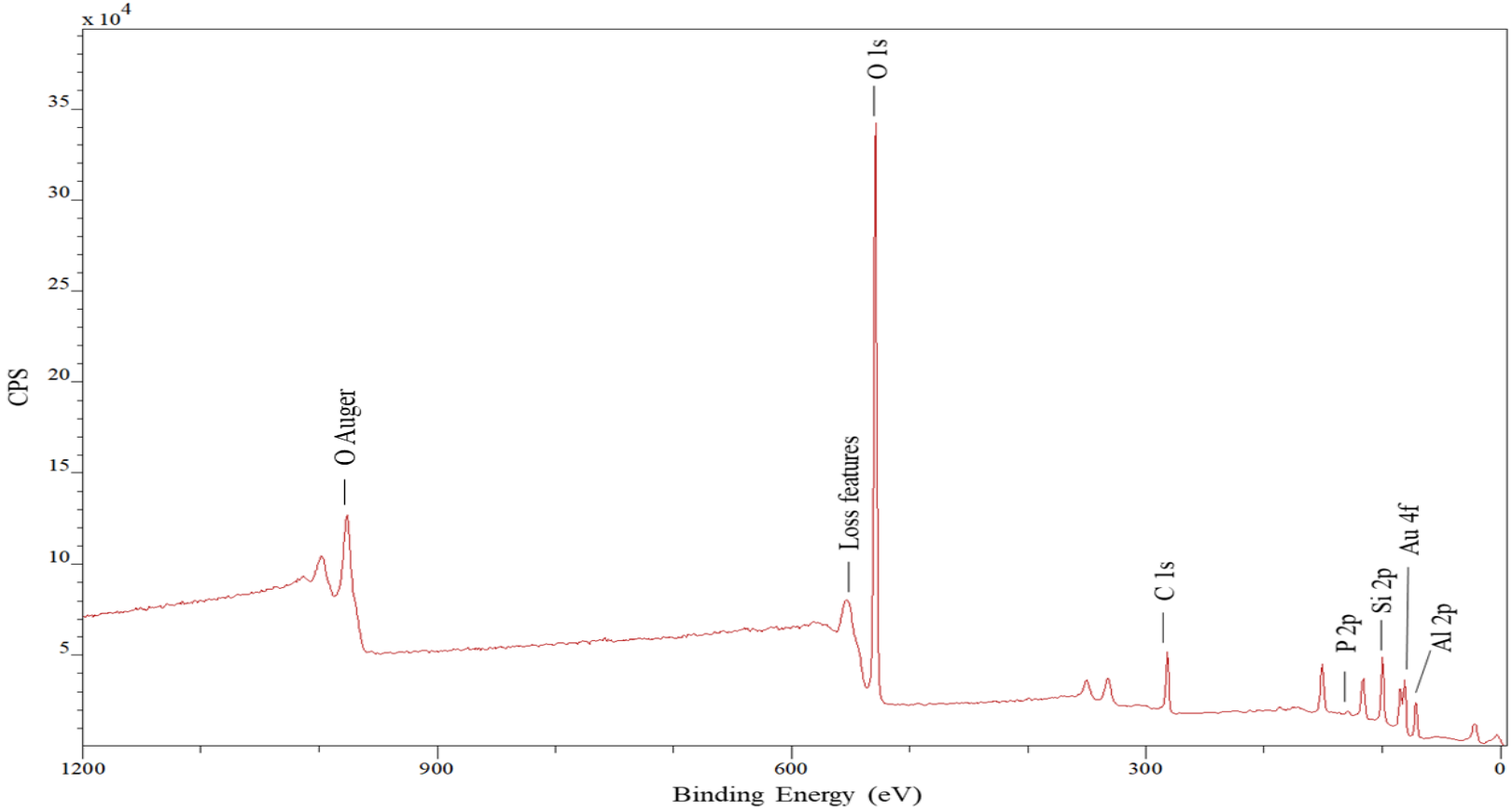

Figure 5.4. XPS spectra of 6Ch halloysite (10 Å) functionalised with small Au nanotag and phosphonic acid terminated linker. The presence of both gold and phosphorus, as well as a higher carbon content than observed in the untreated halloysite samples, indicates that both the silver nanotag and linker are present in the sample.

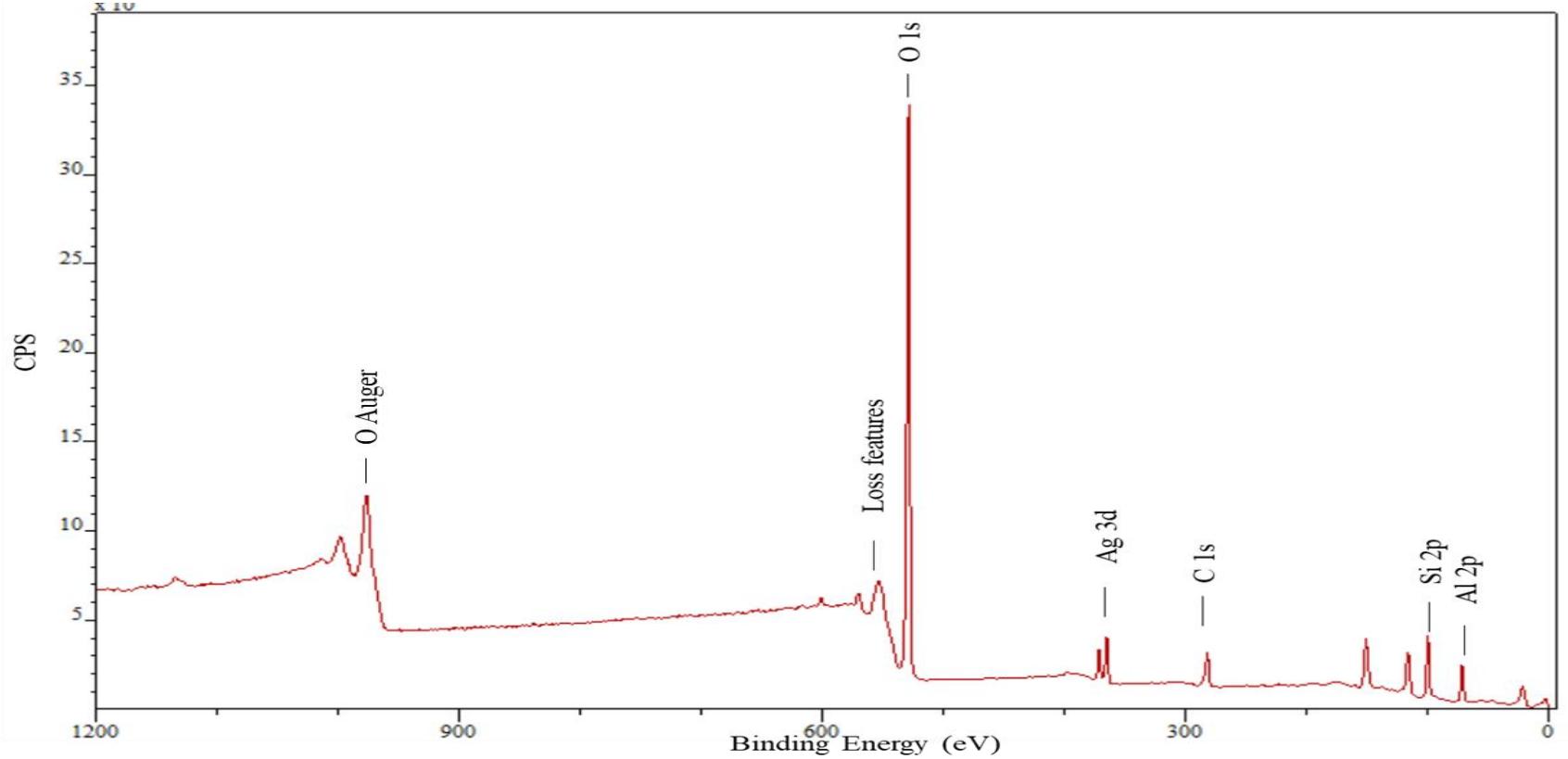

Figure 5.5. XPS spectra of the sample 6Ch halloysite (10 Å) Ag C, where Ag C stands for silver nanotag with carboxylate terminated linker. The presence of both silver and sulphur, as well as a higher carbon content than observed in the untreated halloysite samples, indicates that both the silver nanotag and linker are present in the sample.

5.4.2 Simultaneous thermal analysis (STA) results

Power compensation differential scanning calorimetry (DSC) data (Figures 5.6-5.9) for the samples from Experimental Set 1 show that, for the 4Ch samples with both methyl and phosphonic acid terminated linkers, there are two endothermic peaks observed at temperatures of 250 ℃ and 500 ℃, where the endothermic peaks in this method are pointing upwards. By contrast, for the 17US sample with both methyl and phosphonic acid terminated linkers there is only one observed endothermic peak at 520 ℃.

Thermogravimetric analysis (TGA) shows that, on heating to 600 ℃, the samples lose between 15-18% sample mass. Whilst not included here (see Appendices) first derivatives of the TGA curves result in derivative thermogravimetric curves, DTG, and indicate the transition temperatures of the sample mass loss.

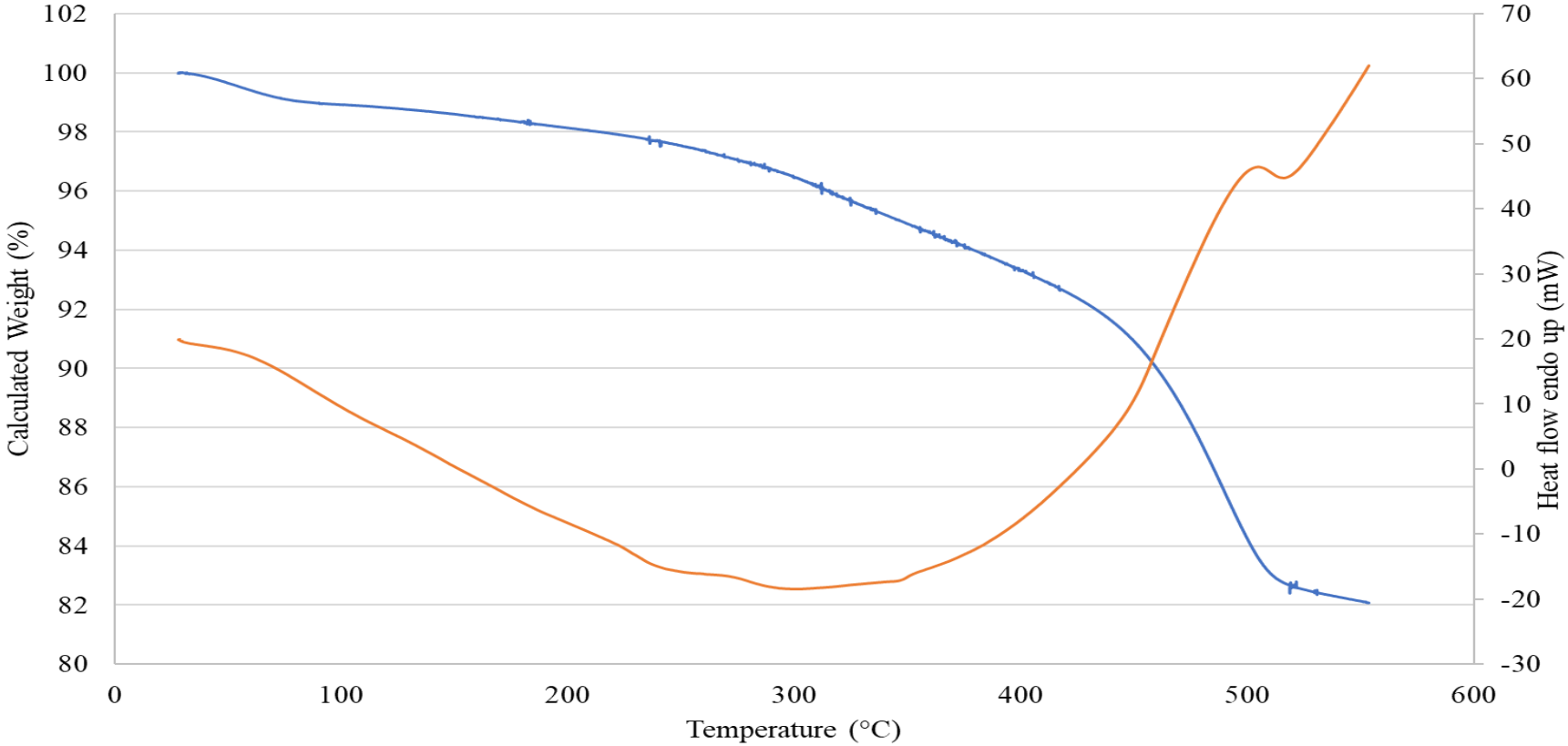

Figure 5.6. Graph of the STA data of cylindrical halloysite (7 Å) 4Ch + Au phosphonic acid where the Au phosphonic acid indicates gold nanotag with phosphonic acid terminated linker. The DSC curve is shown in orange and the TGA mass loss curve is shown in blue.

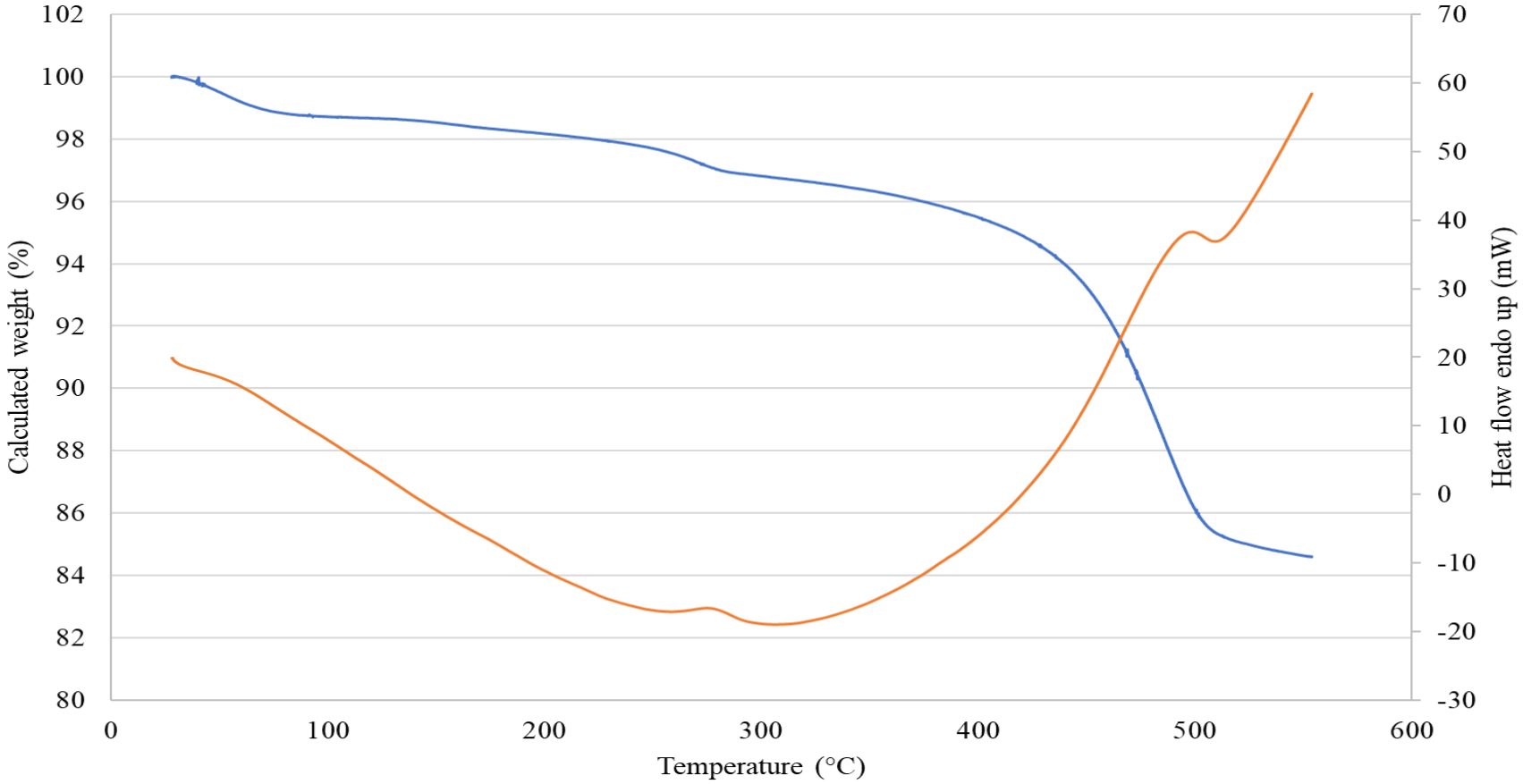

Figure 5.7. Graph of the STA data of cylindrical halloysite (7 Å) 4Ch + Au methyl. where the Au methyl indicates gold nanotag with methyl terminated linker. The DSC curve is shown in orange and the TGA mass loss curve is shown in blue.

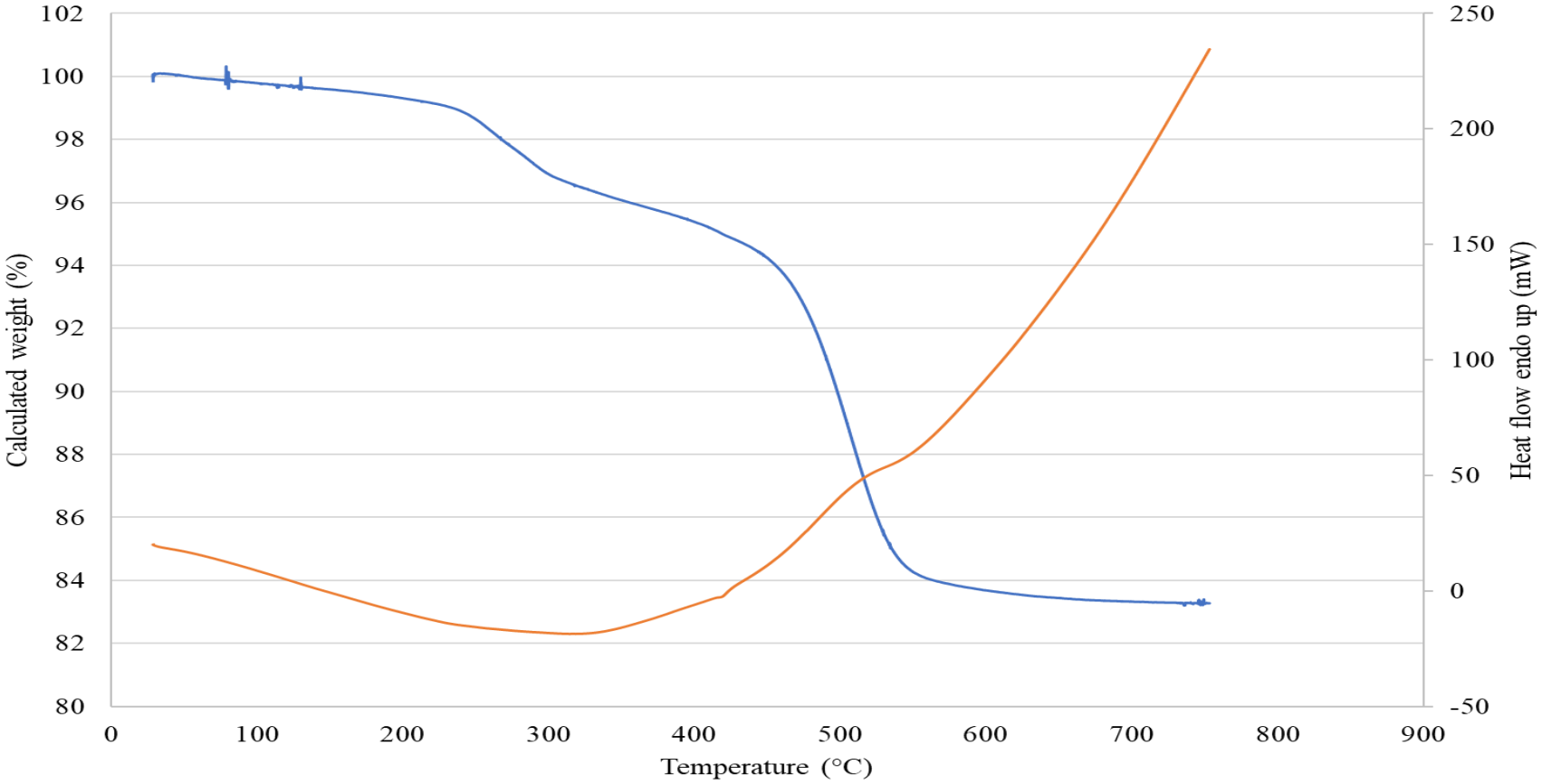

Figure 5.8. Graph of the STA data of prismatic halloysite (7 Å) 17US + Au phosphonic acid, where the Au phosphonic acid indicates gold nanotag with phosphonic acid terminated linker. The DSC curve is shown in orange and the TGA mass loss curve is shown in blue.

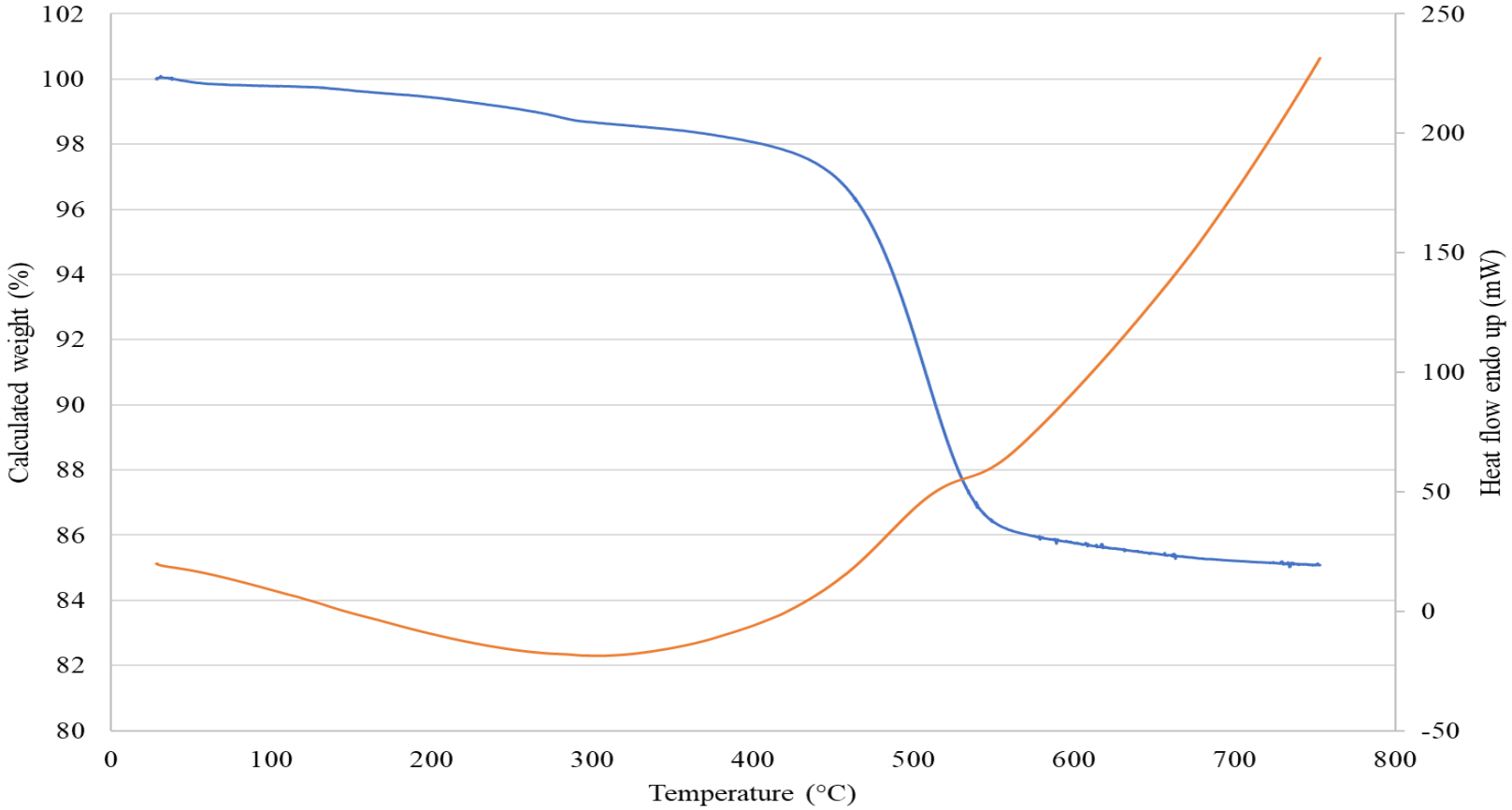

Figure 5.9. Graph of the STA data of prismatic halloysite (7 Å) 17US + Au methyl, where the Au methyl indicates gold nanotag with methyl terminated linker. The DSC curve is shown in orange and the TGA mass loss curve is shown in blue.

5.4.3 Transmission electron microscopy (TEM) results

The samples from Experimental Set 1 were selected for TEM analysis in accordance with the XPS data which suggested the presence of gold nanotags on the surface of the halloysites when the phosphonic acid terminated linkers were used. TEM is an effective tool to detect the 1-2 nm nanotags due to its high magnification capacity. General observation of the gold nanotags in the TEM images indicates that they are of a regular size and roughly cylindrical in shape, although their exact shape is hard to identify due to their small size. The features were confirmed as gold nanotags using *in situ* EDS.

Samples that had been treated with gold nanotags showed the nanotags clearly in the TEM images and provided a visual representation of the location of the gold nanotags on the surface of the halloysite nanotubes. A selection of TEM images are shown in Figures 5.10 and 5.11. *In situ* selected area electron diffraction analysis showed that the samples were dehydrated (Figure 5.12).

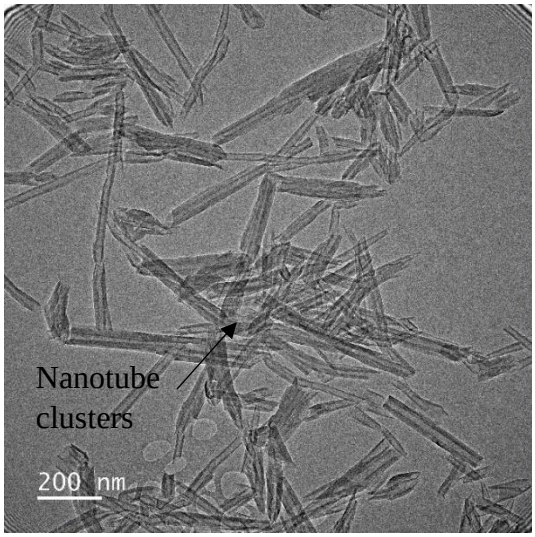

a) 4Ch original

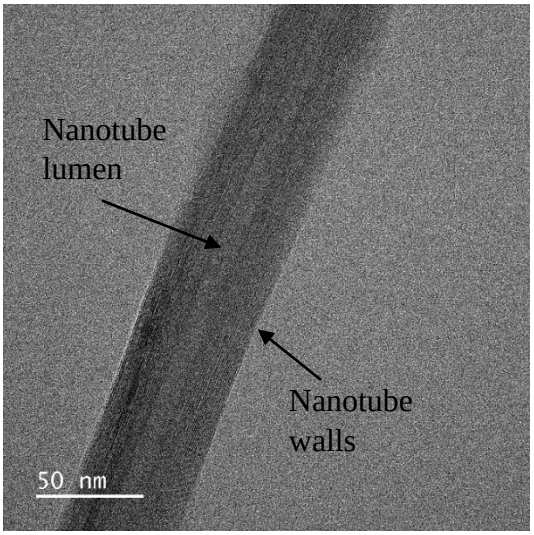

b) 4Ch original

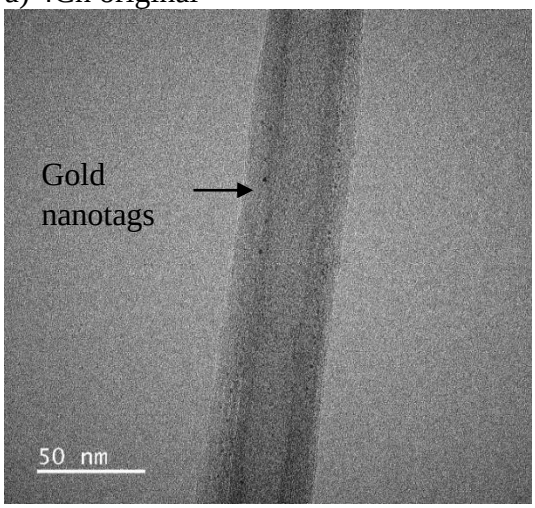

c) 4Ch + Au nanotags

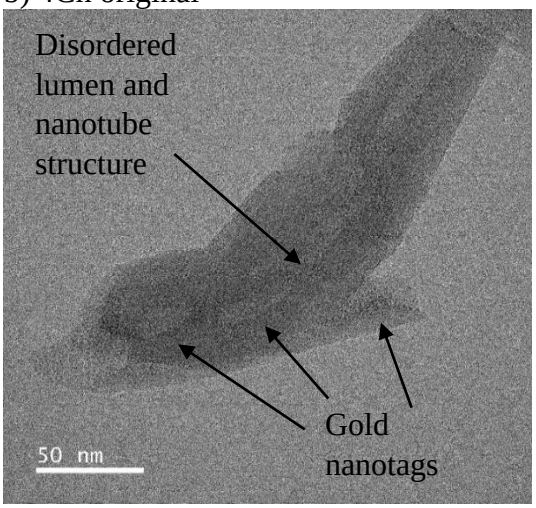

d) 4Ch + Au nanotags

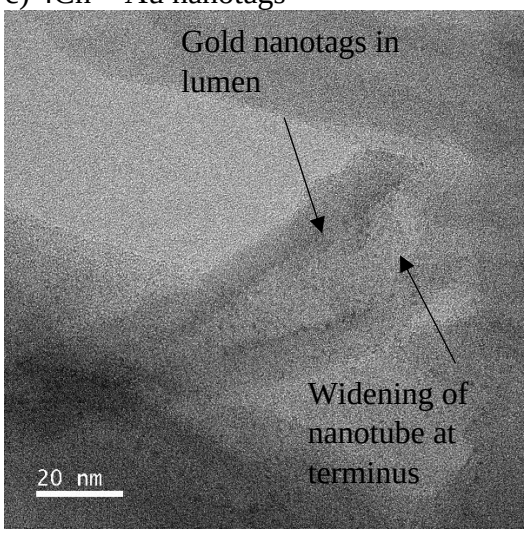

e) 4Ch + Au nanotags

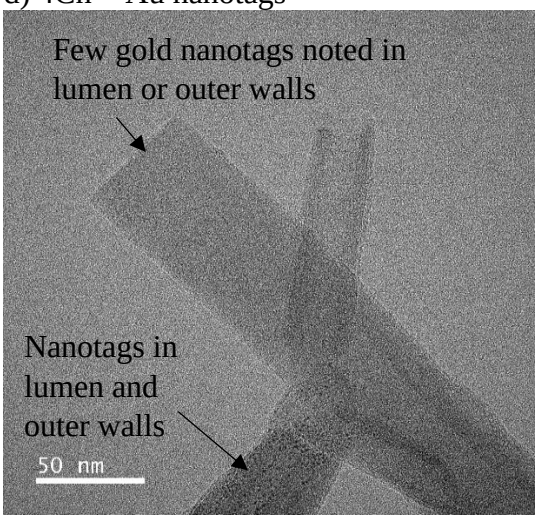

f) 4Ch + Au nanotags

Figure 5.10. Labelled TEM images from Experimental Set 1 of cylindrical 4Ch both untreated and treated with gold nanotags attached via phosphonic acid terminated linkers.

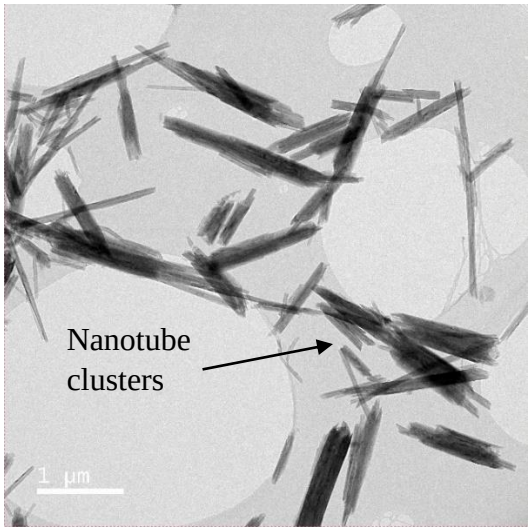

a) 17US original

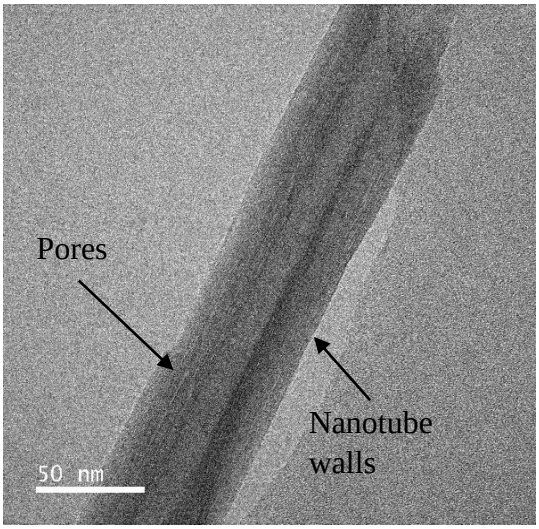

b) 17US original

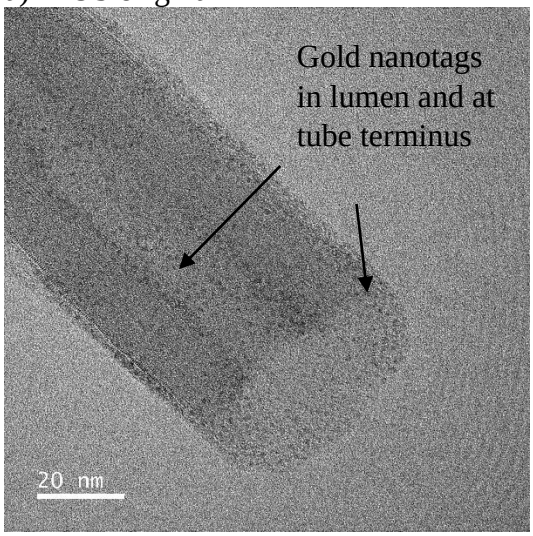

c) 17US + Au nanotags

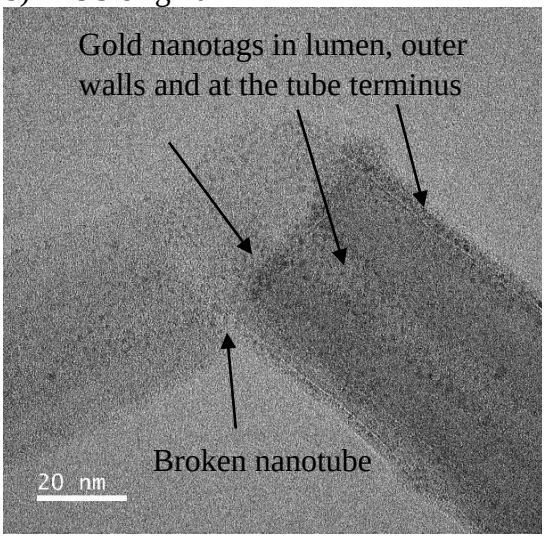

d) 17US + Au nanotags

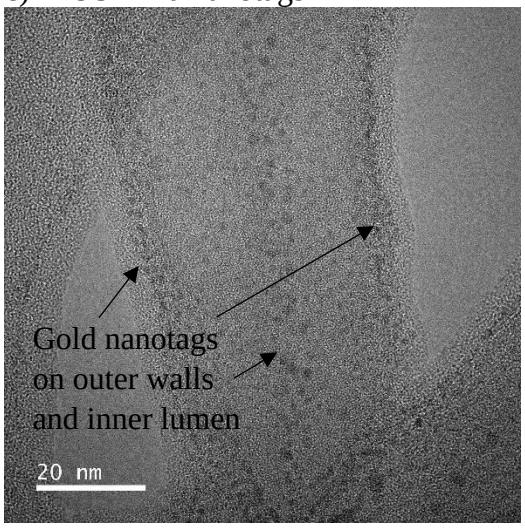

e) 17US + Au nanotags

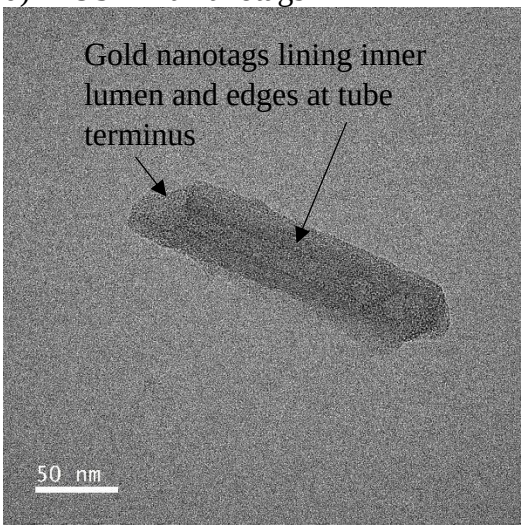

f) 17US + Au nanotags

Figure 5.11. Labelled TEM images from Experimental Set 1 of polygonal prismatic 17US both untreated and treated with gold nanotags attached via phosphonic acid terminated linkers.

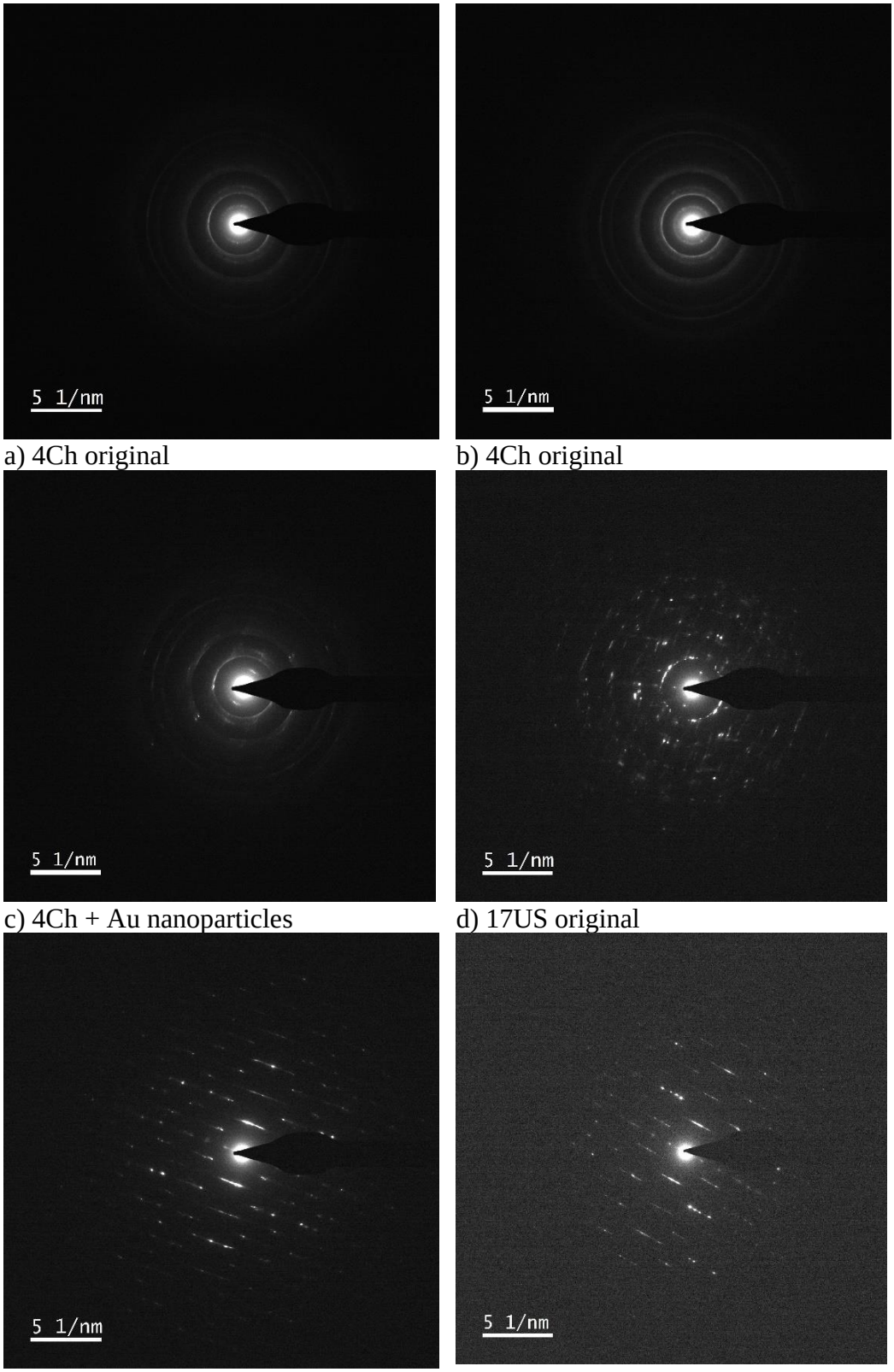

a) 4Ch original b) 4Ch original

c) 4Ch + Au nanoparticles d) 17US original

e) 17US original f) 17US + Au nanoparticles

Figure 5.12. In situ selected area electron diffraction patterns from TEM analysis of both the untreated halloysites and halloysites with gold nanotags attached via phosphonic acid terminated linkers.

The diffraction data obtained by measuring the spacings between the dots and dashes in Figure 5.11 was converted into d-spacings and then compared with the expected d-spacings from XRPD analysis of these samples, as shown in Table 5.6.

Table 5.6. Comparison of peaks detected in Selected Area Electron Diffraction Pattern (SAEDP) analysis with those expected by XRPD for halloysite (7 Å) samples. N.B. the d-spacings expected by XRPD are approximate only and small differences in values may be explained by different crystallinities.

Sample ID	d-spacing SAEDP	d-spacing XRPD	Assignment
4Ch original	7.2	7.2	Halloysite (001)
	4.6	4.4	Halloysite (02,11)
	3.6	3.6	Halloysite (002)
	2.3	2.3-2.6	Halloysite (20,13)
	1.8	1.7	Halloysite
	1.6	1.5	Halloysite (06,33)
4Ch + Au nanotag	7.6		Halloysite (001)
	4.5		Halloysite (02,11)
	3.6		Halloysite (002)
	2.6	2.3-2.6	Halloysite (20,13)
	2.4		Au
	1.5		Halloysite (06,33)
	1.2		Au

Sample ID	d-spacing SAEDP	d-spacing XRPD	Assignment
17US original	7.2	7.2	Halloysite (001)
	4.3	4.4	Halloysite (02,11)
	3.7	3.6	Halloysite (002)
	2.3	2.3-2.6	Halloysite (20,13)
	1.5	1.5	Halloysite (06,33)
	1.3	1.3	Halloysite
17US + Au-nanotag	7.2		Halloysite (001)
	4.5		Halloysite (02,11)
	3.6		Halloysite (002)
	2.5	2.3-2.6	Halloysite (20,13)
	1.5	1.5	Halloysite (06,33)
	1.2		Au
	0.9		Au

Lumen diameter measurements were made from the TEM images of the pure halloysites, the results of these are shown in Table 5.7 and the results are concordant with the measurements made in Chapter 4, Section 4.3.3 from the TEM cross section analysis.

Table 5.7. TEM average lumen diameters.

Sample ID	Average Lumen Diameter (nm)	n	Standard Deviation
4Ch	12.0	43	3.0
17US	11.4	34	2.8

5.4.4 Fourier transform infrared spectroscopy (FTIR) results

FTIR spectra were recorded for all the samples tagged with gold and silver nanotags using the three types of linker. As outlined in Chapter 3, FTIR can be used to identify chemical moieties related to the sites of adsorption on halloysite nanotubes. The data in Chapter 3 showed clearer data for the polygonal prismatic samples due to the greater degree of ordering as outlined in Chapter 2 (Section 2.2.2), resulting in the presence of the diagnostic surface Al-OH stretching peaks observed at around 3670 cm^{-1}.

Results from the first experimental set using 4Ch and 17US with gold nanoparticles and either methyl or phosphonic acid linkers are shown in Figures 5.13-5.20. In addition, the 4Ch and 17US which had been reacted with excess phenyl phosphonic acid (Table 5.1) with no metal nanotags was also analysed.

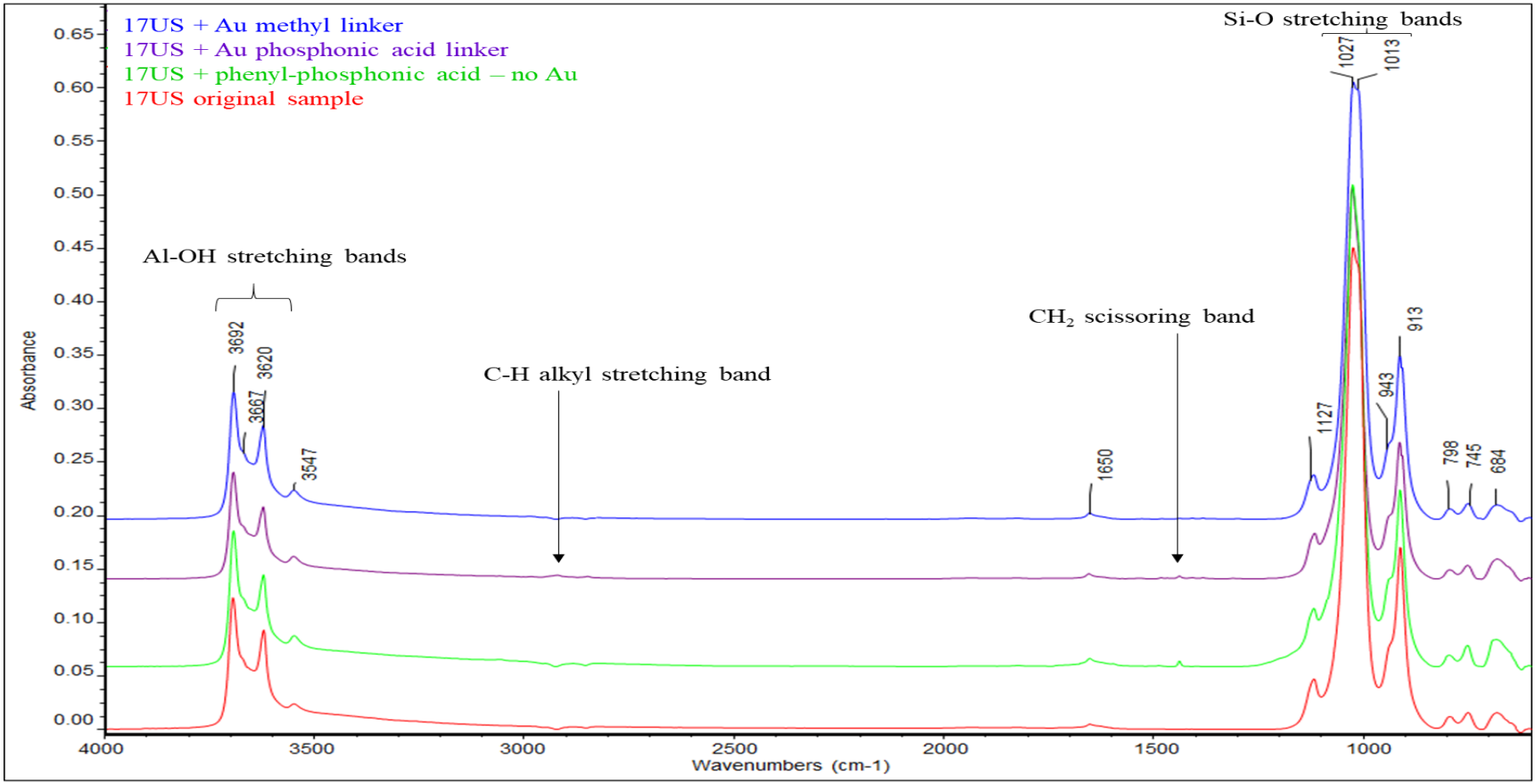

Figure 5.13. FTIR spectra of 17US halloysite (7 Å) from Experimental Set 1. Spectra show traces from pure halloysite and halloysite with Au nanotags and the two linkers, one phosphonic acid terminated and the other methyl group terminated. In addition, the spectra of halloysite plus phenyl-phosphonic acid with no Au nanotag is included.

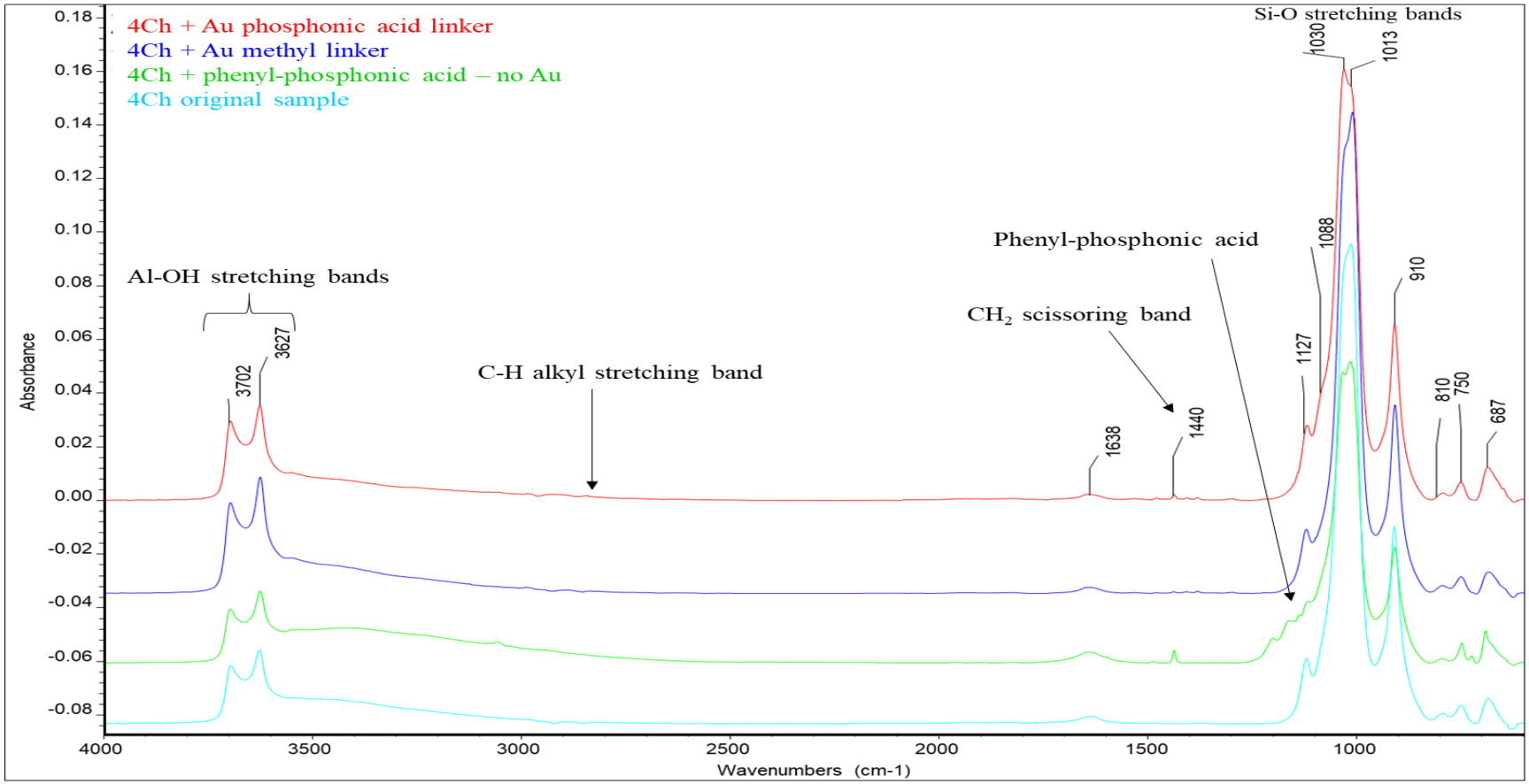

Figure 5.14. FTIR spectra of 4Ch halloysite (7 Å) from Experimental Set 1. Spectra show traces from pure halloysite and halloysite with Au nanotags and the two linkers, one phosphonic acid terminated and the other methyl group terminated. In addition, the spectra of halloysite plus phenyl-phosphonic acid with no Au nanotag is included.

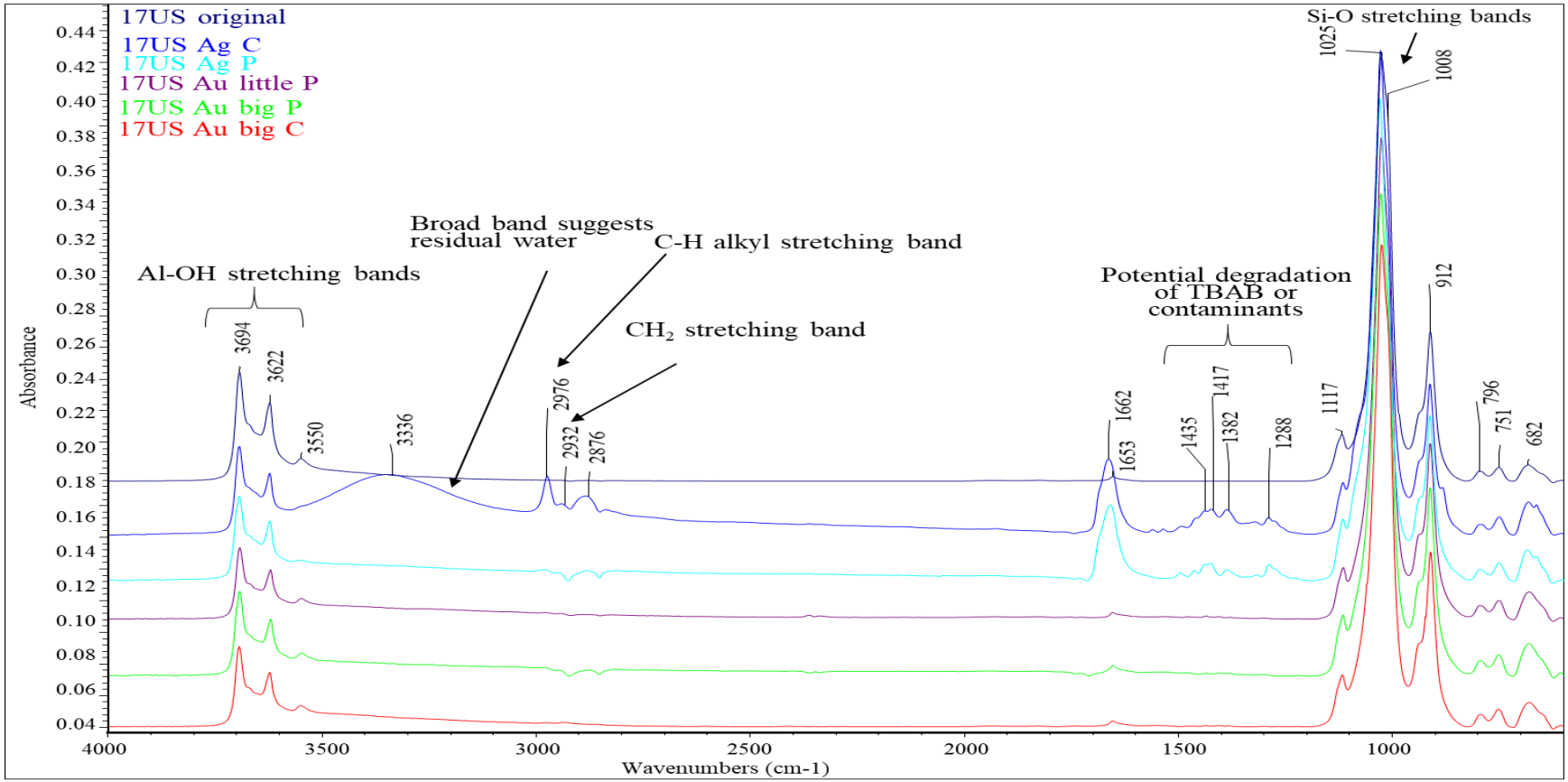

Figure 5.15. FTIR spectra of 17US halloysite (7 Å) from Experimental Set 2. Spectra show traces from the pure halloysite and halloysite with the Au and Ag nanotags of varying sizes with either carboxylate or phosphonic acid terminated linkers.

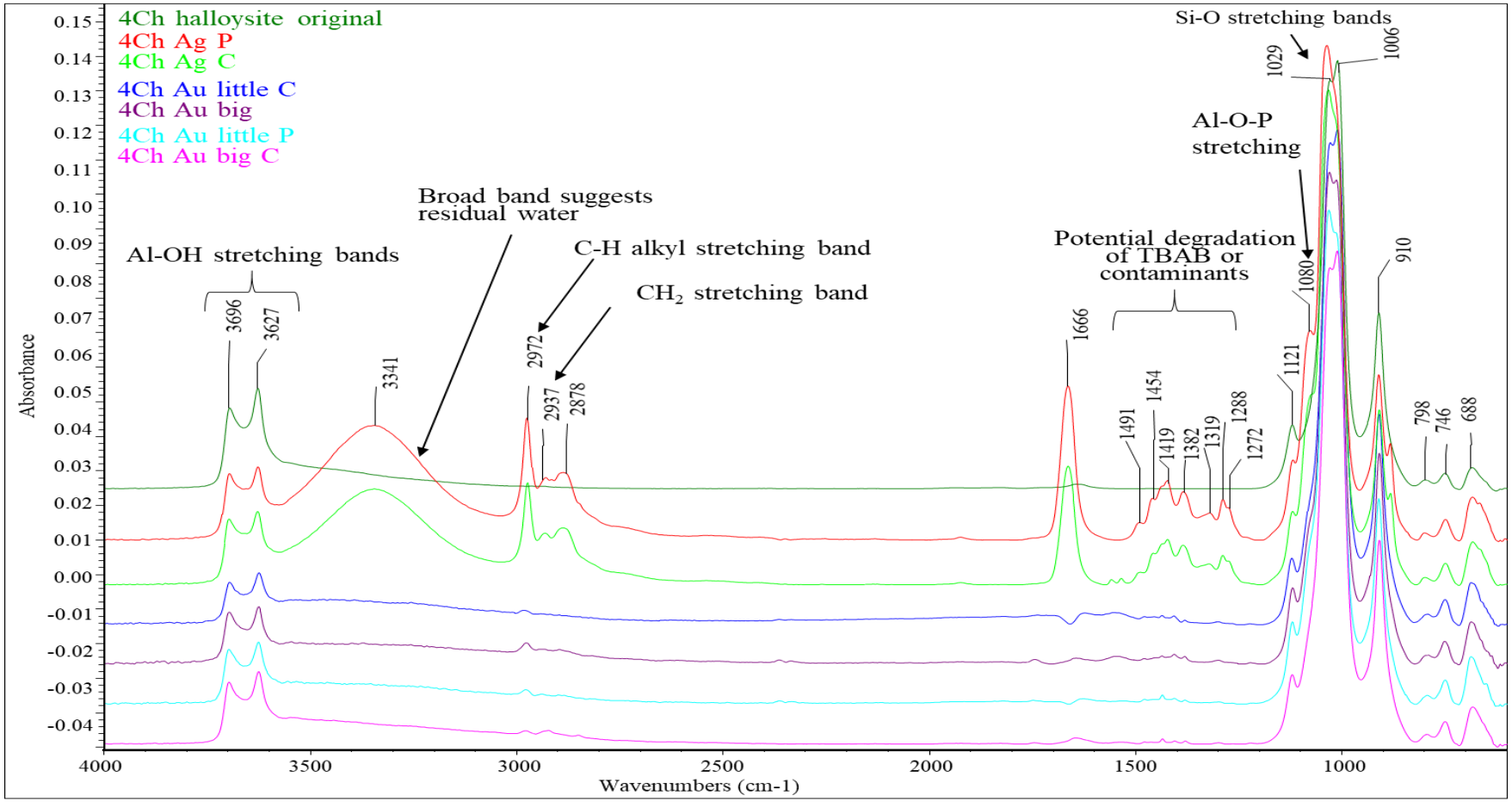

Figure 5.16. FTIR spectra of 4Ch halloysite (7 Å) from Experimental Set 2. Spectra show traces from the pure halloysite and halloysite with the Au and Ag nanotags of varying sizes with either carboxylate or phosphonic acid terminated linkers.

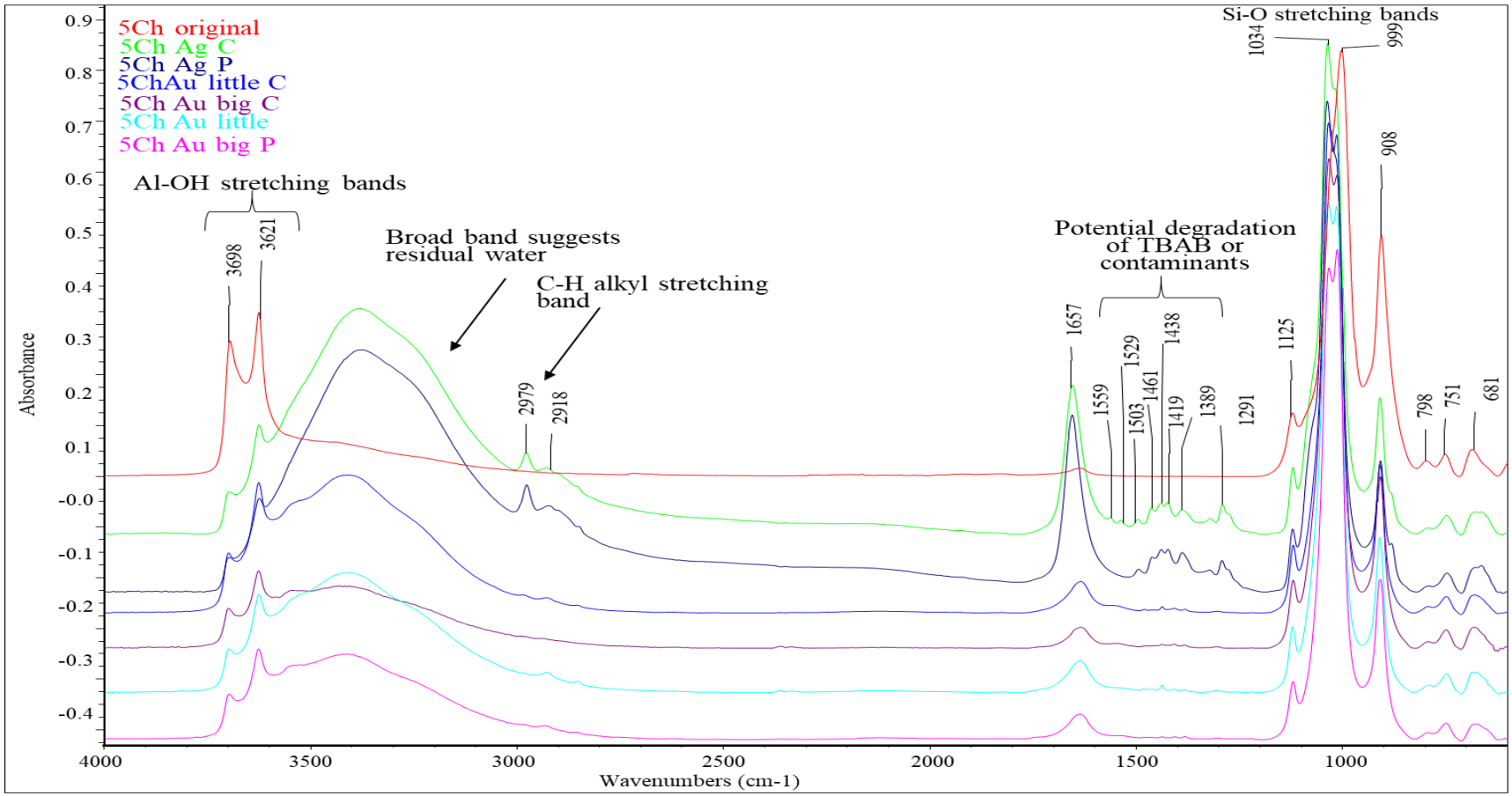

Figure 5.17. FTIR spectra of 5Ch halloysite (10 Å) from Experimental Set 2. Spectra show traces from the pure halloysite and halloysite with the Au and Ag nanotags of varying sizes with either carboxylate or phosphonic acid terminated linkers.

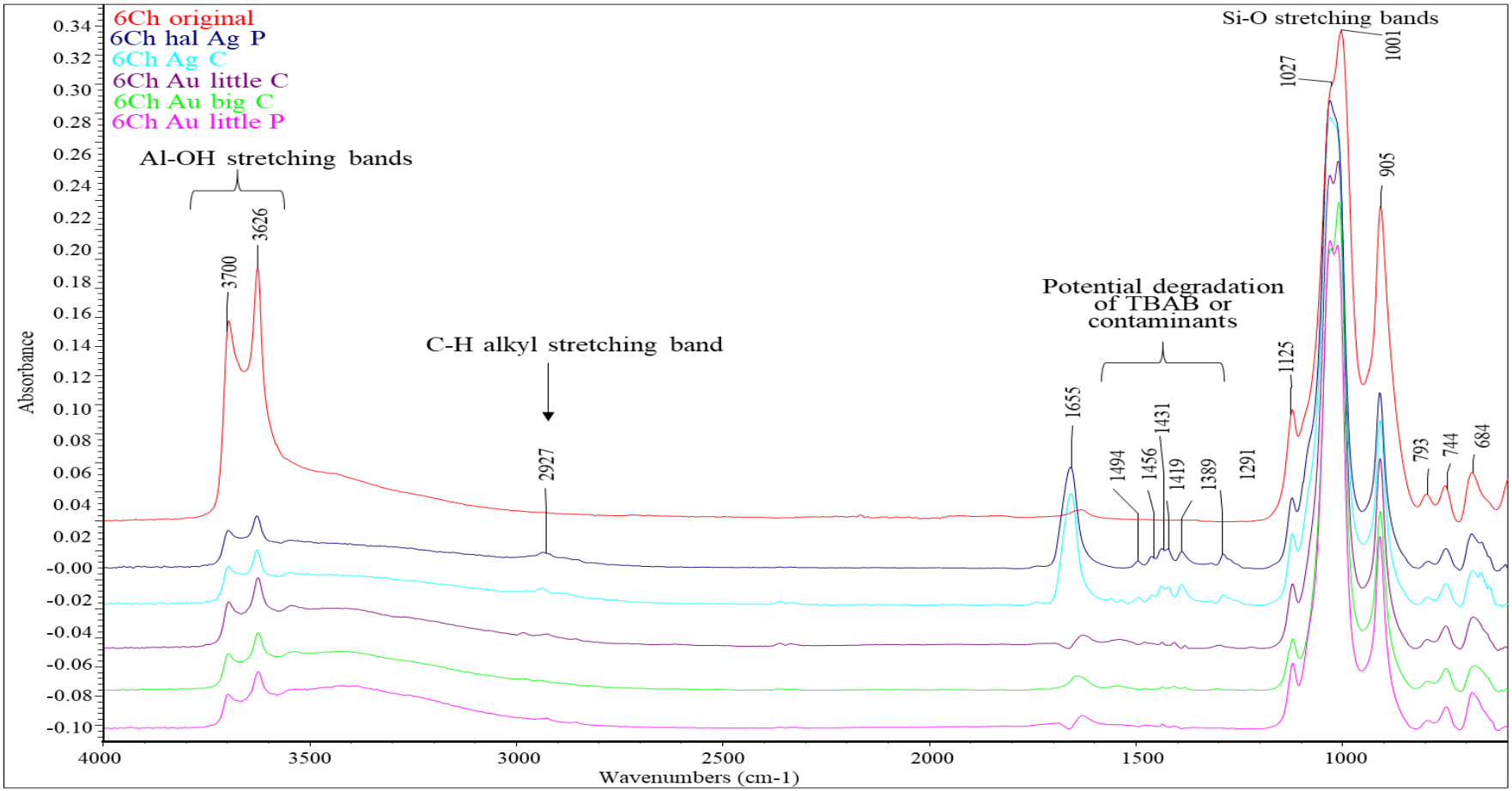

Figure 5.18. FTIR spectra of 6Ch halloysite (10 Å) from Experimental Set 2. Spectra show traces from the pure halloysite and halloysite with the Au and Ag nanotags of varying sizes with either carboxylate or phosphonic acid terminated linkers.

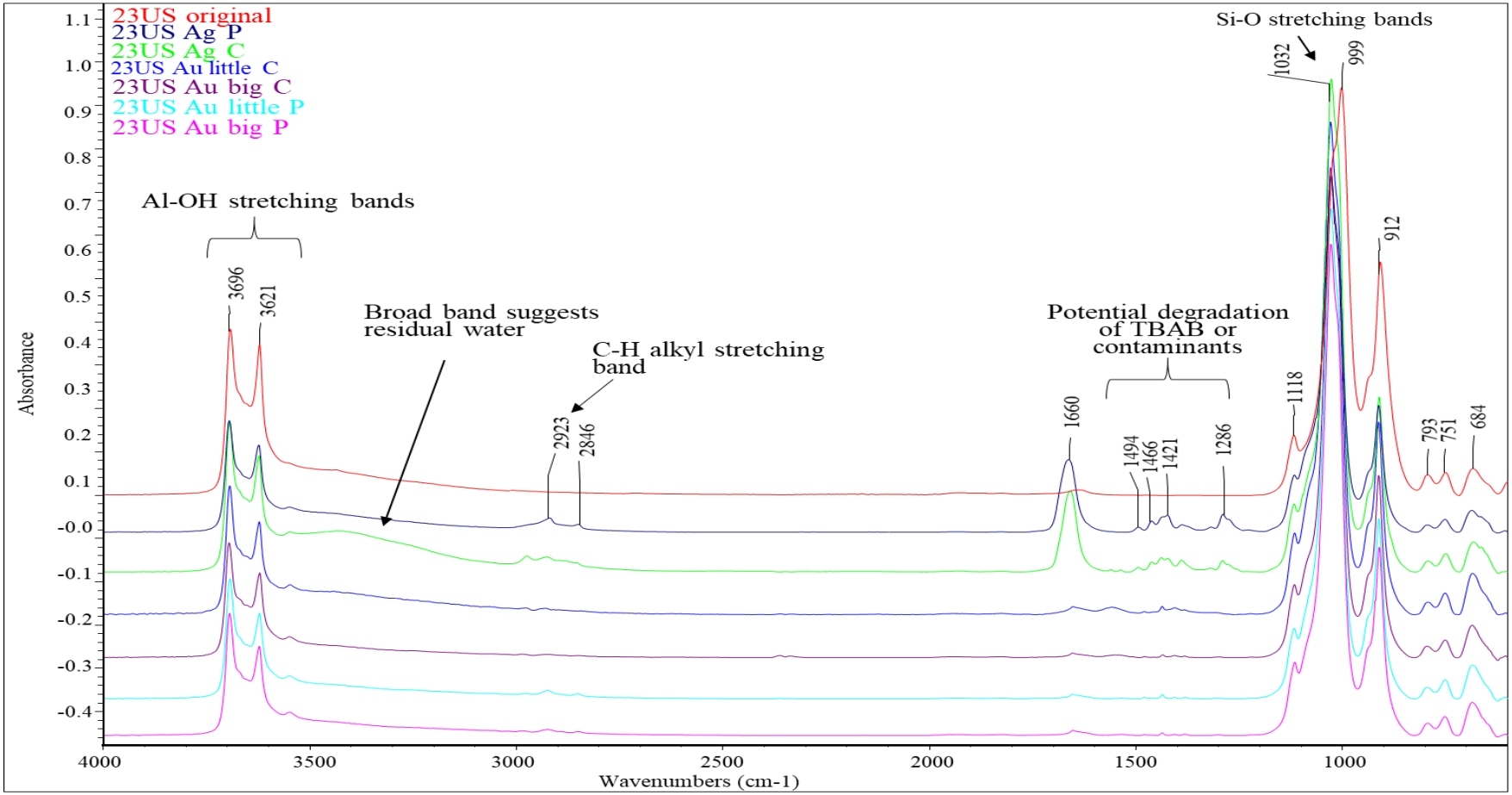

Figure 5.19. FTIR spectra of 23US halloysite (10 Å) from Experimental Set 2. Spectra show traces from the pure halloysite and halloysite with the Au and Ag nanotags of varying sizes with either carboxylate or phosphonic acid terminated linkers.

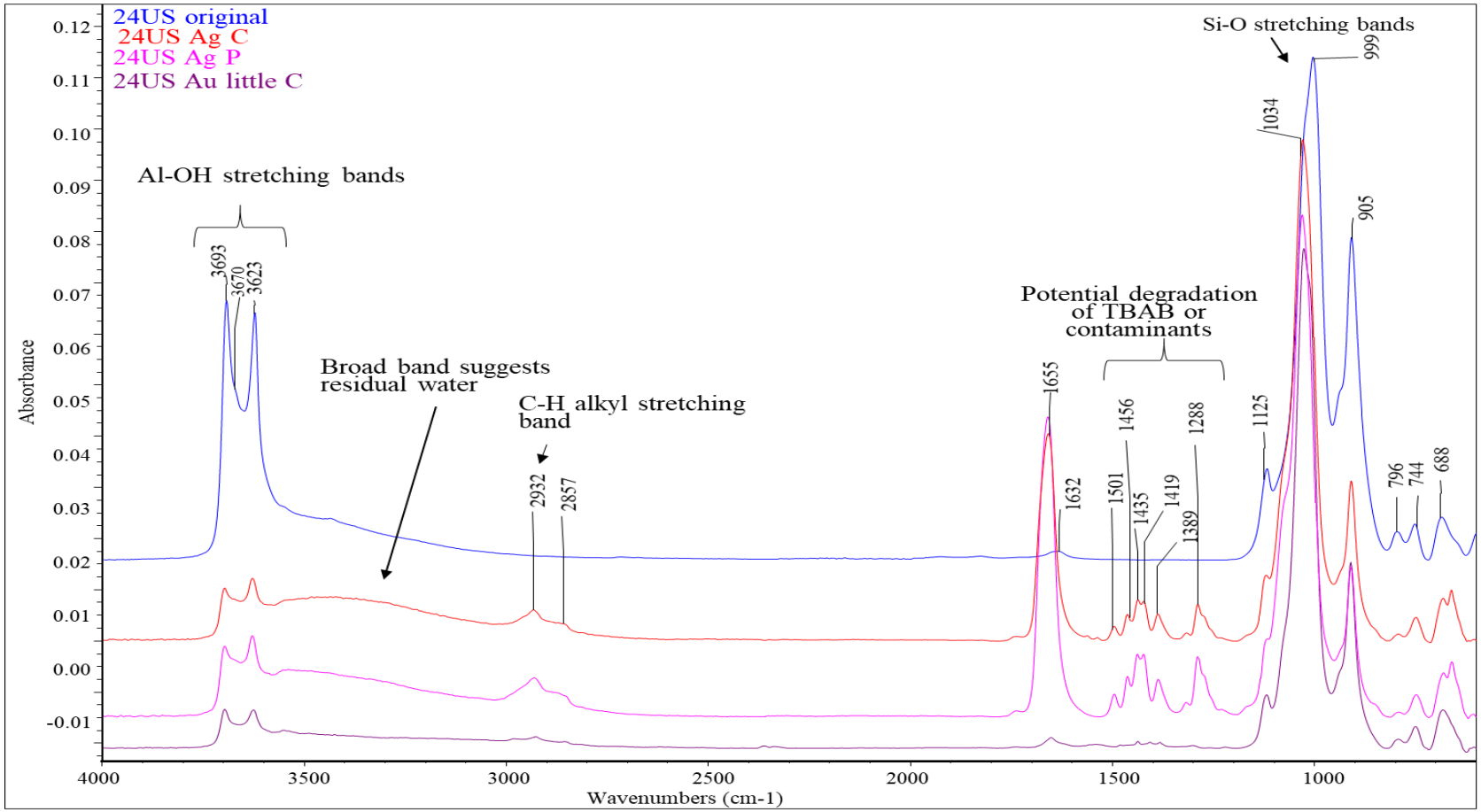

Figure 5.20. FTIR spectra of 24US halloysite (10 Å) from Experimental Set 2. Spectra show traces from the pure halloysite and halloysite with the Au and Ag nanotags of varying sizes with either carboxylate or phosphonic acid terminated linkers.

From the FTIR spectra presented in Figure 5.13-5.20 it appears evident that reaction of the halloysites with either gold or silver nanotags and phosphonic acid and carboxylate terminated linkers results in some additional bands on the spectra which are suggestive of the presence of the alkyl chain linkers (as labelled in Figures 5.13-5.20). When the methyl terminated linker was used (Figures 5.13-5.14) there appeared no evidence of the linker with the halloysite, from which it can be inferred that that no surface adsorption occurred. There appears no clear evidence for a different loading of linkers when the two gold nanotag sizes are compared. Additionally, it was not possible to identify with FTIR the binding mechanism, i.e. mono or bi-dentate.

5.4.5 Optical microscopy results

Optical microscopy was conducted on the samples from Experimental Set 1 as shown in Figure 5.21, where the optical microscopy was used to obtain high resolution images of the colours and dispersion of the nanotag and linker treated halloysite samples. Since the 17US and 4Ch halloysite samples were initially white-ish, any colour change detected using optical microscopy may be seen as indicative of adhesion of the gold nanotags onto the surface of the halloysites.

a) 4Ch and Au nanotag with methyl terminated linker

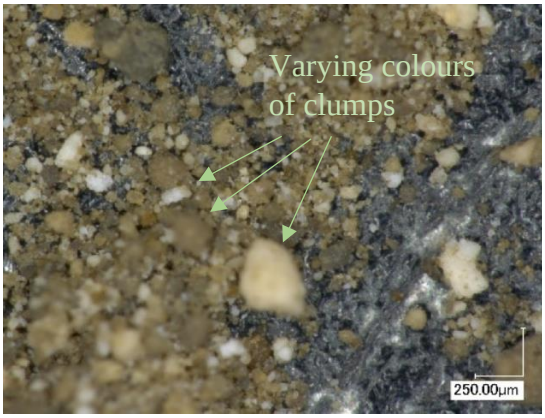

b) 4Ch and Au nanotag with phosphonic acid terminated linker

c) 17US and Au nanotag with methyl t terminated linker

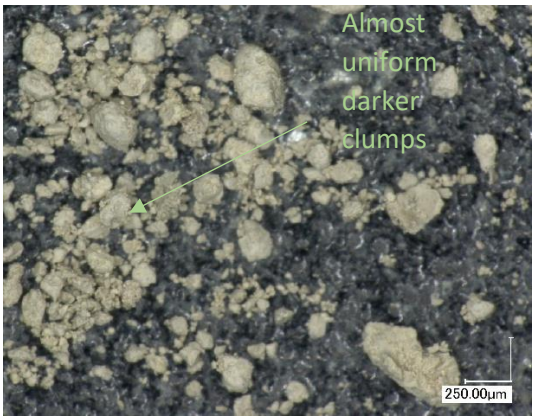

d) 17US and Au nanotag with phosphonic acid terminated linker

Figure 5.21. Labelled optical microscopy images of the halloysite 17US and 4Ch samples from experimental Set 1 with both the methyl terminated and phosphonic acid terminated linkers and Au nanotags.

5.4.6 X-ray powder diffraction results

A selection of 8 samples were run by XRPD to determine whether any evidence of the gold and silver nano-tagging could be detected (Figures 5.22-5.32). Whilst there was no concrete evidence of the pure metals detected in the samples some interesting features were observed, most noticeably the low angle bands in the samples with the gold nanotags. There is also evidence of some silver chloride in the 6Ch samples with silver nanotags (Figures 5.21-5.28). As these samples were run in very small amounts and as hand ground powders, qualitative analysis, not quantitative analysis, has been conducted. From the XRPD traces it appears that the two halloysites studied by XRPD retained some of their interlayer water as there was evidence for the halloysite (10 Å)

band in all the traces. As can be seen in Table 5.4, the overlap of the gold and silver diffraction bands with those of halloysite make any certain identification of these metals present in the traces difficult. It can however be noted that low angle bands are present in all the samples. For the case of the silver tagged samples (Figures 5.22, 5.23, 5.26 and 5.27) these sharp bands may suggest some form of small angle X-ray scattering that can sometimes occur ay low angles if a sample contains very regular sized particles which may be indicative the silver nanotags. In the case of the gold nano-tagged samples (Figures 5.24, 5.25, 5.28 and 5.29) the low angle bands are broader and their identification is less certain.

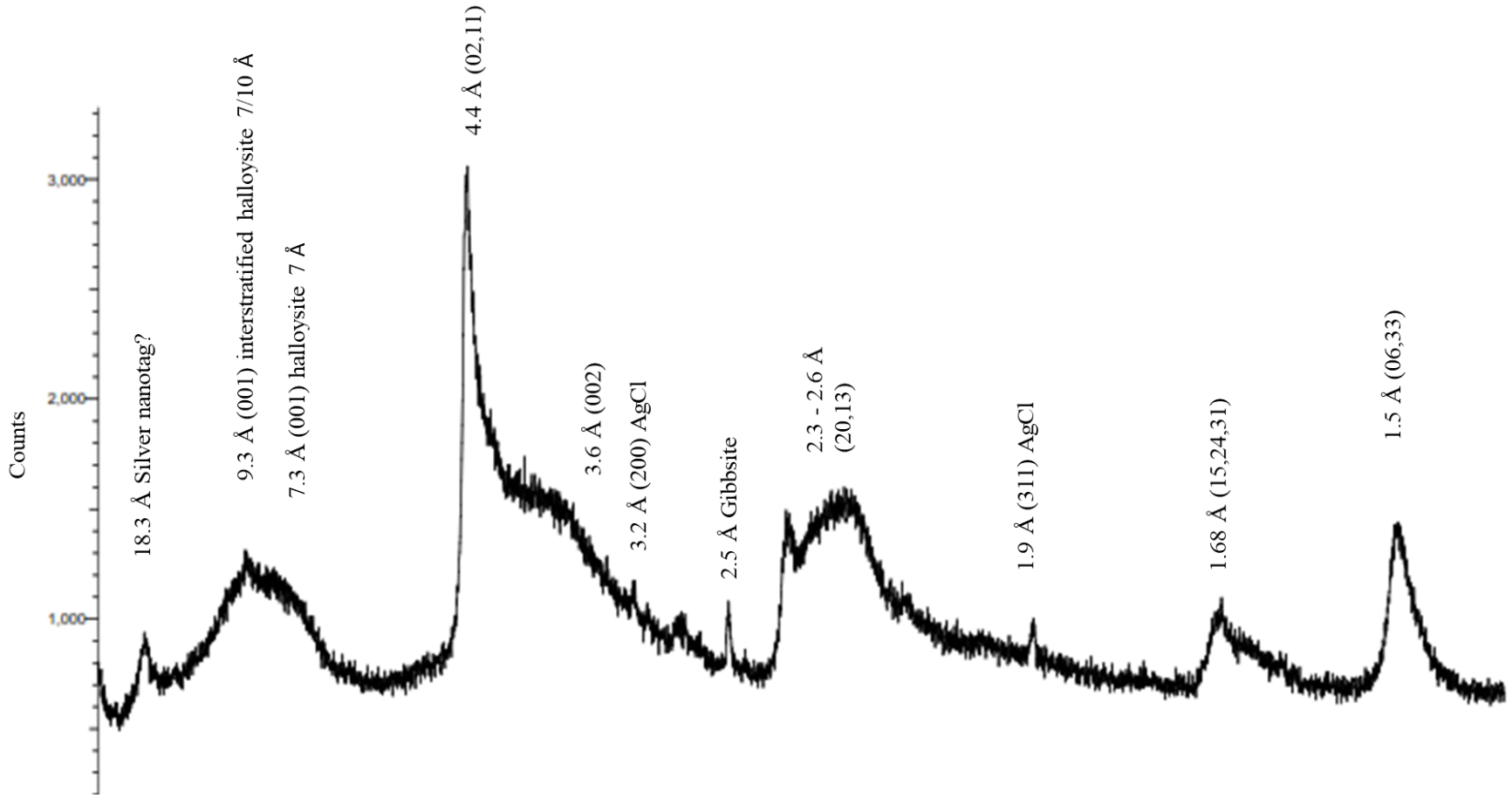

Figure 5.22. XRPD pattern of 6Ch + Ag nanotag with a carboxylate terminated linker. The key basal and non-basal diffraction bands of the halloysite are labelled where it appears that there is evidence of some halloysite (10 Å) remaining. Evidence of traces of silver chloride

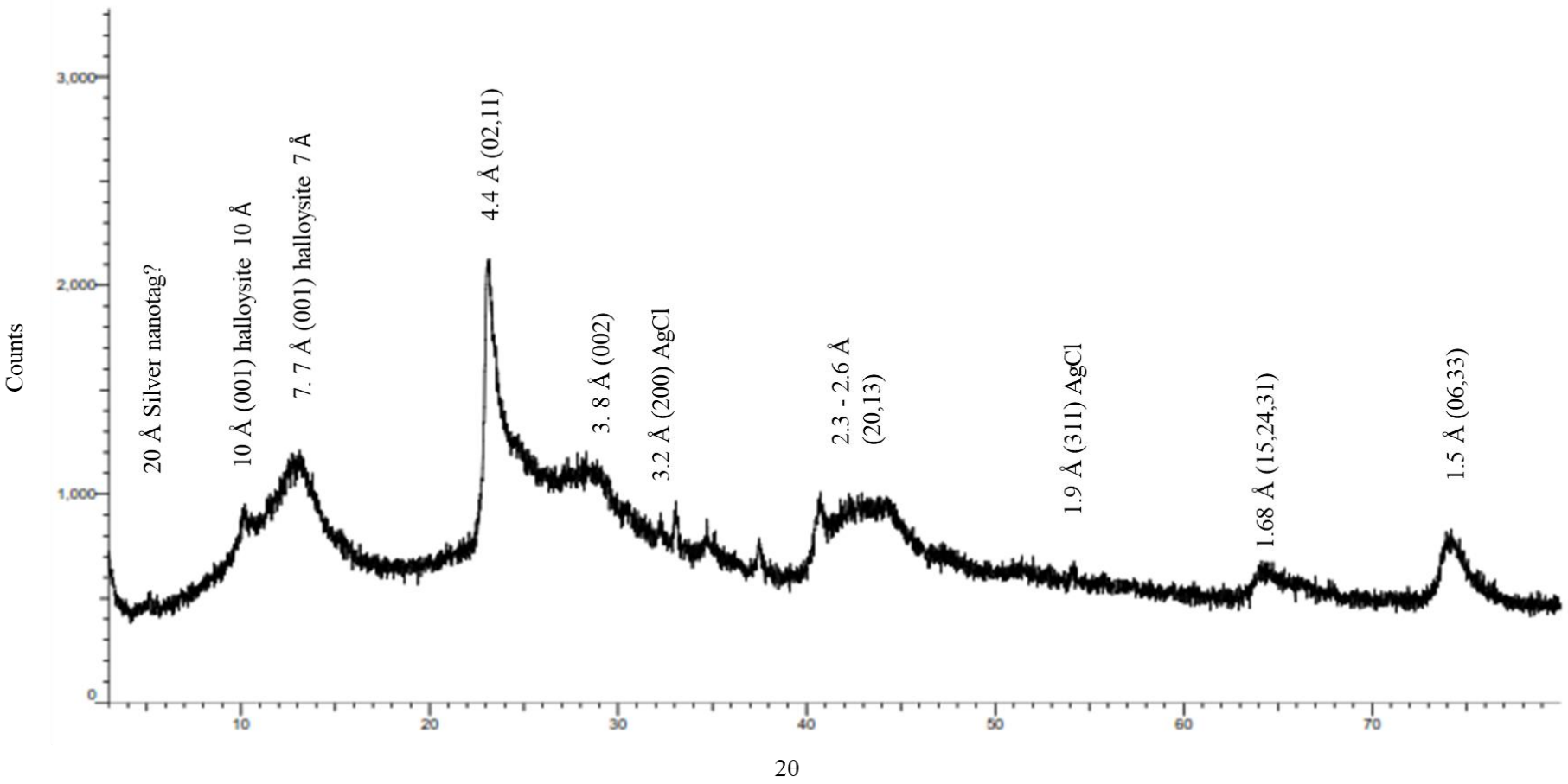

Figure 5.23. XRPD pattern of 6Ch + Ag nanotag with a phosphonic acid terminated linker. The key basal and non-basal diffraction bands of the halloysite are labelled where it appears that there is evidence of some halloysite (10 Å) remaining. Evidence of traces of silver chloride are

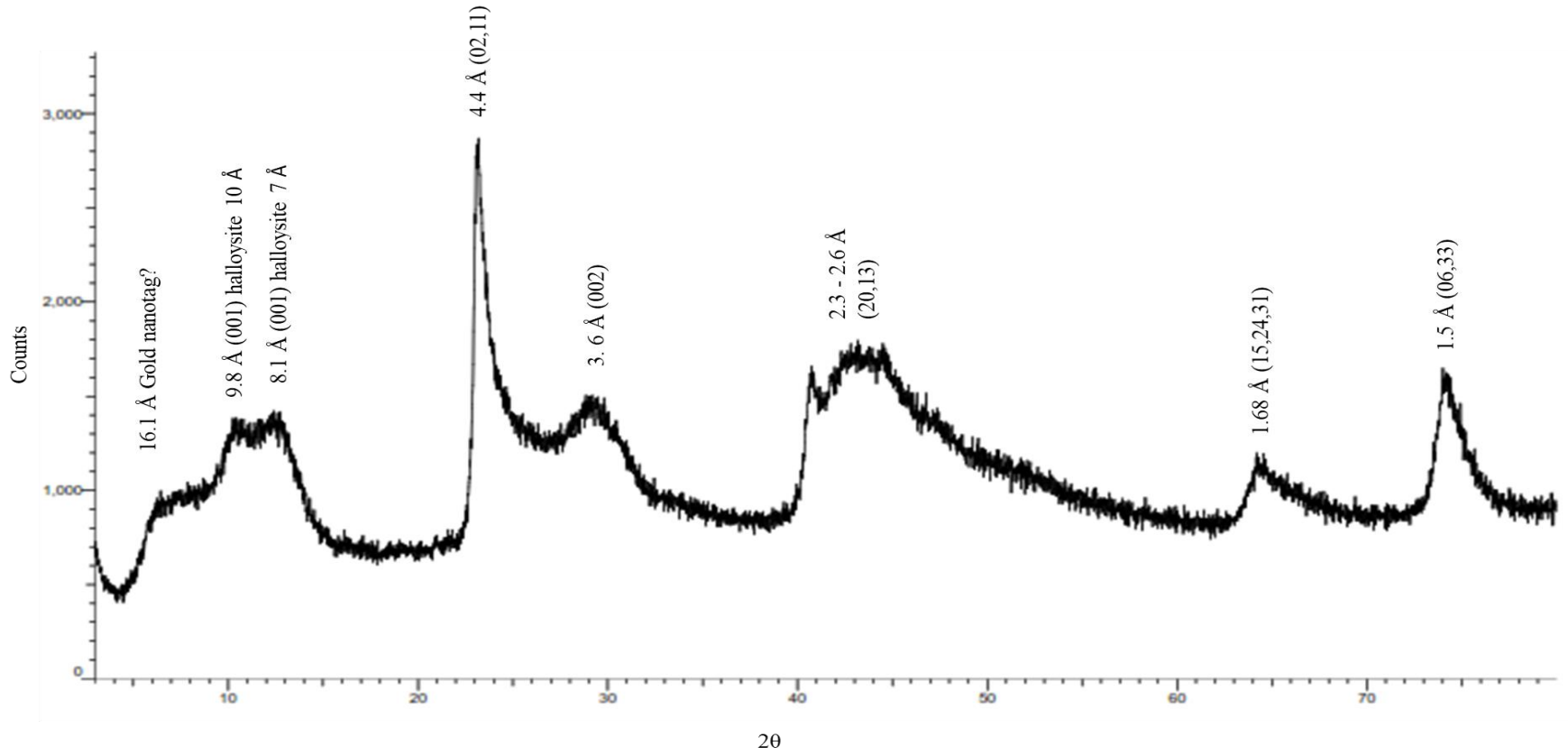

Figure 5.24. XRPD pattern of 6Ch + large Au nanotag with a carboxylate terminated linker. The key basal and non-basal diffraction bands of the halloysite are labelled where it appears that there is evidence of some halloysite (10 Å) remaining. The band at 16.1 Å has been tentatively labelled as the gold metal..

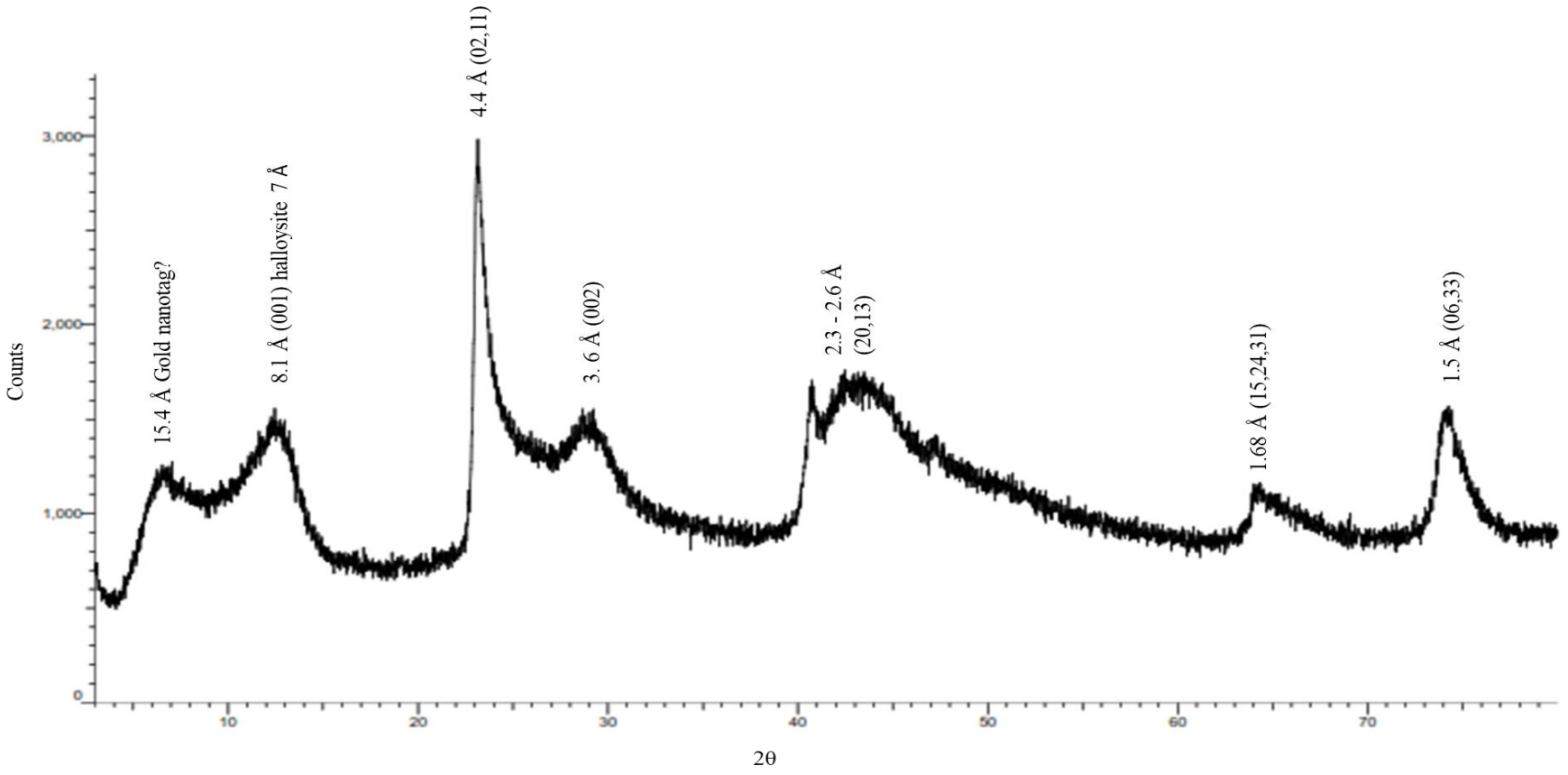

Figure 5.25. XRPD pattern of 6Ch + small Au nanotag with a phosphonic acid terminated linker. The key basal and non-basal diffraction bands of the halloysite are labelled where it appears that there is evidence of some halloysite (10 Å) remaining. The band at 15.4 Å has been tentatively labelled as the gold metal.

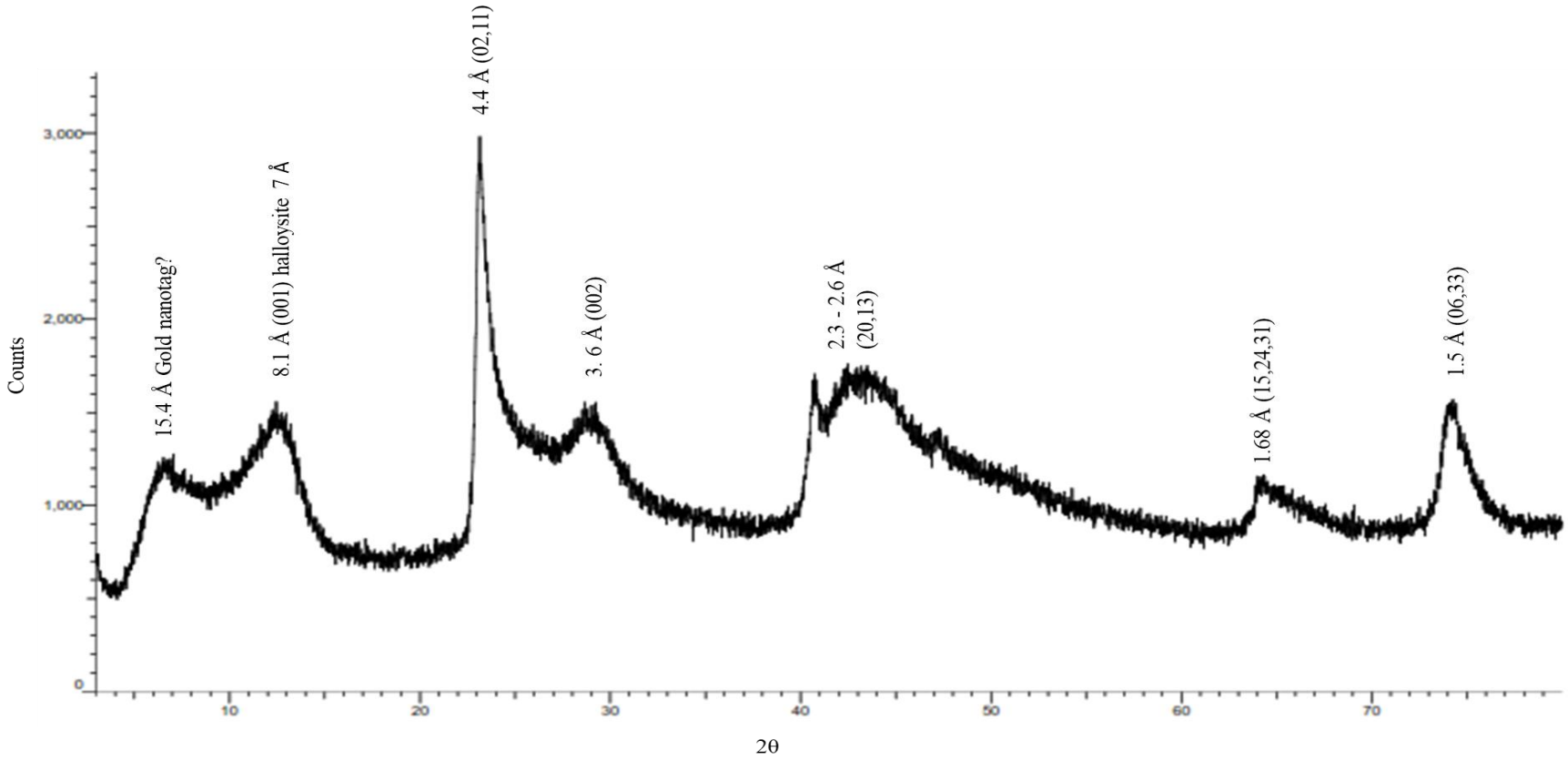

Figure 5.26. XRPD pattern of 23US + Ag nanotag with a carboxylate terminated linker. The key basal and non-basal diffraction bands of the halloysite are labelled where it appears that there is evidence of some halloysite (10 Å) remaining. The band at 18.7 Å has been tentatively labelled as the silver metal.

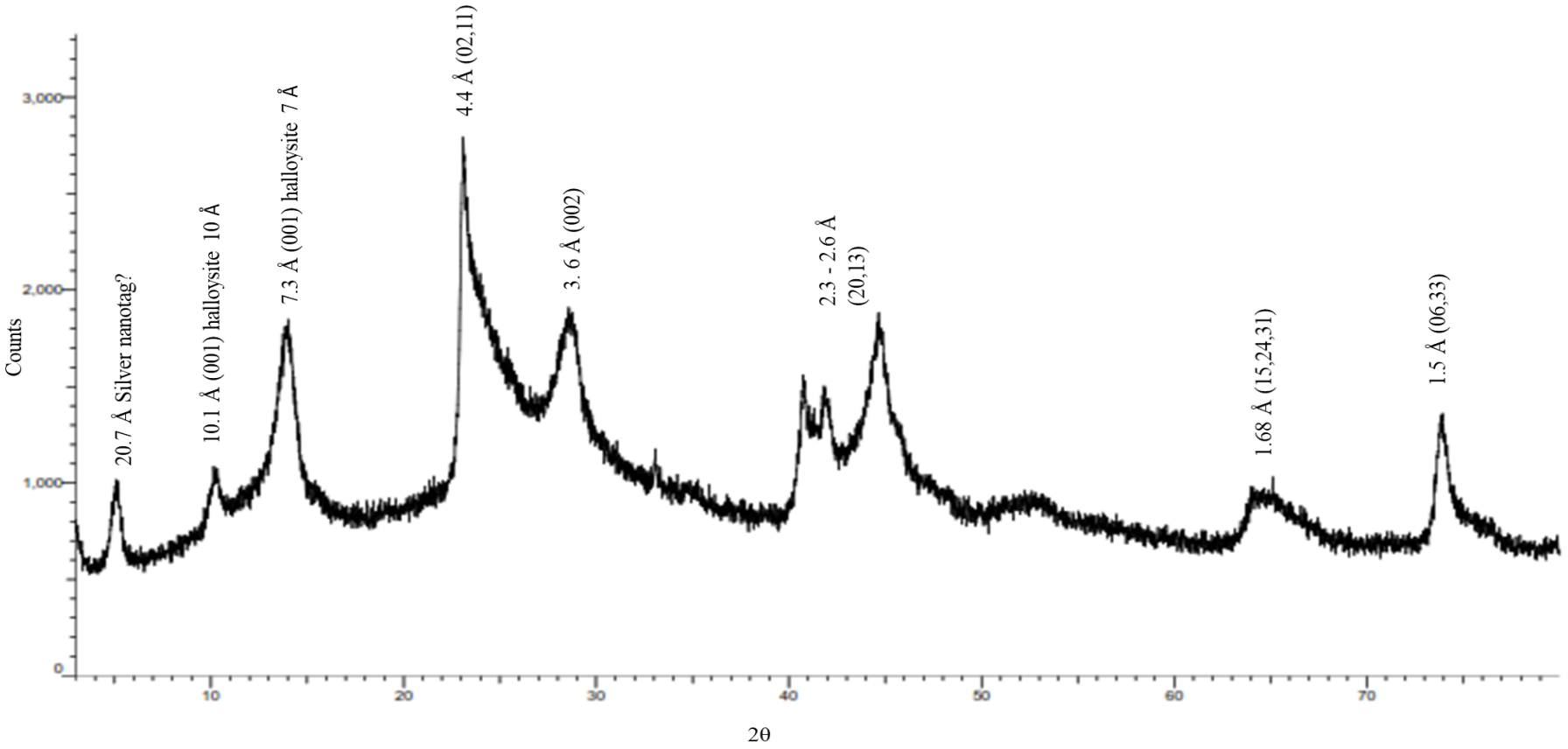

Figure 5.27. XRPD pattern of 23US + Ag nanotag with a phosphonic acid terminated linker. The key basal and non-basal diffraction bands of the halloysite are labelled where it appears that there is evidence of some halloysite (10 Å) remaining. The band at 20.7 Å has been tentatively labelled as the silver metal.

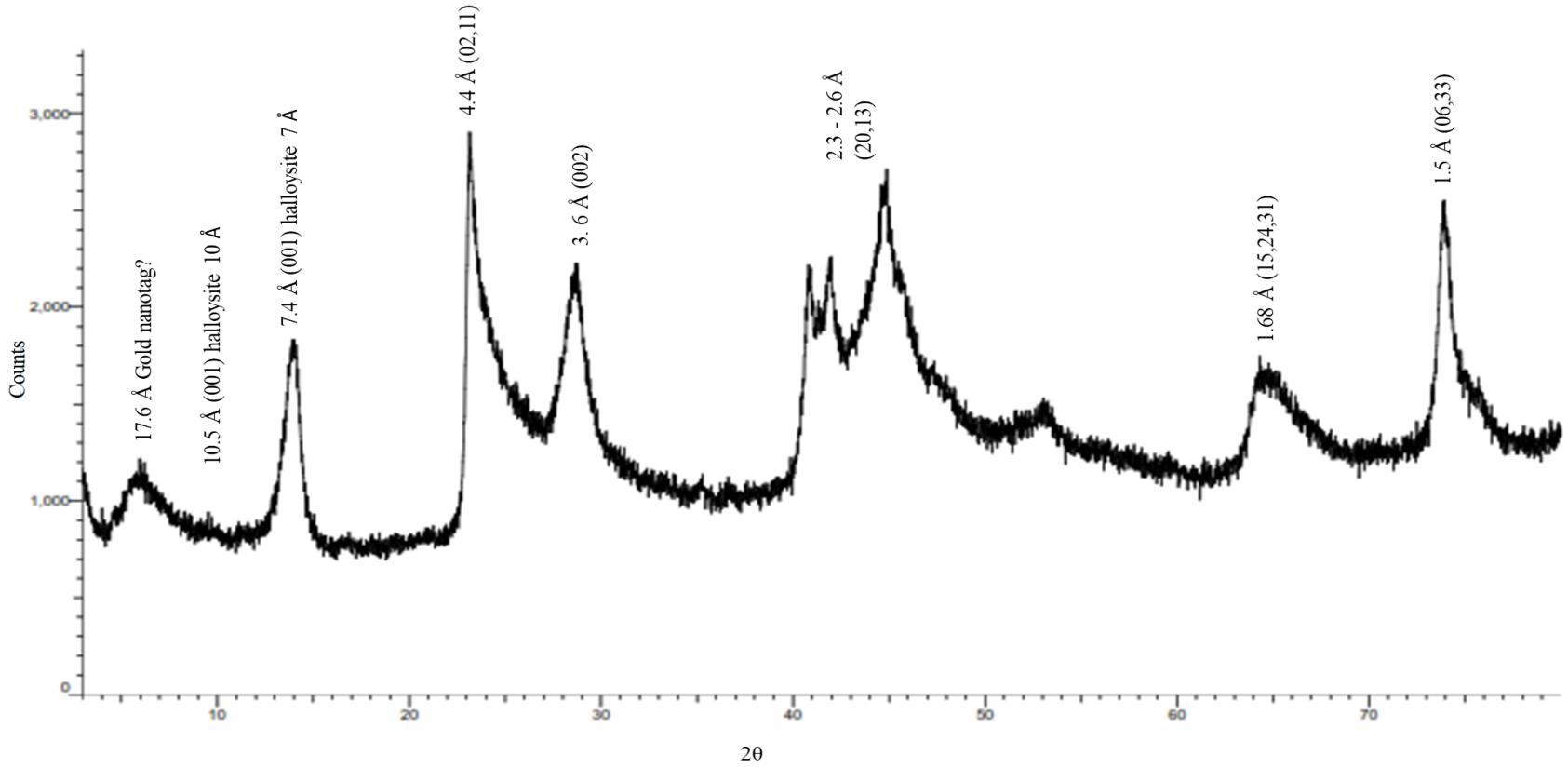

Figure 5.28. XRPD pattern of 23US + large Au nanotag with a carboxylate terminated linker. The key basal and non-basal diffraction bands of the halloysite are labelled where it appears that there is evidence of some halloysite (10 Å) remaining. The band at 17.6 Å has been tentatively labelled as the gold metal.

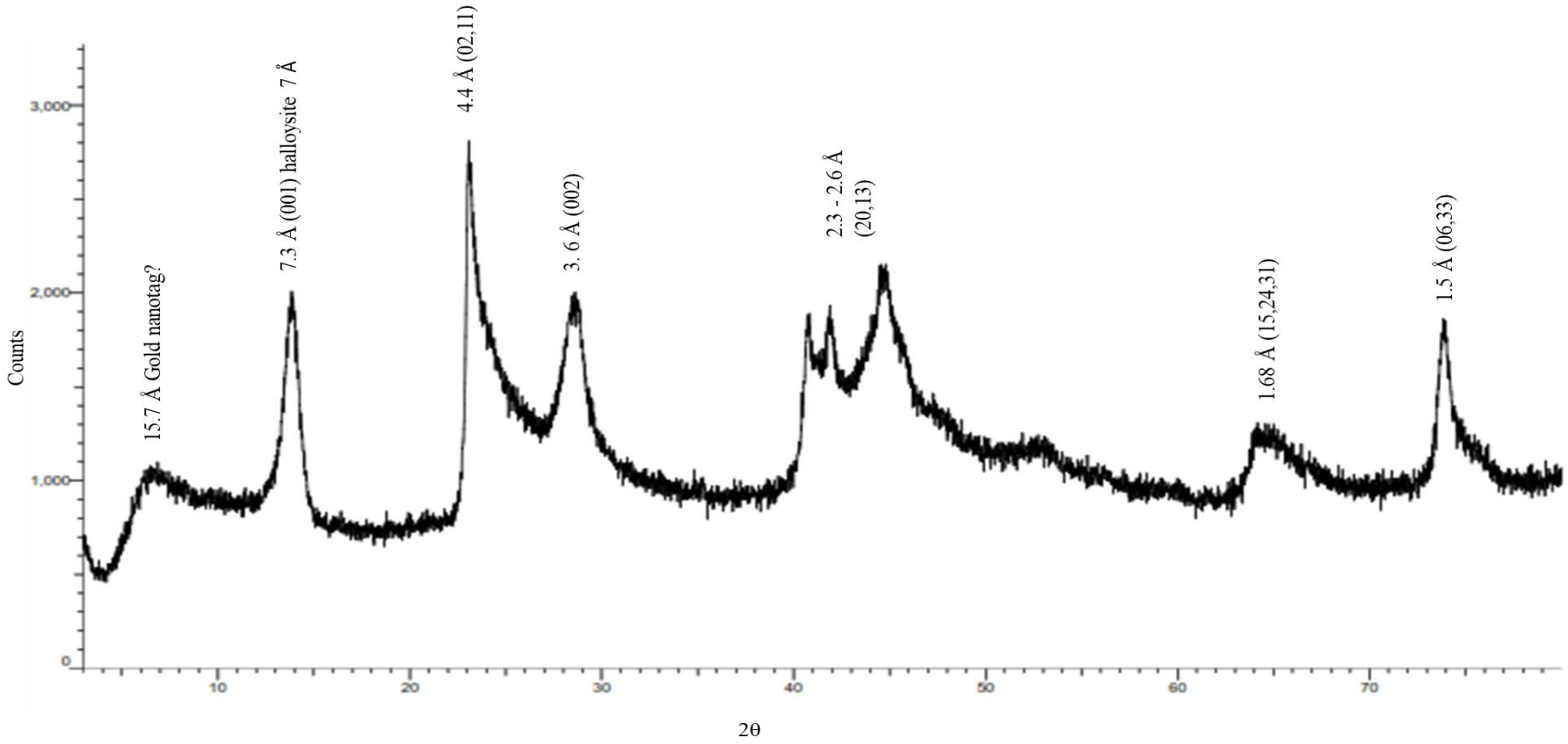

Figure 5.29. XRPD pattern of 23US + large Au nanotag with a phosphonic acid terminated linker. The key basal and non-basal diffraction bands of the halloysite are labelled where it appears that there is evidence of some halloysite (10 Å) remaining. The band at 15.7 Å has been tentatively labelled as the gold metal.

5.5 DISCUSSION

5.5.1 Experimental design for the gold and silver nano-tagging

The experiments discussed in this chapter have been designed to examine what information can be gathered from using linkers with different terminal functional groups and whether the size of the metal nanoparticles and metal used, i.e., gold or silver, affects the adsorption and location of adsorption onto the surface of the halloysite nanotubes.

The experimental design for the synthesis and attachment of the metal nanotags was conceived specifically for the use of the halloysite nanotubes and this study. In following on from the phosphate adsorption work conducted and detailed in Chapter 3, it was decided to use phosphonic acid terminated linkers for both the gold and silver nanotags, with the additional aim of using microscopy methods to visually determine the phosphonic acid adsorption sites on the halloysite nanotubes. The carboxylate terminated linker was used as a comparative anion for the surface adsorption, where previous studies have looked at the adsorption of carboxylate onto the surface of halloysite nanotubes (Du *et al*., 2008). The methyl terminated linkers were not expected to adsorb to the surface of the halloysites due to their lack of charge and so were used as control experiments to verify this. In addition, as outlined in Section 5.1, the method of reacting the metal nanotags with the linkers prior to adsorption on the halloysite nanotubes is one which is less commonly used.

The use of the two sizes of metal nanotags was also important. Multiple methods for nanotag growth control have been proposed in the literature, for example, use of anions such as citrate as stabilisers to limit aggregation (Pillai and Kumat, 2003), reductants (Li *et al*., 2012), reaction temperature (Pacioni *et al*., 2015), and electroreduction (Plieth *et al*., 2005), to name but a few. The synthesis of the three different nanotags for Experimental Set 2 focused on one silver and two gold nanotags of different sizes. For the silver nanotag, the growth was controlled by the use of the capping agent polyvinylpyrrolidone, in line with a previous study where silver was thought to occur by aggregation (Hyning and Zukoski, 1998). In contrast, kinetic control was used for the gold nanotags, by controlling the time between the reduction of gold to gold ions and the addition of the linker molecules which inhibit further growth (Li *et al*., 2012). From fundamental theory, it is known that the colour of a suspension is related to the

size of the particles within the suspension, where, a yellow solution is indicative of increased particle size with long wavelength adsorption (500-800 nm) whilst a rred solution with shorter wavelength (~400 nm) is suggestive of smaller particle sizes, for example. The yellow colour which appeared in the formation of the silver nanotags is infers a particle size of approximately ~5-10 nm (Hyning and Zukoski, 1998). Whilst for the gold nanoparticles the size can be estimated as 0.9 nm for the small nanoparticles and 3.3 nm from the timescales used (Li *et al.,* 2012). Unfortunately, these size estimates were not confirmed by UV-Vis spectroscopy for Experimental Set 2 where the nanotag sizes were estimated on solution colour only.

Whilst the size of the nanotags is an important feature, many papers also focus on controlling the shape of the nanotags, as shape can have a large effect on the reactive properties (Wiley *et al*., 2005). For the case of the nanotags used in these experiments the nanotag shapes are not definitively known. TEM analysis of the 1-2 nm gold nanotags on the surface of two halloysite (7 Å) samples from Experimental Set 1 suggested a circular cross section as viewed in 2D (Section 5.4.3, this chapter) which could indicate spheres or disks. In terms of adsorption onto the surface via the linkers it may be considered that future research using methods which allow strict control of the shape of the nanotags, such as those described by Wiley *et al*. (2005), would be required to investigate whether the shape of the nanotag affects adsorption onto the halloysite surface.

5.5.2 Effect of linker functional group on the nanotag adsorption to the halloysite nanotubes as determined by the various analytical techniques

5.5.2.1 X-ray photoelectron spectroscopy (XPS)

XPS data from Experimental Set 1 verifies that the phosphonic acid tagged metal nanoparticles had adsorbed to the surface of the halloysite nanotubes and, as such, they are effectively acting as an anchor for the gold nanoparticles. Interestingly, when comparing the amounts of phosphorus present, in percent, between the samples from the adsorption studies from Chapter 3 and those from the gold nanotag work carried out in this chapter (Table 5.4), it appears that using the nanotags results in 8 and 19 times greater phosphorus for 4Ch and 17US, respectively. These figures should be taken as an estimate only as they are calculated by comparison of the weight % of phosphorus as found by XPS, where the phosphorus peaks required longer range scan

times (8 seconds per count) due to being near their limit of detection. It cannot conclusively be stated why the difference in adsorption occurs between the two experiments given their different experimental set up such as solvents and P-loadings. Despite this, it can be expected that both phosphate and phosphonic acid would adsorb to the surface via a condensation reaction, resulting in an ester linkage (Al-O-P=O-R).

5.2.2.2 Scanning thermal analysis (STA)

Thermogravimetric analysis (TGA) was run on the samples from Experimental Set 1 with the gold nanotags and phosphonic acid and methyl terminated linkers. The TGA curves (Figures 5.6 and 5.7) indicated that the sample 4Ch + gold nanotag with phosphonic acid terminated linker showed an 18% mass loss over the temperature range 30-800 °C, whilst the sample 4Ch + gold nanotag with methyl terminated linker had a lower mass loss of 15.5% over the same temperature range. From the XPS data where it appears that the gold nanotag with phosphonic acid terminated linker had adsorbed onto the surface, whilst the methyl terminated linker had not, this suggests that 2.5 % of the sample mass of the phosphonic acid terminated linker sample may be attributed to the gold-nanotag and linker although further experiments and repeats would be required to verify this. The TGA curves for the cylindrical (4Ch) samples gold nanotags also differed in their transition temperatures where they showed distinct loss steps.

The losses at around 30-40 °C can be assigned as residual organic solvent whilst loss at around 100 °C is due to associated and or interlayer water loss. Although the samples are dehydrated there is likely still some lumen water/associated surface water present. The significant loss at 430 °C and transitions at 470-500 °C relate to the dehydroxylation of the structural hydroxyls. Dehydroxylation is thought to occur by interaction of two hydroxyl groups to form a water molecule via proton transfer, the loss of this water molecule results in a chemically bonded superoxide anion in the lattice (Kloprogge, 2016). The dehydroxylation temperature of the 4Ch nano-tagged sample with phosphonic acid terminated linker is slightly higher than that of the sample with the methyl terminated linker, 520-530 °C as opposed to 470-500 °C. The dehydroxylation temperature is controlled by several factors, including particle size distribution and sample crystallinity and in this instance, where the same sample is being studied, it is possible that the higher dehydroxylation temperature observed after

reaction with gold nanotag and phosphonic acid terminated linker for 4Ch is a result of the new complex that is formed. Despite this hypothesis, there is no evidence that the phosphonic acid linker adsorbs to the structural hydroxyls and from the research presented in Chapter 3 it seems more probable that it is the edge and surface hydroxyls that are involved in adsorption as opposed to structural hydroxyls. As a result, future work such as FTIR analysis on the samples after heating to the dehydroxylation temperature may be required to understand these changes.

TGA analysis (Figures 5.7 and 5.8) indicated that sample 17US + gold nanotag and phosphonic acid terminated linker showed an 17% mass loss whilst 17US + gold nanotag and methyl terminated linker had a lower mass loss of 15%, suggesting that 2% of the sample mass can be attributed to the gold nanotag and linker. The 17US + gold nanotag and methyl terminated linker shows multiple loss transitions, where again those at 30-40 °C are likely due to residual organic solvent whilst those seen at 130-140 °C can be viewed as associated and or interlayer water loss. The significant loss at 460 °C and losses between 540-550 °C are due to the dehydroxylation of the structural hydroxyls. The dehydroxylation temperature of the 17US + gold nanotag and phosphonic acid terminated linker was occurred at 530 °C. From the TGA analysis it is interesting to note that the structural hydroxyl dehydroxylation temperature for the polygonal prismatic sample (530-550 °C) is slightly higher than that for the cylindrical sample (470-530 °C), this is perhaps due to the more ordered structure of the prismatic halloysite.

The DSC curves for all four samples show endothermic peaks which correspond to the dehydroxylation transitions in the TGA analysis. This can be rationalised by considering that dehydroxylation is an endothermic (bond breaking) process which takes in energy in order to occur. For both cylindrical samples (4Ch) an additional, smaller, endothermic peak is observed at around 270 °C which suggests an additional thermodynamic event at this temperature, which is currently unassigned.

Therefore, it can be concluded that, in line with the XPS results, the TGA analysis infers that the surface adsorption reactions were successful when the phosphonic acid terminated linker was used with the gold nanotags whilst the methyl terminated linker did not result in surface adsorption.

5.2.2.3 Fourier transform infrared spectroscopy (FTIR)

FTIR analysis was conducted on the samples from both experimental sets. Due to too little sample being recovered three samples were not analysed (two from the 24US set and one from the 6Ch set). From the FTIR spectra of Experimental Set 1 (Figures 5.13-5.14), any differences observed in the spectra upon adsorption with gold nanotags and either methyl or phosphonic acid terminated linkers were subtle. The characteristic Al-OH stretching band heights were therefore compared after normalisation to the Si-O band height of the untreated halloysite. No significant change was measured in the band intensities and positions of the Al-OH bands before and after adsorption for the cylindrical 4Ch. In contrast, for the polygonal prismatic 17US sample, after normalisation to the Si-O band height, the 3670 cm^{-1} Al-OH stretching band was seen to reduce in intensity by up to 50% after each of the three treatments which suggests that some adsorption occurred at these sites.

The slight band at around 1440 cm^{-1} can be attributed to the scissoring mode of alkyl chain CH_2 groups (Yah *et al*., 2012). This band is observed in both the 4Ch and 17US samples from Experimental Set 1 with both phosphonic acid or phenyl phosphonic functional groups, thus providing further evidence of their successful adsorption to the surface of the halloysite nanotubes.

The additional bands (Figure 5.14) at low wavenumbers for the 4Ch sample (700-1450 cm^{-1}) can be assigned to the phenyl phosphonic acid, suggesting remnants of the material remain even after washing. No such peaks were observed with the 17US sample.

The spectra from Experimental Set 2 with both gold and silver nanotags are more complicated for all the samples (Figures 5.15-5.20). The presence of extra bands in each spectra that are not associated with halloysite suggest that both phosphonic acid and carboxylate functional groups act as successful linkers. As labelled on the figures, the bands observed at around 2857 cm^{-1} and 2932 cm^{-1} can be assigned as the symmetric and asymmetric stretching bands of CH_2 respectively (Yah *et al*., 2012) which are found in tbe carbon linker chain. For the sample 4Ch (Figure 5.16) the sharp peak at 1080 cm^{-1}, which was most clear in the sample with silver nanotag attached to the surface via phosphonic acid and was not present in the original material, may be

attributed to Al-O-P stretching (Taroni *et al*., 2019). This peak is not visible in the other samples, perhaps due to the broad Si-O stretching band of the halloysite.

Extra peaks not associated with the halloysite structure were observed for both linkers with silver and gold tagged samples. The extra peaks, as labelled on each spectrum, are essentially identical for the silver nanotag and carboxylate terminated linkers and the silver nanotag and phosphonic acid terminated linker samples whilst the extra peaks in the gold nanotag and carboxylate terminated linkers and the gold nanotag and phosphonic acid terminated linker spectra are similar but with subtle differences to the silver nanotag samples. There are two possible reasons for this; one is potential contaminants in the silver and gold nanotags whilst the other explanation is due to the degradation of tert-butylamine-borane (TBAB) resulting in amine/nitrogen/carboxyl type components, although it was not possible to library match any of these exactly. Given the peak positions, particularly in the case of the silver nanotag samples, it is more likely to be due to breakdown products of the tert-butylamine-borane.

The broad band at around 3400 cm^{-1} in sample 5Ch (Figure 5.17) indicates that the cylindrical halloysite retains significant moisture even after drying down under vacuum. Similar observations have been made for this sample (Chapter 6, Section 6.3.1) by XRPD where it appeared to hold onto interlayer water for longer than one of polygonal prismatic samples under the same conditions, most likely due to its smaller size and interparticle pores.

The general trend in all the samples towards a reduction in intensity of all three (where three are present) Al-OH stretching bands after normalisation to the 1024 cm^{-1} Si-O stretching band was observed. Additionally, some of the samples show a change in shape of the two Si-O stretching bands with respect to each other which is, as yet, unexplained. There appears to be no common trend to this feature.

5.2.2.4 Optical microscopy

The optical microscopy images presented in Figure 5.21 provide a clear example that the use of phosphonic acid as a linker for the gold nanotags resulted in gold nanotags being anchored to the surface since these samples changed in colour from white to brownish. The optical microscopy images also showed that for the 17US halloysite with the phosphonic acid linked gold nanotag the colour change in the sample appeared to be even across all of the sample whilst for the 4Ch halloysite under the

same conditions some pure white, and hence unreacted halloysite, remained. This ties in with the TEM observations from Section 5.4.3 and those made in Chapter 3 (Section 4.3.2) where Tyndall measurements showed that the 17US halloysite seemed to disperse more easily in solution and was less prone to forming aggregates. It has been shown in the formation of clay nanocomposites that halloysites disperse more easily than other minerals such as montmorillonite and kaolinite and this was explained as due to the fewer surface hydroxyl groups on the halloysite (Du *et al.*, 2008). This potentially may occur since in halloysite the hydroxyl groups are found primarily in the inner lumen, whereas for kaolinite both sides of its platy form are exposed.

5.5.3 Observations from transmission electron microscopy (TEM) analysis

From the evidence provided by the analytical methods outlined in Section 5.5.2, only the gold nanotags with phosphonic acid terminated linker samples from Experimental Set 1 were analysed by TEM. The TEM analysis provides further and direct evidence for the presence of the gold nanotags on the surface on the nanotubes, as shown in Figures 5.10-5.11. The features observed were verified as gold nanotags using *in situ* EDX. It was noted that the two morphologies of halloysite, cylindrical and prismatic, could be distinguished by TEM, both before and after gold tagging. The cylindrical samples (4Ch) were shown to be much smaller with fewer breakages and truncations at the terminus of the tubes, by contrast, the polygonal prismatic sample (17US) was seen to be much larger with a regular occurrence of splintering observed at the terminus of the tubes, as reported by other authors (Hillier *et al*., 2016) and outlined in Chapter 4. Defects in the layer stacking which appeared to be pores were much more frequently observed in the polygonal prismatic sample than the cylindrical sample, this may be attributed to the disorder caused by the blocky nature of the polygonal prismatic outer layers, where uneven layer formation and large pores have previously been observed in their cross-sections (Churchman *et al*., 1995). Such defects were also observed and discussed in detail in Chapter 4 (Section 4.3.2).

It can clearly be seen that the nanotags are present in the inner lumen of both nanotube morphologies (Figure 15.10 c, d, e, f; Figure 5.11 c, d, e, f). This would appear in line with previous studies that have shown that the adsorption of phosphonic acids occurs on the inner lumen of halloysites (Taroni *et al.*, 2019) which is composed of hydroxyl

groups and indeed correlates with the results found in Chapter 3 which suggested that these aluminol sites are the location of anion adsorption reactions.

In addition, there is some evidence of sparse gold nanotags on the edges and outer surface of the 4Ch cylindrical samples (Figure 15.10c). In the case of those which appeared to be non-uniform and have a high density of defects (Figure 15.10f) the presence of the gold on the edges and outer surfaces was much more frequent. In comparison, the 17US polygonal prismatic sample had a greater density of gold nanotags on these outer surface and edge sites (Figure 15.11 c, d, e, f). The outer nanotube surface is composed of a siloxane sheet which, as outlined in Chapter 3, is not expected to undertake anion adsorption. This leads to the conclusion that the observed nanotags on the external surface may be indicative of steps and edges along the surface. This correlates with the AFM analysis and results discussed in Chapter 4 (Section 4.3.2) where the polygonal prismatic samples appeared to have a greater number of steps and edges, and hence edge aluminol sites, on their outer surfaces when compared to the cylindrical samples.

For some of the TEM images of the 4Ch samples, there appears to be little/no trace of the gold nanotags suggesting that the reaction process was not homogenous across all nanotubes. This correlates with the Tyndall observations made in the phosphate adsorption reactions in Chapter 3 (Section 3.4.2), where the 4Ch sample was less likely to stay in suspension and showed a preference to flocculation. It can be suggested that the 4Ch sample for these reactions may not have fully dispersed to allow all sites to react with the linkers for the gold nanotags. In contrast, the 17US nano-tagged samples appeared to be more evenly affected by the treatment and very few nanotubes were observed with little or no gold. From comparison of the TEM images of both morphologies before and after nano-tagging, there appeared no significant difference in dispersion of the nanotubes although study of a greater number of halloysites from which further analysis of the images, such as counts of nanotubes per area, would be required to verify this observation.

Lumen measurements (Table 5.6) indicate that both tubular morphologies have a similar lumen diameter of around 11-12 nm. This figure corroborates the lumen diameter measurements taken from the cross-sections of the halloysite nanotubes in Chapter 4. One unexplained feature that was observed in the TEM analysis was the

broadening of the 4Ch cylindrical nanotubes at the terminus of the tubes (Figure 5.10e), indeed some of the lumen measurements were measured as 4 times as wide at the ends of the nanotubes compared to the centre. It is not thought that this is due to beam damage and is a feature that is observed more frequently in the pure cylindrical samples as opposed to the polygonal prismatic samples. Future microscopy work may be required to explain this feature.

The next steps in this study were prevented by the COVID-19 pandemic in the Spring and Summer of 2020. Further work had been planned to study a selection of the samples from Experimental Set 2 by TEM to determine whether there was a difference in location of adsorption between the phosphonic acid and carboxylate terminated linkers as well as an effect on the metal nanotag type and size.

5.5.4 Interpretations of the selected area electron diffraction patterns (SAEDP) and X-ray powder diffraction (XRPD) analysis

SAED patterns were recorded for both the pure and gold tagged halloysites. Typically, electron diffraction patterns can give information on the crystalline nature of a material. Generally, when interpreting selected area electron diffraction patterns *h0l* reflections appear as sharp diffraction spots whilst *hkl* reflections appear as streaky diffraction spots (Kohyama, 1978). There is a definite observed difference between the 4Ch and 17US diffraction patterns, where the cylindrical (4Ch) halloysite pattern consists of multiple concentric rings whilst the polygonal prismatic (17US) sample is comprised of a combination of streaks and spots. Both pure 4Ch diffraction patterns were taken of a cluster of nanotubes whilst the pure 17US diffraction patterns were taken of lower density clusters, suggesting that the two cannot be directly compared since it is known that concentric rings may be observed when a material is a collection of a number of crystals of different orientations. Despite this, the 4Ch and gold nanotag pattern which is taken from a low-density cluster shows a mixture of concentric rings and lines indicating that the feature is due to the crystal structure of the nanotube and not an artifact of the nanotube clusters.

The concentric rings observed in the 4Ch sample can be explained by considering that a cylindrical sample has much less crystallographic ordering between adjacent planes of atoms due to its curved layers. The polygonal prismatic sample is more likely to show ordering as the outer layers are planar (Chapter 4, Section 4.3.2). The stacking

of planar sheets is more conducive to ordering between the layers, hence long-range order can occur, resulting in the spots observed in the electron diffraction patterns. Similar results can be seen in the XRPD patterns and resultant 'CP' index between the two materials as discussed in Chapter 2. The disorder between the two tubular morphologies is observed by the degree of definition of the (20,13) bands in XRPD and the structural disorder can arise due to features such as stacking faults or impurities.

The results from the XRPD traces can be viewed as inconclusive. It appeared that there may be some low angle features that are suggestive of regular sized particles which may be the silver nanotags. Due to the general overlap of characteristic identification bands between of both the halloysite and gold and silver, it was not possible to conclusively identify the presence of the metal nanotags. Future work involving conducting XRPD analysis of the raw silver and gold nanotags would be required to verify this.

5.6 CONCLUSION

The experimental results presented in this chapter provide an overall link between Chapters 3 and 4 by validating some of the assumptions made in the anion adsorption reactions and reinforcing the efficacy of imaging techniques for studying clay minerals. Gold and silver nano-tagging on halloysite nanotube supports has many potential applications in the rapidly expanding area of nano-research which is applied to problems faced in everyday industry and technology. Understanding the effect of the morphology of the nanotube, along with the importance of selecting the appropriate linker for surface adsorption has an impact on the efficacy of halloysite nanotubes as supports for these technologies.

The method of first reacting the gold or silver nanotag to the linker before adsorption onto the halloysite surface was shown to be effective where the linkers selected (11-mercaptoudodecanoic acid and 12-mercaptododecylphosphonic acid) for their anionic functional groups, carboxylate and phosphonic acid respectively, adsorbed onto the halloysite surface. There was no evidence of adsorption for the dodecanthiol group which could be explained by the fact that the methyl group shows no affinity for surface adsorption.

Multiple analytical methods have been used in this chapter including XPS, TEM, FTIR, STA, XRPD, SAED and optical microscopy. The general agreement across the methods was that the gold and silver nanotags with phosphonic acid and carboxylate linkers were detected in the presence of the halloysite nanotubes of both tubular morphologies. The TEM analysis of the 17US and 4Ch halloysite (7 Å) samples with the gold nanotags and phosphonic acid terminated linkers provided evidence for the presence of the gold on the nanotubes. It was noted that the polygonal prismatic (17US) nanotubes visibly adsorbed a greater number of nanotags than the cylindrical (4Ch) nanotubes. In the case of the polygonal prismatic nanotubes the gold nanotags seemed prevalent in both the inner lumen and at the edge sites as well as being observed regularly on the outer walls. In contrast, for the cylindrical halloysite the sparse nanotags appeared primarily in the inner lumen, unless high defect nanotubes were present.

From the original aims as laid out in the introduction to this chapter and the experimental results obtained using XPS, FTIR and XRPD, it has been shown that the nano-tagging with the two different metals was successful. In addition, the TEM work was successful in proving that the gold nanotags were present on the surface of the halloysite nanotubes, although this did not directly prove that they adsorbed via the phosphonic acid terminated linkers.

Future work in this area may involve the study of the silver nanotags and the gold nanotags of varying sizes to determine whether the type of metal, the different linkers or size of the nanotag has an effect on the surface adhesion. It would also be interesting to investigate in more detail the dispersion of the nanotags on the surfaces of the halloysite nanotubes under these changing conditions.

5.7 REFERENCES

2011/696/EU: Commission Recommendation of 18 October 2011 on the definition of a nanomaterial. *Official Journal of the European Union*.

Breen, C., D'Mello, N. & Yarwood, J. (2002) The thermal stability of mixed phenylphosphonic acid/water intercalates of kaolin and halloysite. A TG-EGA and VT-drifts study. *Journal of Materials Chemistry*, **12**, 273-278.

Burridge, K., Johnston, J. & Borrmann, T. (2011) Silver nanoparticle–clay composites. *Journal of Materials Chemistry*, **21**, 734-742.

Cao, H., Sun, X., Zhang, Y. & Jia, N. (2012) Electrochemical sensing based on gold nanoparticle-decorated halloysite nanotube composites. *Analytical Biochemistry*, **430**, 111-115.

Cataldo, S., Lazzara, G., Massaro, M., Muratore, N., Pettignano, A. & Riela, S. (2018) Functionalized halloysite nanotubes for enhanced removal of lead(II) ions from aqueous solutions. *Applied Clay Science*, **156**, 87-95.

Churchman, G.J., Davy, T.J., Aylmore, L.A.G., Gilkes, R.J. & Self, P.G. (1995) Characteristics of fine pores in some halloysites. Pp. 89. *Clay Minerals*, 30.

dos Santos, E.C., Rozynek, Z., Hansen, E.L., Hartmann-Petersen, R., Klitgaard, R.N., Løbner-Olesen, A., Michels, L., Mikkelsen, A., Plivelic, T.S., Bordallo, H.N. & Fossum, J.O. (2017) Ciprofloxacin intercalated in fluorohectorite clay: Identical pure drug activity and toxicity with higher adsorption and controlled release rate. *RSC Advances*, **7**, 26537-26545.

Du, M., Guo, B., Lei, Y., Liu, M. & Jia, D. (2008) Carboxylated butadiene–styrene rubber/halloysite nanotube nanocomposites: Interfacial interaction and performance. *Polymer*, **49**, 4871-4876.

Jana, S., Kondakova, A.V., Shevchenko, S.N., Sheval, E.V., Gonchar, K.A., Timoshenko, V.Y. & Vasiliev, A.N. (2017) Halloysite nanotubes with immobilized silver nanoparticles for anti-bacterial application. *Colloids and Surfaces B: Biointerfaces*, **151**, 249-254.

Kim, T., Kim, S., Lee, D.K., Seo, B. & Lim, C.-S. (2017) Surface treatment of halloysite nanotubes with sol–gel reaction for the preparation of epoxy composites. *RSC Advances*, **7**, 47636-47642.

Kloprogge, J.T. (2016) Chapter 6 - characterisation of halloysite by spectroscopy. Pp. 115-136. In P. Yuan, A. Thill, and F. Bergaya, Eds. *Developments in Clay Science*, 7, Elsevier.

Kohyama, N., Fukushima, K. & Fukami, A. (1978) Observation of the hydrated form of tubular halloysite by an electron microscope equipped with an environmental cell. *Clays and Clay Minerals*, **26**, 25-40.

Li, Y., Liu, S., Yao, T., Sun, Z., Jiang, Z., Huang, Y., Cheng, H., Huang, Y., Jiang, Y., Xie, Z., Pan, G., Yan, W. & Wei, S. (2012) Controllable synthesis of gold nanoparticles with ultrasmall size and high monodispersity via continuous supplement of precursor. *Dalton Transactions*, **41**, 11725-11730.

Lvov, Y., Wang, W., Zhang, L. & Fakhrullin, R. (2016) Halloysite clay nanotubes for loading and sustained release of functional compounds. *Advanced Materials*, **28**, 1227-1250.

Mallick, K., Witcomb, M. & Scurrell, M. (2006) Silver nanoparticle catalysed redox reaction: An electron relay effect. *Materials Chemistry and Physics*, **97**, 283-287.

Pacioni, N.L., Borsarelli, C.D., Rey, V. & Veglia, A.V. (2015) Synthetic routes for the preparation of silver nanoparticles. Pp. 13-46. In E.I. Alarcon, M. Griffith, and K.I. Udekwu, Eds. *Silver nanoparticle applications: In the fabrication and design of medical and biosensing devices*,Springer International Publishing, Cham.

Pillai, Z.S. & Kamat, P.V. (2004) What factors control the size and shape of silver nanoparticles in the citrate ion reduction method? *The Journal of Physical Chemistry B*, **108**, 945-951.

Plieth, W., Dietz, H., Anders, A., Sandmann, G., Meixner, A., Weber, M. & Kneppe, H. (2005) Electrochemical preparation of silver and gold nanoparticles:

Characterization by confocal and surface enhanced raman microscopy. *Surface Science*, **597**, 119-126.
Qu, S., Du, C., Song, Y., Wang, Y., Gao, Y., Liu, S., Li, Y. & Zhu, D. (2002) Optical nonlinearities and optical limiting properties in gold nanoparticles protected by ligands. *Chemical Physics Letters*, **356**, 403-408.
Rao, K.S., Ganeev, R.A., Zhang, K., Fu, Y., Boltaev, G.S., Maurya, S.K. & Guo, C. (2019) Comparative analyses of optical limiting effects in metal nanoparticles and perovskite nanocrystals. *Optical Materials*, **92**, 366-372.
Taroni, T., Meroni, D., Fidecka, K., Maggioni, D., Longhi, M. & Ardizzone, S. (2019) Halloysite nanotubes functionalization with phosphonic acids: Role of surface charge on molecule localization and reversibility. *Applied Surface Science*, **486**, 466-473.
Van Hyning, D.L. & Zukoski, C.F. (1998) Formation mechanisms and aggregation behavior of borohydride reduced silver particles. *Langmuir*, **14**, 7034-7046.
Vergaro, V., Abdullayev, E., Lvov, Y.M., Zeitoun, A., Cingolani, R., Rinaldi, R. & Leporatti, S. (2010) Cytocompatibility and uptake of halloysite clay nanotubes. *Biomacromolecules*, **11**, 820-826.
Vinokurov, V.A., Stavitskaya, A.V., Chudakov, Y.A., Ivanov, E.V., Shrestha, L.K., Ariga, K., Darrat, Y.A. & Lvov, Y.M. (2017) Formation of metal clusters in halloysite clay nanotubes. *Science and Technology of Advanced Materials*, **18**, 147-151.
Wiley, B., Sun, Y., Mayers, B. & Xia, Y. (2005) Shape-controlled synthesis of metal nanostructures: The case of silver. *Chemistry – A European Journal*, **11**, 454-463.
Yah, W.O., Takahara, A. & Lvov, Y.M. (2012) Selective modification of halloysite lumen with octadecylphosphonic acid: New inorganic tubular micelle. *Journal of the American Chemical Society*, **134**, 1853-1859.
Yuan, P., Tan, D. & Annabi-Bergaya, F. (2015) Properties and applications of halloysite nanotubes: Recent research advances and future prospects. *Applied Clay Science*, **112-113**, 75-93.
Zhang, X.F., Liu, Z.G., Shen, W. & Gurunathan, S. (2016) Silver nanoparticles: Synthesis, characterization, properties, applications, and therapeutic approaches. *International Journal of Molecular Sciences*, **17**.

Chapter 6

Study of the Interlayer Water of Halloysite Nanotubes using Neutron Scattering

6.1 INTRODUCTION

6.1.1 Background to research aims

The dynamics of surface and interlayer water molecules in clay minerals plays a key role in the diffusion of water in clay type barriers (Bordallo *et al*., 2008) and, as such, this water has been studied by a variety of techniques, one of which is neutron scattering (Bordallo *et al*., 2008; Gates *et al*., 2012; Berg *et al*., 2017; Gates *et al*., 2017).

It has also been well documented (MacEwan, 1947; Bates *et al*., 1950; Churchman and Carr, 1975; Costanzo and Giese, 1985) and outlined in Chapter 1 (Section 1.2.3), that halloysites are the only kaolin polymorph which are formed in nature with interlayer water. The key evidence for this is that irreversible removal of the interlayer water results in the layer d-spacing of halloysites reducing from ~10 Å to ~7 Å. While the occurrence of the interlayer water in halloysites is not disputed, there arises a greater debate as to its role in halloysite formation and of its influence on the morphology of the halloysite minerals. It has been reported that the interlayer water content of hydrated halloysite nanotubes (Figure 6.1) is around 12.3 % mass (Kohyama *et al*., 1978), which corresponds to approximately two water molecules per unit cell. These water molecules are believed to be arranged as a monolayer between the alumina and siloxane sheets.

Subsequent, and more detailed studies have distinguished between two types of interlayer water; namely associated water (Costanzo *et al*., 1984) and ‘hole’ water (Costanzo and Giese, 1985) as outlined in the Introduction chapter (Section 1.2.4). It has been suggested, based on FTIR analysis, that the ‘hole’ water probably forms hydrogen bonds with the oxygen in the ditrigonal holes of the silicate tetrahedra (Costanzo and Giese, 1985).

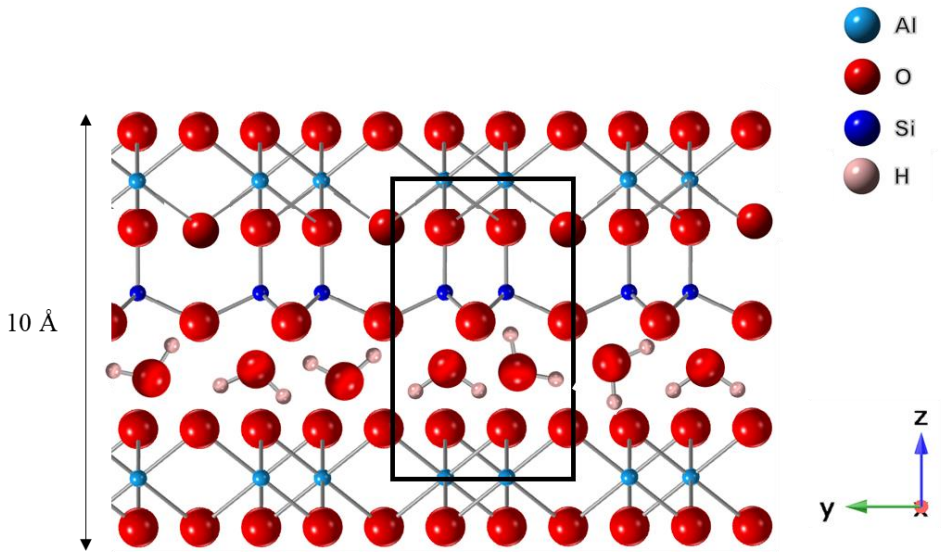

Figure 6.1. Unit cell (black rectangle) of a halloysite (10 Å) sample $Al_2Si_2O_5(OH)_4.2H_2O$, along the (100) direction.

Currently, the orientation of the associated interlayer water with respect to the halloysite layers is not fully understood. Previous research has attempted to model the interaction between water molecules and the halloysite surface using density functional theory (DFT) and classical molecular dynamics modelling (Presti *et al*., 2015). However, in that work, the authors used a kaolinite surface which was not sterically identical to halloysite nanotube surfaces due to the curvature of the nanotubes. Instead, it was effectively a hydrated kaolinite. They concluded that the water molecules arranged themselves in a low-density ice-like orientation with respect to the siloxane layer but that the water molecules orientated towards the alumina layer were much less ordered and showed higher density packing. The ice-like structure at the siloxane surface may arise as this is the lowest energy conformation for the water molecules. They also concluded that interlayer water molecules were much more ordered than those adsorbed to the outer surfaces of the halloysite nanotubes. The study by Presti *et al*. (2015) supported the results from the only neutron scattering work which has been reported on interlayer water in halloysite (Bordallo *et al*., 2008). The Presti paper is also the only report found at the time of writing, which was able to discriminate the dynamics of surface water from that of interlayer water, where previous works such as that by Letellier and Fripait (1978) used NMR to study halloysite (10 Å), but were unable to distinguish between the two types of water. A

more recent study by Ferrante *et al*. (2017) looked at interlayer water in a lightly curved section of halloysite by density functional theory modelling. They found that strong hydrogen bonds existed between the water molecules and the alumina surface, suggesting preferential adsorption to this surface whilst weaker hydrogen bonds existed between the water molecules and the siloxane surface.

This chapter reports on research carried out in collaboration with researchers from Prof Neal Skipper's group at University College London using neutron scattering experiments. These experiments were undertaken at the ISIS Neutron and Muon Source, Didcot. The overarching aim of this work was to use neutron spectroscopy experiments to provide information on the dynamics of the interlayer water and neutron diffraction experiments to provide information on the structure of the interlayer water molecules with respect to the alumina and siloxane surface of the halloysite nanotubes. It was hoped that by understanding more about the structure and dynamics of interlayer water in halloysites that the information gathered can contribute to the debate on the role of the water in the formation of halloysite nanotubes. In addition, a greater comprehension of this interlayer water may enable understanding as to whether, on the atomic scale, the surface of halloysite (10 Å) differs to that of halloysite (7 Å) with respect to adsorption reactions, since the interlayer water effectively cleaves open the halloysite (10 Å) sheets, potentially exposing additional surfaces.

The following section details some key fundamentals related to neutron scattering experiments. Getting access to sufficiently high neutron fluxes requires access to a spallation source, therefore, this is not a common analytical technique. As a result, there are only a select few centres around the world which are equipped to conduct these types of experiments, one of which is the ISIS Neutron and Muon Source at the Rutherford Appleton Laboratories, Oxfordshire.

6.1.2 Fundamental theory behind neutron scattering reactions

Neutron scattering is an effective analytical technique which covers both neutron spectroscopy and neutron diffraction. The interaction of neutrons with the atomic nuclei of matter is often weak and the strength of scattering can be defined either as

the scattering length (b) or the scattering cross-section (σ), which is an area and linked to the scattering length, as shown below in Equation 6.1. The scattering cross-section can be used to compare the different types of interaction between the neutron and the nucleus (Dove, 2002):

Equation 6.1. $\sigma = 4\pi b^2$

Where σ = scattering cross section (barn), b = scattering length (fm)

In the context of studying interlayer water in halloysite (10 Å), the use of neutrons has many benefits over X-ray methods for analysis. For example, although the interaction between neutrons and matter is much weaker than X-ray diffraction, neutrons have a smaller attenuation coefficient than X-rays which enables them to penetrate deeper into the sample, in the order of several cm (IAEA, 2005). Additionally, time scales can be studied in the order of 10 ps to 100 ns whilst length scales can be studied in the order of 10^{-15} m (Dove, 2002). However, the key advantage of neutrons is they can very easily 'see' hydrogen atoms due to their large incoherent scattering cross section (Table 6.1), although it has yet to be explained why hydrogen has a much greater scattering value than other atoms. This variation in incoherent cross-sections in neutron scattering makes it possible to conduct isotope studies as shown by the variation in scattering cross-sections in Table 6.1. In contrast, owing to the low electron density present in hydrogen, it is not possible to assign coordinates to hydrogen atoms in a cell using X-rays.

In this chapter, the halloysite samples were analysed after varying degrees of deuteration, 100 % D_2O, 50% D_2O: 50% H_2O and 35.8 % D_2O (nul) alongside the fully hydrated (100% H_2O) halloysites. In this context, nul refers to no scattering since hydrogen has a negative scatter and deuterium has a positive scatter so, at the ratio of 35.8%, effectively they cancel each other out.

Table 6.1. Incoherent and coherent neutron cross sections for expected atoms in halloysite.

Atom	Incoherent cross section area, σ (barn)	Coherent cross section length, *b* (fm)
H	80.270	-3.741
D	2.050	6.671
Si	0.000	4.107
Al	0.008	3.449
O	0.000	5.803

Table source: National Institute of Standards and Technology (NIST) database.

Incoherent scattering does not provide structural information for a given sample but instead describes the dynamics of individual particles. By comparison, coherent scattering describes correlations between the nuclei. The total scattering of an atom can be described by the sum of its incoherent and coherent cross sections as given in Equation 6.2:

Equation 6.2. $S(\mathbf{Q}, \omega) = S_{inc}(\mathbf{Q}, \omega) + S_{coh}(\mathbf{Q}, \omega)$

Where S = scattering, **Q** = the momentum transferred to the neutron during the scattering process and **ω** = the energy transferred to the neutron during the scattering process.

Neutrons are scattered according to the scattering vector **Q**, where **Q** can be defined as in Equations 6.3-6.4:

Equation 6.3. $\mathbf{Q} = \frac{4\pi sin\Theta}{\lambda} = \frac{2\pi}{d}$

Where d = d-spacing (Å), λ = wavelength and θ = angle of scattering

Equation 6.4. $\mathbf{Q = k\text{-}k'}$

Where **Q** = scattering vector, **k** = incident wave vector and **k' =** scattered wave vector (Figure 6.2).

The three different types of scattering, elastic, inelastic and quasi-elastic are depicted in Figure 6.2. Elastic scattering can be defined as having no energy exchange upon interaction between the neutron and sample ($\hbar\omega=0$). As a result, there is no elastic scattering in a fluid. Whilst inelastic scattering occurs from an exchange in energy of the neutron after interaction with the sample ($\hbar\omega\neq0$) and often occurs due to discrete energy step processes, such as vibrational or stretching modes. Quasi-elastic neutron scattering (QENS), arises with a small energy exchange and occurs when there is a change in momentum of a neutron after interaction with a sample that is centred at energy (E) = 0 ($\hbar\omega \neq 0 \approx$neV). The broadening of the QENS scattering is Q dependent and is associated with non-quantised diffusional behaviour, such as Brownian motion and classical rotation. QENS is used to examine incoherent scattering, which describes the dynamics of individual particles. Hence, this type of analysis probes diffusion at a molecular level and, in the case of interlayer water in halloysites, should provide information on the type of movement preferred by the interlayer water.

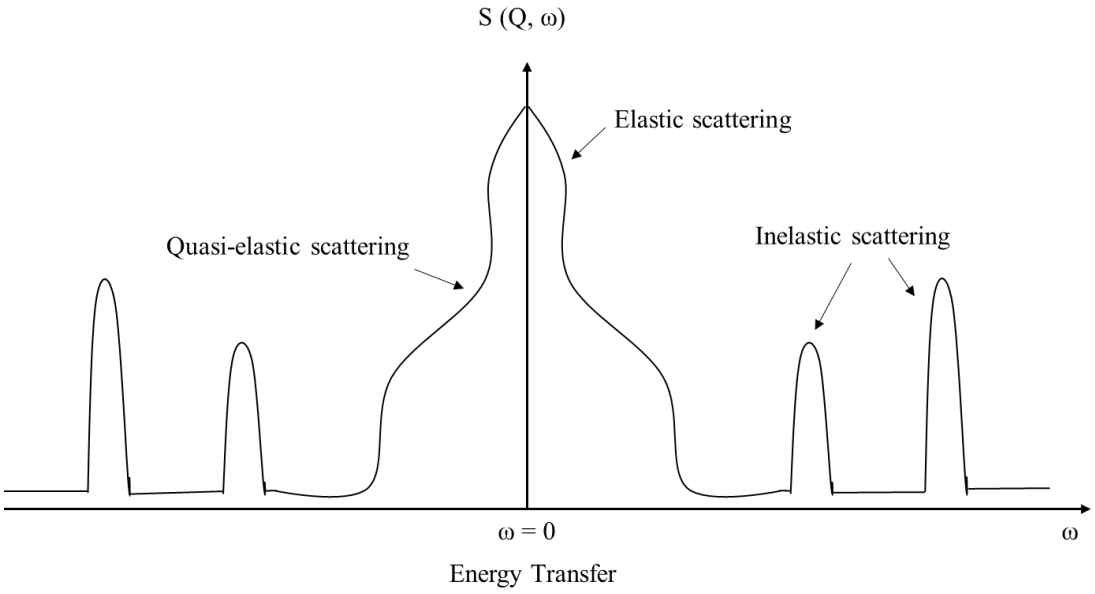

Figure 6.2. Depiction of the different types of energy transfer that occur during neutron scattering.

For the data presented in this thesis, the neutron scattering experiments were conducted on the OSIRIS instrument (www.isis.stfc.ac.uk./Pages/osiris). OSIRIS measures inelastic/quasi-elastic scattering and can be described as an inverted

geometry instrument, whereby only the neutrons that satisfy the Bragg equation are scattered by the sample and are then analysed using a large area crystal array. The scattered neutrons are directed towards the detector bank where 42-element ^{3}He detectors are placed, to enable recording of both elastic and inelastic scattering. In neutron scattering experiments, high Q relates to a large degree of backscattering and arises from inelastic scattering, whilst a low value of Q results from low scattering, i.e. elastic scattering (Figure 6.3).

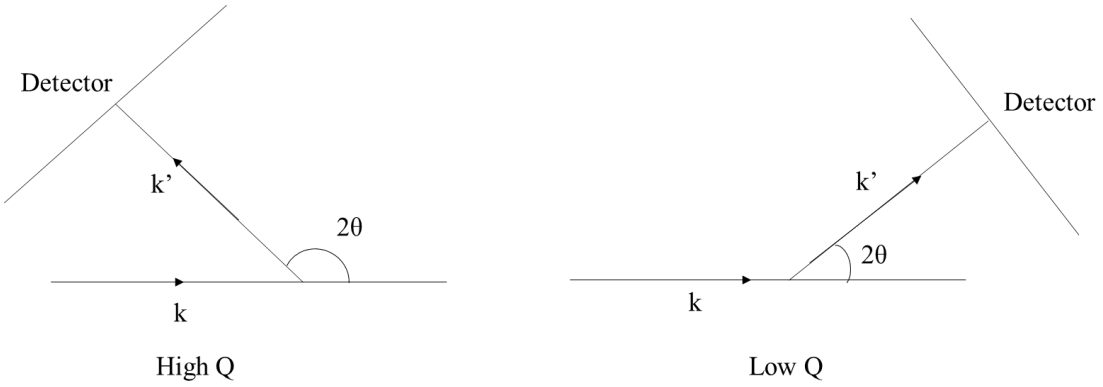

Figure 6.3. Schematic of the relationship between neutron scattering and Q, where Q can be defined as the scattering vector, 2θ is the scattering angle and k and k' are the incident and scattered wave vectors respectively.

Multiple studies have been conducted using QENS to study materials such as $CaCO_3$ chalk (Berg *et al*., 2017), Portland cement (Bordallo *et al*., 2006) and clay minerals such as montmorillonite (Bordallo *et al*., 2008; Gates *et al*., 2012; Gates *et al*., 2017). The only such reported study on halloysite is by Bordallo *et al*. (2008) who compared halloysite to montmorillonite in terms of the effect of the absence or presence, respectively, of interlayer cations on the dynamics of interlayer water in clays. This lack of interlayer cations in halloysite as well as the two distinct uncharged surfaces, alumina and siloxane, which constrain the interlayer water, make halloysite a unique and interesting material to study by neutron scattering methods. The overall aim of this work, therefore, was to study the interlayer water in halloysite nanotubes using neutron scattering techniques to further understand its structure and dynamics.

6.2 METHODS

6.2.1 Deuteration of Halloysites

Four halloysite (10 Å) samples were selected for analysis, 5Ch, 6Ch, 23US and 24US, where their physical characteristics are outlined in Chapter 2, Table 2.1. In preparation for the neutron diffraction experiments, the halloysite (10 Å) samples were deuterated by vapour transport to varying degrees at UCL by another PhD student, Aasim Shaffi. Four levels of deuteration were used; 0% deuteration, 35.8 % deuteration (nul), 50% deuteration and 100% deuteration. Nul refers to no scattering since hydrogen has a negative scatter and deuterium has a positive scatter so, at the ratio of 35.8%, they cancel each other out. The selected deuterated levels were made up into 160 ml stock solutions of deuterium oxide and water at the following ratios of D_2O to H_2O:

1. 100% H_2O: solution of H_2O (160 ml)
2. 35.8 % D_2O/nul: mix D_2O (57.28 ml) with H_2O (102.72 ml)
3. 50% D_2O: mix D_2O (80 ml) with H_2O (80 ml)
4. 100% D_2O: solution of D_2O (160 ml)

The halloysites were briefly hand ground to a powder in a pestle and mortar and transferred to a watch glass. The ground halloysites were placed in a container along with 40 ml of the deuterated solution which was replaced every week for four weeks. Once the deuteration was assumed to be complete, due to the long timescale of four weeks, the samples were rapidly transferred to loosely opened plastic bags within sample bottles which had tissue paper saturated in the D_2O:H_2O ratio equivalent to the sample. The bottle lids were fixed with Parafilm to prevent accidental loosening and fix the lids until ready for analysis. In order to minimise any interlayer water loss from the samples, the handling of the halloysites in open atmosphere was rapid.

In these experiments, the aim was to replace the Al-OH surface hydrogen atoms with the heavier deuterium and maintain and observe the natural orientation and stacking structure of the interlayer water molecules. Whilst previous studies on the deuteration of kaolin minerals have used an organic molecule, such as hydrazine, to expand the kaolin layers prior to deuteration as was reported for kaolinite (Ledoux and White, 1964), such methods were not feasible for these experiments. Where the organic

molecules can be used to expand the interlayers of halloysite, and hence, allow the reintroduction of water, it is not yet known if the water will re-orient itself and occupy the interlayer in the same way as the original interlayer water, or if the same amount of water would enter the interlayer as would naturally occur.

6.2.2 X-ray powder diffraction (XRPD)

Repeat scans were run on a Panalytical X-pert Pro instrument from 3-70 ° 2 θ with a step size of 0.017 ° and a total time per step of 27.31 s. A copper anode was used with a wavelength of 1.5414 Å. The halloysite (10 Å) samples were gently hand ground and quickly packed into the aluminium sample holders. 200 continuous scans of 15 minutes each were run over 51 hours of the samples to observe the rate of *in situ* dehydration of the halloysites.

6.2.3 Fourier transform infrared spectroscopy (FTIR)

ATR-FTIR analysis was run on a Bruker Vertex 70 spectrometer which was dry-air purged before and during analysis. Spectra were measured in the mid-infrared region of 4000 to 400 cm^{-1} at a resolution of 4 cm with 200 scans per sample. FTIR analysis was run on both hydrated and dehydrated samples where the dehydrated samples were oven dried overnight at 200 °C.

6.2.4 Neutron spectroscopy – OSIRIS

Neutron spectroscopy experiments were conducted using the OSIRIS instrument to measure the dynamics of the bulk and interlayer water. OSIRIS is a time of flight pulsed neutron source, where the neutron source was a tantalum target. Incident wavelength of the neutrons was kept fixed at 6.5 Å with an energy of 1.845 meV by pyrolytic graphite. Additionally, graphite moderators were also used to control the neutron speed.

Due to the time required to run each sample, around 4-5 days, one hydrated (100% H_2O) halloysite was studied by this method, the cylindrical 6Ch. The halloysite (10 Å) sample was sealed in an aluminium holder to maintain its moisture state throughout the analysis. A diffraction scan was run at 5 K for 300 µAmpHours within the d-spacing range of d6-d10 (6-10 Å) to verify the hydration state of the halloysite. Unlike

the rest of this thesis, which has used the units degrees Celsius for temperature, the units Kelvin have been used to describe these experiments since they are the standard units for such measurements and were used in the experimental set up and throughout the data analysis. The units µAmp-Hour are simply a measure of the total number of neutrons that are directed towards the sample.

6.2.4.1 Elastic fixed window scans of 6Ch in the (10 Å) state

Elastic fixed window scans measure the elastic scattering of a sample and act in a similar way to a differential scanning calorimetry scans, in that it can be used to detect thermal transitions in a sample (Sakai, 2015). Elastic window scans can be run either from high to low, or low to high temperatures, both of which were conducted in these experiments. To determine the transition temperatures of the halloysite, an elastic fixed window scan was performed between temperatures of 5 – 320 K and measurements were taken at 2 K increments between 102 and 252 K, followed by a diffraction scan at 252 K in the d-spacing range of d6-d10, where this range refers to a d-spacing of between 6-10 Å. The temperature of the sample was then reduced to 5 K.

6.2.4.2 QENS scans of 6Ch in the (10 Å) state

From the elastic window transition temperatures observed, QENS analysis then was carried out at 5 K (2 x 300 µAmp-Hour), 150 K (3 x 300 µAmp-Hour), 200 K (3 x 300 µAmp-Hour) and 250 K (3 x 300 µAmp-Hour). The temperature was then increased at 4 K increments from 254 to 302 K for an additional elastic window scan from which a further QENS measurement was taken at 302 K (3 x 300 µAmp-Hour). A further temperature increase from 304 to 320 K was run at 4 K increments for the elastic window and a final QENS scan run at 320 K (2 x 300 µAmp-Hour). Due to additional time being made available on the instrument at this point, a final diffraction scan was run at 275 K in the d-range d6-d10 to determine the hydration state of the sample at the end of the run. An additional QENS scan was also run at 275 K (2 x 300 µAmp-Hour) to collect further data within the temperature range between 250 K and 300 K.

6.2.4.3 Elastic window and QENS scans of 6Ch in the oven dried (7 Å) state

A fresh portion of the 6Ch sample was dried out to its 7 Å form in an oven at 80 °C under vacuum for 7 hours and packed into an aluminium holder. A continual elastic window scan was conducted on the sample from 270 K to 40 K and a diffraction d-range scan from d1-d10 was run at 10 K to determine the hydration state of the sample. QENS measurements were made on the sample at 5 K (2 x 250 µAmp-Hour), 150 K (1 x 300 µAmp-Hour), 200 K (2 x 300 µAmp-Hour), 250 (2 x 300 µAmp-Hour), 300 K (2 x 300 µAmp-Hour) and 320 K (2 x 300 µAmp-Hour and 1 x 212 µAmp-Hour). The dry sample was run as a comparison with the hydrated sample since it was considered that the OH groups 'seen' by the neutron scattering of the dry sample should be structural hydroxyls, compared to both structural and water hydroxyls in the halloysite (10 Å) sample, hence allowing for distinction between the two at the data analysis stage. The temperatures selected for the dehydrated (7 Å) 6Ch sample for QENS analysis were 5 K, 150 K, 200 K, 250 K, 300 K and 320 K.

6.2.4.4 Elastic window and QENS scan of 6Ch in the (7 Å) state and rehydrated with bulk water

The set up at ISIS allowed additional small experiments to be run where there was availability on the instrument. Therefore, one such further rapid measurement was conducted by our collaborators at UCL, at an additional date, wherein the 6Ch sample was subjected to a humid atmosphere prior to loading in the instrument. The aim of this was to ensure that bulk water only was reintroduced, since halloysites are known not to allow water back into their interlayer once in the 7 Å form. This would aid in distinction between the bulk surface and interlayer water during the data interpretation stages of the experiment. The data for this sample were collected for an elastic run at 101 – 299 K followed by a QENS measurements at 300 K (3 x 300 µAmp-Hour). The neutron spectroscopy data interpretation was conducted using the programme Mantid (O Arnold *et al*., 2014; Mukhopadhyay *et al*., 2019).

6.2.5 Neutron Diffraction - NIMROD

While the results from the NIMROD (Near and Intermediate Range Order Diffractometer) experiments are not presented here, as they are being analysed by our

collaborators at UCL, the outline and rational of the experiments are presented. Here, neutron diffraction was used for its potential to provide information on the structure of the interlayer water molecules. For these measurements, high energy neutrons impinged upon the sample at a rate of around 40 µAmps/hour at low angles, allowing Q to be defined as between 0.5 – 50 $Å^{-1}$. NIMROD has 2268 detectors, all at angles of less than 40^{o} in front of the sample. As a result, elastic, coherent scattering only was measured.

The results were obtained in terms of g(r) which describes the probability of finding another atom in radius, r, according to the pair correlation function (Muller *et al*., 1986). The results were analysed using the programme Gudrun, which transforms the data into F(Q). This can then be compared to simulations run using the Empirical Potential Structure Refinement (EPSR) models and further simulations of the diffraction data are to be run using Monte Carlo method simulations.

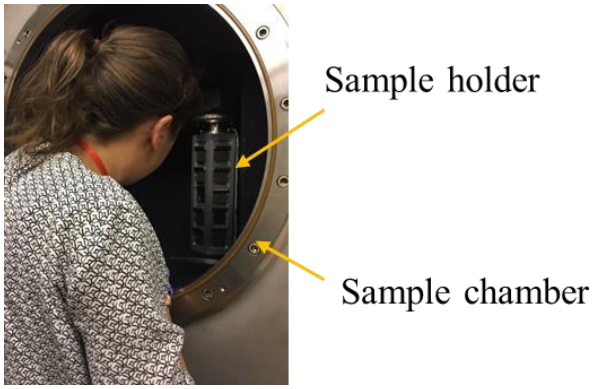

Figure 6.4. Loading the samples into the NIMROD instrument.

6.3 RESULTS

6.3.1. X-ray powder diffraction (XRPD) results

Time series XRPD scans are shown in Figures 6.5-6.8. The dehydration of the samples is shown by the transition from the dominant peak at 10 Å to 7.2 Å. The four different halloysites can be seen to dehydrate at different rates. For the sample 23US (Figure 6.7), the drop in background intensity of the final (red) scan in the inset is due to shrinkage of the halloysite in the steel sample holder upon dehydration.

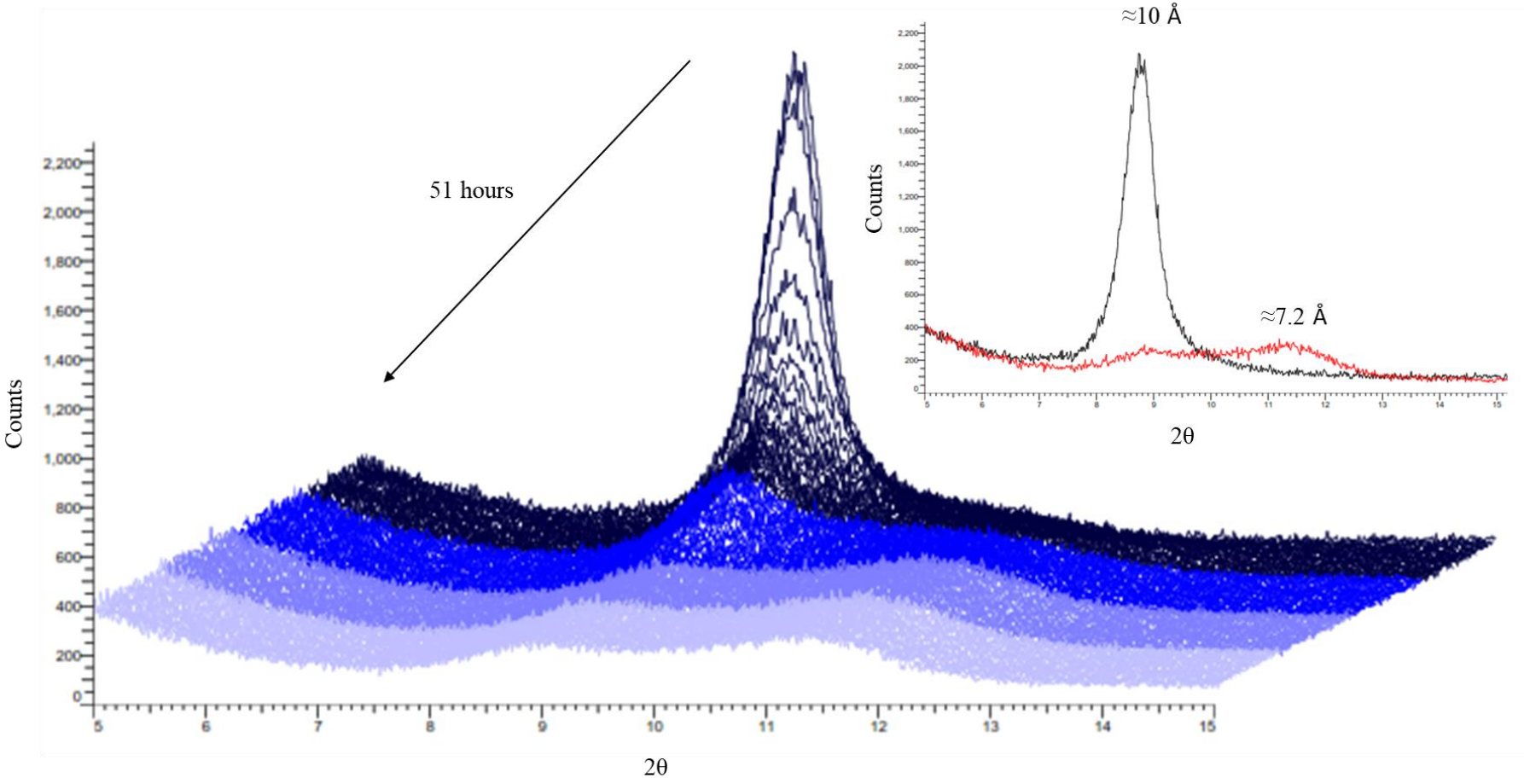

Figure 6.5. X-ray powder diffraction pattern of in situ dehydration of 5Ch, the hydrated peak seen at 10 Å and transition to dehydrated peak at 7.2 Å is seen over a period of 51 hours. Inset shows the first and last scans. The different colour blocks are of approximately 12 hours each.

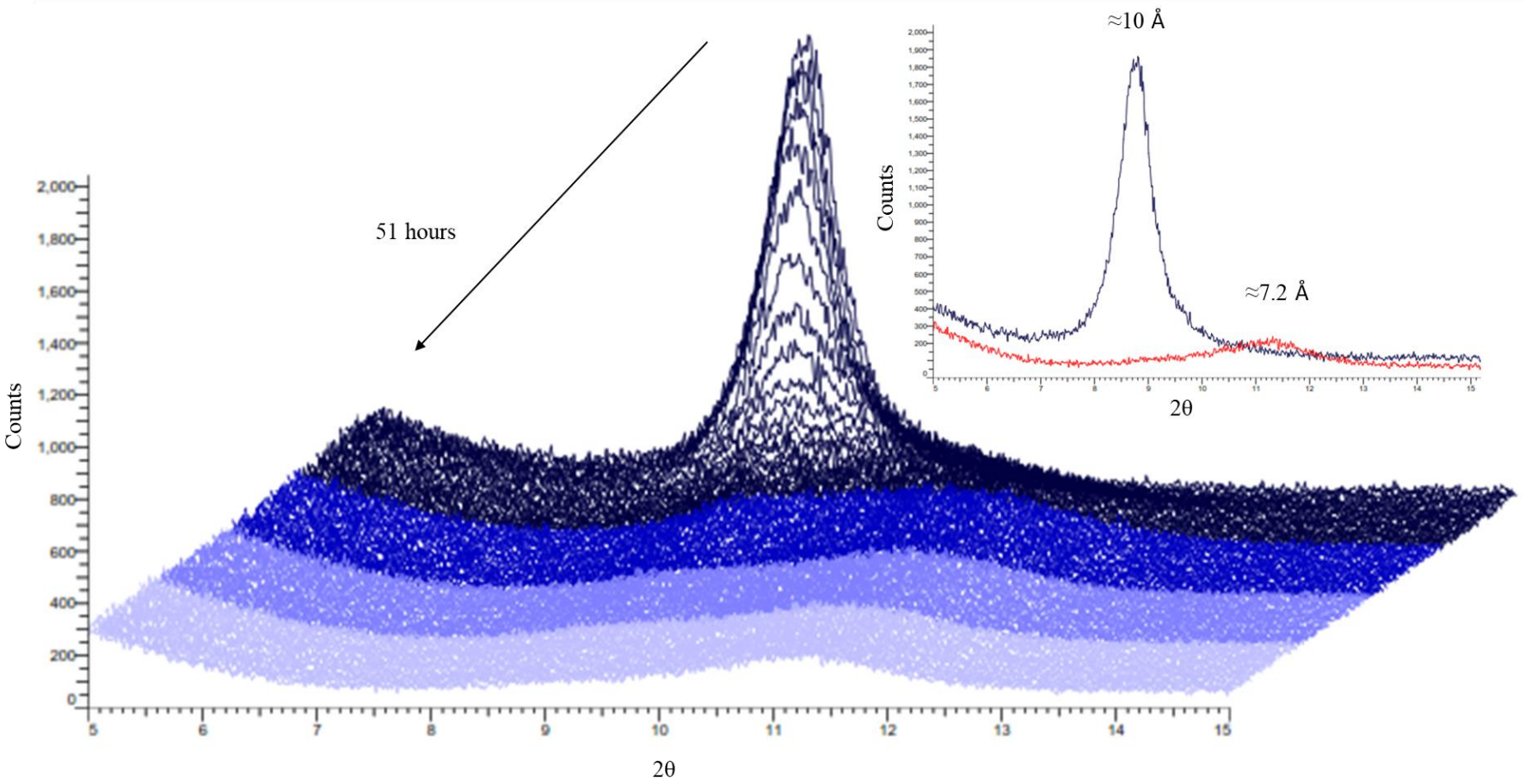

Figure 6.6. X-ray powder diffraction pattern of in situ dehydration of 6Ch, hydrated peak seen at 10 Å and transition to dehydrated peak at 7.2 Å is seen over a period of 51 hours. Inset shows the first and last scans. The different colour blocks are of approximately 12 hours each.

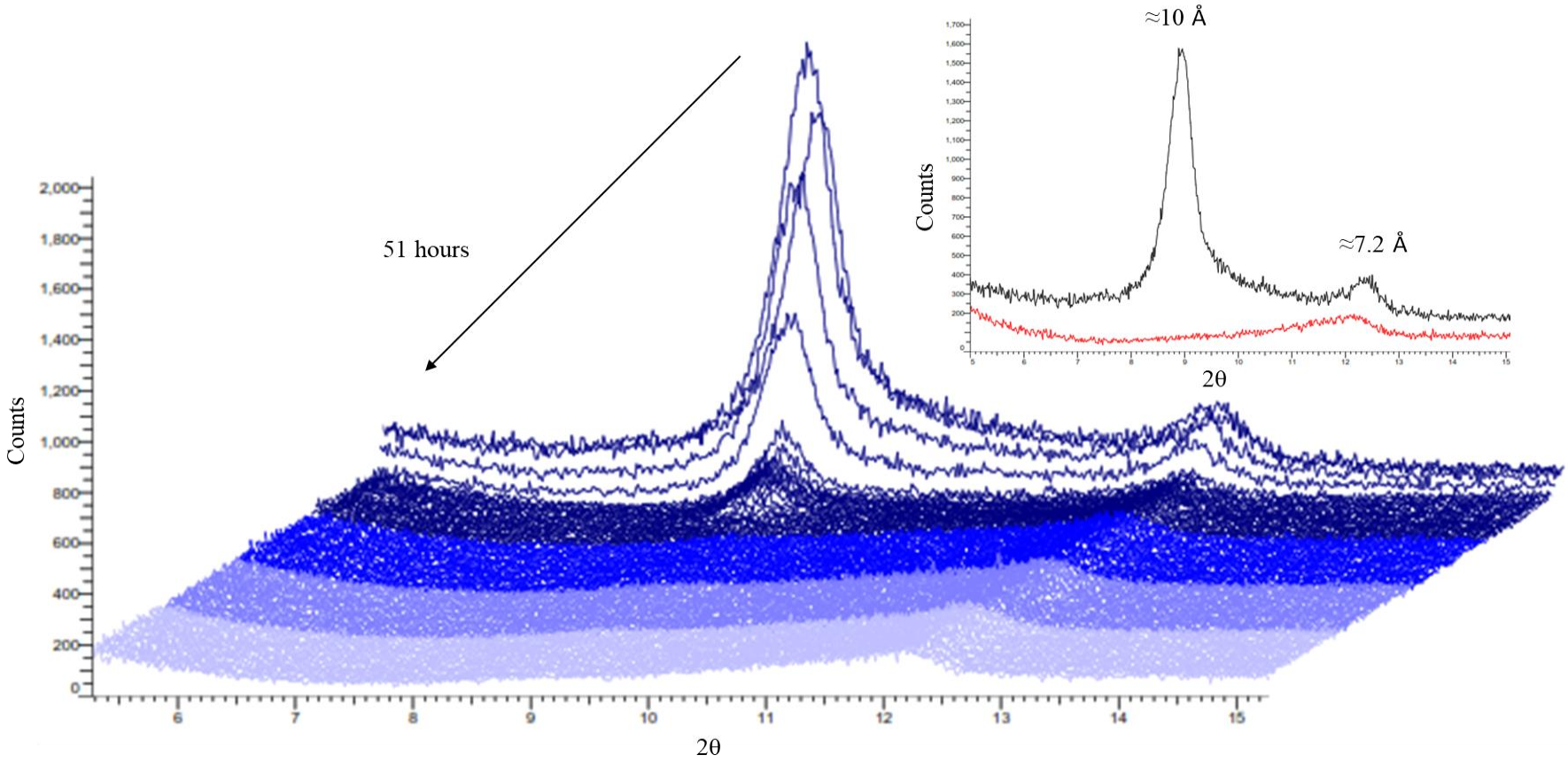

Figure 6.7. X-ray powder diffraction pattern of in situ dehydration of 23US, hydrated peak seen at 10 Å and transition to dehydrated peak at 7.2 Å is seen over a period of 51 hours. Inset shows the first and last scans. The different colour blocks are of approximately 12 hours each. The drop in background intensity of the final (red) scan in the inset is due to shrinkage of the halloysite upon dehydration.

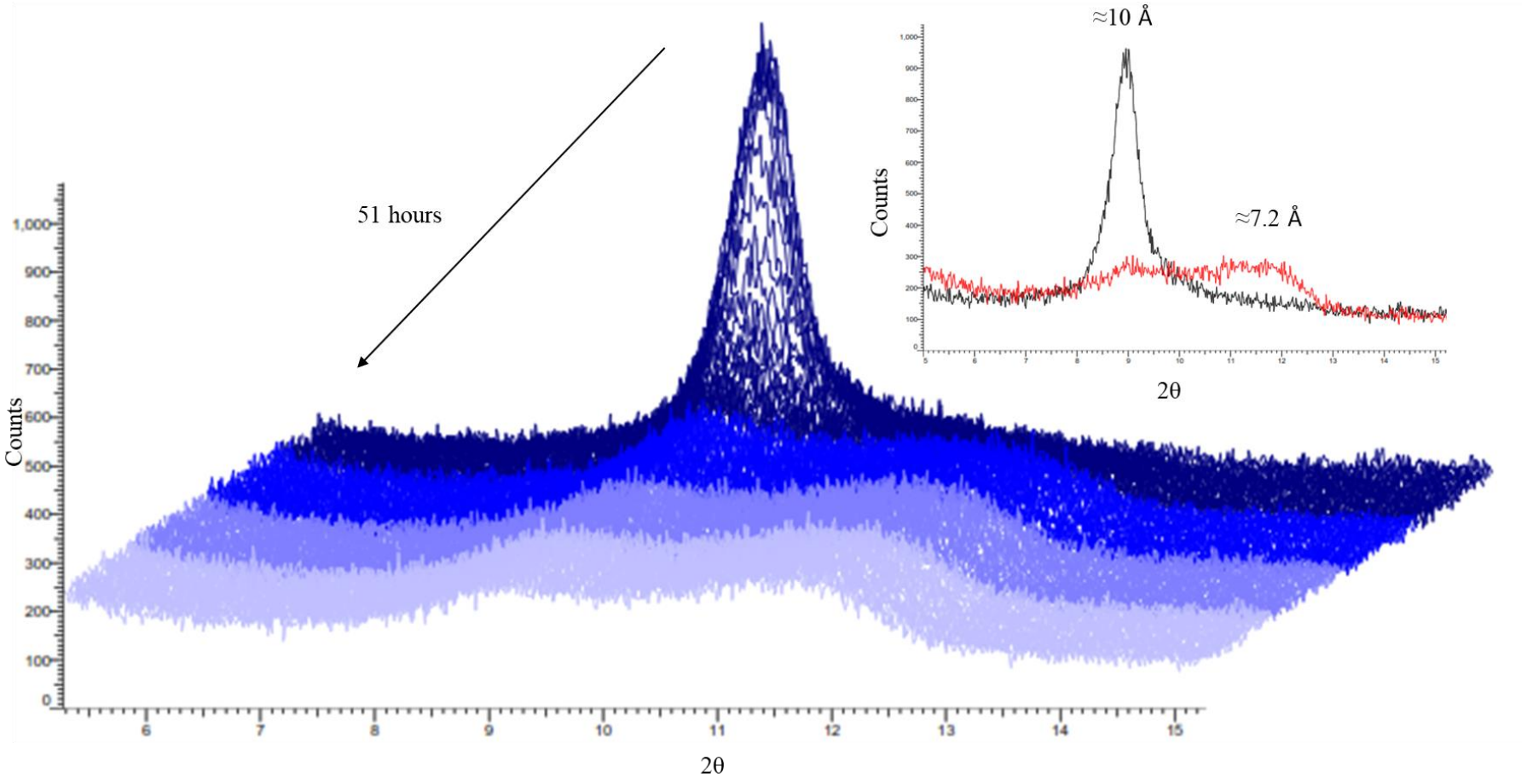

Figure 6.8. X-ray powder diffraction pattern of in situ dehydration of 24US, hydrated peak seen at 10 Å and transition to dehydrated peak at 7.2 Å is seen over a period of 51 hours. Inset shows the first and last scans. The different colour blocks are of approximately 12 hours

6.3.2 Fourier transform infrared spectroscopy (FTIR) results

FTIR analysis was conducted on the deuterated samples to determine the extent of deuteration of the samples. From the FTIR analysis, it is apparent that even when the samples were in a vapour atmosphere of 100% D_2O, complete exchange of surface hydroxyls did not occur as the Al-OH stretching bands between 3520-3700 cm^{-1} (Figure 6.9) were not completely removed. Instead, they decreased slightly in intensity, whilst their corresponding Al-OD bands between 2600 – 2735 cm^{-1} (Table 6.2) increased in intensity. The labelled FTIR spectra are shown in Figures 6.11-6.18. The Al-OH and Al-OD band heights were normalised to the most intense SiO_2 samples' height, as measured in OMNIC^{TM} software, and the percentage height loss from Al-OH to Al-OD is presented in Table 6.3.

The ratio of the intensity of the diagnostic Al-OH bands at 3700 and 3620 cm^{-1} with no deuterated treatment and with treatment by 100% deuterated vapour is shown in Table 6.3. For each sample, the ratio between the two bands were seen to decrease after deuteration and a key observation can be inferred from the differing behaviour of the two morphologies. In the case of the cylindrical samples the higher frequency surface Al-OH stretching band is less intense than the lower frequency, inner structure Al-OH stretching band. The reverse was noted for the polygonal prismatic samples. This effect has been previously observed and, in that report, the researchers suggested that this was due to the ordered, more kaolinite-like character of the polygonal prismatic samples (Hillier *et al*., 2016).

Table 6.2. FTIR band assignment, comparison of the OH and OD stretching and bending bands.

OH band wavelength (cm^{-1})	Assignment	OD band wavelength (cm^{-1})	Assignment
3700	OH stretching band, surface Al-OH	2735	OD stretching band, surface Al-OD[a]
3670	OH stretching band, surface Al-OH	2700	OD stretching band, surface Al-OD[a]
3620	OH stretching band, inner Al-OH	2680	OD stretching band, inner Al-OD[a]
3560	OH stretching band, hole water	2600	OD stretching band, hole water
3430/3880	OH stretching band, 'associated' interlayer water[b] and bulk surface water	1630	OD stretching band, 'associated' interlayer water and bulk surface water
1650	OH bending band, hole water	1445	OD bending band, hole water
1630	OH bending band, 'associated' interlayer water[b] and bulk surface water	1210	OD bending band, 'associated' interlayer water and bulk surface water
935	OH bending band, surface OH groups	723	OD bending band, surface OD groups[a]

[a]Wada (1967)

[b]Costanzo *et al*. (1984); Giese (1988)

Table 6.3. Ratio of the diagnostic surface and inner OH bands for each dehydrated (7 Å) halloysite sample with different levels of deuteration.

Sample ID	Deuteration level	Ratio 3700/3620 cm^{-1} band height
5Ch	100% H_2O	0.93
5Ch	100% D_2O	0.61
6Ch	100% H_2O	0.88
6Ch	100% D_2O	0.65
23US	100% H_2O	1.45
23US	100% D_2O	1.26
24US	100% H_2O	1.46
24US	100% D_2O	1.27

Additionally, as outlined in Chapter 1 (Figure 1.4), important information about the nature of the water present in the halloysite (10 Å) samples can be gathered from the FTIR spectra (Madejová, 2003). The weak adsorption at around 3430 cm^{-1} has been suggested as being related to the OH stretching of 'associated' interlayer water (Costanzo *et al*., 1984) and the corresponding OH bending band is seen at 1630 cm^{-1}. The OH stretching band at 3550 cm^{-1} and OH bending band at 1650 cm^{-1} are assigned to interlayer 'hole water' (Costanzo *et al*., 1984; Giese, 1988) as outlined in Table 6.2. Upon deuteration of the hydrated samples these bands were significantly reduced in intensity and new bands at around 1445 cm^{-1} and 1210 cm^{-1} appear which are associated with deuterated interlayer associated and 'hole' water, respectively.

Both polygonal prismatic halloysites displayed a shoulder in the deuteration bands at around 2700 cm^{-1} (Figure 6.10) which would be expected to correspond to the out-of-plane hydroxyl band observed around 3670 cm^{-1}. In this work, the relative intensities of these bands have not been compared since they are too weak in intensity to accurately measure their peak heights. The weak deformation band around 935 cm^{-1} is observed in the prismatic samples in line with previous reports that they possess a more ordered, 'kaolinite' character (Farmer, 1964; Hillier *et al*., 2016). This band is seen to reduce in intensity with increased deuteration. Previously this has been reported to be replaced by a band at around 723 cm^{-1} (Wada, 1967). However, in this chapter, this new peak was observed at around 745 cm^{-1}. For the halloysite (7 Å) sample 24US, a shoulder is observed at this band after 100% deuteration, as indicated by the arrow on Figure 6.13.

Table 6.4. Comparison of percentage height loss of characteristic OH to OD bands in FTIR analysis for the four dehydrated halloysites.

Sample ID	Band ID	Percentage height loss between 100% H_2O sample and 100% D_2O sample
5Ch	Surface OH stretching	39.4
5Ch	Inner OH stretching	7.8
6Ch	Surface OH stretching	45.5
6Ch	Inner OH stretching	26.1
23US	Surface OH stretching	27.9
23US	Inner OH stretching	17.1
24US	Surface OH stretching	58.7
24US	Inner OH stretching	52.2

From Table 6.4 no observable pattern can be identified between the four samples and the percentage height loss which is taken as an indication of the deuteration level of the halloysite.

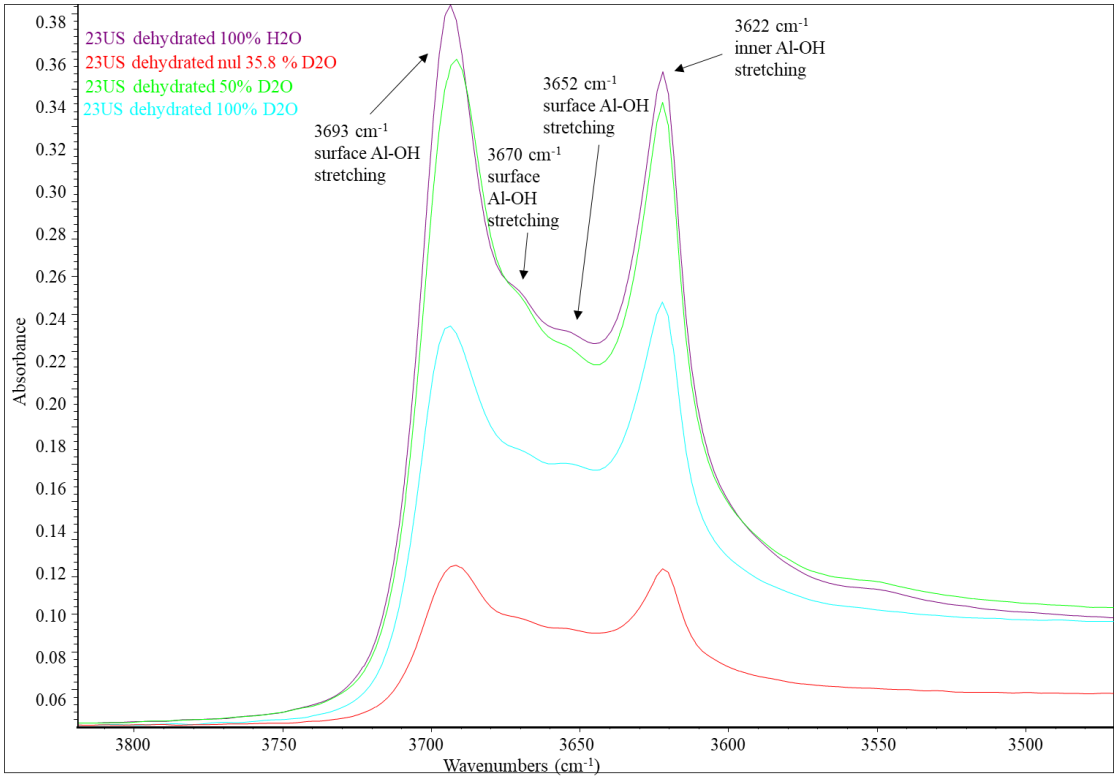

Figure 6.9. Close up of the diagnostic FTIR Al-OH stretching bands. The sample shown (23US) is a polygonal prismatic halloysite which features the intermediate bands at around 3652 and 3670 cm^{-1}. Intermediate bands are not observed in the cylindrical samples.

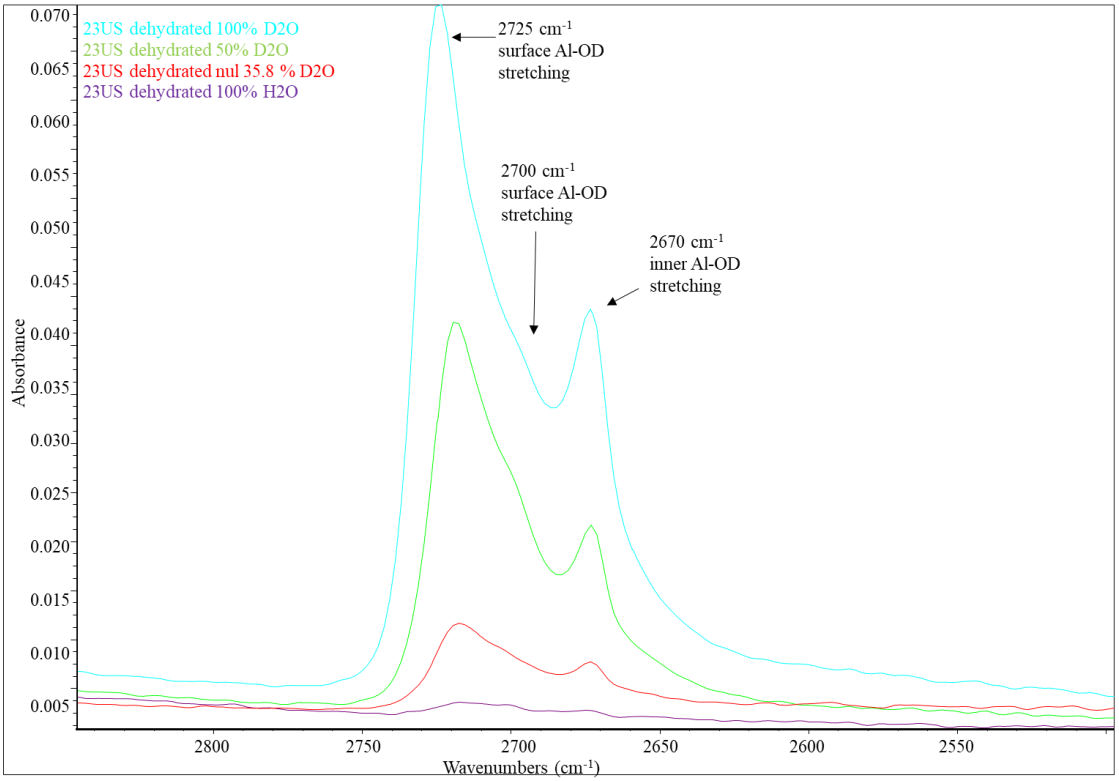

Figure 6.10. Close up of the diagnostic FTIR Al-OD stretching bands. The sample shown (23US) is a polygonal prismatic halloysite which features the intermediate band at around 2700 cm^{-1}. Intermediate bands are not observed in the cylindrical samples.

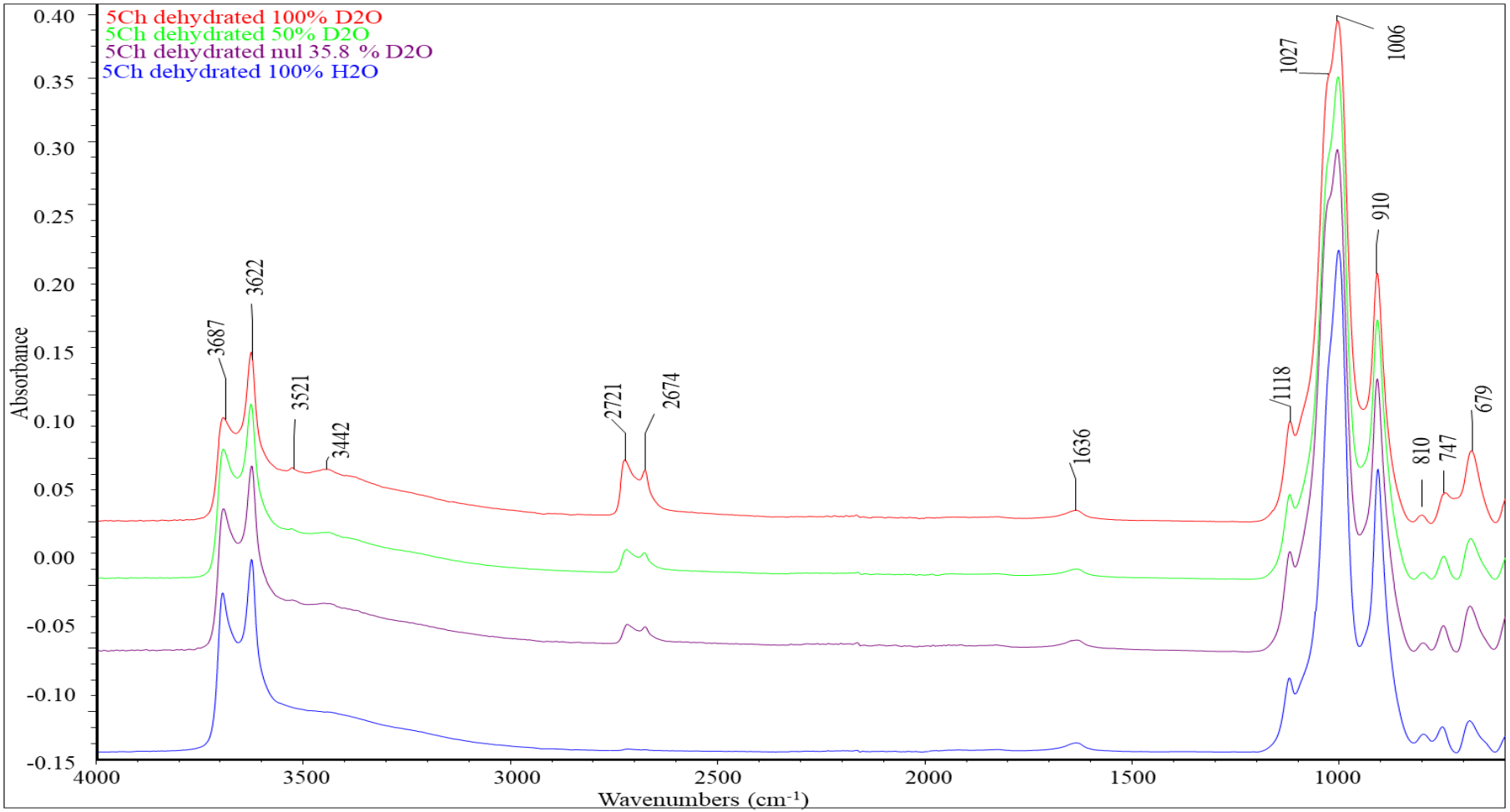

Figure 6.11. FTIR spectra of dehydrated 5Ch cylindrical halloysite (7 Å) with the varying deuteration treatments.

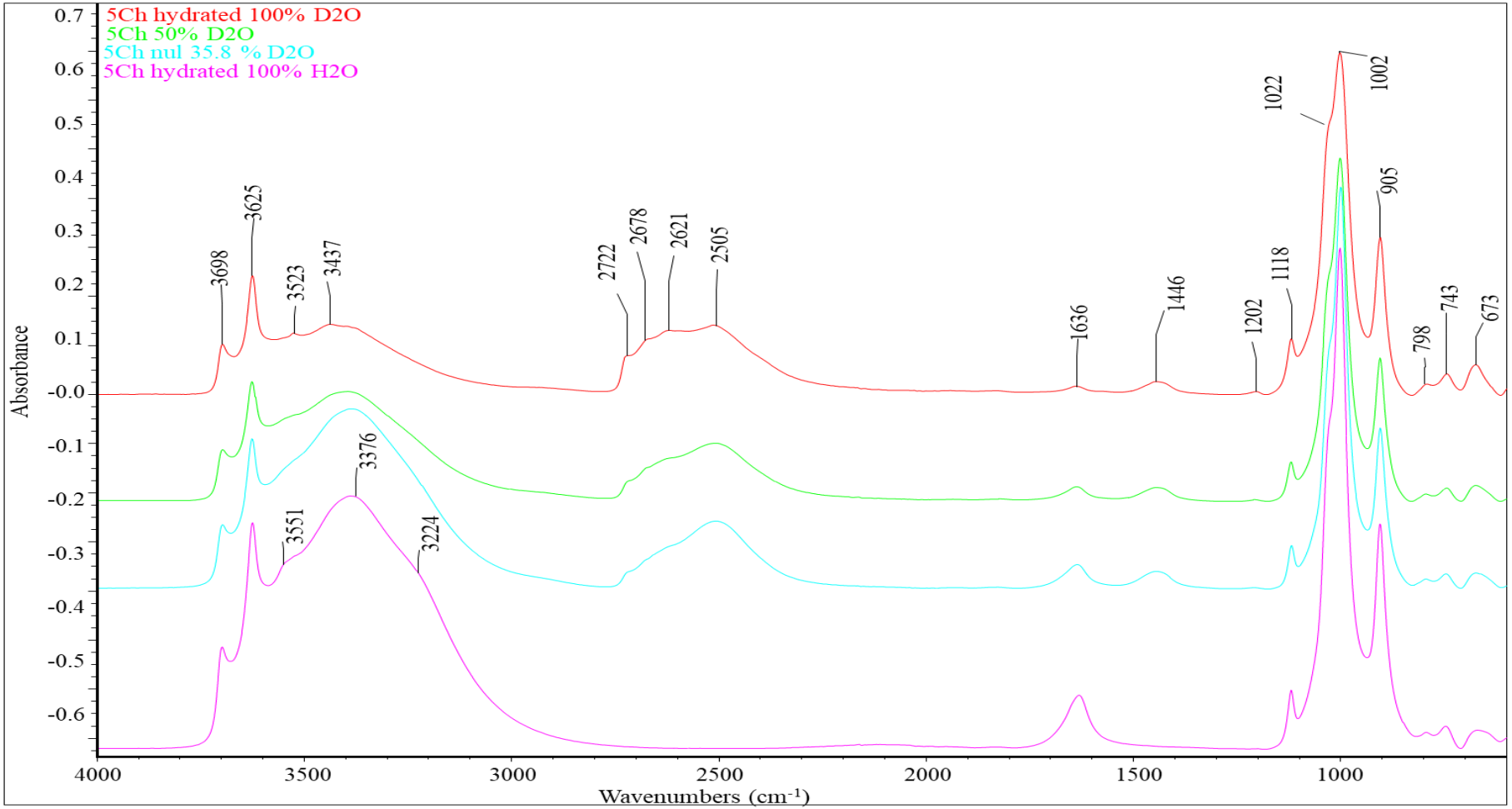

Figure 6.12. FTIR spectra of hydrated 5Ch cylindrical halloysite (10 Å) with the varying deuteration treatments.

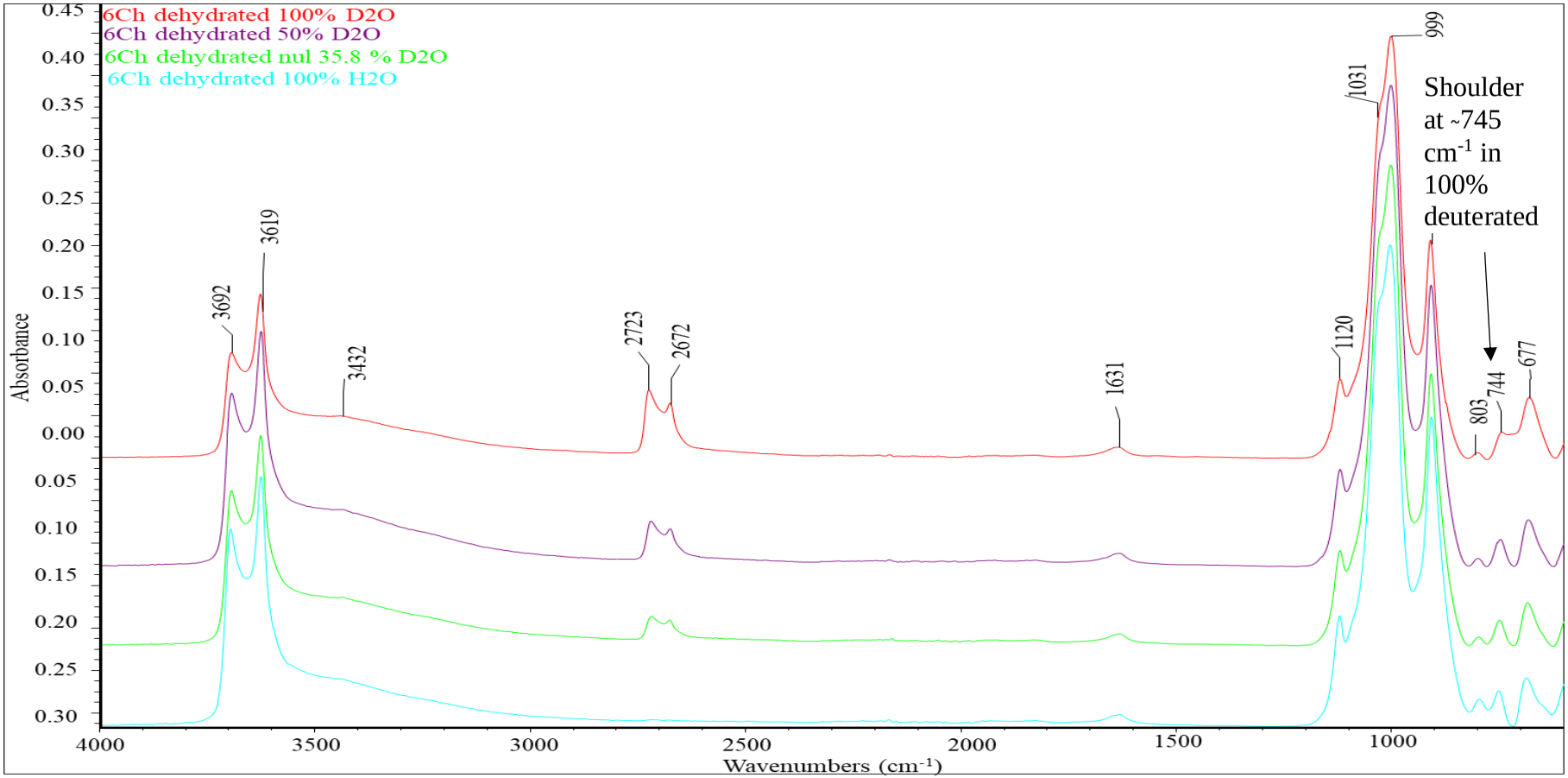

Figure 6.13. FTIR spectra of dehydrated 6C cylindrical halloysite (7 Å) with the varying deuteration treatments.

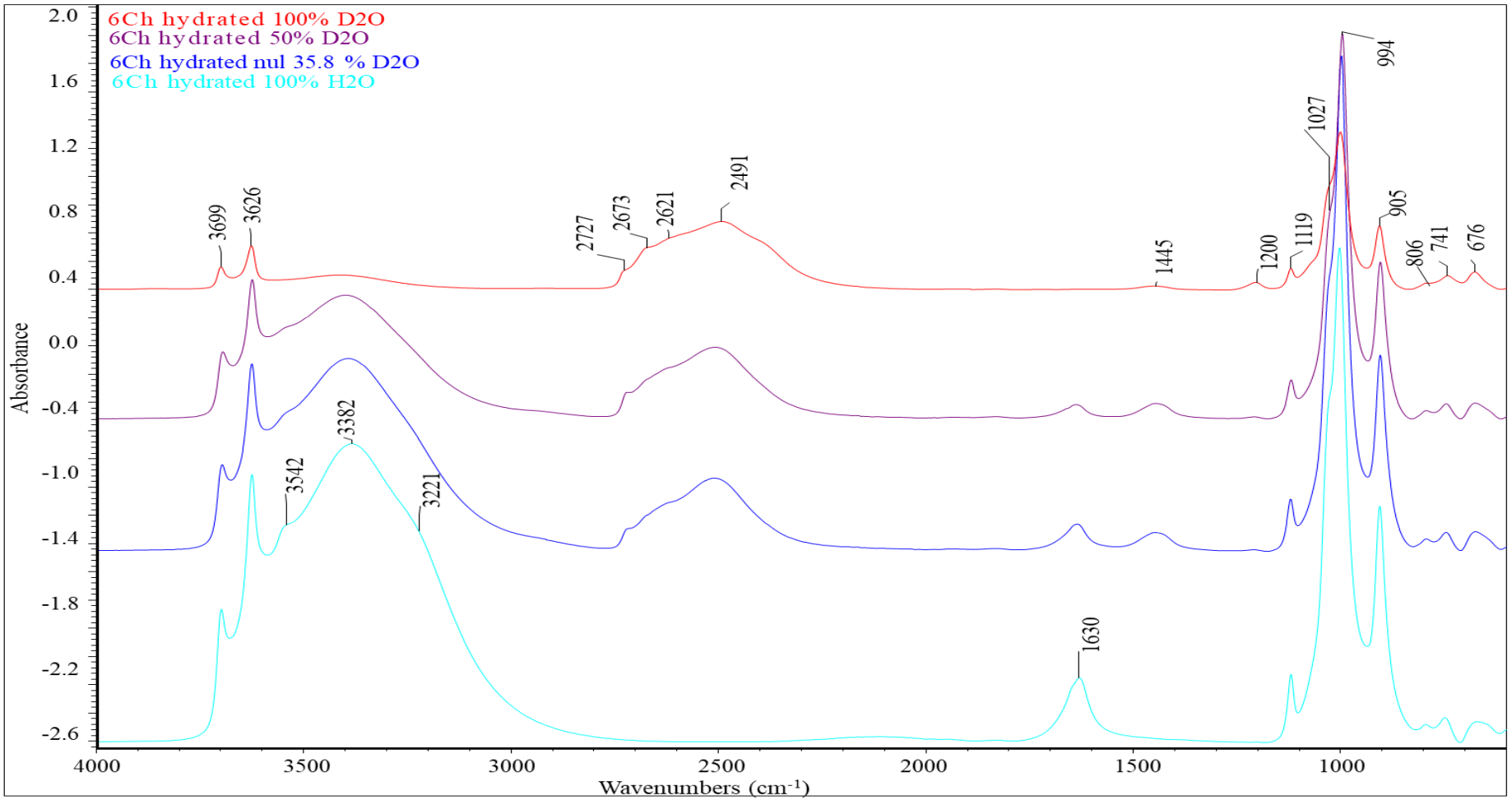

Figure 6.14. FTIR spectra of hydrated 6Ch cylindrical halloysite (10 Å) with the varying deuteration treatments.

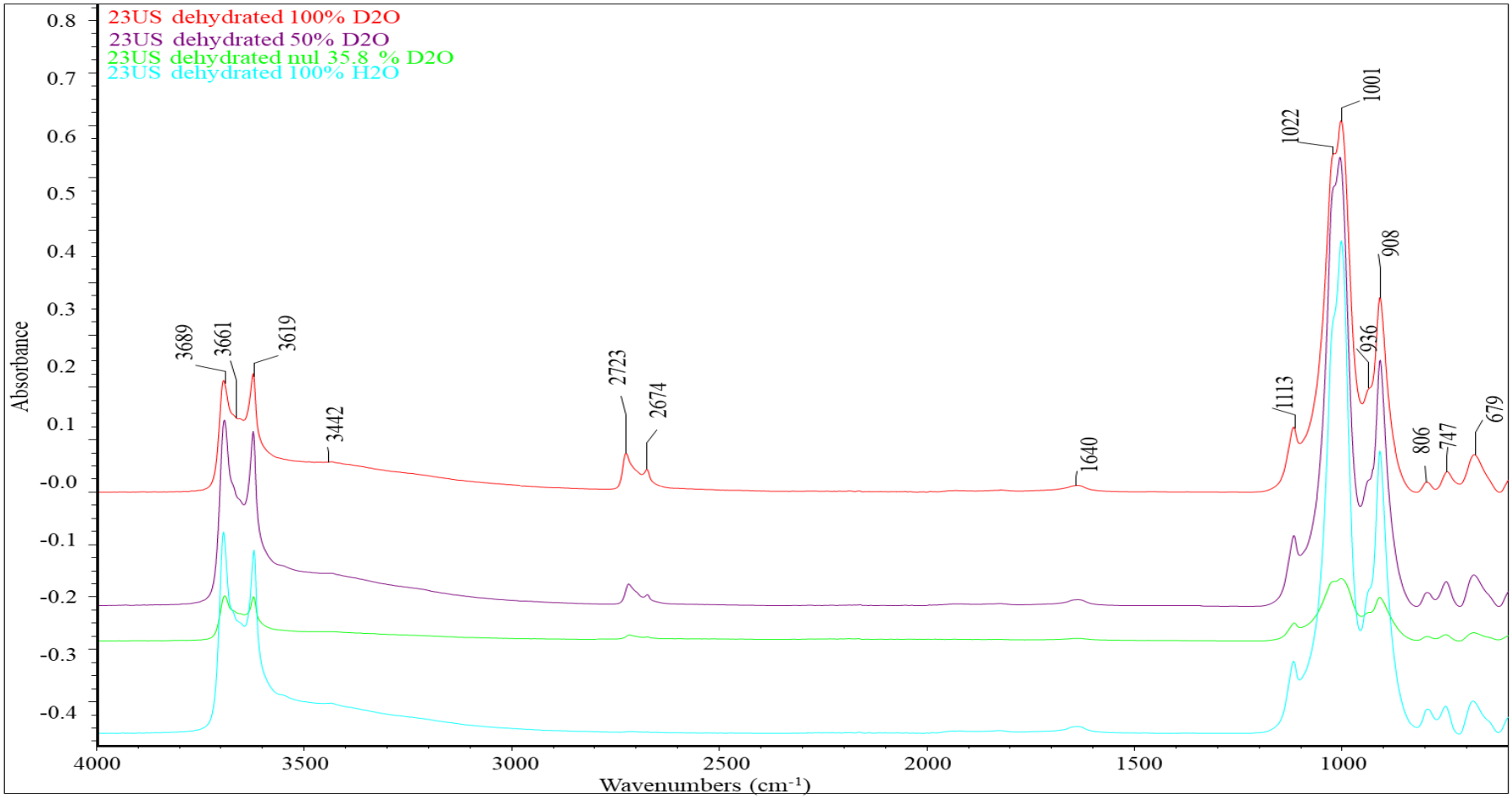

Figure 6.15. FTIR spectra of dehydrated 23US prismatic halloysite (7 Å) with the varying deuteration treatments.

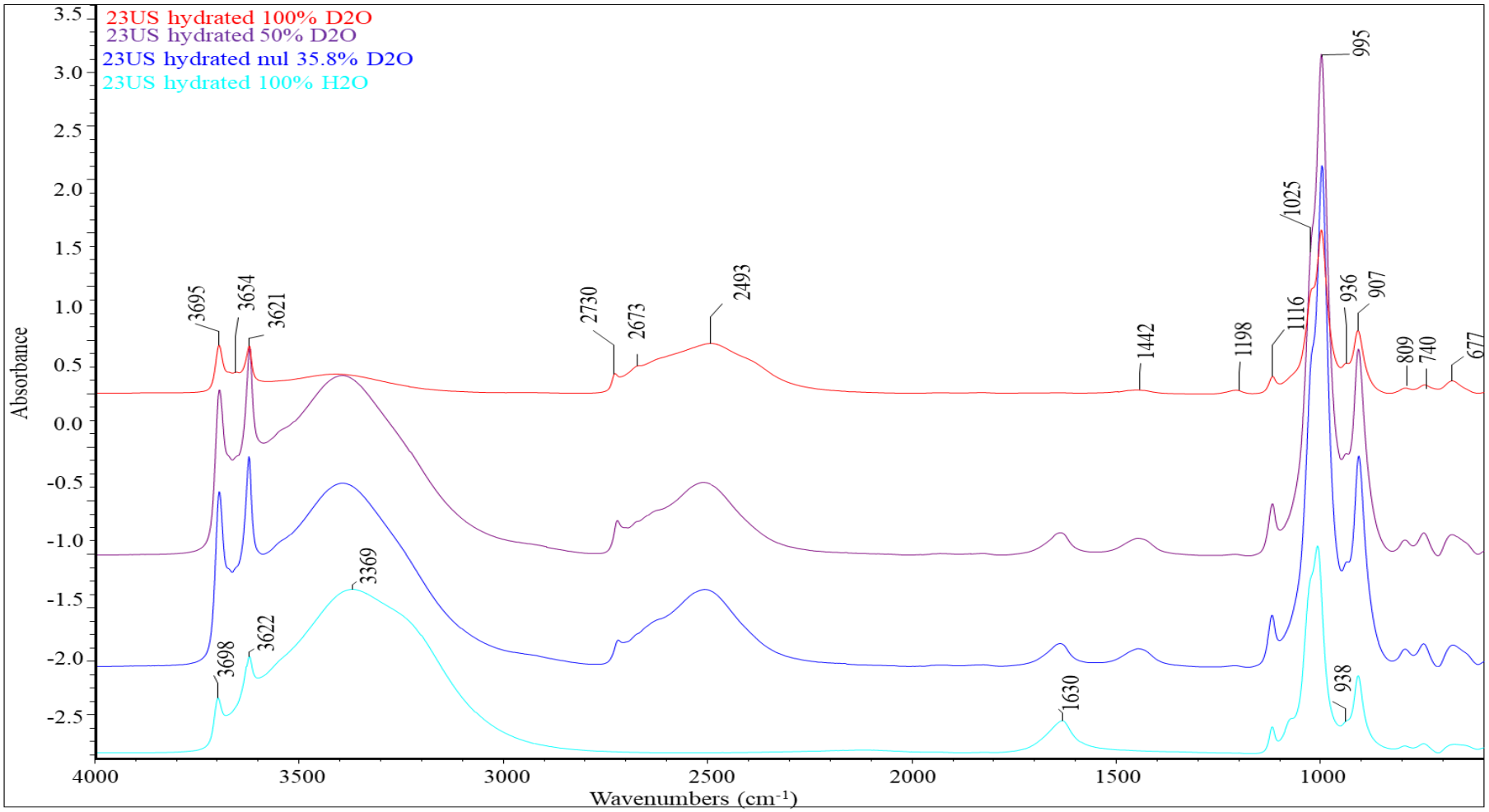

Figure 6.16. FTIR spectra of hydrated 23US prismatic halloysite (10 Å) with the varying deuteration treatments.

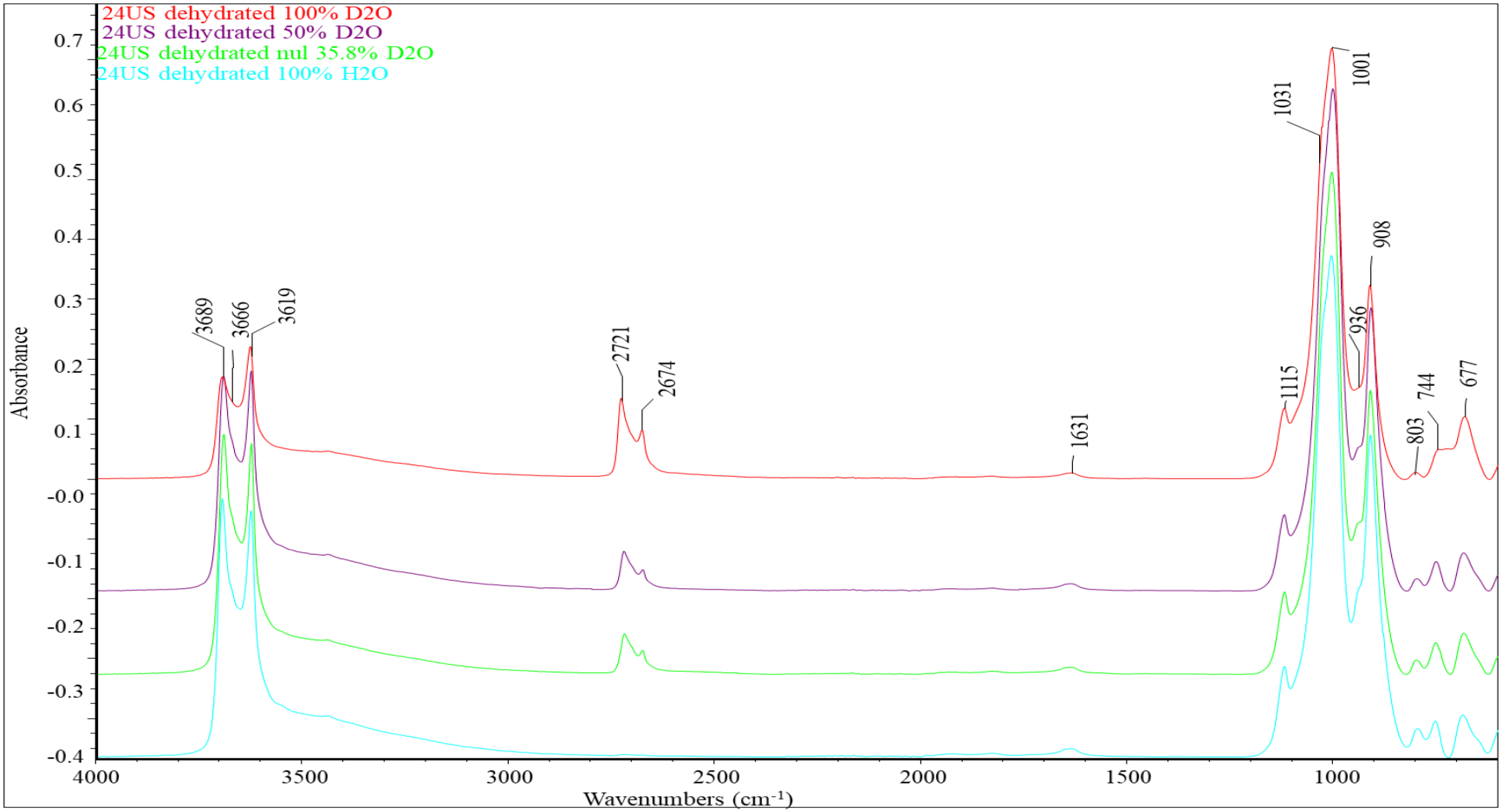

Figure 6.17. FTIR spectra of dehydrated 24US prismatic halloysite (7 Å) with the varying deuteration treatments.

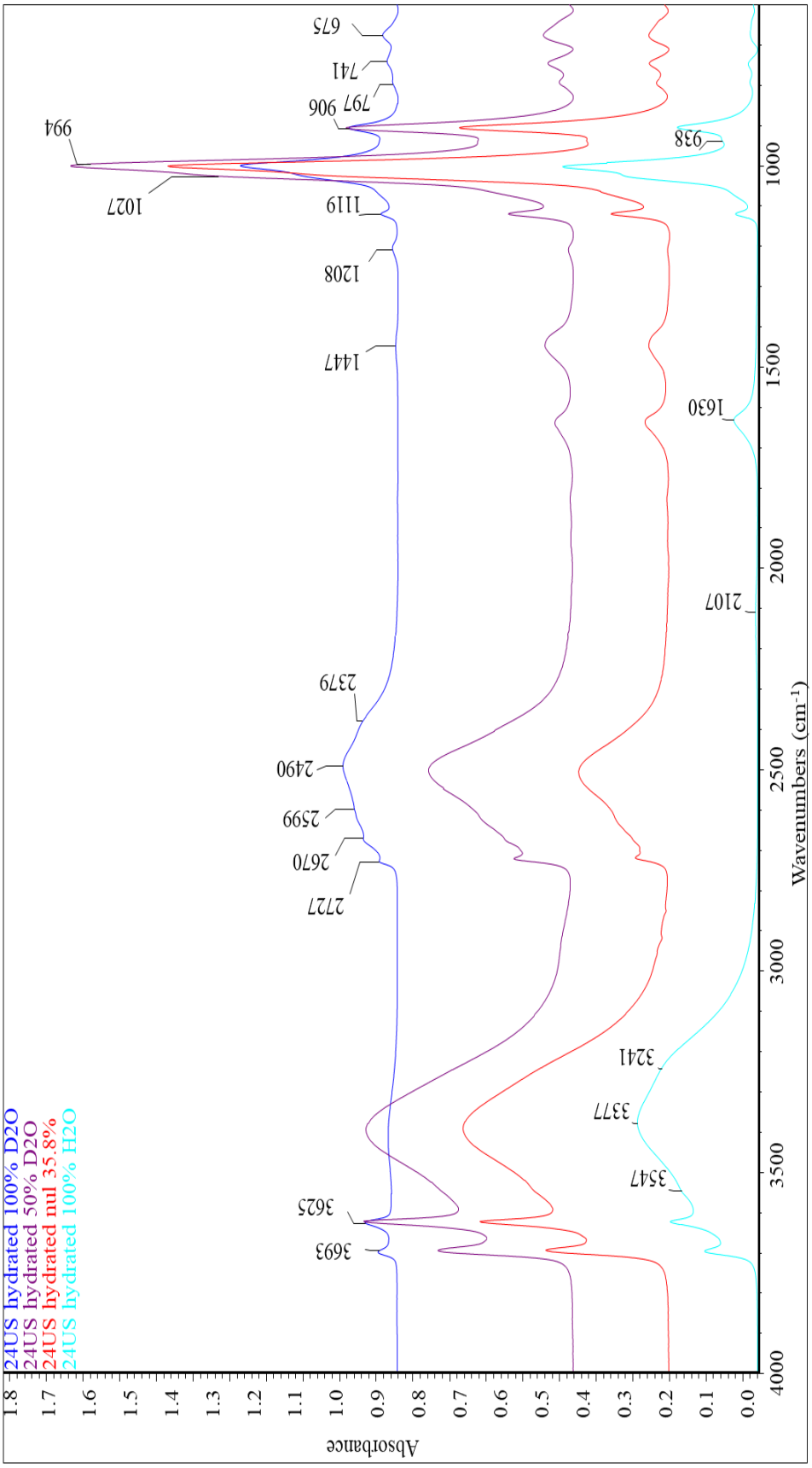

Figure 6.18. FTIR spectra of hydrated 24US prismatic halloysite (10 Å) with the varying deuteration treatments.

From the XRPD analysis, it can be inferred that the halloysites behaved differently in terms of their dehydration behaviour as shown by the repeated scans over 51 hours. The scans also verified that small exposures to the air in terms of sample preparation would not result in dehydration of the halloysite samples. The FTIR analysis was effective in understanding more about the deuteration of each halloysite (10 Å) sample which will aid in the modelling of the data for the neutron diffraction work. It can be concluded from the FTIR analysis that the surface hydroxyls in the alumina layer were most susceptible to deuterium exchange and that the four halloysite samples showed varying levels of deuteration. The next step of this work therefore was to consider the neutron spectroscopy data.

6.3.3 OSIRIS neutron scattering results

As discussed previously, due to the time taken to perform the analysis and the high demand for instrument access, only one halloysite (10 Å) sample was selected for measurement, the cylindrical 6Ch sample. Diffraction scans were run *in situ* at temperatures of 25 K and 275 K to verify that the samples were in the hydrated (10 Å) state throughout the experiments as shown by the bands at 10 Å (Figure 6.20). The drop in intensity between the hydrated (10 Å) and dehydrated (7 Å) sample is thought to arise due to fewer protons in the dehydrated (7 Å) sample which would result in lower scattering. The sharp bands that can be seen at 1.5 Å and 2 Å occur due to the aluminium sample holder.

Elastic window scans bear a resemblance to differential scanning calorimetry scans in that they can be used to locate transitions (Sakai, 2015). In this instance, the gradient changes highlighted by the straight lines and arrows suggest changes in the dynamics of the interlayer water (Figure 6.20). The temperatures at which these changes occur are used to guide the temperatures at which to conduct the QENS measurements.

In the experimental design, the well-known difficulties that can arise in distinguishing between interlayer water in the halloysite nanotubes and bulk or surface water in the pores of the specimen were considered. To help establish which was being observed in the elastic window graph (Figure 6.20), elastic window graphs were run for a dried out sample and a rehydrated sample (Figure 6.21) and the datasets were compared to

the original halloysite (10 Å) sample. The thought process here was that the rehydrated sample would not contain interlayer water; it has been well reported and detailed in Chapter 1 (Section 1.2.3) that halloysite (7 Å) will not rehydrate to halloysite (10 Å), but that this sample would still contain reintroduced bulk/surface water. A comparison of the three transitions showed that the gradient change at 100 K may have had a contribution of bulk/surface water. The data suggest that there may also be a small contribution from bulk/surface water at around 240 K as labelled in Figure 6.21.

In addition, the dynamics of the hydroxyl groups in the halloysite nanotubes can be considered as moving too slowly for the time window of the QENS measurements and, hence, they will contribute only to the elastic scattering measurements. As a result, it can be considered that the QENS measurements reported here only take into account the water dynamics (Mamontov, 2005; Bordallo *et al*., 2008).

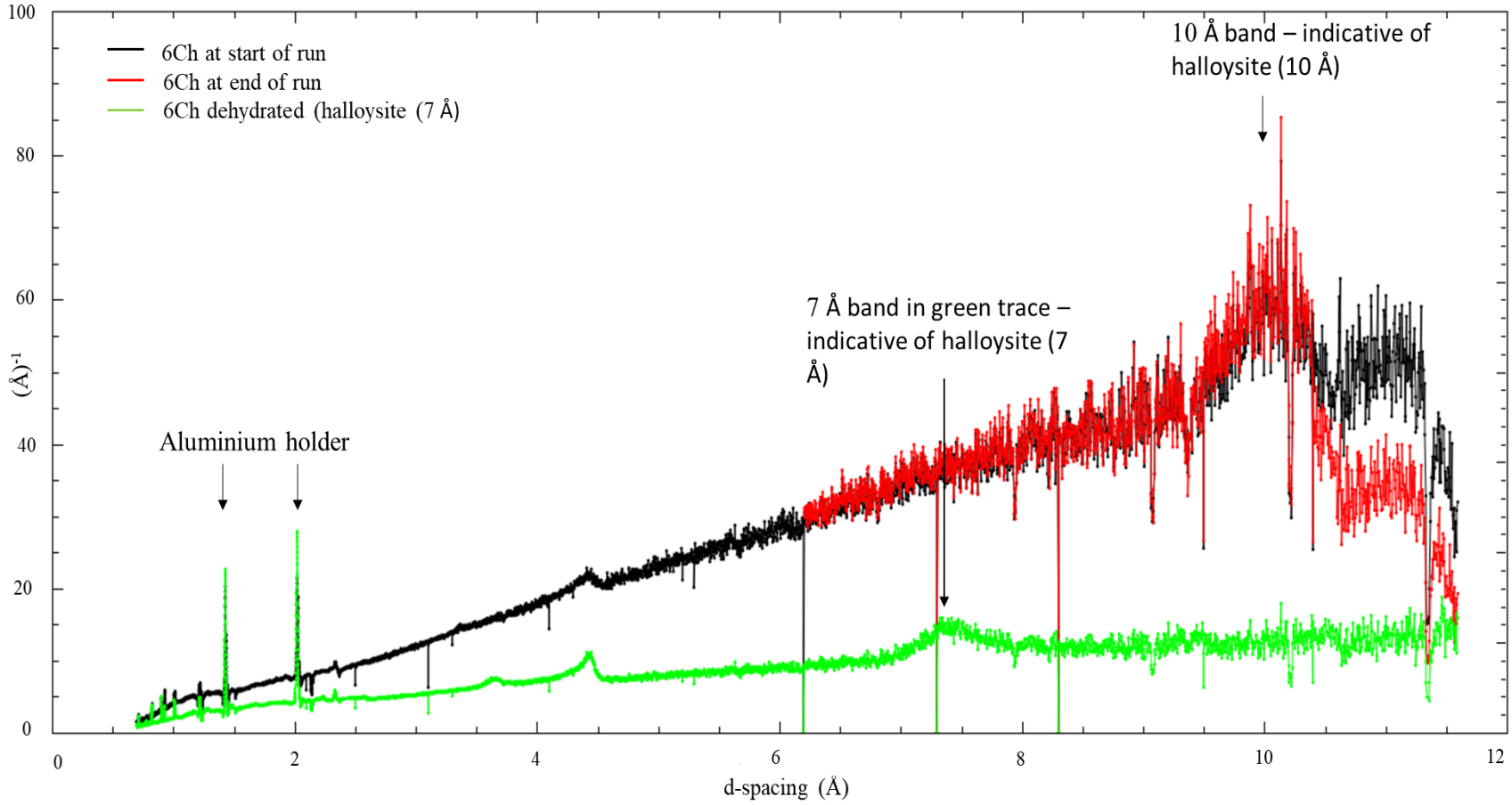

Figure 6.19. Comparison of diffraction patterns of 6Ch sample at the start (red) and end (black) of the run along with dehydrated (7 Å) 6Ch (green). Comparison of the red and black traces demonstrate that the sample remains hydrated throughout the experiment.

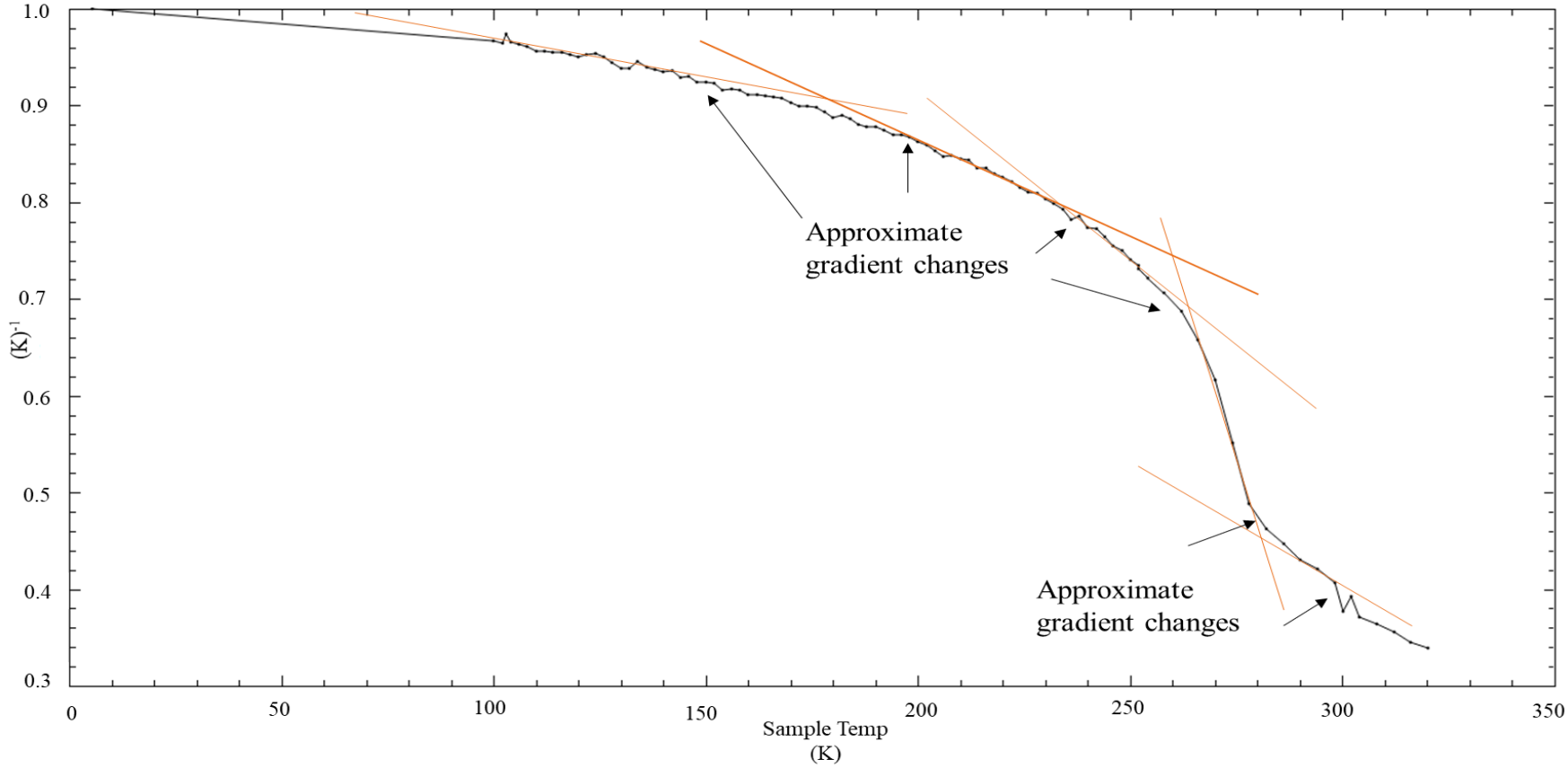

Figure 6.20. Elastic window scan of 6Ch (10 Å). Arrows indicate temperatures of gradient changes which are suggestive of transition changes in the dynamics of the water present in the sample. These temperatures were subsequently used as a guide for the QENS measurements.

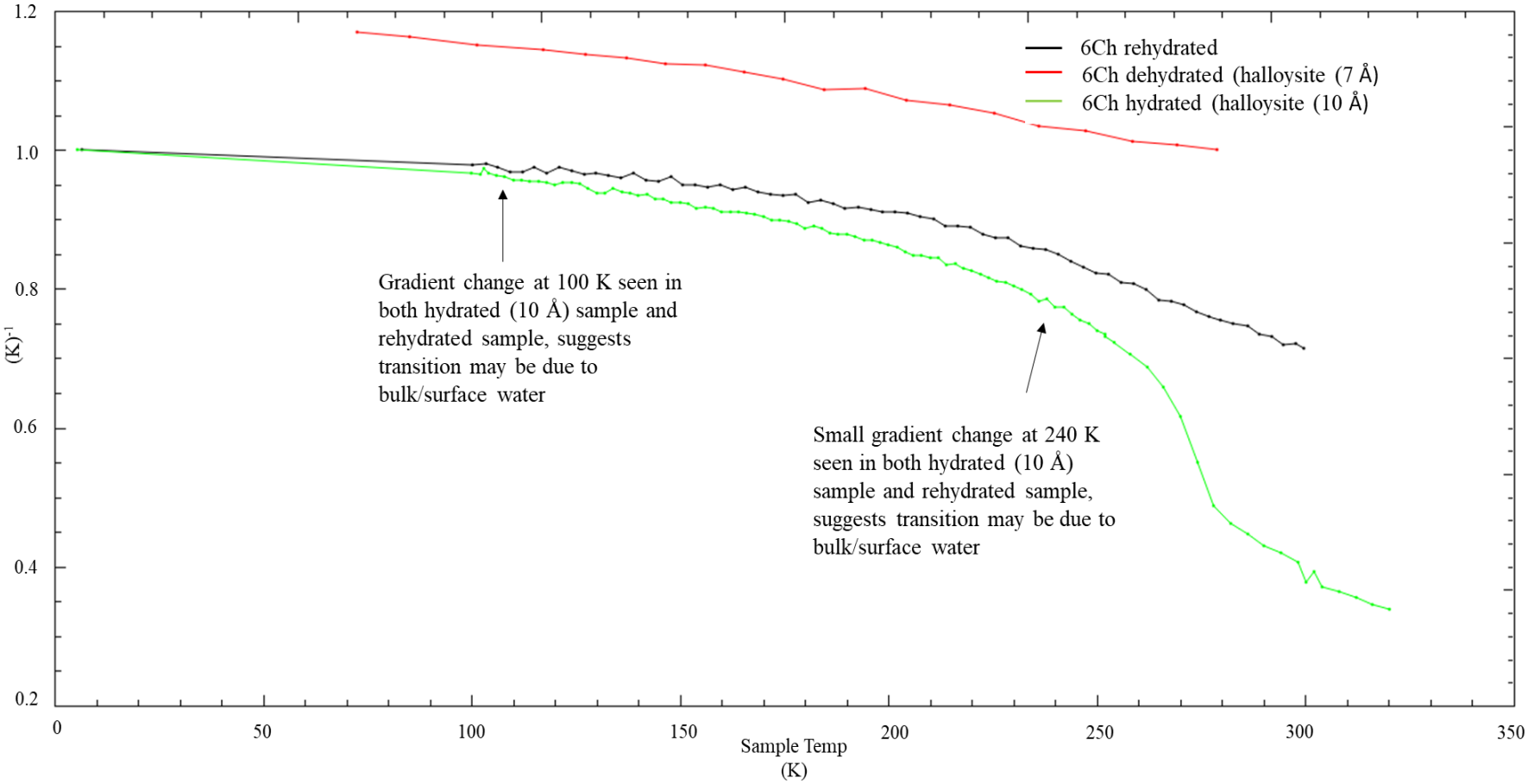

Figure 6.21. Comparison of three elastic window graphs for dehydrated halloysite (7 Å) 6Ch (red), hydrated halloysite (10 Å) 6Ch (green) and rehydrated 6Ch (black). Fewer transitions (i.e. gradient changes) can be observed in the red and black traces.

The QENS graphs for elastic scattering with varying temperature dependence at low Q are shown in Figure 6.22. The QENS graphs display a decrease in intensity of the elastic peak, which is centred at 0 meV, with increasing temperature. This infers that, as the temperature is increased, there is an increase in QENS scattering as shown by a broadening of the peak. At low temperatures, the protons can be considered as at the bottom of harmonic potential wells and hence require a thermal energy input to jump between adjacent wells, as depicted by the reduction in elastic scattering and increase in QENS scattering with increasing temperature and as shown in the inset of Figure 6.22.

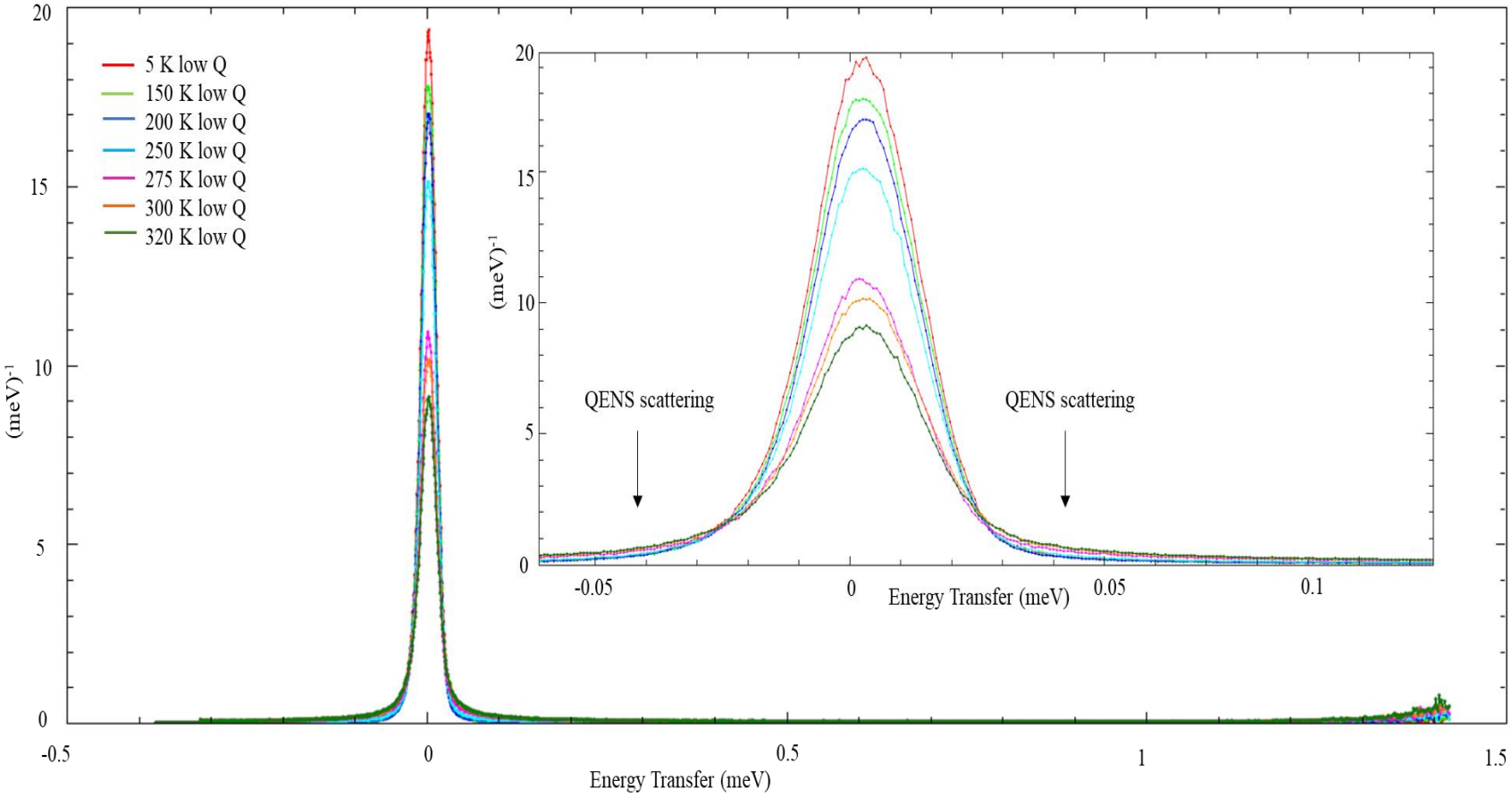

Figure 6.22. QENS graph for hydrated 6Ch sample at the seven temperatures and run at low Q. Inset shows zoomed in QENS peak where deviation from quasi-elastic scattering (E =0) can be observed for the higher temperatures, as indicated with the arrows.

The next step of data analysis was to fit Lorentzian curves to the QENS graphs, where the number of the Lorentzian curves required to obtain a good fit is motion type dependent. The aim from this was to study the type of movement of the interlayer water by fitting the half width half maxima (HWHM) of the QENS graphs at each fixed temperature in terms of their Q dependence. The analytical model that was used for this assumed separated translational and rotational motion of the protons as shown in Equation 6.5 (Bordallo *et al*., 2008).

Equation 6.5. $Sm(Q,\omega) = e^{-<u(T)^2>Q^{\frac{2}{3}}} T(Q,\omega) \otimes R(Q,\omega)$

The first term in Equation 6.5 is described as the Debye-Waller factor, where Q = the scattering constant, **ω** = the energy transferred to the neutron during the scattering process, $<(uT)^2>$ = the mean square displacement of the atoms around the equilibrium positions of the H atoms, S = scattering, T(Q,ω) describes the translational contribution and R(Q,ω) describes the rotational contribution.

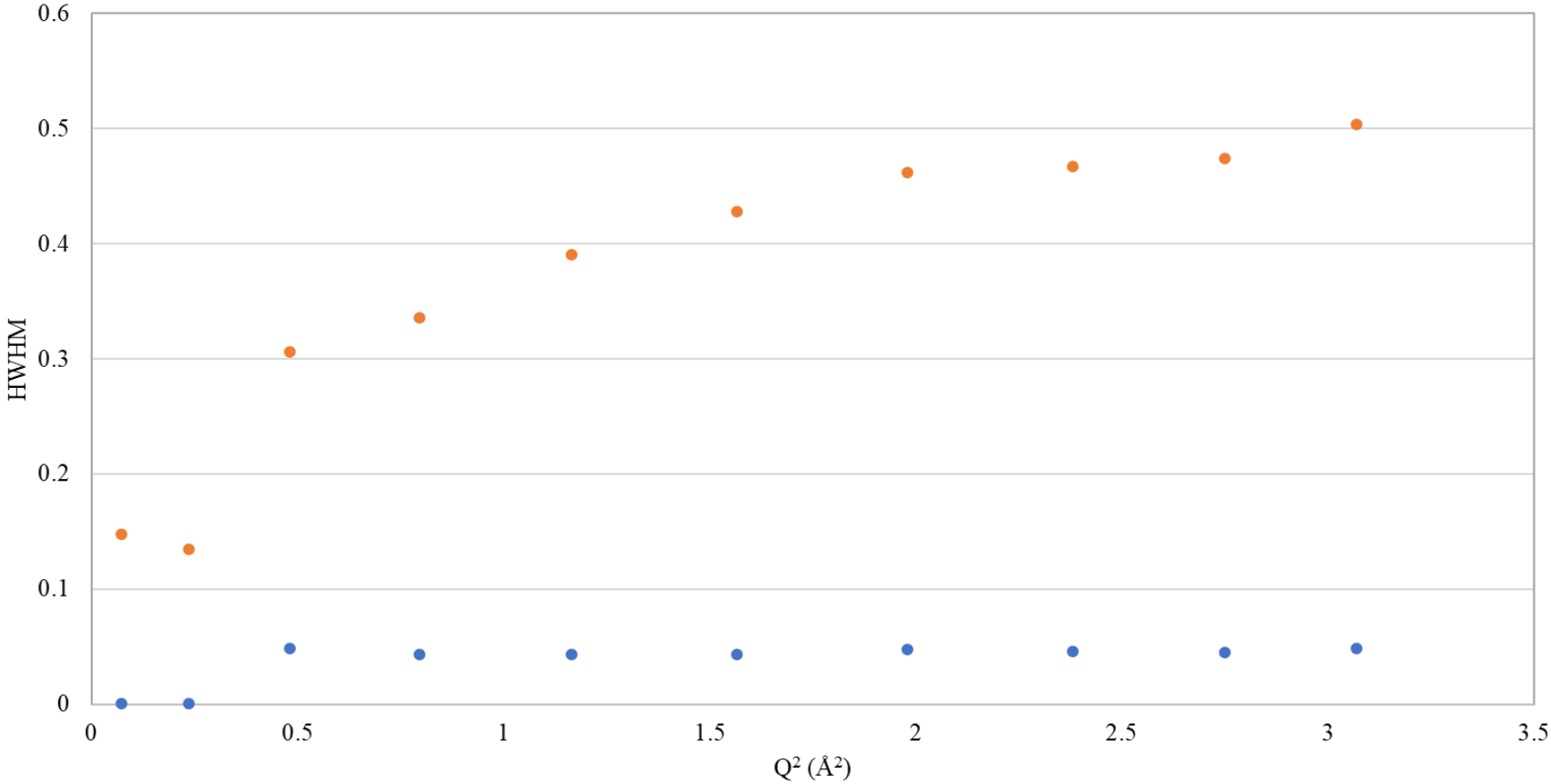

Figure 6.23. Half width half maxima graph of QENS data at 5 K. Orange dots = translation of interlayer water molecules; blue dots = rotation of interlayer water molecules.

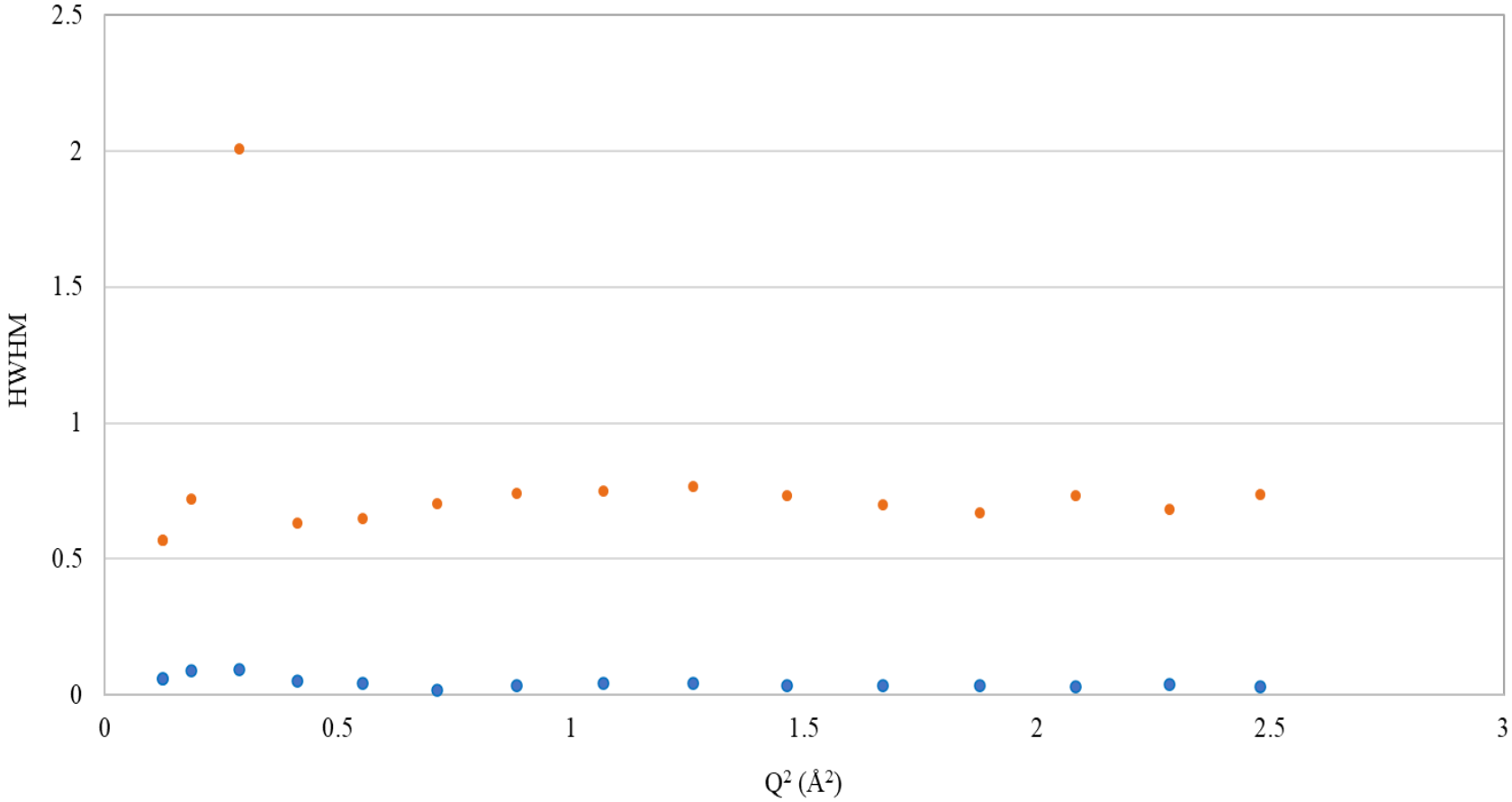

Figure 6.24. Half width half maxima graph of QENS data at 200 K. Orange dots = translation of interlayer water molecules; blue dots = rotation of interlayer water molecules.

From this data analysis, the different types of water transition could be distinguished where rotation was independent of Q whilst diffusion was Q dependent (Figures 6.23-6.24).

6.4 DISCUSSION

6.4.1 Stability of the hydrated (10 Å) halloysites as determined by time-lapse X-ray powder diffraction

Time lapse XRPD patterns showed that even within the same tubular morphology, variations in the dehydration time of the halloysites were observed and the overall effect of dehydration did not appear to be morphology dependent. Samples 5Ch (cylindrical) and 24US (polygonal prismatic) showed the highest retention of their interlayer water and indeed even after 51 hours of dehydration, the final scans (insets Figures 6.5, 6.8) showed that some hydrated (10 Å) halloysite was still present as evidenced by a residual 10 Å d-spacing. In comparison, the samples 6Ch (cylindrical) and 23US (polygonal prismatic) both appeared to dehydrate much more rapidly, approximately 10 hours and 18 hours respectively, and no hydrated halloysite (10 Å) was apparent in the final XRPD scan (insets Figures 6.6-6.7). While subtle differences in sample packing and grain size may account for variations in the dehydration rates observed for the four halloysites, it is not thought likely that these could account for such a large distinction over the significant time period of the scans. Indeed, variations occur between the two polygonal prismatic samples used here where 23US is in an initial putty form, wherein it was malleable and hence smeared in the crucible when attempts were made to crush this sample. In contrast, 24US was a soft solid which easily crushed to a powder, allowing greater surface exposure. The dehydration scans can be viewed as reassurance that the short handling times, a couple of minutes, of transferring the samples to the vessels for analysis by neutron scattering would not result in dehydration of the halloysite samples. Future scans over a larger sample set would be required to determine whether the morphology of the nanotubes or other factors such as initial moisture content and consistency can be used to predict the expected dehydration rate of different nanotubes. It also must be considered that both 23US and 24US contain a substantial amount of cylindrical nanotubes as inferred by

their ‘CP’ index and so future scans using purer polygonal prismatic halloysites may result in clearer distinctions along the lines of tubular morphology.

6.4.2 Deuteration level of the halloysite nanotubes as determined by Fourier transform infrared (FTIR)

The FTIR analysis of the deuterated halloysites provides important information on the structure of the halloysites used. There appears to be no clear pattern between the extent of deuteration of the samples (Table 6.4), where an indication of the level of deuteration can be inferred from the height loss between the ~3700 cm^{-1} surface OH stretching band between 0% and 100% deuteration. The samples all showed a reduction in intensity of the inner OH stretching band at around ~3620 cm^{-1} after 100% deuterated water vapour treatment, although to a lesser extent than the higher frequency band. The ratio of the two bands at 3700/3620 cm^{-1} with no deuterated treatment (100% H_2O) and 100% deuterated treatment can be seen in Table 6.3. From the data it can be observed that the ratio decreases after deuteration, highlighting that the surface hydroxyls are more available for exchange with deuterium than the inner aluminol hydroxl groups. This can be expected when it is considered that they are more easily accessible for exchange, compared to the inner hydroxyl. Although a different deuteration mechanism was employed this has been previously observed by Wada (1967) for halloysite and kaolinite.

The continued presence of the Al-OH stretching FTIR bands, even after deuteration with 100% deuterated water vapour suggests that complete deuteration of the surface hydroxyls did not occur in any of the samples. This can be rationalised by considering that the system under deuterated vapour would form an equilibrium, wherein the exchange of hydrogens in the surface OH groups for deuterium would eventually result in 50% of the vapour D_2O being converted to HDO. Whilst the deuterated vapour was changed weekly for four weeks in order to drive the equilibrium further (by removal of HDO), it appears that this was insufficient stimulus to obtain 100% deuteration. It is not yet known why the different samples respond in different ways to the deuteration treatment. It can be hypothesised that the low deuteration of the polygonal prismatic 23US sample is due to its ‘putty-like’ texture which meant it was not possible to finely crush the sample and hence expose as high a surface area to the

deuteration. Taking this into account and considering the 23US sample as an anomaly, it may be considered that the cylindrical samples deuterated to a similar extent (40-45 %) whilst the polygonal prismatic 24US was the most susceptible to deuteration at almost 60%. From understanding of the cross-sections of the different morphologies (Chapter 4, Section 4.3.2), it was observed that the outer layers of polygonal prismatic halloysites were less tightly rolled than their cylindrical counterparts and the presence of the slits and pores within their structure may, in theory, allow greater access for the deuterated water to exchange with the interlayer water. In addition, from the Tyndall observations in the phosphate adsorption experiments (Chapter 3, Section 3.4.4) it was noted that the polygonal prismatic halloysite 17US went into suspension more easily than the cylindrical 4Ch, suggesting a difference in the external surface behaviour between the cylindrical and polygonal prismatic morphologies. This propensity to disperse more easily may account for less agglomeration of the samples and hence a greater exposure of nanotubes which are available for deuterium exchange.

From the halloysite (10 Å) FTIR spectra, it is apparent by the loss of intensity of the bulk water band at around 3380 cm^{-1} and the increase in intensity of the O-D stretching band at around 2500 cm^{-1} that the bulk and interlayer water underwent almost complete deuteration, where this is thought to occur as a 2-step process via HOD. The replacement of the OH stretching band of hole water at around 3560 cm^{-1}, resulting in an OD band at 2600 cm^{-1}, was observed for all four samples. This is in contrast to previous work by Theng *et al*. (1982) who noted that the OH stretching band of the hole water at 3560 cm^{-1} exchanged very slowly. Persistence of the 3560 cm^{-1} band was suggestive of inaccessible nature of adsorbed water. This difference may be rationalised by considering that their study was of deuteration within 16 hours whilst the samples here were deuterated over the longer time scale of 4 weeks, suggesting that the deuteration process for the hole water may be controlled by kinetics.

Despite the long timescale for deuteration, the evidence provided by FTIR analysis suggests that complete deuteration of the Al-OH groups in the samples does not occur, in line with previous research into this area (Theng *et al*., 1982). Additionally, Wada (1967) proposed that incomplete deuteration of halloysites, and indeed all four kaolin polymorphs, occurred and that a slightly lower OH-OD exchange for halloysites may

arise due to their larger surface area. Future work in this area should consider NIR which may allow a greater insight into the water interaction modes.

As mentioned in the introduction to this chapter (Section 6.1.2) one of the benefits of neutron scattering is the ability to distinguish between isotopes, hence the deuteration of the halloysite nanotubes. Despite this, the neutron spectroscopy experiments were conducted on the halloysite (10 Å) 6Ch sample with no deuteration and so the calculated level of deuteration does not affect the results. However, understanding the level and location of deuteration becomes vital when looking at the data from the neutron diffraction experiments which were conducted on the NIMROD instrument and the subsequent surface modelling. This is because the presence of deuterium will affect properties such as bond energy and bond length. As mentioned in the introduction to this chapter, this work is being conducted at UCL.

6.4.3 Neutron spectroscopy to investigate the dynamics of interlayer water

It can be surmised from the diffraction experiments (Figure 6.19) undertaken as part of the neutron spectroscopy experiments that the halloysite (10 Å) 6Ch sample was effectively packed into the sample holder and sealed throughout the experiments, which were carried out over several days.

From comparison of the elastic window scans at varying hydration states (Figure 6.22), the transitions due to interlayer water can be verified as occurring at 5 K, 200 K, 250 K, 300 K and 320 K. QENS analysis was therefore conducted at these temperatures, as has been protocol for other material studies (Gates *et al*., 2012). Determination of the Q dependence on the half width half maxima of the scattering and the fitting of the data to two Lorentzian curves suggests that both rotation and translation of interlayer water is occurring, in line with the only previous study on halloysite (Bordallo *et al*., 2008). The underlying rationale being that the long-range translation of water can be thought to occur by Brownian motion, whilst the rotation of water molecules occurs around the centre of mass of the water molecule itself. Thus, the diffusional curvature could be fitted by one of many available models, such as the jump diffusional model which calculates the speed of the ‘rests and jumps’ of the water molecules (Bordallo *et al*., 2008). Whilst this modelling is out of the scope of this PhD

and planned to be conducted at UCL with our collaborators, the results presented in this thesis provide a brief overview of the experimental process for the neutron spectroscopy experiments and prevent the initial results which suggest that the interlayer water shows both rotational and translational degrees of movement.

The initial neutron spectroscopy results presented here therefore can be seen to contribute towards a greater understanding of the dynamics of the interlayer water, where it appears that the interlayer water moves via both translations and rotations, although further work is required on the data gathered to verify this.

6.5 CONCLUSION

The work presented in this chapter provides a brief snapshot of the potential of neutron studies to learn more about the structure and dynamics of interlayer water in halloysite nanotubes. The FTIR studies have shown that complete deuteration of the structural OH groups in halloysites does not occur. This is not thought to have a large bearing on the neutron spectroscopy results presented here as they are focused on the interlayer water, it will, however, have a greater impact on the neutron diffraction work and subsequent modelling processes. For this reason, future work is being undertaken out with this PhD on *in situ* deuteration and FTIR analysis of the halloysite nanotubes where it is hoped that this will provide more insight into the deuteration mechanism and respective access of the different OH groups to deuterium exchange.

The XRPD timescale analysis which highlighted the differing timescales of the four halloysite (10 Å) samples with respect to dehydration to halloysite (7 Å) emphasises the difference between the halloysite samples, even out-with their respective tubular morphologies. It was also useful to verify that the short transfer times from sealed sample containers to sample vessels for analysis would not be sufficient to allow dehydration to occur in the samples.

The effectiveness of neutron scattering experiments for the study of the interlayer water in halloysite can be observed by the quality of the data generated at the ISIS Neutron and Muon Source. Whilst the question of the behaviour in terms of the structure and dynamics of interlayer water in halloysite nanotubes is a large one, and

not one that has been fully answered within the context of this thesis chapter, it has been shown that the interlayer water likely moves via both rotation and translation in the interlayer. It is hoped that a greater understanding of the interlayer water may contribute to the discussion about the role of this water in the formation of halloysite nanotubes as well as aiding in the understanding at the atomic scale of the processes, such as adsorption, that occur in halloysite (10 Å) samples.

The overall aim of the neutron diffraction work, where further analysis is being undertaken at UCL, is to enable a clearer understanding of the positioning of this interlayer water with respect to both the alumina and siloxane surfaces. Where previous works have attempted to understand this via modelling methods (Presti *et al*., 2015; Ferrante *et al*., 2017), this is the first time, at the time of writing this thesis, that neutron diffraction experiments are being used to approach this problem. Future work is also being undertaken by our collaborators at UCL on halloysites using neutron diffraction and spectrometry experiments which includes study of the materials with methanol in the interlayer.

6.6 REFERENCES

National Institute of Standards and Technology (NIST) database.

www.isis.stfc.ac.uk./Pages/osiris

Arnold, O., Bilheux, J.C., Borreguero, J.M., Buts, A., Campbell, S.I., Chapon, L., Doucet, M., Draper, N., Ferraz Leal, R., Gigg, M.A., Lynch, V.E., Markvardsen, A., Mikkelson, D.J., Mikkelson, R.L., Miller, R., Palmen, K., Parker, P., Passos, G., Perring, T.G., Peterson, P.F., Ren, S., Reuter, M.A., Savici, A.T., Taylor, J.W., Taylor, R.J., Tolchenov, R., Zhou, W. & Zikovsky, J. (2014) Mantid—data analysis and visualization package for neutron scattering and μ sr experiments. *Nuclear Instruments and Methods in Physics Research Section A: Accelerators, Spectrometers, Detectors and Associated Equipment*, **764**, 156-166.

Bates, T.F., Hildebrand, F.A. & Swineford, A. (1950) Morphology and structure of endellite and halloysite. *American Mineralogist*, **35**, 463-484.

Berg, M.C., Dalby, K.N., Tsapatsaris, N., Okhrimenko, D.V., Sørensen, H.O., Jha, D., Embs, J.P., Stipp, S.L.S. & Bordallo, H.N. (2017) Water mobility in chalk: A quasielastic neutron scattering study. *The Journal of Physical Chemistry C*, **121**, 14088-14095.

Bordallo, H.N., Aldridge, L.P., Churchman, G.J., Gates, W.P., Telling, M.T.F., Kiefer, K., Fouquet, P., Seydel, T. & Kimber, S.A.J. (2008) Quasi-elastic neutron scattering studies on clay interlayer-space highlighting the effect of the cation

in confined water dynamics. *The Journal of Physical Chemistry C*, **112**, 13982-13991.

Bordallo, H.N., Aldridge, L.P. & Desmedt, A. (2006) Water dynamics in hardened ordinary portland cement paste or concrete: From quasielastic neutron scattering. *The Journal of Physical Chemistry B*, **110**, 17966-17976.

Churchman, G.J. & Carr, R.M. (1975) The definition and nomenclature of halloysites. *Clays and Clay Minerals*, **23**, 382-388.

Costanzo, P.M. & Giese, R.F. (1985) Dehydration of synthetic hydrated kaolinites: A model for the dehydration of halloysite(10 Å). *Clays and Clay Minerals*, **33**, 415-423.

Costanzo, P.M., Giese, R.F. & Clemency, C.V. (1984) Synthesis of a 10-Å hydrated kaolinite. *Clays and Clay Minerals*, **32**, 29-35.

Dove, M.T. (2002) An introduction to the use of neutron scattering methods in mineral sciences. *European Journal of Mineralogy*, **14**, 203-224.

Farmer, V.C. & Farmer, V.C. (1974) The layer silicates. Pp. 0. *The infrared spectra of minerals*, **4**, Mineralogical Society of Great Britain and Ireland.

Ferrante, F., Armata, N., Cavallaro, G. & Lazzara, G. (2017) Adsorption studies of molecules on the halloysite surfaces: A computational and experimental investigation. *The Journal of Physical Chemistry C*, **121**, 2951-2958.

Gates, W.P., Aldridge, L.P., Carnero-Guzman, G.G., Mole, R.A., Yu, D., Iles, G.N., Klapproth, A. & Bordallo, H.N. (2017) Water desorption and absorption isotherms of sodium montmorillonite: A QENS study. *Applied Clay Science*, **147**, 97-104.

Gates, W.P., Bordallo, H.N., Aldridge, L.P., Seydel, T., Jacobsen, H., Marry, V. & Churchman, G.J. (2012) Neutron time-of-flight quantification of water desorption isotherms of montmorillonite. *The Journal of Physical Chemistry C*, **116**, 5558-5570.

Hillier, S., Brydson, R., Delbos, E., Fraser, T., Gray, N., Pendlowski, H., Phillips, I., Robertson, J. & Wilson, I. (2016) Correlations among the mineralogical and physical properties of halloysite nanotubes (HNTs). *Clay Minerals*, **51**, 325-350.

IAEA (2005) *Measurement of residual stress in materials using neutrons*. INTERNATIONAL ATOMIC ENERGY AGENCY, Vienna.

Kohyama, N., Fukushima, K. & Fukami, A. (1978) Observation of the hydrated form of tubular halloysite by an electron microscope equipped with an environmental cell. *Clays and Clay Minerals*, **26**, 25-40.

MacEwan, D. (1947) The nomenclautre of the halloysite minerals. *Mineralogical Magazine and Journal of the Mineralogical Society*, **28**, 196.

Madejová, J. (2003) FTIR techniques in clay mineral studies. *Vibrational Spectroscopy*, **31**, 1-10.

Mamontov, E. (2005) High-resolution neutron-scattering study of slow dynamics of surface water molecules in zirconium oxide. *The Journal of Chemical Physics*, **123**, 024706.

Mukhopadhyay, S., Hewer, B., Howells, S. & Markvardsen, A. (2019) A modern approach to QENS data analysis in Mantid. *Physica B: Condensed Matter*, **563**, 41-49.

Müller, A., Bühler, E., Lamparter, P. & Steeb, S. (1987) Neutron- and X-ray-diffraction study on the structure of amorphous $Co_{25}Ti_{75}$. *Zeitschrift für Naturforschung A*, **42**, 7.

Presti, D., Pedone, A., Mancini, G., Duce, C., Tiné, M.R. & Barone, V. (2016) Insights into structural and dynamical features of water at halloysite interfaces probed by DFT and classical molecular dynamics simulations. *Physical Chemistry Chemical Physics*, **18**, 2164-2174.

Sakai, V.G. (2015) 15th Oxford School of Neutron Scattering, Science and Technologies Facilities Council, ISIS.

Theng, B.K.G., Russell, M., Churchman, G.J. & Parfitt, R.L. (1982) Surface properties of allophane, halloysite, imogolite. *Clays and Clay Minerals*, **30**, 143-149.

Wada, K. (1967) A study of hydroxyl groups in kaolin minerals utilizing selective deuteration and infrared spectroscopy. *Clay Minerals*, **7**(1), 51-61.

Chapter 7

Conclusions and Future Work

7.1 SUMMARY

The research presented throughout Chapters 3-6, has focused on the surface chemistry and functionality of tubular halloysite nanotubes. As emphasised throughout this thesis, halloysite nanotubes are rapidly becoming an area of interest in a myriad of technological applications, primarily due to their high length to aspect ratio, nano-scale diameter and their nanotube shape (Pasbakhsh *et al*., 2013; Yuan *et al*., 2015; Churchman *et al*., 2016). Whilst halloysite nanotubes are readily used in multiple technologies, there remains some key questions over the fundamental features of these minerals which have therefore been explored in this thesis.

One of the key threads throughout the chapters was the distinction between the two main tubular morphologies, cylindrical and polygonal prismatic, where the use of the two morphologies has been clearly labelled and their features contrasted throughout. Whilst this feature has been noted in several publications (Dixon and McKee, 1974; Churchman *et al*., 1995; Kogure *et al*., 2013), there are few papers which attempt to address the distinction in behaviour between the two (Gray *et al*., 2016; Hillier *et al*., 2016).

7.1.1 Phosphate adsorption capacity of halloysite nanotubes

The phosphate adsorption experiments presented in Chapter 3 highlight the variation in surface properties and features of the two morphologies. Whilst it was shown that the cylindrical halloysites adsorbed up to 2.5 times more phosphate than the polygonal prismatic halloysite under identical conditions, at 1.1 mg/g and 0.45 mg/g respectively, the adsorption capacity was observed to be more closely related when normalised to specific surface area.

While the phosphate adsorption capacity of the two tubular morphologies were found to vary, a strong dependence of pH was noted, as has previously been reported for kaolinites (Edzwald *et al*., 1976; Manning and Goldberg, 1996), with a maximum adsorption occurring at around pH 6. The effect of pH on the anion adsorption is

significant since the alumina and siloxane surfaces have different points of zero charge (Gupta and Miller, 2010) and so will subsequently be affected by different anion loading at specific pH's.

In contrast to recent work on the phosphate adsorption on tubular halloysite which obtained a good fit of experimental data to Langmuir isotherms (Almasri *et al*., 2019; Saki *et al*., 2019), although the tubular morphology was not identified, it could be seen in Chapter 3 that the two tubular halloysites behaved differently when fitted to Langmuir adsorption isotherms. From the experimental results, the prismatic sample obtained a good fit, with the maximum phosphate adsorption estimated at 0.43 mg/g at pH 6, whilst the cylindrical sample did not fit the Langmuir isotherm. As mentioned in Chapter 3, further work on a larger range of samples would be required to verify this.

7.1.2 Function of the interlayer water in halloysite nanotubes

The question of the role of the interlayer water in controlling the anion adsorption capacities is one that can only be understood by achieving a greater understanding of the structure and amount of interlayer water itself. Although greatly debated, the role of the interlayer water in both the formation of the nanotubular shape and subsequent reactivities of the halloysite nanotubes is not yet fully understood and, as such, remains a key and fundamental question in halloysite clay research.

In Chapter 3, the phosphate adsorption of both halloysite (10 Å) and halloysite (7 Å) morphologies were compared. When normalised to their specific surface area, the two hydrated cylindrical halloysite (10 Å) samples were shown to have a higher phosphate adsorption capacity (~0.50 μmol/m^2) when compared to the hydrated polygonal prismatic halloysite (10 Å) sample (~0.20 μmol/m^2). It may be considered that this difference between the two morphologies arose due to differences in sample purity where the polygonal prismatic (10 Å) sample contained around 13.1 % of impurities such as quartz, kaolinite and iron oxides, as determined by X-ray powder diffraction. However, the results are more conclusive when compared with the normalised halloysite (7 Å) samples where both morphologies showed an average lower adsorption (~0.35-0.40 μmol/m^2). Therefore, it may be inferred that the halloysite (10 Å) samples had a higher adsorption capacity. This has been suggested by previous authors in terms of cation adsorption (Grim, 1968), but had not yet been shown for

anion adsorption. It can be hypothesised that the increase in adsorption capacity for halloysite (10 Å) samples occurs because the interlayer water effectively cleaves apart the interlayers, hence, allowing greater access for adsorption at the edge sites. A comparison of the halloysite surfaces in the presence and absence of interlayer water is considered the respective space filling models of each surface and cross section (Figures 7.1-7.2). Figures 7.1-7.2 demonstrate that although the alumina and siloxane surfaces are identical, regardless of hydration state, the presence of interlayer water may allow for greater access to a greater number of Al-hydroxyls for adsorption.

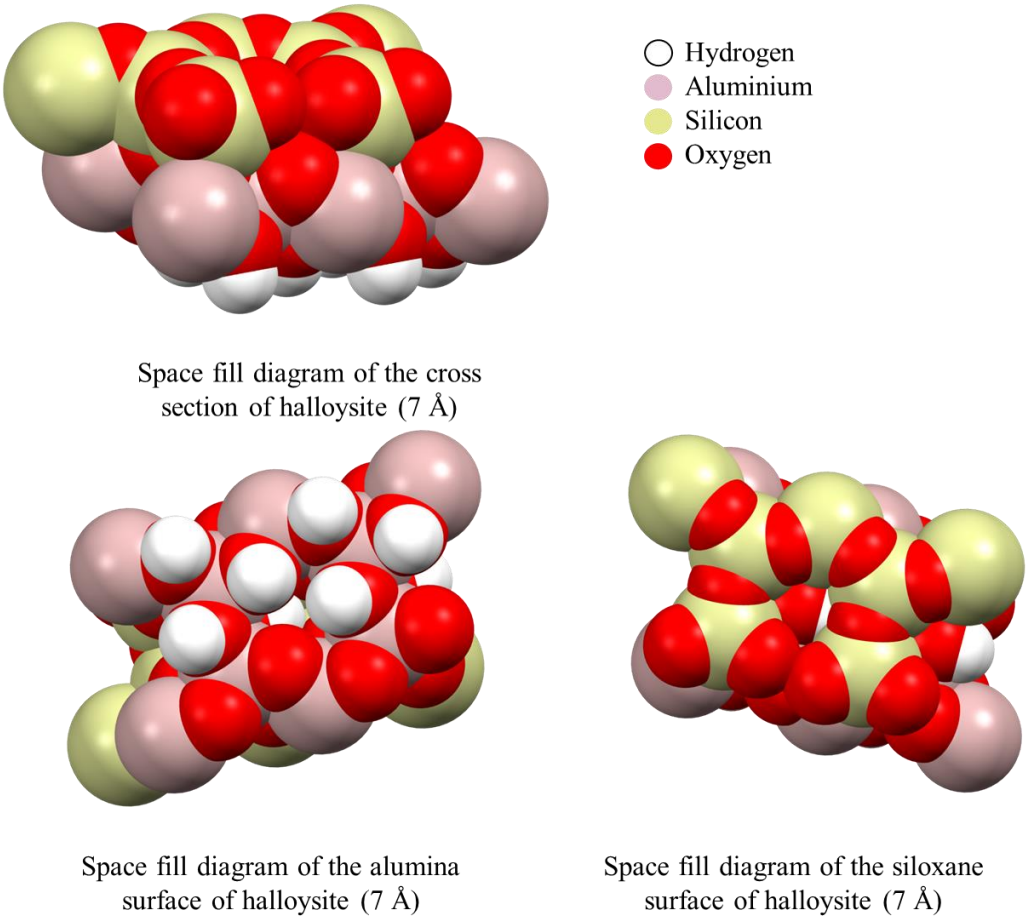

Figure 7.1. Space filling models of the alumina and siloxane surface in halloysite (7 Å).

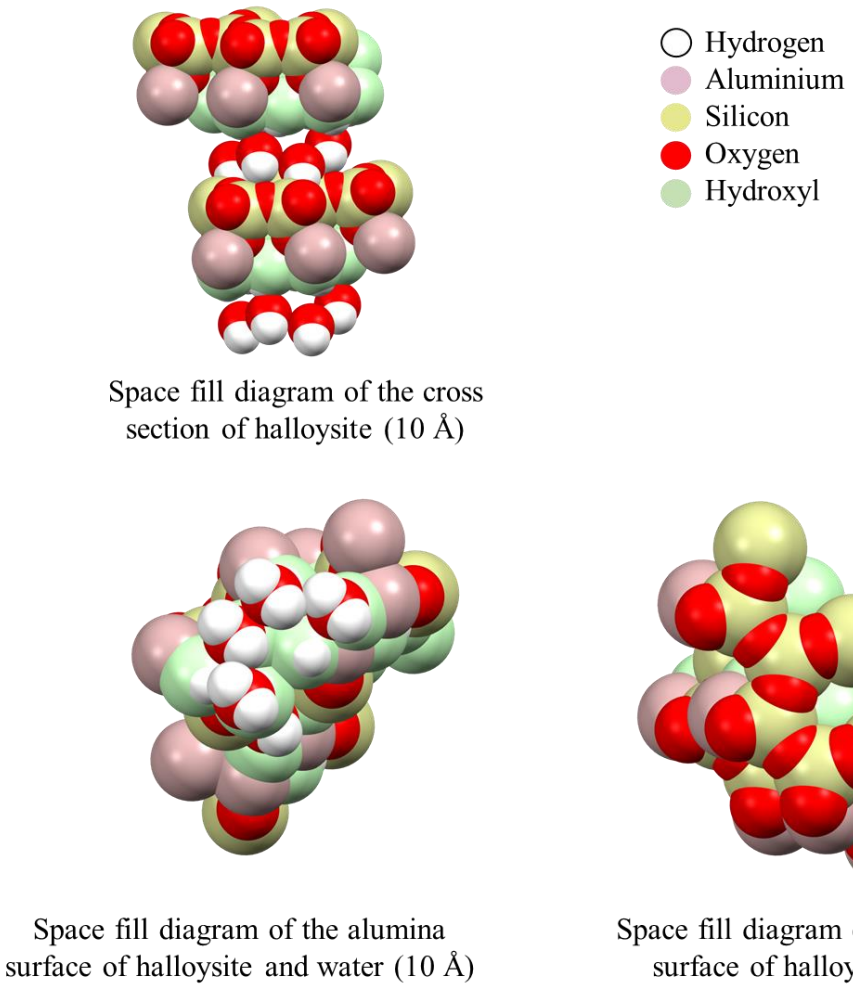

Figure 7.2. Space filling models of the alumina and siloxane surface in halloysite (10 Å).

Through use of neutron scattering experiments, both the structure and dynamics of the interlayer water were conducted and the initial results which tackled the dynamics of interlayer water are presented in Chapter 6. Whilst these are the initial findings only and the remainder of the work is being conducted in collaboration with University College London, they demonstrate that the interlayer water appears to be moving by both rotations and translations and is in agreement with the only previous study using this technique (Bordallo *et al*., 2008). The neutron diffraction work, which is focused on the structure of the interlayer water, hopes to understand more about the orientation of the interlayer water with respect to the alumina and siloxane surfaces. This will be achieved by employing Monte Carlo and Empirical Potential Structure Refinement (EPSR) models to the data generated from neutron diffraction. This goes further than previous research which has used modelling methods, such as density function theory

(DFT) on kaolinite (Presti *et al*., 2016) or curved halloysite layers (Ferrante *et al*., 2015) without also conducting experimental work to gather the data.

The dehydration behaviour of four halloysite (10 Å) samples of differing tubular morphologies was also investigated in Chapter 6 by repeated X-ray powder diffraction scans over a timescale of 51 hours. The resultant graphs showed that the halloysites all dehydrated along different timescales. This is in accordance with previous work which indicated that the dehydration of halloysites is variable and depends on the halloysite being studied (Joussein *et al*., 2006).

7.1.3 Surface chemistry of halloysite nanotubes

Further understanding of the surface chemistry of the halloysite nanotubes was gathered by consideration of the deuteration of the samples by FTIR, where it was concluded that the surface hydroxyls, as opposed to the inner hydroxyl, in the alumina layer were most susceptible to deuterium exchange, where they can be viewed in Figure 7.1 as being most accessible. Whilst similar behaviour has been previously observed (Theng *et al*., 1982), the work here quantified the level of deuteration and demonstrated that, between the four dehydrated samples, the level of deuteration varied. Additional samples would need to be analysed to determine whether this was due to the differing morphologies of the samples or other factors such as texture and purity where one of the polygonal prismatic samples (23US) was 'putty like' in texture and lower in purity.

7.1.4 Surface features of halloysite nanotubes as studied using advanced microscopy techniques

In-depth studies of the surface features of the halloysite nanotubes are outlined in Chapters 4 and 5 with the use of advanced microscopy techniques. As emphasised throughout the thesis, often when considered for technological applications, halloysite nanotubes are viewed as a simplistic model with the focus for the reaction sites being the inner lumen surface and the edge sites of the nanotubes. The experiments outlined in Chapter 4 effectively demonstrated the heterogeneity of the external siloxane surface of the polygonal prismatic nanotubes, in particular, through use of AFM and TEM analysis. Additional measurements that were made on these samples estimated the step sizes on the halloysite nanotubes (11.8 ± 5.9 nm) from which the edge sites were calculated to contribute an additional 10 % of available edge area. This is greater

than previous estimations for kaolinites, where Zbik and Smart (1998) proposed that the steps and edges on a poorly crystalline kaolinite resulted in an additional 6% edge site contribution whilst Brady et al. (1996) calculated an additional 5% edge site contribution for kaolinite. Hence, it can be inferred that, compared to kaolinites, halloysites have a greater number of steps and edges on their external surface.

The AFM analysis has resulted in an alternative proposal to the simplistic model of halloysite often suggested, where the two are shown for comparison in Figure 7.2. The significance of these extra steps and edges on the external surface of halloysite was indicated by Yuan *et al*. (2008) who anticipated that any extra hydroxyl groups arising from surface defects would have a considerable effect on the surface chemistry of the halloysite nanotubes, and hence, may act as additional reaction sites for surface modification processes.

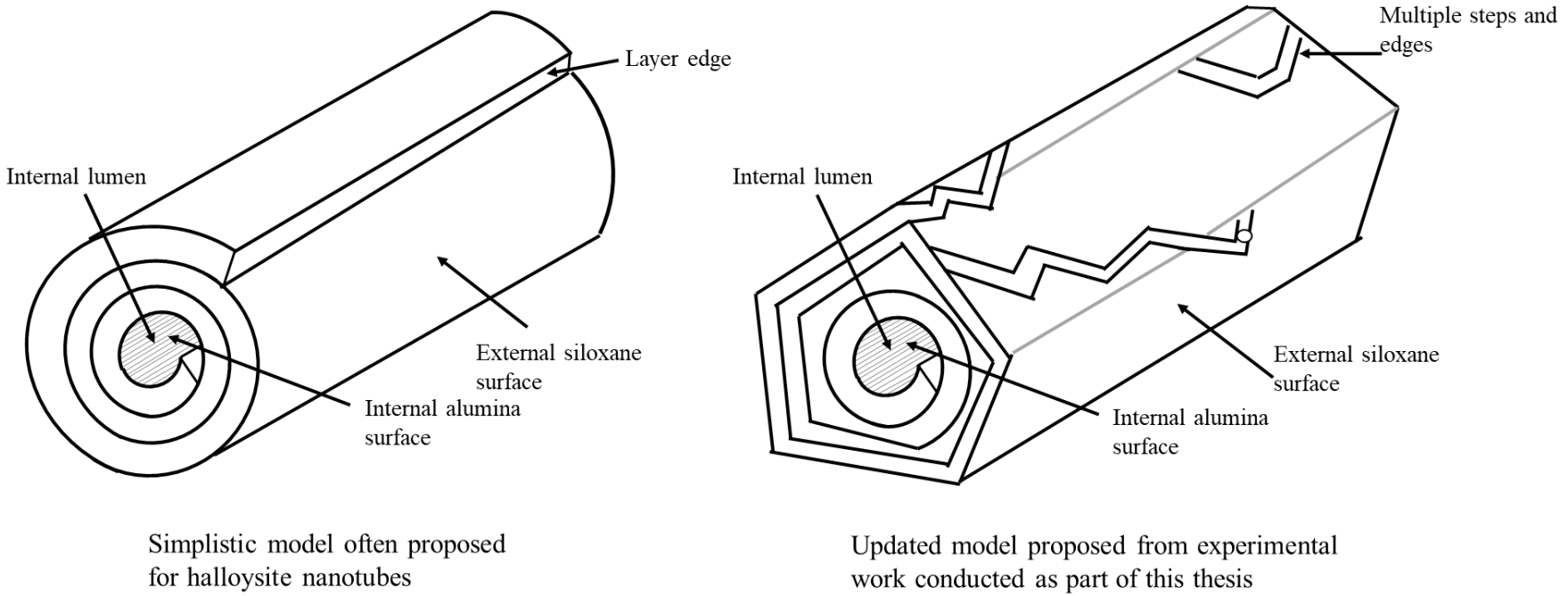

Figure 7.3. A comparison of the simplistic model of halloysite nanotubes as often considered in the literature compared to the version proposed from the advanced microscopy techniques employed in this thesis.

7.1.5 Relationship between the two tubular morphologies

Whilst it has been referenced that the two morphologies of tubular halloysites can be found together (Churchman *et al*., 1995), the exact relation between the two continues to be a matter of debate and further investigation into this relationship was one of the initial aims of the thesis. Cross-sectional TEM analysis was conducted and detailed in Chapter 4 of this thesis where it was hypothesised from the images taken and subsequent analysis that the polygonal prismatic samples occur as a result of continued growth of the cylindrical samples. This work validates previous hypothesises made by Hillier *et al*. (2016) and goes further than previous pioneering TEM cross section work by Dixon and McKee (1974) in understanding the morphologies of the tubular halloysites. In addition, the evidence of pore and slits in the polygonal prismatic samples as viewed in the cross section TEM images agreed with previous published work where they had been observed (Dixon and McKee, 1974; Kohyama *et al.*,1974; Churchman *et al*., 1995; Pasbakhsh *et al*., 2013).

7.1.6 Metal nano-tagging on the surfaces of halloysite nanotubes as observed by electron microscopy

With the aim of using electron microscopy, along with another analytical techniques such as XPS, FTIR and XRPD, to visualise the anion adsorption sites on halloysite nanotubes the use of gold nanotag decoration of the halloysite nanotubes was explored in Chapter 5 of the thesis. Through the novel use of attaching phosphonate terminated linkers to the nanotags prior to adsorption on the halloysite nanotubes, it was hoped to obtain use the nanotag as a visual probe as to the surface sites for phosphate adsorption on the halloysite nanotubes. With the caveat that some free gold nanotags may adsorb onto the surfaces, it was found that the work was successful and the nanotags were observed using TEM on the inner lumen and edge sites of the halloysites. In the case of the polygonal prismatic sample, however, the presence of the gold nanotags was also noted on the external surface. This may correlate to pH dependent hydroxyl groups which are available for anion adsorption and occur on the external surface due to the steps and edges noted in the AFM analysis of Chapter 4. Again, a distinction was noted in behaviour of the two morphologies where the polygonal prismatic morphology obtained a more even coverage, as observed using optical microscopy,

and appeared to have a greater concentration of nanotags on the edge sites when compared to the cylindrical halloysite (Figure 7.4).

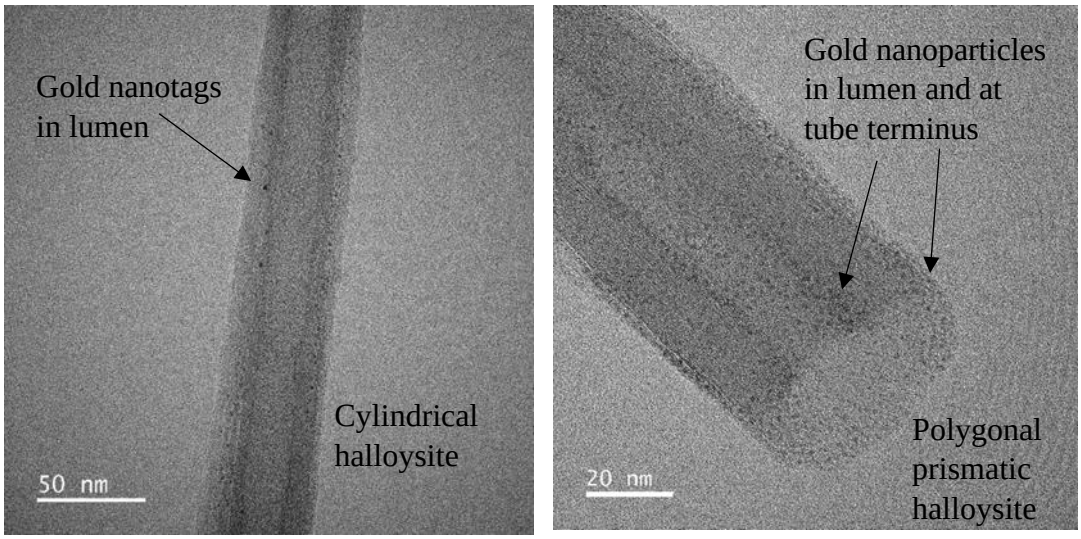

Figure 7.4. Comparison of dispersion of gold nanotags on a cylindrical (4Ch) and polygonal prismatic (17US) halloysite.

7.2 FUTURE WORK

Whilst this thesis has attempted to fully answer all the research questions posed in the introductory chapters, inevitably there are some questions remaining and some new questions that have arisen as knowledge has been gained.

Chapter 3 explored the adsorption and desorption of phosphate onto halloysite nanotubes of varying morphologies and hydration states. Several questions arose from this work which would require further study and experimental time. Primarily, the differing behaviours of the two tubular morphologies to fitting of the Langmuir isotherms, where the cylindrical sample (4Ch) did not fit the isotherm, inferring two types of adsorption sites. In order to confirm this observation, and therefore determine whether morphology was the driver behind this difference in behaviour, further experiments would be required on a wider range of cylindrical and polygonal prismatic samples. In addition, the experimental desorption results were summarised as inconclusive, despite two methods being trialled. Whilst only the adsorption of phosphate anions was studied in this thesis, it would be interesting to measure competitive sorption processes of two or more anions to determine the effects of competitive anion adsorption on the surface. While this can be done in similar batch adsorption experiments another potential method would be to use synthesised silver

and gold nanotags with the same phosphate-terminated linker and then to modify one of the nanotags with a nitro-terminated linker, for example, to visually compare phosphate versus nitrate sorption by TEM.

Chapter 4 used advanced microscopy techniques to study the internal and external surfaces of the halloysite nanotubes and, by examining the surface features on the nm scale, began to link morphological features with unit cell characteristics. Due to various limitations on instrument and staff time, the time taken to obtain each image, along with their small sample size, it was not possible to get many well resolved images of the external surfaces of the cylindrical samples. To obtain a clear comparison between the two morphologies in terms of edge sites and defects on the surface, this is an avenue that should be further explored. As mentioned earlier in this chapter, the presence of pores and slits in the TEM images of the polygonal prismatic samples agrees with previous studies of halloysite nanotubes. There remains debate, however, as to how these pores arise, with some authors suggesting that it is the dehydration of halloysite (10 Å) samples which results in these features (Dixon and McKee, 1974; Kohyama *et al.*,1974; Churchman *et al*., 1995) as opposed to them being formed upon nanotube growth. To explore this process further, future experiments could consider investigating a wider range of halloysite (10 Å) samples to determine if the presence of pores could be detected. One of the key conclusions from Chapter 4 was the provision of further evidence towards the theory that polygonal prismatic nanotubes are formed from the extended growth of cylindrical nanotubes, as opposed to being formed upon dehydration of cylindrical (10 Å) samples. To further examine this theory, future experiments have been planned at Leeds University using the TEM wherein halloysite (10 Å) samples will be examined in their hydrated (10 Å) state using a sealed vessel to determine the morphology using *in situ* electron diffraction studies. In theory, this work may also verify the presence of pores in the halloysite (10 Å) samples since they were observed along the elongated nanotubes of the halloysite (7 Å) samples in Chapter 5.

Some of the final experiments from Chapter 5 were placed on hold due to the Covid-19 pandemic and, as such, these could form work to conduct in the future. In particular, TEM analysis of the halloysites samples from the second set of experiments decorated with gold and silver nanotags. It would also be of interest to determine whether there

is a pattern of the nanotags on the external surfaces of the halloysite nanotubes that may correspond to the steps and edges observed in the AFM images of Chapter 4, hence affirming these as additional adsorption sites.

The neutron scattering work conducted at the ISIS Neutron and Muon Source on the structure and dynamics of interlayer water in halloysite is also still ongoing. The initial results of the neutron spectroscopy on the dynamics of the interlayer water were outlined in Chapter 6 of this thesis. However, these results are initial only and future work which will be conducted in collaboration with UCL include the modelling of these results to obtain a clearer picture of the diffusion constants of the interlayer water. This would also allow comparison with other clay minerals. The neutron diffraction analysis is also ongoing, where this work is being conducted by UCL, the results from which will hope to inform as to the structure of the interlayer water with respect to the alumina and siloxane surfaces.

7.3 CONCLUDING REMARKS

To conclude, the research conducted as part of this thesis achieved many of the initial aims. The effect of tubular morphology, which is rarely addressed in halloysite research, was shown throughout the thesis to have an effect on the surface chemistry of the nanotube. Additionally, further evidence was provided in the debate on the relationship between the two morphologies, where it was inferred from the cross-section TEM analysis of the nanotubes that the polygonal prismatic nanotubes arise from continued growth of the cylindrical nanotubes. In line with previous research on other clay minerals (Siretanu *et al.*, 2016) it was observed using AFM that the external surfaces of the polygonal prismatic nanotubes, in particular, had multiple steps and edge which would be available for additional adsorption reactions. The gold nano-tagging work effectively demonstrated this for the polygonal prismatic samples. Initial explorations using neutron scattering to study the fundamental question of the function of interlayer water in halloysite agreed with previous work in this area (Bordallo *et al.*, 2008) where novel work analysis the neutron diffraction data is underway.

Much of the recent research focuses on the application of halloysite nanotubes to materials research and technology (Bertolino *et al.*, 2020; Danyliuk *et al.*, 2020; Daza-Gómez *et al.*, 2020; Lisuzzo *et al.*, 2020) which requires an understanding of the

potential differences between the reaction behaviour of the halloysite nanotube selected for use (Pasbakhsh *et al*., 2013). The results and subsequent discussions presented in this thesis contribute to the current research interests of halloysite nanotubes by providing more information on the fundamental theory of the surface chemistry and behaviour of these fascinating minerals.

7.4 REFERENCES

Almasri, D.A., Saleh, N.B., Atieh, M.A., McKay, G. & Ahzi, S. (2019) Adsorption of phosphate on iron oxide doped halloysite nanotubes. *Scientific Reports*, **9**, 3232.

Bertolino, V., Cavallaro, G., Milioto, S. & Lazzara, G. (2020) Polysaccharides/halloysite nanotubes for smart bionanocomposite materials. *Carbohydrate Polymers*, **245**, 116502.

Bordallo, H.N., Aldridge, L.P., Churchman, G.J., Gates, W.P., Telling, M.T.F., Kiefer, K., Fouquet, P., Seydel, T. & Kimber, S.A.J. (2008) Quasi-elastic neutron scattering studies on clay interlayer-space highlighting the effect of the cation in confined water dynamics. *The Journal of Physical Chemistry C*, **112**, 13982-13991.

Churchman, G.J., Davy, T.J., Aylmore, L.A.G., Gilkes, R.J. & Self, P.G. (1995) Characteristics of fine pores in some halloysites. Pp. 89. *Clay Minerals*, 30.

Churchman, G.J., Pasbakhsh, P. & Hillier, S. (2016) The rise and rise of halloysite. *Clay Minerals*, **51**, 303-308.

Danyliuk, N., Tomaszewska, J. & Tatarchuk, T. (2020) Halloysite nanotubes and halloysite-based composites for environmental and biomedical applications. *Journal of Molecular Liquids*, **309**, 113077.

Daza-Gómez, L.-C., Ruiz-Ruiz, V.-F., Mendoza-Nieto, J.A., Pfeiffer, H. & Díaz, D. (2020) Co_3O_4 nanostructures and Co_3O_4 supported on halloysite nanotubes: New highly active and thermally stable feasible catalysts for Co oxidation. *Applied Clay Science*, **190**, 105590.

Dixon, J.B. & McKee, T.R. (1974) Internal and external morphology of tubular and spheroidal halloysite particles. *Clays and Clay Minerals*, **22**, 127-137.

Edzwald, J.K., Toensing, D.C. & Leung, M.C.-Y. (1976) Phosphate adsorption reactions with clay minerals. *Environmental Science & Technology*, **10**, 485-490.

Ferrante, F., Armata, N., Cavallaro, G. & Lazzara, G. (2017) Adsorption studies of molecules on the halloysite surfaces: A computational and experimental investigation. *The Journal of Physical Chemistry C*, **121**, 2951-2958.

Gray, N., Lumsdon, D.G. & Hillier, S. (2016) Effect of pH on the cation exchange capacity of some halloysite nanotubes. *Clay Minerals*, **51**, 373-383.

Grim, R.E. (1968) *Clay mineralogy*. New York.

Gupta, V., Hampton, M.A., Nguyen, A.V. & Miller, J.D. (2010) Crystal lattice imaging of the silica and alumina faces of kaolinite using atomic force microscopy. *Journal of Colloid and Interface Science*, **352**, 75-80.

Hillier, S., Brydson, R., Delbos, E., Fraser, T., Gray, N., Pendlowski, H., Phillips, I., Robertson, J. & Wilson, I. (2016) Correlations among the mineralogical and

physical properties of halloysite nanotubes (HNTs). *Clay Minerals*, **51**, 325-350.

Joussein, E., Petit, S., Fialips, C.-I., Vieillard, P. & Righi, D. (2006) Differences in the dehydration-rehydration behavior of halloysites: New evidence and interpretations. *Clays and Clay Minerals*, **54**, 473-484.

Kogure, T., Mori, K., Drits, V.A. & Takai, Y. (2013) Structure of prismatic halloysite. *American Mineralogist*, **98**, 1008-1016.

Kohyama, N., Fukushima, K. & Fukami, A. (1978) Observation of the hydrated form of tubular halloysite by an electron microscope equipped with an environmental cell. *Clays and Clay Minerals*, **26**, 25-40.

Lisuzzo, L., Cavallaro, G., Milioto, S. & Lazzara, G. (2020) Effects of halloysite content on the thermo-mechanical performances of composite bioplastics. *Applied Clay Science*, **185**, 105416.

Manning, B.A. & Goldberg, S. (1996) Modeling arsenate competitive adsorption on kaolinite, montmorillonite and illite. *Clays and Clay Minerals*, **44**, 609-623.

Pasbakhsh, P., Churchman, G.J. & Keeling, J.L. (2013) Characterisation of properties of various halloysites relevant to their use as nanotubes and microfibre fillers. *Applied Clay Science*, **74**, 47-57.

Presti, D., Pedone, A., Mancini, G., Duce, C., Tiné, M.R. & Barone, V. (2016) Insights into structural and dynamical features of water at halloysite interfaces probed by DFT and classical molecular dynamics simulations. *Physical Chemistry Chemical Physics*, **18**, 2164-2174.

Saki, H., Alemayehu, E., Schomburg, J. & Lennartz, B. (2019) Halloysite nanotubes as adsorptive material for phosphate removal from aqueous solution. *Water*, **11**, 203.

Churchman, G.J., Pasbakhsh, P. & Hillier, S. (2016) The rise and rise of halloysite. *Clay Minerals*, **51**, 303-308.

Hillier, S., Brydson, R., Delbos, E., Fraser, T., Gray, N., Pendlowski, H., Phillips, I., Robertson, J. & Wilson, I. (2016) Correlations among the mineralogical and physical properties of halloysite nanotubes (HNTs). *Clay Minerals*, **51**, 325-350.

Siretanu, I., van den Ende, D. & Mugele, F. (2016) Atomic structure and surface defects at mineral-water interfaces probed by *in situ* atomic force microscopy. *Nanoscale*, **8**, 8220-8227.

Theng, B.K.G., Russell, M., Churchman, G.J. & Parfitt, R.L. (1982) Surface properties of allophane, halloysite, imogolite. *Clays and Clay Minerals*, **30**, 143-149.

Yuan, P., Southon, P.D., Liu, Z., Green, M.E.R., Hook, J.M., Antill, S.J. & Kepert, C.J. (2008) Functionalization of halloysite clay nanotubes by grafting with γ-aminopropyltriethoxysilane. *The Journal of Physical Chemistry C*, **112**, 15742-15751.

Yuan, P., Tan, D. & Annabi-Bergaya, F. (2015) Properties and applications of halloysite nanotubes: Recent research advances and future prospects. *Applied Clay Science*, **112-113**, 75-93.

Zbik, M. & Smart, R.S.C. (1998) Nanomorphology of kaolinites: Comparative SEM and AFM studies. *Clays and Clay Minerals*, **46**, 153-160.

Bibliography

www.appliedminerals.com

www.isis.stfc.ac.uk./Pages/osiris

www.mindat.org

National Institute of Standards and Technology (NIST) database

2011/696/EU: Commission Recommendation of 18 October 2011 on the definition of a nanomaterial. *Official Journal of the European Union*.

Abendroth, R.P. (1970) Behavior of a pyrogenic silica in simple electrolytes. *Journal of Colloid and Interface Science*, **34**, 591-596.

Alexander, L.T., Faust, G.T., Hendricks, S.B., Insley, H. & McMurdie, H.F. (1943) Relationship of the clay minerals halloysite and endellite. *American Mineralogist*, **28**, 1-18.

Almasri, D.A., Saleh, N.B., Atieh, M.A., McKay, G. & Ahzi, S. (2019) Adsorption of phosphate on iron oxide doped halloysite nanotubes. *Scientific Reports*, **9**, 3232.

Andrés, E., Araya, F., Vera, I., Pozo, G. & Vidal, G. (2018) Phosphate removal using zeolite in treatment wetlands under different oxidation-reduction potentials. *Ecological Engineering*, **117**, 18-27.

Arnold, O., Bilheux, J.C., Borreguero, J.M., Buts, A., Campbell, S.I., Chapon, L., Doucet, M., Draper, N., Ferraz Leal, R., Gigg, M.A., Lynch, V.E., Markvardsen, A., Mikkelson, D.J., Mikkelson, R.L., Miller, R., Palmen, K., Parker, P., Passos, G., Perring, T.G., Peterson, P.F., Ren, S., Reuter, M.A., Savici, A.T., Taylor, J.W., Taylor, R.J., Tolchenov, R., Zhou, W. & Zikovsky, J. (2014) Mantid—data analysis and visualization package for neutron scattering and μ sr experiments. *Nuclear Instruments and Methods in Physics Research Section A: Accelerators, Spectrometers, Detectors and Associated Equipment*, **764**, 156-166.

Bache, B.W. (1990) G. Sposito 1989. The chemistry of soils. Xiii + 277 pp. New York, Oxford: Oxford university press. Isbn 0 19 504615 3. *Geological Magazine*, **127**, 190-191.

Bailey, S.W. (1980) Summary of recommendations of AIPEA nomenclature committee. *Clays and Clay Minerals*, **28**, 73-78.

Brindley. (1990) Halloysite- a critical assessment. *Sciences Geologiques-Memoires*, **86**, 89-98.

Baronnet, A., Mellini, M. & Devouard, B. (1994) Sectors in polygonal serpentine. A model based on dislocations. *Physics and Chemistry of Minerals*, **21**, 330-343.

Bates, T.F., Hildebrand, F.A. & Swineford, A. (1950) Morphology and structure of endellite and halloysite. *American Mineralogist*, **35**, 463-484.

Berg, M.C., Dalby, K.N., Tsapatsaris, N., Okhrimenko, D.V., Sørensen, H.O., Jha, D., Embs, J.P., Stipp, S.L.S. & Bordallo, H.N. (2017) Water mobility in chalk: A quasielastic neutron scattering study. *The Journal of Physical Chemistry C*, **121**, 14088-14095.

Berthier, P. (1826) Analyse de l'halloysite. *Ann. Chim. Phys*, **32**, 332-335.

Berthonneau, J., Grauby, O., Jeannin, C., Chaudanson, D., Joussein, E. & Baronnet, A. (2015) Native morphology of hydrated spheroidal halloysite observed by environmental transmission electron microscopy. *Clays and Clay Minerals*, **63**, 368-377.

Bish, D.L. (1993) Rietveld refinement of the kaolinite structure at 1.5 k. *Clays and Clay Minerals*, **41**, 738-744.

Bordallo, H.N., Aldridge, L.P., Churchman, G.J., Gates, W.P., Telling, M.T.F., Kiefer, K., Fouquet, P., Seydel, T. & Kimber, S.A.J. (2008) Quasi-elastic neutron scattering studies on clay interlayer-space highlighting the effect of the cation in confined water dynamics. *The Journal of Physical Chemistry C*, **112**, 13982-13991.

Bordallo, H.N., Aldridge, L.P. & Desmedt, A. (2006) Water dynamics in hardened ordinary portland cement paste or concrete: From quasielastic neutron scattering. *The Journal of Physical Chemistry B*, **110**, 17966-17976.

Borden, D. & Giese, R.F. (2001) Baseline studies of the clay minerals society source clays: Cation exchange capacity measurements by the ammonia-electrode method. *Clays and Clay Minerals*, **49**, 444-445.

Borggaard, O.K. (1983) Effects of surface area and mineralogy of iron oxides on their surface charge and anion-adsorption properties. *Clays and Clay Minerals*, **31**, 230-232.

Brady, P.V., Cygan, R.T. & Nagy, K.L. (1996) Molecular controls on kaolinite surface charge. *Journal of Colloid and Interface Science*, **183**, 356-364.

Bretti, C., Cataldo, S., Gianguzza, A., Lando, G., Lazzara, G., Pettignano, A. & Sammartano, S. (2016) Thermodynamics of proton binding of halloysite nanotubes. *The Journal of Physical Chemistry C*, **120**, 7849-7859.

Breen, C., D'Mello, N. & Yarwood, J. (2002) The thermal stability of mixed phenylphosphonic acid/water intercalates of kaolin and halloysite. A TG-EGA and VT-drifts study. *Journal of Materials Chemistry*, **12**, 273-278.

Brindley, G.W. & Comer, J.J. (1955) The structure and morphology of a kaolin clay from Les Eyzies (France). *Clays and Clay Minerals*, **4**, 61-66.

Burridge, K., Johnston, J. & Borrmann, T. (2011) Silver nanoparticle–clay composites. *Journal of Materials Chemistry*, **21**, 734-742.

Cao, H., Sun, X., Zhang, Y. & Jia, N. (2012) Electrochemical sensing based on gold nanoparticle-decorated halloysite nanotube composites. *Analytical Biochemistry*, **430**, 111-115.

Carpenter, S.R., Caraco, N.F., Correll, D.L., Howarth, R.W., Sharpley, A.N. & Smith, V.H. (1998) Nonpoint pollution of surface waters with phosphorus and nitrogen. *Ecological Applications*, **8**, 559-568.

Chipera, S.J. & Bish, D.L. (2013) Fitting full X-ray diffraction patterns for quantitative analysis: A method for readily quantifying crystalline and disordered phases. *Advances in Materials Physics and Chemistry*, **3**, 47-53.

Churchman, G.J. (2018) Game changer in soil science. Functional role of clay minerals in soil. *Journal of Plant Nutrition and Soil Science*, **181**, 99-103.

Churchman, G.J., Aldridge, L.P. & Carr, R.M. (1972) The relationship between the hydrated and dehydrated states of an halloysite. *Clays and Clay Minerals*, **20**, 241-246.

Churchman, G.J. & Carr, R.M. (1975) The definition and nomenclature of halloysites. *Clays and Clay Minerals*, **23**, 382-388.

Churchman, G.J., Davy, T.J., Aylmore, L.A.G., Gilkes, R.J. & Self, P.G. (1995) Characteristics of fine pores in some halloysites. Pp. 89. *Clay Minerals*, 30.

Churchman, G.J. & Lowe, D.J. (2012) Alteration, formation and occurence of minerals in soils. Pp. 20.21-20.72. In P.M. Huang, Y. Li, and M.E. Sumner, Eds. *Handbook of soil sciences. Properties and processes, second edition*,CRC Press, Boca Raton, Florida

Churchman, G.J. & Theng, B.K.G. (1984) Interactions of halloysites with amides; mineralogical factors affecting complex formation. *Clay Minerals*, **19**, 161-175.

Churchman, G.J., Pasbakhsh, P. & Hillier, S. (2016) The rise and rise of halloysite. *Clay Minerals*, **51**, 303-308.

Costanzo, P.M. & Giese, R.F. (1985) Dehydration of synthetic hydrated kaolinites: A model for the dehydration of halloysite (10 Å). *Clays and Clay Minerals*, **33**, 415-423.

Costanzo, P.M., Giese, R.F., Lipsicas, M. & Straley, C. (1982) Synthesis of a quasi-stable kaolinite and heat capacity of interlayer water. *Nature*, **296**, 549-551.

Costanzo, P.M. & Giesse, R.F. (1986) Ordered halloysite; dimethylsulfoxide intercalate. *Clays and Clay Minerals*, **34**, 105-107.

Cravero, F., Fernández, L., Marfil, S., Sánchez, M., Maiza, P. & Martínez, A. (2016) Spheroidal halloysites from patagonia, argentina: Some aspects of their formation and applications. *Applied Clay Science*, **131**, 48-58.

Cravero, F., Maiza, P.J. & Marfil, S.A. (2012) Halloysite in Argentinian deposits: Origin and textural constraints. *Clay Minerals*, **47**, 329-340.

Cressey, B.A., & Zussman, J. (1976) Electron microscopic studies of serpentines. *Canadian Mineralogist*, ***14****, 307-313.*

Croudace, I., Warwick, P., Taylor, R. & Dee, S. (1998) Rapid procedure for plutonium and uranium determination in soils using a borate fusion followed by ion-exchange and extraction chromatography. *Analytica Chimica Acta*, **371**, 217-225.

Davis, J.A. & Kent, D.B. (1990) Surface complexation modeling in aqueous geochemistry. *Reviews in Mineralogy and Geochemistry*, **23**, 177-260.

Derkowski, A., Drits, V.A. & McCarty, D.K. (2012) Rehydration of dehydrated-dehydroxylated smectite in a low water vapor environment. *American Mineralogist*, **97**, 110-127.

Dixon, J.B. & McKee, T.R. (1974) Internal and external morphology of tubular and spheroidal halloysite particles. *Clays and Clay Minerals*, **22**, 127-137.

dos Santos, E.C., Rozynek, Z., Hansen, E.L., Hartmann-Petersen, R., Klitgaard, R.N., Løbner-Olesen, A., Michels, L., Mikkelsen, A., Plivelic, T.S., Bordallo, H.N. & Fossum, J.O. (2017) Ciprofloxacin intercalated in fluorohectorite clay: Identical pure drug activity and toxicity with higher adsorption and controlled release rate. *RSC Advances*, **7**, 26537-26545.

Dove, M.T. (2002) An introduction to the use of neutron scattering methods in mineral sciences. *European Journal of Mineralogy*, **14**, 203-224.

Drits, V.A., Sakharov, B.A. & Hillier, S. (2018) Phase and structural features of tubular halloysite (7 å). *Clay Minerals*, **53**, 691-720.

Du, M., Guo, B., Lei, Y., Liu, M. & Jia, D. (2008) Carboxylated butadiene–styrene rubber/halloysite nanotube nanocomposites: Interfacial interaction and performance. *Polymer*, **49**, 4871-4876.

Edzwald, J.K., Toensing, D.C. & Leung, M.C.-Y. (1976) Phosphate adsorption reactions with clay minerals. *Environmental Science & Technology*, **10**, 485-490.

Farmer, V.C. & Farmer, V.C. (1974) The layer silicates. Pp. 0. *The Infrared Spectra of Minerals*, **4**, Mineralogical Society of Great Britain and Ireland.

Ferrante, F., Armata, N., Cavallaro, G. & Lazzara, G. (2017) Adsorption studies of molecules on the halloysite surfaces: A computational and experimental investigation. *The Journal of Physical Chemistry C*, **121**, 2951-2958.

Flegmann, A.W., Love, G. & Scott, V.D. (1971) Electron-optical study of the prism surfaces of kaolinite microcrystals. *Clay Minerals*, **9**, 245-249.

Gates, W.P., Aldridge, L.P., Carnero-Guzman, G.G., Mole, R.A., Yu, D., Iles, G.N., Klapproth, A. & Bordallo, H.N. (2017) Water desorption and absorption isotherms of sodium montmorillonite: A QENS study. *Applied Clay Science*, **147**, 97-104.

Gates, W.P., Bordallo, H.N., Aldridge, L.P., Seydel, T., Jacobsen, H., Marry, V. & Churchman, G.J. (2012) Neutron time-of-flight quantification of water desorption isotherms of montmorillonite. *The Journal of Physical Chemistry C*, **116**, 5558-5570.

Garrett, W. & Walker, G. (1959) The cation-exchange capacity of hydrated halloysite and the formation of halloysite-salt complexes. *Clay Minerals Bull*, **4**, 75-80.

Gérard, F. (2016) Clay minerals, iron/aluminum oxides, and their contribution to phosphate sorption in soils — a myth revisited. *Geoderma*, **262**, 213-226.

Giese, R.F. (1988) Kaolin minerals; structures and stabilities. *Reviews in Mineralogy and Geochemistry*, **19**, 29-66.

Gimsing, A.L. & Borggaard, O.K. (2002) Competitive adsorption and desorption of glyphosate and phosphate on clay silicates and oxides. *Clay Minerals*, **37**, 509-515.

Golberg, S. (1985) Chemical modeling of anion competition on goethite using the constant capacitance model. *Soil Science Society America*, **49**, 851-856.

Gray, N., Lumsdon, D.G. & Hillier, S. (2016) Effect of pH on the cation exchange capacity of some halloysite nanotubes. *Clay Minerals*, **51**, 373-383.

Grim, R.E. (1968) *Clay mineralogy*. New York.

Gu, X.Y. & Evans, L.J. (2008) Surface complexation modelling of Cd(II), Cu(II), Ni(II), Pb(II) and Zn(II) adsorption onto kaolinite. *Geochimica Et Cosmochimica Acta*, **72**, 267-276.

Gupta, V., Hampton, M.A., Nguyen, A.V. & Miller, J.D. (2010) Crystal lattice imaging of the silica and alumina faces of kaolinite using atomic force microscopy. *Journal of Colloid and Interface Science*, **352**, 75-80.

Guthrie, G.D. & Veblen, D.R. (1989) High-resolution transmission electron microscopy of mixed-layer illite/smectite: Computer simulations. *Clays and Clay Minerals*, **37**, 1-11.

Gustafsson, J.P., Mwamila, L.B. & Kergoat, K. (2012) The pH dependence of phosphate sorption and desorption in swedish agricultural soils. *Geoderma*, **189**, 304-311.

Habibiandehkordi, R., Quinton, J.N. & Surridge, B.W.J. (2014) Effect of equilibration time on estimates of the maximum phosphorus sorption capacity of industrial by-products using the langmuir model. *Journal of Soils and Sediments*, **14**, 1818-1828.

Han, Y., Liu, W., Zhou, J. & Chen, J. (2016) Interactions between kaolinite aloh surface and sodium hexametaphosphate. *Applied Surface Science*, **387**, 759-765.

Hayes, K.F. & Leckie, J.O. (1987) Modeling ionic strength effects on cation adsorption at hydrous oxide/solution interfaces. *Journal of Colloid and Interface Science*, **115**, 564-572.

Haygarth, P.M., Bardgett, R.D. & Condron, L.M. Nitrogen and phosphorus cycles and their management. Pp. 132-159. *Soil conditions and plant growth*.

He, L., W. Zelazny, L., C. Martens, D., Baligar, V. & D. Ritchey, K. (1997) Ionic strength effects on sulfate and phosphate adsorption on γ-alumina and kaolinite: Triple-layer model. *Soil Science Society of America Journal - SSSAJ*, **61**.

He, Y., Lin, H., Dong, Y. & Wang, L. (2017) Preferable adsorption of phosphate using lanthanum-incorporated porous zeolite: Characteristics and mechanism. *Applied Surface Science*, **426**, 995-1004.

Heal, K.V., Younger, P.L., Smith, K.A., Glendinning, S., Quinn, O. & Dobbie, K.E. (2003) Novel use of ochre from mine waste treatment plants to reduce point and diffuse phosphorus pollution. *Land Contamination and Reclamation*, **11**, 145-152.

Hill, D., Holliman, P.J., Jones, E.W., McGettrick, J., Worsley, D.A., Appleman, M. & Chatterjee, P. (2019) Desorption of carboxylates and phosphonates from galvanized steel: Towards greener lubricants. *Surface and Interface Analysis*, **51**, 934-942.

Hillier, S. (1999) Use of an air brush to spray dry samples for X-ray powder diffraction. *Clay Minerals*, **34**, 127-135.

Hillier, S., Brydson, R., Delbos, E., Fraser, T., Gray, N., Pendlowski, H., Phillips, I., Robertson, J. & Wilson, I. (2016) Correlations among the mineralogical and physical properties of halloysite nanotubes (HNTs). *Clay Minerals*, **51**, 325-350.

Holliman, P.J., Vaca Velasco, B., Butler, I., Wijdekop, M. & Worsley, D.A. (2008) Studies of dye sensitisation kinetics and sorption isotherms of direct red 23 on titania. *International Journal of Photoenergy*, **2008**.

Hooshiar, A., Uhlík, P., Kaminsky, H.W., Shinbine, A., Omotoso, O., Liu, Q., Ivey, D.G. & Etsell, T.H. (2010) High resolution transmission electron microscopy study of clay mineral particles from streams of simulated water based bitumen extraction of athabasca oil sands. *Applied Clay Science*, **48**, 466-474.

Huang, X., Foster, G.D., Honeychuck, R.V. & Schreifels, J.A. (2009) The maximum of phosphate adsorption at pH 4.0: Why it appears on aluminum oxides but not on iron oxides. *Langmuir*, **25**, 4450-4461.

Huertas, F.J., Chou, L. & Wollast, R. (1998) Mechanism of kaolinite dissolution at room temperature and pressure: Part 1. Surface speciation. *Geochimica Et Cosmochimica Acta*, **62**, 417-431.

Huggett, J.M. (2005) Clay minerals. Pp. 358-365. In R.C. Selley, L.R.M. Cocks, and I.R. Plimer, Eds. *Encyclopedia of geology*, Elsevier, Oxford.

IAEA (2005) *Measurement of residual stress in materials using neutrons*. INTERNATIONAL ATOMIC ENERGY AGENCY, Vienna.

Ioannou, A. & Dimirkou, A. (1997) Phosphate adsorption on hematite, kaolinite, and IAEA (2005) *Measurement of residual stress in materials using neutrons*. INTERNATIONAL ATOMIC ENERGY AGENCY, Vienna.

kaolinite–hematite (k–h) systems as described by a constant capacitance model. *Journal of Colloid and Interface Science*, **192**, 119-128.

Ioannou, Z., Dimirkou, A. & Ioannou, A. (2013) Phosphate adsorption from aqueous solutions onto goethite, bentonite, and bentonite–goethite system. *Water, Air, & Soil Pollution*, **224**, 1374.

Jana, S., Kondakova, A.V., Shevchenko, S.N., Sheval, E.V., Gonchar, K.A., Timoshenko, V.Y. & Vasiliev, A.N. (2017) Halloysite nanotubes with immobilized silver nanoparticles for anti-bacterial application. *Colloids and Surfaces B: Biointerfaces*, **151**, 249-254.

Joo, Y., Sim, J.H., Jeon, Y., Lee, S.U. & Sohn, D. (2013) Opening and blocking the inner-pores of halloysite. *Chemical Communications*, **49**, 4519-4521.

Joussein, E., Petit, S., Churchman, J., Theng, B., Righi, D. & Delvaux, B. (2005) Halloysite clay minerals - a review. *Clay Minerals*, **40**, 383-426.

Joussein, E., Petit, S., Fialips, C.-I., Vieillard, P. & Righi, D. (2006) Differences in the dehydration-rehydration behavior of halloysites: New evidence and interpretations. *Clays and Clay Minerals*, **54**, 473-484.

Kamiyango, M.W., Masamba, W.R.L., Sajidu, S.M.I. & Fabiano, E. (2009) Phosphate removal from aqueous solutions using kaolinite obtained from linthipe, Malawi. *Physics and Chemistry of the Earth, Parts A/B/C*, **34**, 850-856.

Kaufhold, S. & Dohrmann, R. (2013) The variable charge of dioctahedral smectites. *Journal of Colloid and Interface Science*, **390**, 225-233.

Kautz, C.Q. & Ryan, P.C. (2003) The 10 Å to 7 Å halloysite transition in a tropical soil sequence, Costa Rica. *Clays and Clay Minerals*, **51**, 252-263.

Kim, T., Kim, S., Lee, D.K., Seo, B. & Lim, C.-S. (2017) Surface treatment of halloysite nanotubes with sol–gel reaction for the preparation of epoxy composites. *RSC Advances*, **7**, 47636-47642.

Kloprogge, J.T. (2016) Chapter 6 - characterisation of halloysite by spectroscopy. Pp. 115-136. In P. Yuan, A. Thill, and F. Bergaya, Eds. *Developments in Clay Science*, 7, Elsevier.

Kogure, T., Mori, K., Drits, V.A. & Takai, Y. (2013) Structure of prismatic halloysite. *American Mineralogist*, **98**, 1008-1016.

Kogure, T., Mori, K., Kimura, Y. & Takai, Y. (2011) Unraveling the stacking structure in tubular halloysite using a new tem with computer-assisted minimal-dose system. *American Mineralogist*, **96**, 1776-1780.

Kohyama, N., Fukushima, K. & Fukami, A. (1978) Observation of the hydrated form of tubular halloysite by an electron microscope equipped with an environmental cell. *Clays and Clay Minerals*, **26**, 25-40.

Krumina, L., Kenney, J.P.L., Loring, J.S. & Persson, P. (2016) Desorption mechanisms of phosphate from ferrihydrite and goethite surfaces. *Chemical Geology*, **427**, 54-64.

Kubicki, J.D., Paul, K.W., Kabalan, L., Zhu, Q., Mrozik, M.K., Aryanpour, M., Pierre-Louis, A.-M. & Strongin, D.R. (2012) ATR-FTIR and density functional theory study of the structures, energetics, and vibrational spectra of phosphate adsorbed onto goethite. *Langmuir*, **28**, 14573-14587.

Levis, S.R. & Deasy, P.B. (2002) Characterisation of halloysite for use as a microtubular drug delivery system. *Int J Pharm*, **243**, 125-134.

Li, Y., Liu, S., Yao, T., Sun, Z., Jiang, Z., Huang, Y., Cheng, H., Huang, Y., Jiang, Y., Xie, Z., Pan, G., Yan, W. & Wei, S. (2012) Controllable synthesis of gold nanoparticles with ultrasmall size and high monodispersity via continuous supplement of precursor. *Dalton Transactions*, **41**, 11725-11730.

Lin, Y., Wang, X., Liu, J. & Miller, J.D. (2017) Natural halloysite nano-clay electrolyte for advanced all-solid-state lithium-sulfur batteries. *Nano Energy*, **31**, 478-485.

Loganathan, P., Vigneswaran, S., Kandasamy, J. & Bolan, N.S. (2014) Removal and recovery of phosphate from water using sorption. *Critical Reviews in Environmental Science and Technology*, **44**, 847-907.

Lu, C. & Tian, H. (2017) Global nitrogen and phosphorus fertilizer use for agriculture production in the past half century: Shifted hot spots and nutrient imbalance. *Earth Syst. Sci. Data*, **9**, 181-192.

Lvov, Y., Wang, W., Zhang, L. & Fakhrullin, R. (2016) Halloysite clay nanotubes for loading and sustained release of functional compounds. *Advanced Materials*, **28**, 1227-1250.

Ma, C. & Eggleton, R.A. (1999) Cation exchange capacity of kaolinite. *Clays and Clay Minerals*, **47**, 174-180.

MacEwan, D. (1947) The nomenclautre of the halloysite minerals. *Mineralogical Magazine and Journal of the Mineralogical Society*, **28**, 196.

Madejová, J. (2003) FTIR techniques in clay mineral studies. *Vibrational Spectroscopy*, **31**, 1-10.

Mallick, K., Witcomb, M. & Scurrell, M. (2006) Silver nanoparticle catalysed redox reaction: An electron relay effect. *Materials Chemistry and Physics*, **97**, 283-287.

Mamontov, E. (2005) High-resolution neutron-scattering study of slow dynamics of surface water molecules in zirconium oxide. *The Journal of Chemical Physics*, **123**, 024706.

Manning, B.A. & Goldberg, S. (1996) Modeling arsenate competitive adsorption on kaolinite, montmorillonite and illite. *Clays and Clay Minerals*, **44**, 609-623.

Martin, R.T. (1980) Data handbook for clay materials and other non-metallic minerals. *Clays and Clay Minerals*, **28**, 160-160.

Massaro, M., Lazzara, G., Milioto, S., Noto, R. & Riela, S. (2017) Covalently modified halloysite clay nanotubes: Synthesis, properties, biological and medical applications. *Journal of Materials Chemistry B*, **5**, 2867-2882.

Middleton, A.P. & Whittaker, E.J.W. (1976) The structure of povlen-type chrysotile. *The Canadian Mineralogist*, **14**, 301-306.

Mounteney, I., Burton, A.K., Farrant, A.R., Watts, M.J., Kemp, S.J. & Cook, J.M. (2018) Heavy mineral analysis by ICP-AES a tool to aid sediment provenancing. *Journal of Geochemical Exploration*, **184**, 1-10.

Mukhopadhyay, S., Hewer, B., Howells, S. & Markvardsen, A. (2019) A modern approach to QENS data analysis in Mantid. *Physica B: Condensed Matter*, **563**, 41-49.

Müller, A., Bühler, E., Lamparter, P. & Steeb, S. (1987) Neutron- and X-ray-diffraction study on the structure of amorphous $Co_{25}Ti_{75}$. *Zeitschrift für Naturforschung A*, **42**, 7.

Norrish, K. (1995) *An unusual fibrous halloysite*. Pp. 275-284. CSIRO Publishing, Melbourne, Australia.

Oelkers, E.H. & Valsami-Jones, E. (2008) Phosphate mineral reactivity and global sustainability. *Elements*, **4**, 83-87.

Omotoso, O., McCarty, D.K., Hillier, S. & Kleeberg, R. (2006) Some successful approaches to quantitative mineral analysis as revealed by the 3rd reynolds cup contest. *Clays and Clay Minerals*, **54**, 748-760.

Pacioni, N.L., Borsarelli, C.D., Rey, V. & Veglia, A.V. (2015) Synthetic routes for the preparation of silver nanoparticles. Pp. 13-46. In E.I. Alarcon, M. Griffith, and K.I. Udekwu, Eds. *Silver nanoparticle applications: In the fabrication and design of medical and biosensing devices*,Springer International Publishing, Cham.

Pasbakhsh, P., Churchman, G.J. & Keeling, J.L. (2013) Characterisation of properties of various halloysites relevant to their use as nanotubes and microfibre fillers. *Applied Clay Science*, **74**, 47-57.

Parfitt, R.L. (1979) Anion adsorption by soils and soil materials. *Advances in Agronomy*, **30**, 1-50.

Peacock, C.L. & Sherman, D.M. (2005) Surface complexation model for multisite adsorption of copper(II) onto kaolinite. *Geochimica Et Cosmochimica Acta*, **69**, 3733-3745.

Pillai, Z.S. & Kamat, P.V. (2004) What factors control the size and shape of silver nanoparticles in the citrate ion reduction method? *The Journal of Physical Chemistry B*, **108**, 945-951.

Plieth, W., Dietz, H., Anders, A., Sandmann, G., Meixner, A., Weber, M. & Kneppe, H. (2005) Electrochemical preparation of silver and gold nanoparticles: Characterization by confocal and surface enhanced raman microscopy. *Surface Science*, **597**, 119-126.

Pouvreau, M., Greathouse, J.A., Cygan, R.T., Kalinichev, A.G. (2019) Structure of hydrated kaolinite edge surfaces: DFT results and further development of the ClayFF Classical Force Field with Metal-O-H angle bending terms. *Journal of Physical Chemistry C*, **123**, 11628-11638.

Presti, D., Pedone, A., Mancini, G., Duce, C., Tiné, M.R. & Barone, V. (2016) Insights into structural and dynamical features of water at halloysite interfaces probed by DFT and classical molecular dynamics simulations. *Physical Chemistry Chemical Physics*, **18**, 2164-2174.

Qu, S., Du, C., Song, Y., Wang, Y., Gao, Y., Liu, S., Li, Y. & Zhu, D. (2002) Optical nonlinearities and optical limiting properties in gold nanoparticles protected by ligands. *Chemical Physics Letters*, **356**, 403-408.

Rao, K.S., Ganeev, R.A., Zhang, K., Fu, Y., Boltaev, G.S., Maurya, S.K. & Guo, C. (2019) Comparative analyses of optical limiting effects in metal nanoparticles and perovskite nanocrystals. *Optical Materials*, **92**, 366-372.

Ren, X., Yang, S., Tan, X., Chen, C., Sheng, G. & Wang, X. (2012) Mutual effects of copper and phosphate on their interaction with γ-Al_2O_3: Combined batch macroscopic experiments with DFT calculations. *Journal of Hazardous Materials*, **237-238**, 199-208.

Saki, H., Alemayehu, E., Schomburg, J. & Lennartz, B. (2019) Halloysite nanotubes as adsorptive material for phosphate removal from aqueous solution. *Water*, **11**, 203.

Schneider, C.A., Rasband, W.S. & Eliceiri, K.W. (2012) Nih image to ImageJ: 25 years of image analysis. *Nature Methods*, **9**, 671-675.

Schroth, B.K. & Sposito, G. (1997) Surface charge properties of kaolinite. *Clays and Clay Minerals*, **45**, 85-91.

Singh, B. (1996) Why does halloysite roll?—a new model. *Clays and Clay Minerals*, **44**, 191-196.

Singh, B. & Gilkes, R.J. (1992) An electron optical investigation of the alteration of kaolinite to halloysite. *Clays and Clay Minerals*, **40**, 212-229.

Siretanu, I., van den Ende, D. & Mugele, F. (2016) Atomic structure and surface defects at mineral-water interfaces probed by in situ atomic force microscopy. *Nanoscale*, **8**, 8220-8227.

Sposito, G. (1984) *The surface chemistry of soils*. Pp. 234. Oxford University Press, New York,.

Takahashi, T., Dahlgren, R. & van Susteren, P. (1993) Clay mineralogy and chemistry of soils formed in volcanic materials in the xeric moisture regime of Northern California. *Geoderma*, **59**, 131-150.

Tarì, G., Bobos, I., Gomes, C.S.F. & Ferreira, J.M.F. (1999) Modification of surface charge properties during kaolinite to halloysite-7 Å transformation. *Journal of Colloid and Interface Science*, **210**, 360-366.

Taroni, T., Meroni, D., Fidecka, K., Maggioni, D., Longhi, M. & Ardizzone, S. (2019) Halloysite nanotubes functionalization with phosphonic acids: Role of surface charge on molecule localization and reversibility. *Applied Surface Science*, **486**, 466-473.

Theng, B.K.G., Russell, M., Churchman, G.J. & Parfitt, R.L. (1982) Surface properties of allophane, halloysite, imogolite. *Clays and Clay Minerals*, **30**, 143-149.

Uzunova, E.L. & Mikosch, H. (2016) Adsorption of phosphates and phosphoric acid in zeolite clinoptilolite: Electronic structure study. *Microporous and Mesoporous Materials*, **232**, 119-125.

Valsami-Jones, E. (2005) *Phosphorus in environmental technology: Principles and applications*. IWA Publishing.

Van Emmerik, T.J., Sandström, D.E., Antzutkin, O.N., Angove, M.J. & Johnson, B.B. (2007) ^{31}P solid-state nuclear magnetic resonance study of the sorption of phosphate onto gibbsite and kaolinite. *Langmuir*, **23**, 3205-3213.

Van Hyning, D.L. & Zukoski, C.F. (1998) Formation mechanisms and aggregation behavior of borohydride reduced silver particles. *Langmuir*, **14**, 7034-7046.

Vergaro, V., Abdullayev, E., Lvov, Y.M., Zeitoun, A., Cingolani, R., Rinaldi, R. & Leporatti, S. (2010) Cytocompatibility and uptake of halloysite clay nanotubes. *Biomacromolecules*, **11**, 820-826.

Vinokurov, V.A., Stavitskaya, A.V., Chudakov, Y.A., Ivanov, E.V., Shrestha, L.K., Ariga, K., Darrat, Y.A. & Lvov, Y.M. (2017) Formation of metal clusters in halloysite clay nanotubes. *Science and Technology of Advanced Materials*, **18**, 147-151.

Vitousek, P.M. & Howarth, R.W. (1991) Nitrogen limitation on land and in the sea: How can it occur? *Biogeochemistry*, **13**, 87-115.

Wada, K. (1961) Lattice expansion of kaolin minerals by treatment with potassium acetate. *American Mineralogist*, **46**, 78-91.

Wada, K. (1967) A study of hydroxyl groups in kaolin minerals utilizing selective deuteration and infrared spectroscopy. *Clay Minerals*, **7**(1), 51-61.

Wei, S., Tan, W., Liu, F., Zhao, W. & Weng, L. (2014) Surface properties and phosphate adsorption of binary systems containing goethite and kaolinite. *Geoderma*, **213**, 478-484.

Weng, L., Van Riemsdijk, W.H. & Hiemstra, T. (2012) Factors controlling phosphate interaction with iron oxides. *J Environ Qual*, **41**, 628-635.

White, G.N. & Dixon, J.B. (2002) Kaolin-serpentine minerals. *Soil Science Society America*, **7**, 367-388.

Wilson, I. & Keeling, J. (2016) Global occurrence, geology and characteristics of tubular halloysite deposits. *Clay Minerals*, **51**, 309-324.

Wilson, I.R. (2004) Kaolin and halloysite deposits of China. *Clay Minerals*, **39**, 1-15.

Wisawapipat, W., Kheoruenromne, I., Suddhiprakarn, A. & Gilkes, R.J. (2009) Phosphate sorption and desorption by Thai upland soils. *Geoderma*, **153**, 408-415.

Yada, K & Lui, W. (1987) Polygonal microstructures of Polven chrysotile observed by high resolution electron microscopy. Sixth Meet. Europ. Clay. Group (Seville, Spain), 596-597.

Yah, W.O., Takahara, A. & Lvov, Y.M. (2012) Selective modification of halloysite lumen with octadecylphosphonic acid: New inorganic tubular micelle. *Journal of the American Chemical Society*, **134**, 1853-1859.

Yu, W., Xu, H., Tan, D., Fang, Y., Roden, E.E. & Wan, Q. (2020) Adsorption of iodate on nanosized tubular halloysite. *Applied Clay Science*, **184**, 105407.

Yuan, P., Southon, P.D., Liu, Z., Green, M.E.R., Hook, J.M., Antill, S.J. & Kepert, C.J. (2008) Functionalization of halloysite clay nanotubes by grafting with γ-aminopropyltriethoxysilane. *The Journal of Physical Chemistry C*, **112**, 15742-15751.

Yuan, P., Tan, D. & Annabi-Bergaya, F. (2015) Properties and applications of halloysite nanotubes: Recent research advances and future prospects. *Applied Clay Science*, **112-113**, 75-93.

Zbik, M. & Smart, R.S.C. (1998) Nanomorphology of kaolinites: Comparative SEM and AFM studies. *Clays and Clay Minerals*, **46**, 153-160.

Zhang, S., Liu, Q., Gao, F., Li, X., Liu, C., Li, H., Boyd, S.A., Johnston, C.T. & Teppen, B.J. (2017) Mechanism associated with kaolinite intercalation with urea: Combination of infrared spectroscopy and molecular dynamics simulation studies. *The Journal of Physical Chemistry C*, **121**, 402-409.

Zhang, X.F., Liu, Z.G., Shen, W. & Gurunathan, S. (2016) Silver nanoparticles: Synthesis, characterization, properties, applications, and therapeutic approaches. *International Journal of Molecular Sciences*, **17**.

Zhou, Z. & Gunter. William, D. (1992) The nature of the surface charge of kaolinite. *Clays and Clay Minerals*, **40**, 365-368.

Appendices

Derivative thermogravimetric curves (DTG) are included here where the work is outlined in Chapter 5, Section 5.4.2.

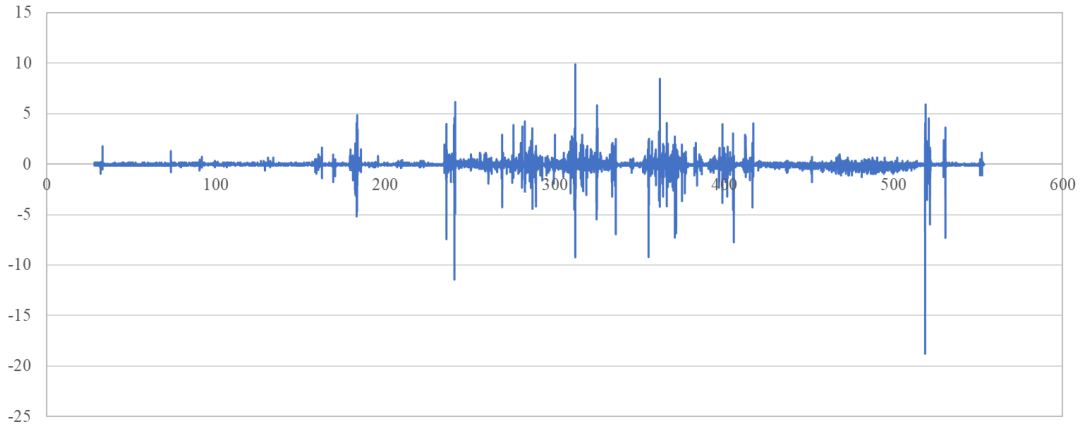

Figure 8.1. Graph of the DTG data of cylindrical halloysite (7 Å) 4Ch + Au phosphonic acid where the Au phosphonic acid indicates gold nanotag with phosphonic acid terminated linker.

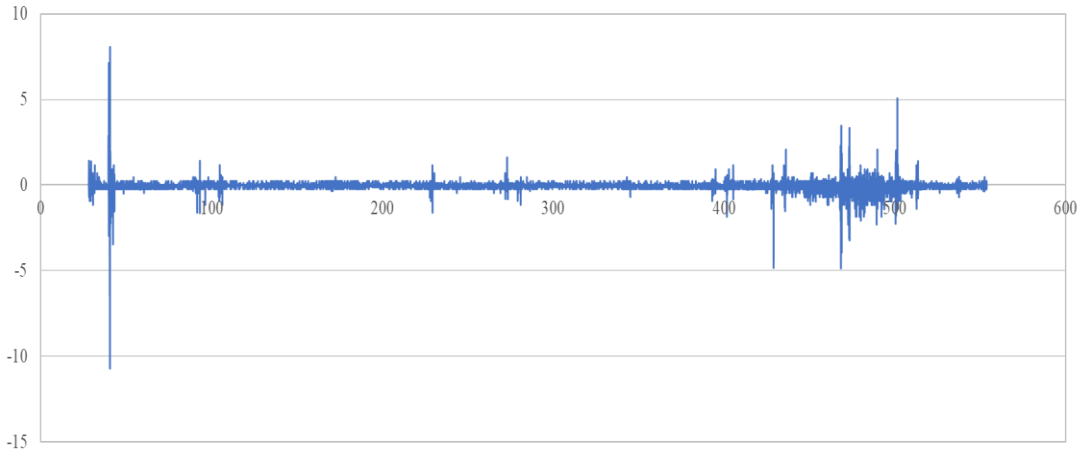

Figure 8.2. Graph of the DTG data of cylindrical halloysite (7 Å) 4Ch + Au methyl, where the Au methyl indicates gold nanotag with methyl terminated linker.

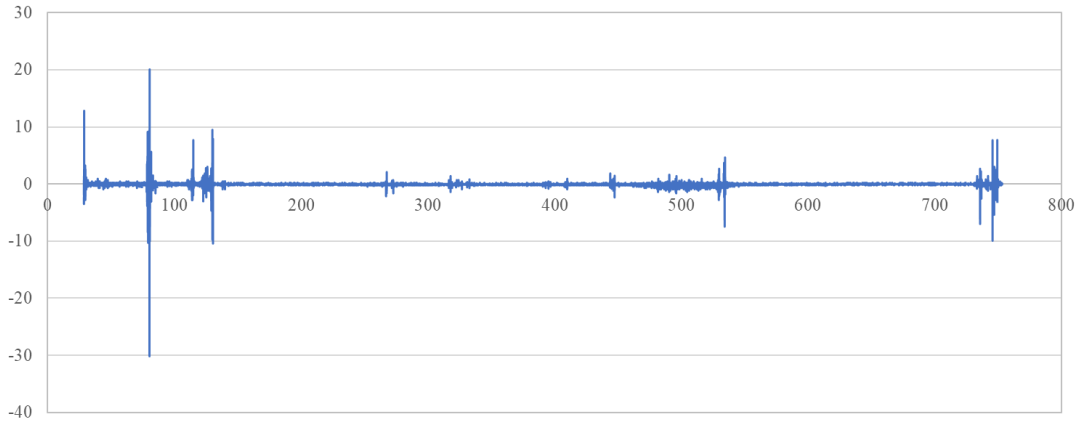

Figure 8.3. Graph of the DTG data of prismatic halloysite (7 Å) 4Ch + Au phosphonic acid, where the Au phosphonic acid indicates gold nanotag with phosphonic acid terminated linker.

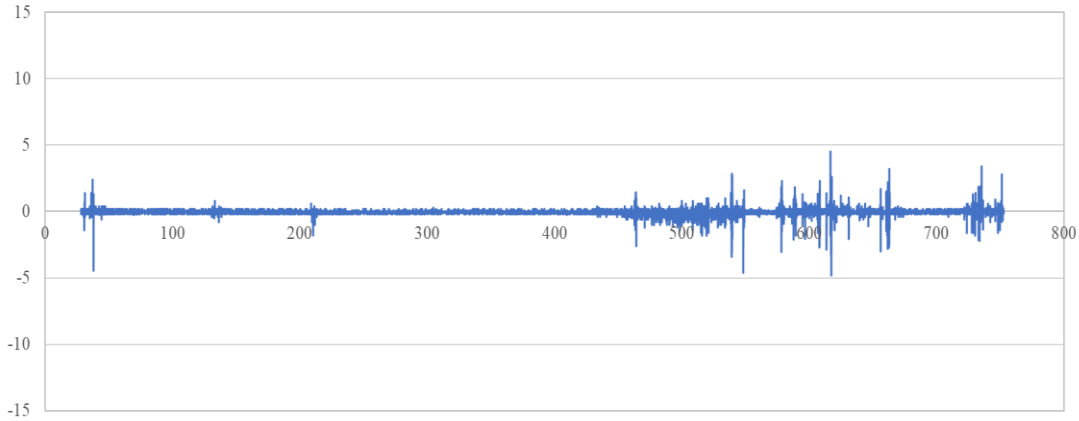

Figure 8.4. Graph of the DTG data of prismatic halloysite (7 Å) 17US + Au methyl, where the Au methyl indicates gold nanotag with methyl terminated linker.